Dissertation zur Erlangung des Doktorgrades
der Fakultät für Chemie und Pharmazie
der Ludwig-Maximilians-Universität München

Synthesis, Characterization and Quantum-Chemical Analysis of $\{FeNO\}^7$ Compounds with Oxygen-Donor Ligands

Georg Monsch
aus
Karaganda, Kasachstan

2020

Erklärung
Diese Dissertation wurde im Sinne von § 7 der Promotionsordnung vom 28. November 2011 von Herrn Prof. Dr. Peter Klüfers betreut.

Eidesstattliche Versicherung
Diese Dissertation wurde eigenständig und ohne unerlaubte Hilfe erarbeitet.

München, 07.01.2020

Georg Monsch

Dissertation eingereicht am 07.01.2020
1. Gutachter: Prof. Dr. Peter Klüfers
2. Gutachter: Prof. Dr. Hans-Christian Böttcher
Mündliche Prüfung am 06.02.2020

Contents

List of Figures

List of Tables

Abbreviations

ATR	attenuated total reflection
Bn	benzyl
br	broad
calc	calculated
CShM	continuous shape measurement
DFT	density functional theory
DBU	1,8-Diazabicyclo(5.4.0)undec-7-ene
Et	ethyl
equiv	equivalent, equivalents
FAB	fast atom bombardment
FMN	flavin mononucleotide
FNOR	flavodiiron nitric oxide reductase
HOMO	highest occupied molecular orbital
IR	infrared
L	ligand
LUMO	lowest unoccupied molecular orbital
m	medium (IR spectroscopy) / multiplet (NMR spectroscopy)
M	metal
Me	methyl
MO	molecular orbital
MS	mass spectrometry
NMR	nuclear magnetic resonance
OC-6	octahedron (hexacoordinated)
Ph	phenyl
PLI	photoinduced linkage isomerism
PPN	bis(triphenylphosphine)iminium
q	quartet
R	residue
s	strong (IR spectroscopy)
solv	solvent
SP-4	square planar (tetracoordinated)
SPY-5	square pyramid (pentacoordinated)

t	triplet
$TBPY$-5	trigonal bipyramid (pentacoordinated)
TD-DFT	time dependent density functional theory
THF	tetrahydrofurane
UV-VIS	ultraviolet-visible
vOC-5	vacant octahedron (pentacoordinated)
vs	very strong
vw	very weak
w	weak

Disambiguations for abbreviations of quantum-chemical methods can be found in Section 5.3.

Overview of numbered compounds

Bis(perfluoropinacolato)ferrates(II)

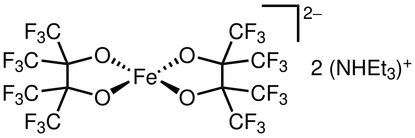

$(NHEt_3)_2[Fe(fpin)_2]$

1a

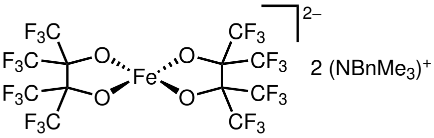

$(NBnMe_3)_2[Fe(fpin)_2]$

1b

Mono(perfluoropinacolato)iron(II) compounds

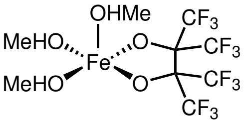

$[Fe(fpin)(MeOH)_3]$

2a

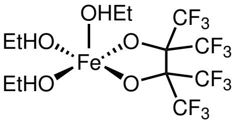

$[Fe(fpin)(EtOH)_3] \cdot EtOH$

2b

Dinuclear perfluoropinacolatoiron(II) compounds

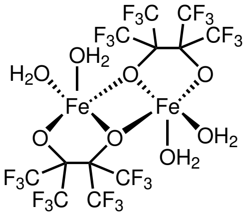

$[Fe_2(fpin\text{-}1\kappa O{:}1,1'\kappa O')_2(H_2O)_4] \cdot 2\,H_2O$

3a

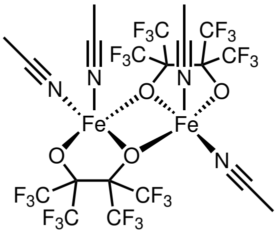

$[Fe_2(fpin\text{-}1\kappa O{:}1,1'\kappa O')_2(MeCN)_4]$

3b

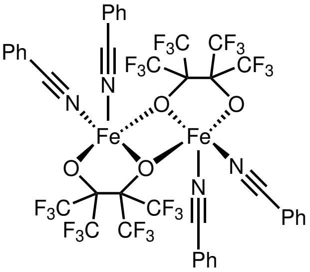

$[Fe_2(fpin\text{-}1\kappa O{:}1,1'\kappa O')_2(PhCN)_4]$

3c

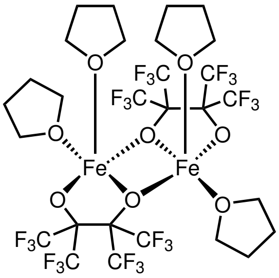

$[Fe_2(fpin\text{-}1\kappa O{:}1,1'\kappa O')_2(thf)_4]$

3d

Aquanitrosyliron compounds

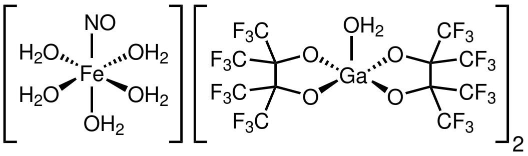

$[Fe(H_2O)_5(NO)][Ga(fpin)_2(H_2O)]_2 \cdot 8.34\,H_2O$

4a

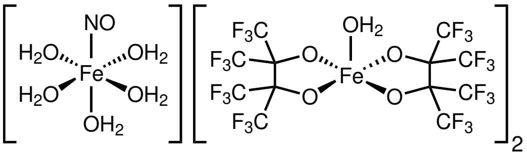

$[Fe(H_2O)_5(NO)][Fe(fpin)_2(H_2O)]_2 \cdot 8.31\,H_2O$

4b

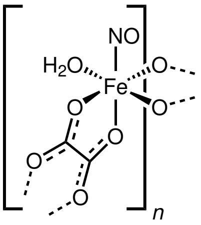

$[\{Fe(H_2O)(NO)(\mu\text{-}ox)\}_{n/n}] \cdot H_2O$

5

Nitrosylbis(perfluoropinacolato)ferrates

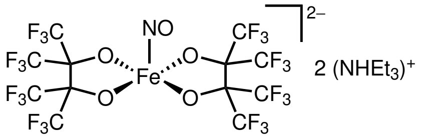

$(NHEt_3)_2[Fe(fpin)_2(NO)]$

6

Neutral nitrosylperfluoropinacolatoiron compounds

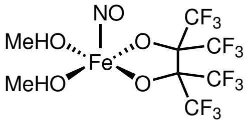

$[Fe(fpin)(MeOH)_2(NO)] \cdot MeOH$

7a

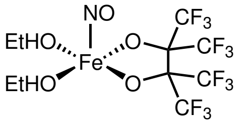

$[Fe(EtOH)_2(fpin)(NO)]$

7b

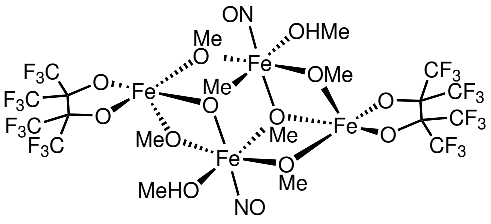

$[\{Fe_2(fpin\text{-}1\kappa O, O')(MeOH\text{-}2\kappa O)(NO\text{-}2\kappa N)\text{-}$
$(OMe\text{-}1{:}2\kappa O{,}1{:}2'\kappa O{,}1{:}2{:}2'\kappa O)_3\}_2] \cdot 2\,MeOH$

8a

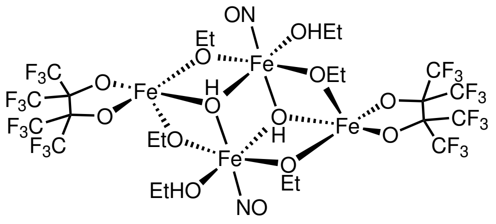

$[\{Fe_2(EtOH\text{-}2\kappa O)(fpin\text{-}1\kappa O, O')(NO\text{-}2\kappa N)\text{-}$
$(OEt\text{-}1{:}2\kappa O{,}1{:}2'\kappa O)_2(OH\text{-}$
$1{:}2{:}2'\kappa O)\}_2] \cdot 2\,EtOH$

8b

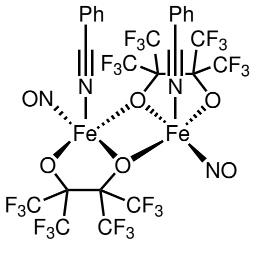

$[\{Fe(fpin\text{-}1\kappa O{:}1{,}1'\kappa O')(NO)(PhCN)\}_2]$

9

1 Introduction

1.1 Properties and biological relevance of nitric oxide

Nitric oxide is the simplest binary nitrogen oxide and a highly endothermic product of its elements, nitrogen and oxygen.[1]

$$N_2 + O_2 \longrightarrow 2\,NO \qquad \Delta_R H^{\ominus} = 180.62\,\mathrm{kJ\,mol^{-1}} \tag{1.1}$$

At ambient conditions nitric oxide is a colorless gas. It has a low dipole moment of $5.29 \times 10^{-31}\,\mathrm{C\,m}$[2] making it poorly soluble in water.[3,4] As NO has an uneven number of 15 electrons, it is a paramagnetic radical. The unpaired electron is located in the antibonding π^*-orbital resulting in a bond order of 2.5 (Figure 1.1).

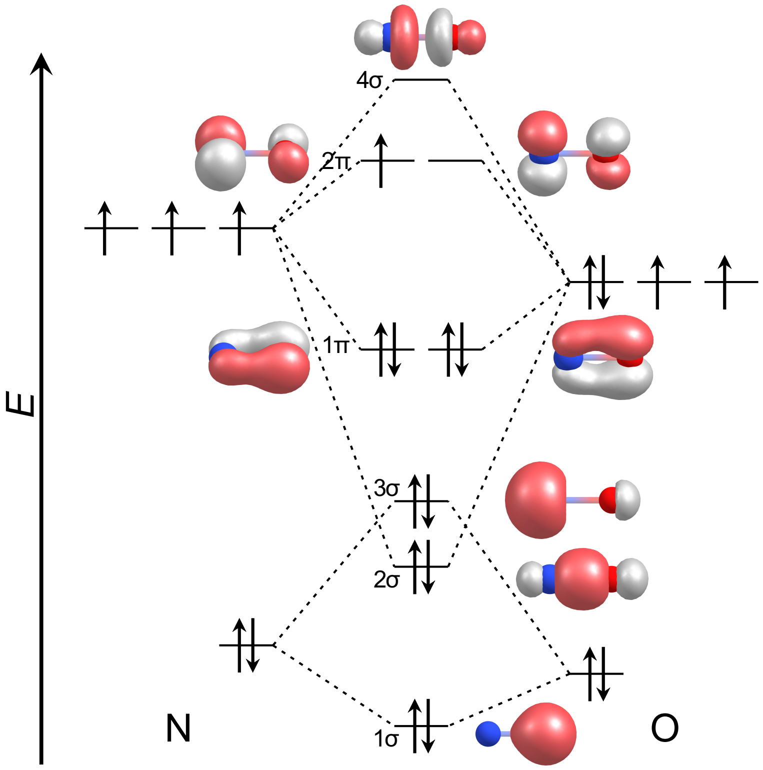

Figure 1.1: Qualitative molecular orbital diagram of nitric oxide. Calculated using a CASSCF approach with a (15, 10) active space and the def2-tzvp basis set. Isovalue 0.16.

Nitric oxide is highly reactive and shows apparent reactivity when exposed to oxygen such as from ambient air, yielding brown gaseous NO_2. Furthermore, nitric oxide can easily be oxidized to the nitrosyl (also nitrosonium) cation NO^+ or reduced to the nitroxyl anion NO^-. Electron transfer can also be performed upon coordination of a redox-active metal center via oxidative or reductive nitrosylation. For this reason the nitrosyl ligand is labeled as a non-innocent ligand. Thus, it is not possible to determine the exact oxidation state of the metal center M, as the nitrosylation product can be described as $M–NO^0$, as well as $M^+–NO^-$ and $M^-–NO^+$ — each with different oxidation states. In consequence, Enemark and Feltham proposed a notation that omits the use of formal oxidation states to avoid further confusion. Instead, it uses the sum of the electrons m in the metal d orbitals and the π^* orbitals in the number n of nitrosyl ligands to formulate the metal-nitrosyl fragment according to $\{M(NO)_n\}^m$.[5]

The ligand properties of NO are predominantly determined by its frontier orbitals, the HOMO 2π orbitals (orbital labels according to Figure 1.1). Through the 3σ orbital nitrosyl can act as a σ donor and can form σ bonds with empty orbitals of the metal. The influence of the 2π orbitals, however, is highly dependent on the number of occupying electrons. Generally, it can be said that a NO^+ ligand, isoelectronic to CO, enables π backbonding — preferably to Lewis basic metal centers — and therefore is supposed to favor a linear coordination. Consequently, a neutral NO^0 ligand, isoelectronic to $O_2^{\bullet+}$, is assumed to coordinate in a slightly bent manner at an angle of around 140°. A NO^- ligand, like its isoelectronic counterpart O_2, can be in a singulet or a triplet state. While $^3NO^-$ should show an almost linear coordination of 160 to 180°, MNO fragments containing a $^1NO^-$ ligand are expected to exhibit an angle of around 120°.[6,7] The associated orbital interactions are displayed in Figure 1.2.

Although the size of the lobes on the nitrogen atom shows the preference towards κN coordination (Figure 1.1), NO shows ambident behavior and, thus, can also bind via the oxygen atom as nitrosyl-κO (also isonitrosyl) and in a side-on configuration as nitrosyl-$\kappa^2 N,O$.[6] In certain cases, the binding mode can be switched by irradiation with light of a certain wavelength through photoinduced linkage isomerism (PLI), as was first discovered in $Na_2[Fe(CN)_5(NO)] \cdot 2\,H_2O$.[8]

As a main character in the everlasting and, especially due to recent news coverage,[9–12] lately intensifying discussion regarding air pollutants responsible for acid rain,[13] promoting cancer[14,15] and depletion of the ozone layer[16–18], nitric oxide has received a rather dubious reputation. At the same time its high significance for biological systems has been uncovered in the last three decades. It was found to have vasodilatory properties, rendering it a regulatory function in blood pressure.[19] Also it acts as a neurotransmitter in the brain and the peripheral nervous system,[20] as an anti-tumor agent[15] and is released in mammalian immune response.[21]

NO is synthesized by NO synthases (NOS) in mammalian cells, for example in the endothelium, upon oxidation of L-arginine to L-citrulline (Figure 1.3).[22]

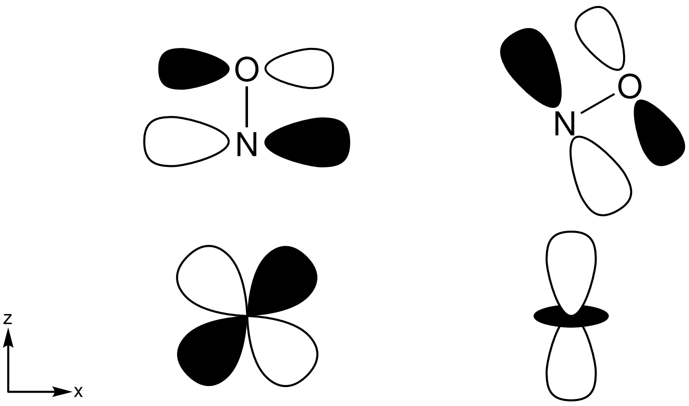

Figure 1.2: Schematic illustration of molecular orbitals involved in metal-nitrosyl bonding. Left: π bond ($2\pi_{xz}+d_{xz}$, $2\pi_{yz}+d_{yz}$), right: σ bond ($2\pi_{xz}+d_{z^2}$).

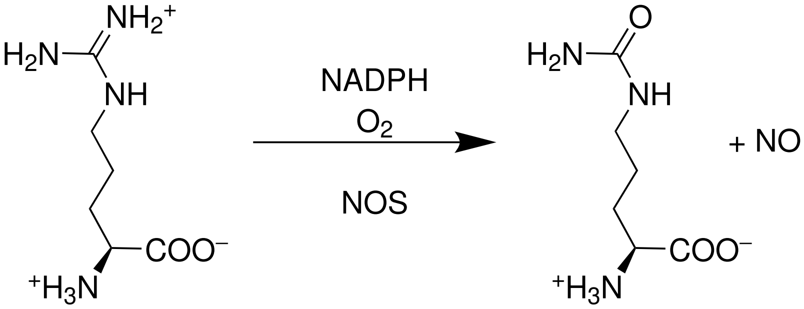

Figure 1.3: NO synthesis catalyzed by nitric-oxide synthase. Adapted from Reference [22].

In consequence of its biochemical importance, it was nominated molecule of the year in 1992 by *Science*[23,24] and in 1998 Furchgott, Ignarro and Murad were awarded the Nobel prize "for their discoveries concerning nitric oxide as signaling molecule in the cardiovascular system".[25–28]

1.2 High-spin $\{FeNO\}^7$ compounds in coordination chemistry

This thesis focuses on high-spin $\{FeNO\}^7$ compounds according to the Enemark–Feltham notation, which can be generated from Fe^{II} ($Fe\text{-}d^6$) precursors and gaseous nitric oxide. In accordance with the spin state of $S = 3/2$, the designations as high-spin $\{FeNO\}^7$, quartet $\{FeNO\}^7$ and $\{FeNO\}^7(S = 3/2)$ are equivalent and will, therefore, be used synonymously in the following.

The parent compound of the $\{FeNO\}^7(S = 3/2)$ family, the $[Fe(H_2O)_5(NO)]^{2+}$ cation, has been known since the 19th century. Observed both as the chromophore in the "brown-ring" of the nitrate test and as a reaction product of aqueous solutions containing ferrous salt, such as ferrous sulfate with gaseous nitric oxide, its cationic nature and its equimolar amount of iron and nitric oxide was found by the groups of Manchot and Kohlschütter.[29,30]

Since then, the oxidation state of the metal center has been a matter of discussion. In 1958 Wilkinson *et al.* formulated the $[Fe(H_2O)_5(NO)]^{2+}$ cation comprising a Fe^{I} center with a $^{1}NO^{+}$ ligand, as a result of the determined $S = 3/2$ spin state and the nitrosyl stretching frequency found at approximately 1810 cm^{-1}.[31] However, in 2002 the groups of Stochel and van Eldik postulated, based on spectroscopic data, a $Fe^{III}(S = 5/2)$ center antiferromagnetically coupled to a $^{3}NO^{-}$ ligand.[32] Furthermore, in 2004 DFT studies by Cheng *et al.* indicated a linear FeNO moiety with an $Fe^{II}(S = 2)$ center and an antiferromagnetically coupled neutral $^{2}NO^{0}$ ligand.[33] Conradie *et al.* presented an unusually flat bending potential of the FeNO moiety, in their studies also leading to a linear FeNO unit.[34]

Due to the high tendency of the $[Fe(H_2O)_5(NO)]^{2+}$ cation to release nitric oxide once it has been removed from the NO saturated medium, a structural characterization has not yet been feasible. In a survey on the stability of various $\{FeNO\}^7(S = 3/2)$ compounds in respect to NO loss, the $[Fe(H_2O)_5(NO)]^{2+}$ cation showed the highest tendency to release nitric oxide among all tested compounds.[35]

Another high-spin $\{FeNO\}^7$ species closely related to the $[Fe(H_2O)_5(NO)]^{2+}$ cation is the $[FeCl_3(NO)]^{-}$ anion. First found by Kohlschütter in his studies on the "brown-ring" chromophore in 1904 and 1907 in a similar reaction as the green product of ferrous chloride and nitric oxide in concentrated hydrochloric acid,[29,36] a crystal structure was not published until 1983 by the Beck group.[37]

While $\{FeNO\}^7(S = 3/2)$ compounds are by now quite established in literature, O-donor ligands still play an underwhelming role. In most cases coordination is established either by mixed N,O-chelators like aminecarboxylates, their respective esters[38–41], and aminealcoholates and -phenolates respectively (e.g. salen-type)[42–46], or mixed ligand spheres of N-donors and O-donors like carboxylates,[39,44,46–50] (weakly) coordinating anions,[51–58] coordinating solvents and other aqua-based (aqua, hydroxido, oxido) ligands.[38–40,45,47,48,51,57,59,60] Regarding high-spin $\{FeNO\}^7$ complexes with pure O-donor co-ligands, examples of structurally characterized compounds are still rare. The only instances are $[Tl(\mu{-}Mes_2ArCO_2)_3Fe(NO)]$ (Mes_2ArCO_2 = 2,6-dimesitylbenzoate), $[Fe_4(Mes_2ArCO_2)_4(NO)_4(\mu_3{-}OH)_4]$,[47], $(PPN)_2[Fe(NO_2\text{-}\kappa O)_3(NO_2\text{-}\kappa^2 O)(NO)]$ (PPN = bis(triphenylphosphane)iminium),[55] $(PPN)_2[Fe(NO_3\text{-}\kappa O)_3(NO_3\text{-}\kappa^2 O)(NO)]$[56] and $[Fe(H_2O)_2(NO)(oda)]$ (oda = oxodiacetate).[39]

High-spin $\{FeNO\}^7$ compounds show relevance for bioinorganic chemistry. They occur, for example, in the active site of flavodiiron-nitric-oxide reductases (FNORs), which are capable of catalyzing the reduction of nitric oxide to nitrous oxide according to Equation 1.2.[61]

$$2\,NO + 2\,e^{-} + 2\,H^{+} \longrightarrow N_2O + H_2O \tag{1.2}$$

This reaction is used by various pathogenic bacteria as a defense mechanism against the release of nitric oxide in the mammalian immune response.[61–64] In doing so, nitric oxide is converted into less toxic nitrous oxide, enabling the pathogens to proliferate and, in consequence, cause harmful infections in mammalians.[65] In the case of *Desulfovibrio gigas*, the active site features two fivefold coordinated ferrous centers at a Fe–Fe distance of 3.2 – 3.6 Å. The linkage is realized by a bridging aspartato and an aqua-based ligand (Figure 1.4). The rest of the coordination spheres of both iron centers is occupied by two histidine and one glutamato ligands in one case and one aspartato, one aqua and one histidine ligand in the other case. A flavin mononucleotide cofactor is situated in close proximity, allowing fast electron transfer with the diiron core and, thus, aid with the reduction.[61,66]

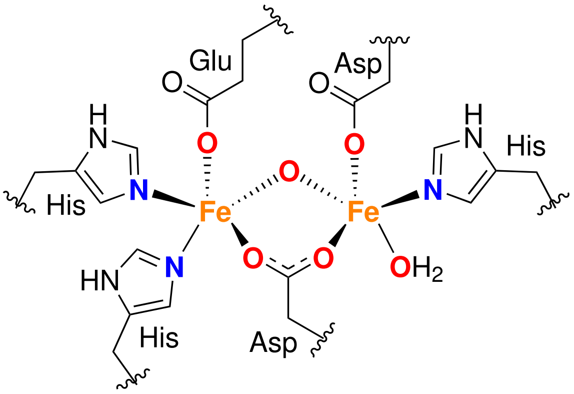

Figure 1.4: Schematic depiction of the active site in a flavodiiron-nitric-oxide reductase found in *Desulfovibrio gigas*.[66]

The mechanism of the nitric-oxide reduction still is a matter of discussion. Three pathways have been deemed to be the most likely. They are each labeled after their defining intermediate species or reaction step according to diFeNO, with a dinuclear {FeNO}^{7} species, hyp, with a hyponitrito species, and sr, showing FMNH$_2$-mediated "super-reduction". The common first step, the nitrosylation of the diferrous Fe^{II}Fe^{II} species with less than 1 equiv nitric oxide, leads to a stable mononitrosylated Fe^{II}{FeNO}^{7} species. In the hyp mechanism, upon addition of a second equivalent of NO, it reacts directly with the {FeNO}^{7} center, leading to a diferric intermediate with a bridging hyponitrito ligand (step 1hyp). The intermediate species then decays in a rate-limiting step under release of nitrous oxide to the diferric Fe^{III}Fe^{III} species (step 2hyp).[67] Both the diFeNO and sr mechanism propose instead, that the binding of a second equivalent of NO leads to a [{FeNO}^{7}]$_2$ intermediate (step 1diFeNO, 1sr). Then, the diFeNO mechanism suggests a rate-limiting N–N bond formation between both nitrosyl ligands, succeeded by protonation and release of nitrous oxide and water (step 2diFeNO). The alternative sr mechanism proposes instead the "super-reduction" of the [{FeNO}^{7}]$_2$ intermediate by FMNH$_2$ to a highly reactive [{Fe(H)NO}^{8}]$_2$ species (step 2sr), which, in consequence, releases N$_2$O and H$_2$O to give the diferrous Fe^{II}Fe^{II} species (step 3sr).

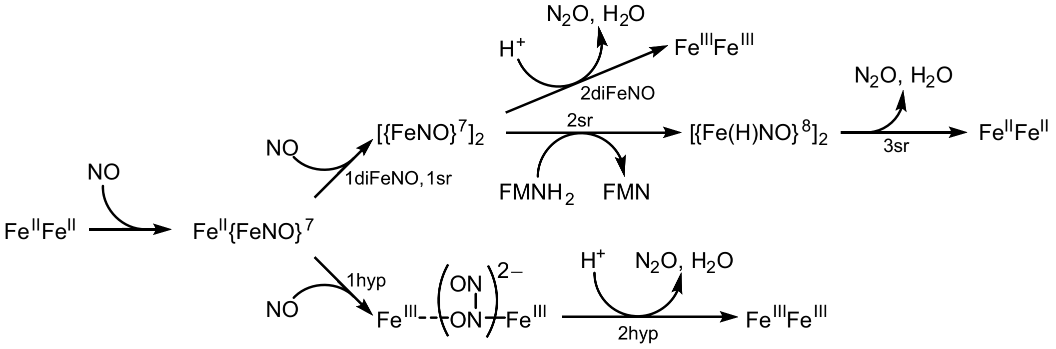

Figure 1.5: Proposed mechanisms for the reduction of nitric oxide by flavodiiron-nitric-oxide reductases.

1.3 Aim of this work

As was shown in Section 1.2, to this day, there are still relatively few known examples of structurally characterized nitrosyliron complexes with O-donor co-ligands. Especially $\{FeNO\}^7(S = 3/2)$ compounds with pure O-donor coordination of the FeNO entity are very rare, as only four cases have been published yet. In this respect, it has to be mentioned that not even the parent species of $\{FeNO\}^7(S = 3/2)$ compounds, the tentative $[Fe(H_2O)_5(NO)]^{2+}$ cation, has been isolated as a solid salt. Therefore its structure could only be speculated upon.

Hence, this work aims to prepare and crystallize further $\{FeNO\}^7(S = 3/2)$ compounds with O-donor ligands such as diolates, carboxylates and coordinating solvents. Of special interest was the crystallization of stable $[Fe(H_2O)_5(NO)]^{2+}$ salts. As far as applicable, the products obtained should then serve as subjects for further photoirradiation experiments and quantum-chemical examination. Square-planar high-spin ferrates(II) with dianionic diolato ligands, that are known for anhydroerythritolato[68] and perfluoropinacolato[69,70] ligands, served as a starting point in this work. Of both ligands perfluoropinacolate presented itself as especially suitable, as it allows work under acidic as well as slightly alkaline conditions. Facile deprotonation is thereby enabled by the highly negative inductive effect of the CF_3 substituents leading to pK_a values of $pK_{a1} = 5.8$ and $pK_{a2} = 10.1$. With that in mind, reaction conditions such as the solvent, pH and reactant ratios were varied. Among all tested ligands, this work focuses on reactions with perfluoropinacolato and oxalato co-ligands.

2 Results

2.1 Synthesis of $A_2[Fe(fpin)_2]$ ($A=NHEt_3^+$, $NBnMe_3^+$; 1a, 1a)

The synthesis of bis(perfluoropinacolato)ferrates(II) followed a modified procedure, published by Wurzenberger, where iron(II) triflate was treated with 2 equiv of perfluoropinacol and 4 equiv of a base in methanolic solution.[69] The use of NEt_3 as base yielded $(NHEt_3)_2[Fe(fpin)_2]$ (**1a**) while $NBnMe_3(OMe)$ gave $(NBnMe_3)_2[Fe(fpin)_2]$ (**1b**). **1a** was poorly soluble in methanol with an almost colorless supernatant solution and was completely precipitated by the addition of water. After filtration the product was washed with water and dried *in vacuo*. **1a** was obtained as a lavender powder in 91% yield. Crystals were obtained after recrystallization in methanol.

1b showed a higher solubility in methanol than **1a** leading to deep blue solutions. For isolation of the product the solvent was removed *in vacuo* and then washed with cold methanol. **1b** was obtained as a lavender powder in 74% yield. Crystals formed in a saturated reaction solution after cooling. Both compounds quickly showed discoloration upon contact with ambient oxygen. Characterization of **1a** and **1b** was performed by single-crystal X-ray diffraction, elemental analysis, IR and UV/Vis spectroscopy. In addition, FAB-MS was conducted on **1b**. The UV/Vis spectra both of solid **1a** diluted with $BaSO_4$ and a solution in acetone featured absorption bands below <380 nm and at approximately 580 nm. In methanolic solutions of **1b** an absorption band was observed at 647 nm.

The FAB^+ mass spectrum of **1b** showed peaks for the cationized compound $[M]^+$ at $m/z = 1020.1$ and the $NBnMe_3^+$ cation at $m/z = 150.2$. In the FAB^- mass spectrum peaks for the anionized compounds $[M + H]^-$ at $m/z = 1021.9$, $[M - NBnMe_3]^-$ at $m/z = 870.1$ and $[M - 2\,NBnMe_3]^-$ at $m/z = 720.0$ were present.

Both compounds crystallized in the monoclinic space group $P2_1/n$. The respective structures are displayed in Figure 2.1 (**1a**) and Figure 2.2 (**1b**). Relevant distances, angles and CShM values are listed in the captions. In both cases, the primitive cell contained two formula units of **1a** with each asymmetric unit consisting of half a complex anion and one cation. In the complex anions, the central iron atoms were coordinated by two perfluoropinacolato ligands in a square plane that was slightly distorted towards a rectangle as indicated by the deviation of the O_{fpin}–Fe–O_{fpin} angles from 90°. The mean Fe–O distances were 1.974 Å (**1a**) and 1.9767 Å (**1b**). In **1a**, each perfluoropinacolato ligand showed disorder across all atom positions at a ratio of both parts of 52:48 with a twist of 17.2° of the respective O_{fpin}–Fe–O_{fpin} planes, O1–Fe1–O2 and O1B–Fe1–O2B, against one another.

In **1a**, the $NHEt_3^+$ cations formed classical hydrogen bonds to O1 and O1B respectively with N1 as donor and O1 and O1B as acceptors, alongside non-classical hydrogen bonds with C13 and C15 as donors and O2 and O2B respectively as acceptors (Table 2.1). The $NBnMe_3^+$ cation and the complex anion in **1b** showed interactions via non-classical hydrogen bonds, donated by C7 and C15 to each of the acceptors O1 and O2 (Table 2.2). In addition, the phenyl groups in the $NBnMe_3^+$ cation exhibited parallel-displaced stacking with a distance alternating from layer to layer between 3.5 and 5.3 Å.

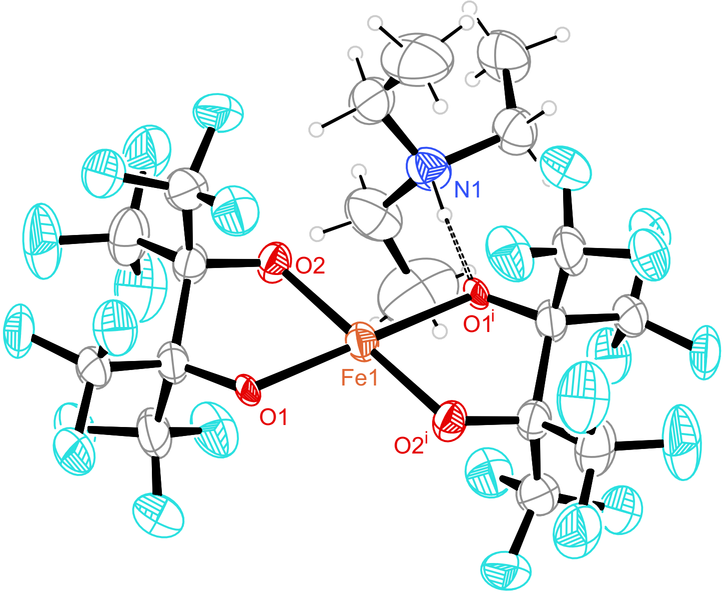

Figure 2.1: *Ortep* plot of $(NHEt_3)_2[Fe(fpin)_2]$ in crystals of **1a** (major disorder form). Measurement temperature: 143(2) K. Space group: $P2_1/n$. CShM$_{SP\text{-}4}$: 0.670. The thermal ellipsoids are drawn at 50% probability level. Atoms: carbon (gray), hydrogen (light gray), fluorine (green), iron (orange), nitrogen (blue), oxygen (red). Interatomic distances (Å) and angles (°) with the standard deviation in parentheses: Fe1–O1 2.116(15), Fe1–O2 1.966(7); O1–Fe1–O2 81.6(3), O1–Fe1–O2^i 98.4(3), O1–Fe1–O1^i 180.0, O2–Fe1–O2^i 180.0. Symmetry code: $^i 1-x, 1-y, 1-z$.

Table 2.1: Hydrogen bonds in crystals of **1a**. Coordinates of hydrogen atoms were calculated in idealized positions, riding on their parent atoms.

D–H···A	d(D–H)/Å	d(H···A)/Å	d(D–A)/Å	∠(D–H···A)/°
N1–H1···O1^i	1.00	1.76	2.758(13)	177.9
N1–H1···O1B^i	1.00	1.93	2.927(14)	173.6
C13–H13A···O2	0.99	2.75	3.479(7)	130.4
C13–H13A···O2B	0.99	2.43	3.192(8)	133.2
C15–H15B···O2	0.99	2.32	3.130(7)	138.1
C15–H15B···O2B	0.99	2.53	3.281(7)	132.5

Symmetry code: $^i 1-x, 1-y, 1-z$

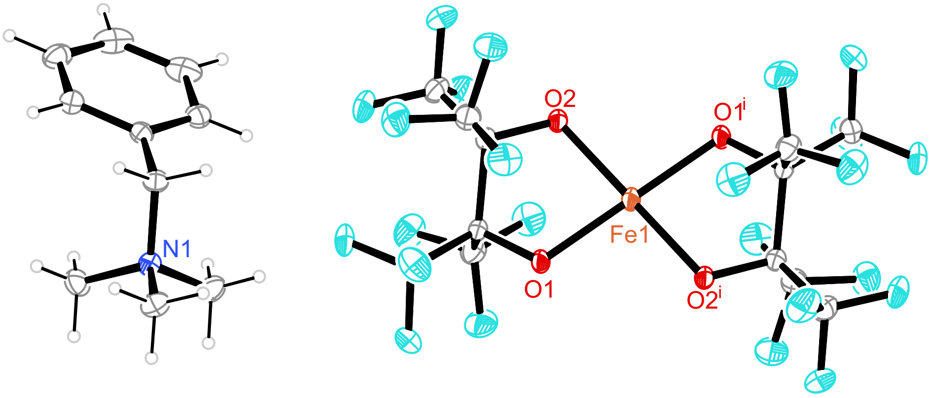

Figure 2.2: *Ortep* plot of $(NBnMe_3)_2[Fe(fpin)_2]$ in crystals of **1b**. Measurement temperature: 100(2) K. Space group: $P2_1/n$. CShM$_{SP\text{-}4}$: 0.436. The thermal ellipsoids are drawn at 50% probability level. Atoms: carbon (gray), hydrogen (light gray), fluorine (green), iron (orange), nitrogen (blue), oxygen (red). Interatomic distances (Å) and angles (°) with the standard deviation in parentheses: Fe1–O1 1.9827(17), Fe1–O2 1.9706(18); O1–Fe1–O2 82.44(7), O1–Fe1–O2^{i} 97.56(7), O1–Fe1–O1^{i} 180.0, O2–Fe1–O2^{i} 180.0. Symmetry code: ^{i} $1-x, 1-y, -z$

Table 2.2: Hydrogen bonds in crystals of **1b**. Coordinates of hydrogen atoms were calculated in idealized positions, riding on their parent atoms.

D–H···A	d(D–H)/Å	d(H···A)/Å	d(D–A)/Å	∠(D–H···A)/°
C7–H7A···O1^{ii}	0.99	2.38	3.258(3)	148.0
C7–H7B···O2^{iii}	0.99	2.58	3.251(3)	125.1
C15–H15B···O1^{ii}	0.98	2.47	3.265(3)	138.1
C15–H15C···O2^{iii}	0.98	2.49	3.231(3)	132.3

Symmetry code: ^{ii} $1/2+x, 1/2-y, 1/2+z$, ^{iii} $3/2-x, -1/2+y, 1/2-z$

2.2 Synthesis of [Fe(fpin)(solv)$_3$] (solv = MeOH, EtOH; 2a, 2b)

Mono(perfluoropinacolato)iron(II) compounds of the general formula [Fe(fpin)(solv)$_3$] (solv = MeOH, EtOH; **2a**, **2b**) were obtained from methanol and ethanol to yield the respective product. They were synthesized by the treatment of iron(II) triflate with 1 equiv of perfluoropinacol and 2 equiv of a base like *n*-butyllithium or potassium methoxide. Upon concentration, colorless precipitates were filtered off, recrystallized and washed with the cold alcohol and *n*-pentane. The presence of ammonium cations, introduced by bases like triethylamine or benzyltriethylammonium methoxide, and an overdosage of perfluoropinacol and base tended to give blue solutions, suggesting the formation of bis(perfluoropinacolato)ferrates(II). Solutions, as well as the solid products, showed a high sensitivity to air. Contact with oxygen resulted in a gray-to-orange color of both solution and solid. **2a** was obtained in 21% yield. Colorless rod-shaped crystals were directly obtained from the reaction solution. **2b** · EtOH was synthesized in 53% yield. The formation of colorless rod-shaped crystals was observed after recrystallization from ethanol.

Both compounds were characterized by single-crystal X-ray diffraction, elemental analysis, IR and UV/Vis spectroscopy. In accordance with the apparent absence of color, UV/Vis spectroscopy of a solution of **2a** in methanol exhibited no absorption in the visible region and was observed only in the UV region at 244 nm. Solutions of **2b** in ethanol featured absorption bands at <350, 652 and 867 nm.

Crystallization occurred in the triclinic space group $P\bar{1}$ for **2a** and for **2b** in the monoclinic space group $P2_1/c$ with one molecule of ethanol of crystallization as **2b** · EtOH. The molecular structures are displayed in Figure 2.3 (**2a**) and Figure 2.4 (**2b** · EtOH) with the relevant distances, angles and CShM values in the respective caption. The primitive cell in **2a** contained four formula units with two crystallographically independent molecules of **2a** per asymmetric unit. In **2b** · EtOH, 12 formula units with each three crystallographically independent units of **2b** and three molecules of ethanol of crystallization per asymmetric unit comprised the primitive cell. In all complex entities of both compounds, an iron(II) center was coordinated by three alcohol ligands and one perfluoropinacolato ligand via a five-membered chelate ring, in total, implying a fivefold coordination. The coordination spheres are best described as in between square pyramids and a vacant octahedra. Mean Fe–O bond lengths are 2.052 Å in **2a** and 2.063 Å in **2b** · EtOH. A molecule of ethanol of crystallization exhibited disorder (O18–C41–C42 approx. 73%; O19–C42–C44 approx. 27%) in **2b** · EtOH with two different spatial arrangements, both maintaining hydrogen bonding towards the complex molecule incidental to Fe2.

The crystal structure of both compounds showed extensive systems of intermolecular hydrogen bonds. In the network in **2a**, each complex molecule was connected to its neighboring molecule alternatingly via two and three hydrogen bonds (Table 2.3) in one-dimensional chains along [$\bar{1}$11] (Figure 2.5). Two ring motifs with the descriptors $R^1_2(6)$ (e.g. binary

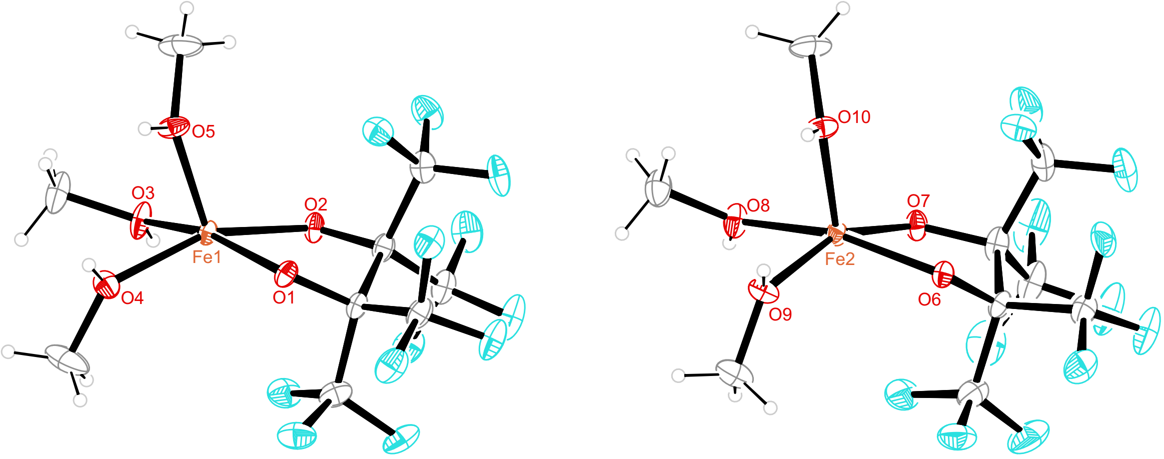

Figure 2.3: *Ortep* plot of both entities of [Fe(fpin)(MeOH)$_3$] in crystals of **2a**. Note that the relative arrangement does not resemble the actual arrangement in the crystal structure. Measurement temperature: 100(2) K. Space group: $P\bar{1}$. CShM$_{SPY\text{-}5}$(Fe1) = 2.016, CShM$_{SPY\text{-}5}$(Fe2) = 1.988; CShM$_{vOC\text{-}5}$(Fe1) = 1.697, CShM$_{vOC\text{-}5}$(Fe2) = 1.700. The thermal ellipsoids are drawn at 50% probability level. Atoms: carbon (gray), hydrogen (light gray), fluorine (green), iron (orange), oxygen (red). Interatomic distances (Å) and angles (°) with the standard deviation in parentheses: Fe1–O1 2.064(2), Fe1–O2 2.010(2), Fe1–O3 2.040(3), Fe1–O4 2.083(3), Fe1–O5 2.054(3), Fe2–O7 2.013(2), Fe2–O8 2.044(3), Fe2–O6 2.059(2), Fe2–O10 2.064(3), Fe2–O9 2.091(3); O1–Fe1–O2 79.45(9), O1–Fe1–O3 164.00(10), O1–Fe1–O5 96.68(10), O1–Fe1–O4 92.72(10), O2–Fe1–O3 93.01(10), O2–Fe1–O4 158.27(11), O2–Fe1–O5 115.44(11), O3–Fe1–O4 89.23(11), O3–Fe1–O5 99.30(11), O4–Fe1–O5 85.41(11), O7–Fe2–O8 94.06(10), O7–Fe2–O6 79.16(9), O8–Fe2–O6 164.88(10), O7–Fe2–O10 115.50(11), O8–Fe2–O10 97.38(11), O6–Fe2–O10 97.74(10), O7–Fe2–O9 157.51(11), O8–Fe2–O9 89.32(11), O6–Fe2–O9 91.99(10).

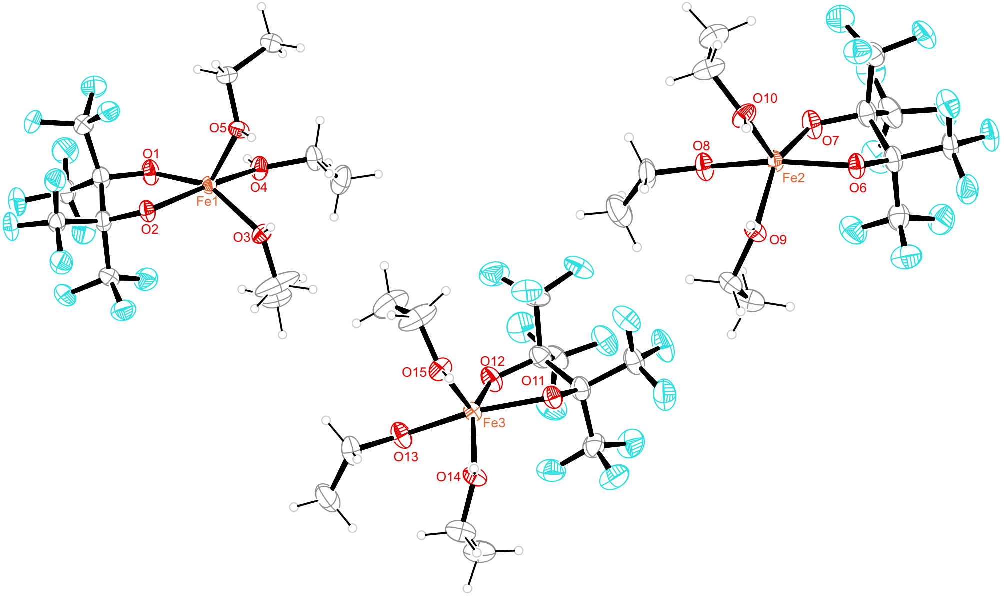

Figure 2.4: *Ortep* plot of the three entities of [Fe(EtOH)$_3$(fpin)] in crystals of **2b** · EtOH. Note that the relative arrangement does not resemble the actual arrangement in the crystal structure. Measurement temperature: 123(2) K. Space group: $P2_1/c$. $\text{CShM}_{SPY\text{-}5}$(Fe1) = 2.361, $\text{CShM}_{SPY\text{-}5}$(Fe2) = 1.715, $\text{CShM}_{SPY\text{-}5}$(Fe3) = 2.048; $\text{CShM}_{vOC\text{-}5}$(Fe1) = 2.956, $\text{CShM}_{vOC\text{-}5}$(Fe2) = 2.533, $\text{CShM}_{vOC\text{-}5}$(Fe3) = 2.926. The thermal ellipsoids are drawn at 50% probability level. Atoms: carbon (gray), hydrogen (light gray), fluorine (green), iron (orange), oxygen (red). Interatomic distances (Å) and angles (°) with the standard deviation in parentheses: Fe1–O1 2.006(2), Fe1–O2 2.060(2), Fe1–O3 2.101(2), Fe1–O4 2.065(2), Fe1–O5 2.071(2), Fe2–O7 2.016(2), Fe2–O6 2.051(2), Fe2–O8 2.056(2), Fe2–O10 2.080(2), Fe2–O9 2.123(2), Fe3–O12 2.008(2), Fe3–O11 2.050(2), Fe3–O13 2.055(2), Fe3–O15 2.081(2), Fe3–O14 2.120(2); O1–Fe1–O2 79.00(9), O1–Fe1–O3 152.06(10), O1–Fe1–O4 88.22(9), O1–Fe1–O5 124.15(10), O2–Fe1–O3 93.33(9), O2–Fe1–O4 163.93(9), O2–Fe1–O5 100.61(9), O3–Fe1–O4 93.49(9), O3–Fe1–O5 83.55(9), O4–Fe1–O5 94.61(10), O7–Fe2–O6 79.13(9), O7–Fe2–O8 88.85(10), O6–Fe2–O8 161.69(10), O7–Fe2–O10 121.55(11), O6–Fe2–O10 100.06(10), O8–Fe2–O10 97.99(10), O7–Fe2–O9 152.34(11), O6–Fe2–O9 91.59(9), O8–Fe2–O9 92.83(10), O10–Fe2–O9 85.56(10), O12–Fe3–O11 79.23(9), O12–Fe3–O13 88.24(10), O11–Fe3–O13 162.10(10), O12–Fe3–O15 124.39(10), O11–Fe3–O15 101.08(10), O13–Fe3–O15 96.53(10), O12–Fe3–O14 150.54(10), O11–Fe3–O14 91.55(9), O13–Fe3–O14 93.24(10), O15–Fe3–O14 84.71(10), C25–O11–Fe3 114.5(2), C26–O12–Fe3 118.4(2), C31–O13–Fe3 131.9(2), C31–O13–H813 109.5, Fe3–O13–H813 118.2.

graph-set H809–O9–Fe2–O10–H810· · ·O6^{i}) and five with $R_2^2(8)$ (e.g. binary graph-set O2–Fe1–O3–H803· · ·O7–Fe2–O8–H808) were formed.

The hydrogen bonds in crystals of **2b** · EtOH led to the formation of discrete networks. In each of these fragments two complex molecules were connected via four hydrogen bonds that can be expressed as two ring motifs with the descriptor $R_2^1(6)$ (e.g. binary graph-set H83–O3–Fe1–O5–H85···O6). The two remaining hydrogen-bond donor and acceptor functions of each complex molecule were saturated by the formation of ring motifs with an ethanol molecule (descriptor $R_2^2(6)$, for example binary graph-set O1–Fe1–O4–H84· · ·O17–H817). Table 2.4 shows a list of independent hydrogen bonds in crystals of **2b** · EtOH.

Table 2.3: Hydrogen bonds in crystals of **2a**. Coordinates of hydrogen atoms bonded to oxygen atoms were refined freely with a SADI constraint for equivalent H–O bonds (standard deviation: H–O 0.01). All other hydrogen atoms were calculated in idealized positions, riding on their parent atoms.

D–H· · ·A	d(D–H)/Å	d(H· · ·A)/Å	d(D–A)/Å	∠(D–H· · ·A)/°
O3–H803· · ·O7	0.76(5)	1.87(5)	2.626(4)	171(6)
O4–H804· · ·O1	0.75(4)	2.07(4)	2.760(3)	154(4)
O5–H805· · ·O1	0.76(3)	1.96(3)	2.676(4)	156(4)
O8–H808· · ·O2	0.76(3)	1.87(4)	2.620(4)	170(4)
O9–H809· · ·O6^{i}	0.76(4)	2.04(4)	2.760(4)	159(4)
O10–H810· · ·O6^{i}	0.76(3)	1.97(3)	2.702(4)	163(5)

Symmetry code: $^{i}1-x, 1-y, 1-z$

Table 2.4: Hydrogen bonds in crystals of **2b** · EtOH. Coordinates of hydrogen atoms were calculated in idealized positions, riding on their parent atoms.

D–H· · ·A	d(D–H)/Å	d(H· · ·A)/Å	d(D–A)/Å	∠(D–H· · ·A)/°
O3–H83· · ·O6	0.84	2.01	2.792(3)	154.0
O4–H84· · ·O17	0.84	1.90	2.633(3)	145.0
O5–H85· · ·O6	0.84	1.92	2.711(3)	155.6
O8–H88· · ·O18	0.84	1.91	2.619(4)	141.3
O8–H88· · ·O19	0.84	1.88	2.676(9)	158.3
O9–H89· · ·O2	0.84	2.03	2.827(3)	157.0
O10–H810· · ·O2	0.84	1.92	2.710(3)	156.6
O13–H813· · ·O16	0.84	1.88	2.635(4)	148.5
O14–H814· · ·O11^{i}	0.84	2.01	2.796(3)	156.6
O15–H815· · ·O11^{i}	0.84	1.92	2.717(3)	158.5
O16–H816· · ·O12	0.84	1.92	2.666(4)	146.7
O17–H817· · ·O1	0.84	1.92	2.655(3)	145.9
O18–H818· · ·O7	0.84	1.96	2.684(4)	144.5
O19–H819· · ·O7	0.84	1.96	2.679(9)	143.1

Symmetry code: $^{i}1-x, 1-y, 1-z$

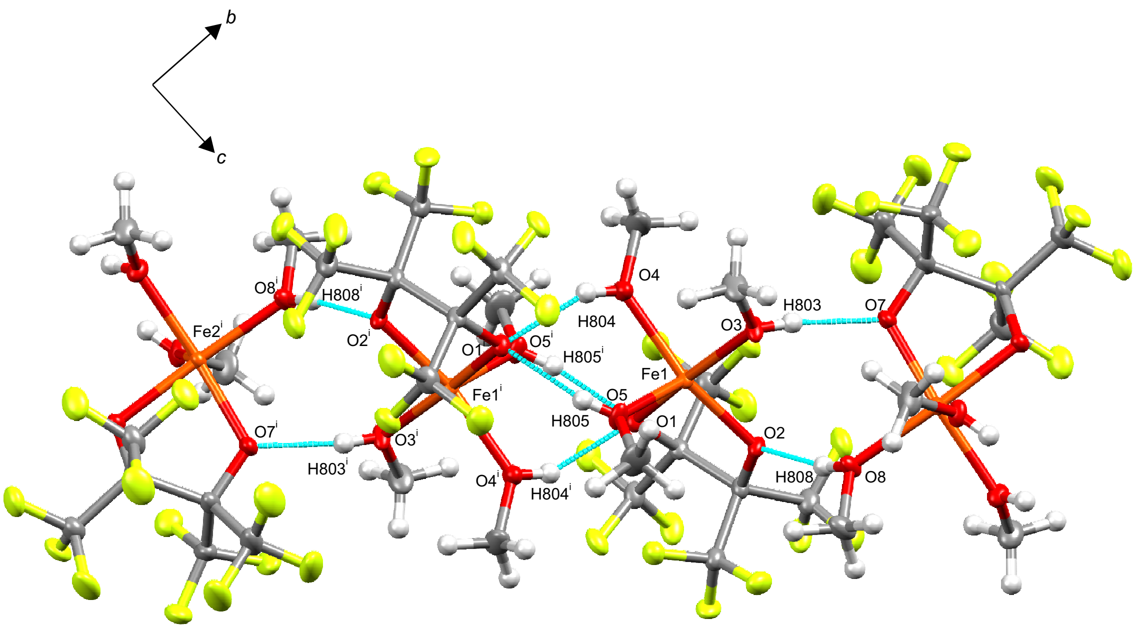

Figure 2.5: *POV-Ray* plot of the hydrogen-bond network (cyan dashed lines) in crystals of **2a** with view along [100].

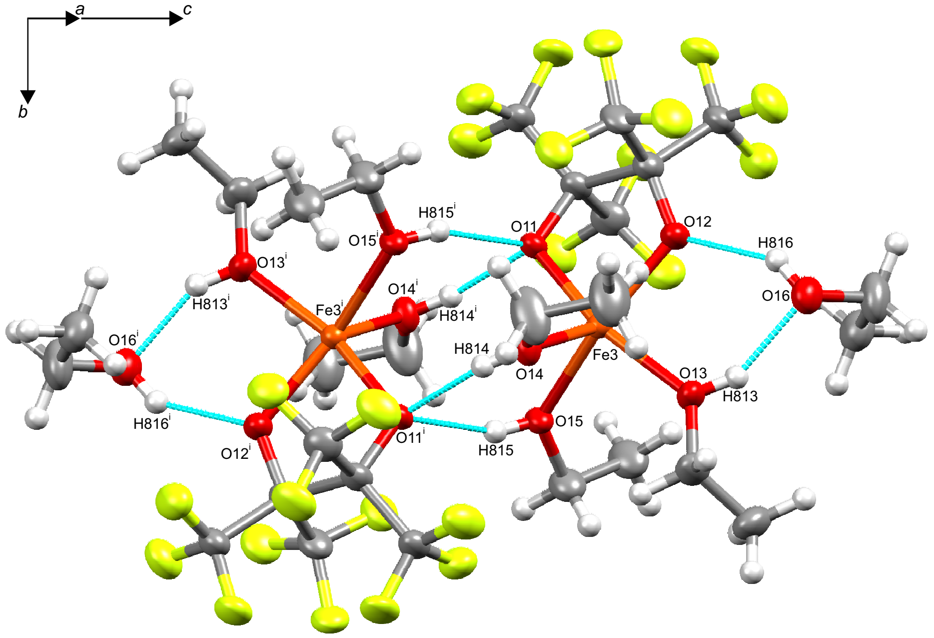

Figure 2.6: *POV-Ray* plot of the hydrogen-bond network (cyan dashed lines) in crystals of **2b** · EtOH with view along $[\overline{4}01]$.

2.3 Synthesis of dinuclear perfluoropinacolatoiron(II) compounds

The synthesis of dinuclear perfluoropinacolatoiron(II) compounds of the type $[Fe_2(fpin\text{-}1\kappa O{:}1,1'\kappa O')_2(solv)_4]$ (solv = H_2O, MeCN, PhCN, thf; **3a**, **3b**, **3c**, **3d**) was analogous to the synthesis of mono(perfluoropinacolato)iron(II) compounds (Section 2.2). They were prepared by the reaction of 1 equiv of iron(II) triflate with 1 equiv perfluoropinacol and 2 equiv of a base. In contrast to the mono(perfluoropinacolato)iron(II) compounds, which were prepared in methanol and ethanol, the synthesis in water, acetonitrile, benzonitrile and tetrahydrofurane led to the formation of neutral dinuclear species. **3a** was obtained as colorless crystals from water using sodium hydroxide as the dihydrate **3a** · 2 H_2O in a yield of 64%. Pale violet crystals of **3b** and light green crystals of **3c** were prepared from acetonitrile and benzonitrile, respectively, with triethylamine as the base in yields of 70% (**3b**) and 68% (**3c**). **3d** was synthesized in 3.8% yield after the addition of elemental lithium in THF as a colorless solid with the formation of crystals from a saturated solution at 7 °C after two weeks. All compounds showed high sensitivity towards oxygen as indicated by the observed change of color.

3a, **3b** and **3c** were characterized by single-crystal X-ray diffraction, elemental analysis, IR and UV/Vis spectroscopy. **3d** was characterized by single-crystal X-ray diffraction, elemental analysis and IR spectroscopy. The UV/Vis spectra featured absorption bands at 208, 291 and 970 nm for solutions of **3a** in water, at 250 and 832 nm for solutions of **3b** in acetonitrile and at <400 and 835 nm in the solid-state spectra for mixtures of **3c** and $BaSO_4$.

3a · 2 H_2O, **3c** and **3d** crystallized in the triclinic space group $P\bar{1}$. **3b** exhibited the chiral monoclinic space group $C2$ [Flack parameter = 0.068(17)]. **3b** and **3d** were refined as two-component crystals [**3b**: Transformation matrix of the minor component as analyzed by *CELL_NOW* = −1 0 0 0 −1 0 0.92 0 1. BASF = 0.09093; **3d**: Transformation matrix of the minor component as analyzed by *Platon* = −0.5 −0.5 0 −1.5 0.5 0 0 0 −1. BASF = 0.453]. The molecular structures are shown in Figure 2.7 (**3a** · 2 H_2O), Figure 2.8 (**3b**), Figure 2.9 (**3c**) and Figure 2.10 (**3d**). Relevant distances, angles and CShM values are listed in the respective caption. The primitive cells each contained one formula unit in the cases of **3a** · 2 H_2O and **3c**, and four formula units in **3d**. In **3b**, four formula units were present in the unit cell. The asymmetric units consisted of half a formula unit each per asymmetric unit in the cases of **3a** · 2 H_2O and **3c**, two crystallographically independent halves of a formula unit in **3b** and two crystallographically independent formula units in **3d**. In all compounds, the complex molecules contained two iron centers, each coordinated by one bidentate perfluoropinacolato chelate ligand via a five-membered chelate ring as well as by one bridging O-donor function of the other respective perfluoropinacolato ligand, connecting both iron centers. To attain pentacoordination, the two remaining coordination sites on each iron center were saturated by solvent ligand molecules. The coordination spheres can be best described as in between a square pyramids and a vacant octahedra, with **3c** showing a tendency towards a square pyramidal environment. Mean Fe–O distances are 2.061 Å in **3a**, 2.043 Å in **3b** (mean Fe–N: 2.146 Å), 2.0414 Å in **3c** (mean Fe–N: 2.1161Å) and 2.083 Å in **3d**.

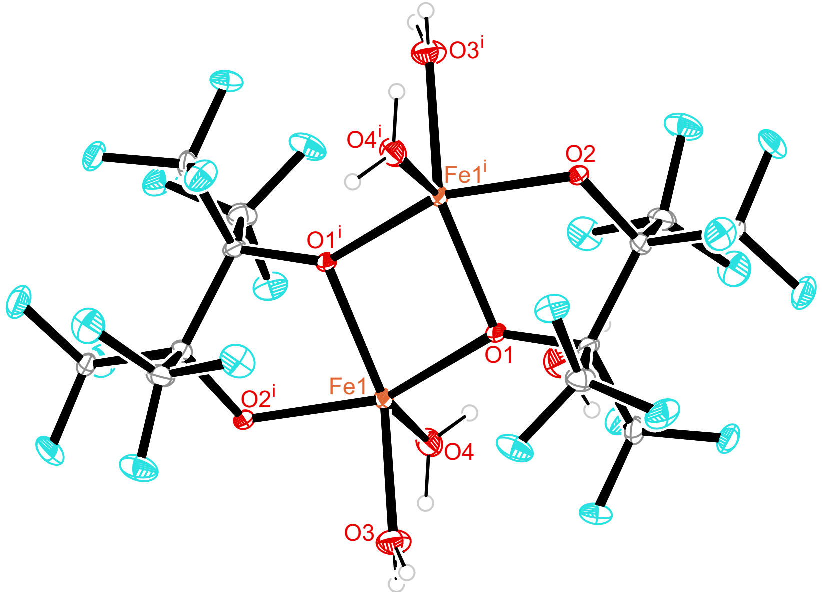

Figure 2.7: *Ortep* plot of one entity of $[\mathrm{Fe}_2(\mathrm{fpin}\text{-}1\kappa O{:}1,1'\kappa O')_2(\mathrm{H}_2\mathrm{O})_4]$ in crystals of **3a** · 2 $\mathrm{H}_2\mathrm{O}$. Measurement temperature: 103(2) K. Space group: $P\bar{1}$. CShM$_{SPY\text{-}5}$(Fe1) = 2.780, CShM$_{vOC\text{-}5}$(Fe1) = 3.776, CShM$_{TBPY\text{-}5}$(Fe1) = 6.143. The thermal ellipsoids are drawn at 50% probability level. Atoms: carbon (gray), hydrogen (light gray), fluorine (green), iron (orange), oxygen (red). Interatomic distances (Å) and angles (°) with the standard deviation in parentheses: Fe1–Fe1$^{\mathrm{i}}$ 3.1854(11), Fe1–O1 2.025(3), Fe1–O1$^{\mathrm{i}}$ 2.108(3), Fe1–O2$^{\mathrm{i}}$ 2.026(2), Fe1–O3 2.086(3), Fe1–O4 2.058(3); O1–Fe1–O1$^{\mathrm{i}}$ 79.16(11), O1–Fe1–O2$^{\mathrm{i}}$ 154.98(11), O1–Fe1–O3 106.07(11), O1–Fe1–O4 106.61(11), O1$^{\mathrm{i}}$–Fe1–O4 121.88(11), O2–Fe1$^{\mathrm{i}}$–O1 77.97(10), O2$^{\mathrm{i}}$–Fe1–O3 88.86(11), O2$^{\mathrm{i}}$–Fe1–O4 94.06(11), O3–Fe1–O4 86.31(12). Symmetry code: $^{\mathrm{i}}1-x, 1-y, -z$.

The crystal structure of **3a** · 2 $\mathrm{H}_2\mathrm{O}$ showed two-dimensional layers parallel to (001) in which the complex molecules and molecules of water of crystallization are connected via hydrogen bonds. The backbones of the perfluoropinacol ligands with the CF_3 moieties point towards the faces of the layers resulting in weak interactions between the layers. According to graph-set analysis two ring motifs with the descriptor $R_2^2(8)$ (e.g. unary graph-set O3–H831· · ·O2$^{\mathrm{iv}}$–Fe1$^{\mathrm{v}}$–O3$^{\mathrm{v}}$–H831$^{\mathrm{v}}$· · ·O2$^{\mathrm{i}}$–Fe1$^{\mathrm{i}}$) and two chain motifs with the descriptor $C_1^1(6)$ (e.g. unary graph-set Fe1–O1–Fe1$^{\mathrm{i}}$–O2· · ·H831$^{\mathrm{iv}}$–O3$^{\mathrm{iv}}$) are formed. Table 2.5 shows a list of independent hydrogen bonds in crystals of **3a** · 2 $\mathrm{H}_2\mathrm{O}$. In **3c**, stabilization of the crystalline structure was attained through intermolecular π–π interaction with a stacking distance of approximately 3.5 Å between the phenyl rings of the benzonitrile ligands.

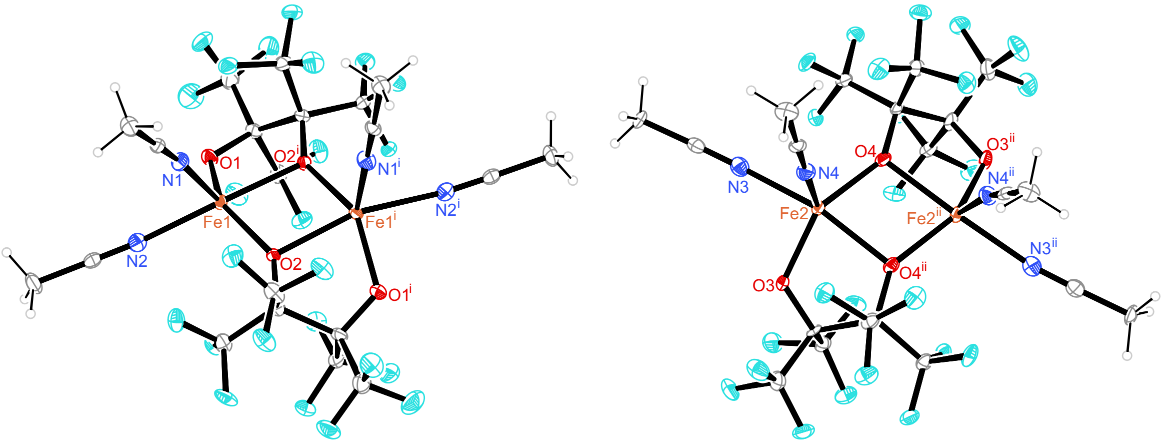

Figure 2.8: *Ortep* plot the two entities of [Fe_2(fpin-1κO:1,1′κO')$_2$(MeCN)$_4$] in crystals of **3b**. Note that the relative arrangement does not resemble the actual arrangement in the crystal structure. Measurement temperature: 103(2) K. Space group: $C2$. CShM$_{SPY\text{-}5}$(Fe1) = 3.008, CShM$_{vOC\text{-}5}$(Fe1) = 3.889; CShM$_{SPY\text{-}5}$(Fe2) = 2.668, CShM$_{vOC\text{-}5}$(Fe2) = 3.542, CShM$_{TBPY\text{-}5}$(Fe2) = 4.747. The thermal ellipsoids are drawn at 50% probability level. Atoms: carbon (gray), hydrogen (light gray), fluorine (green), iron (orange), nitrogen (blue), oxygen (red). Interatomic distances (Å) and angles (°) with the standard deviation in parentheses: Fe1–Fe1^{i} 3.2806(15), Fe2–Fe2^{i} 3.2637(15), Fe1–O1 1.949(3), Fe1–O2 1.996(3), Fe1–O2^{i} 2.177(3), Fe1–N1 2.126(5), Fe1–N2 2.178(5), Fe2–O3 1.950(4), Fe2–O4 2.002(3), Fe2–N4 2.128(5), Fe2–N3 2.150(5), Fe2–O4^{ii} 2.182(3); O1–Fe1–O2 144.02(15), O1–Fe1–O2^{i} 77.78(13), O1–Fe1–N1 111.36(17), O1–Fe1–N2 89.49(16), O2–Fe1–O2^{i} 76.28(13), O2–Fe1–N1 100.11(17), O2–Fe1–N2 110.68(15), N1–Fe1–O2^{i} 107.87(16), N1–Fe1–N2 85.20(18), N3–Fe2–O4^{ii} 165.64(16), N4–Fe2–N3 85.81(18), N4–Fe2–O4^{ii} 106.47(16), O3–Fe2–N3 90.95(16), O3–Fe2–N4 111.46(17), O3–Fe2–O4 144.52(15), O3–Fe2–O4^{ii} 77.78(14), O4–Fe2–N3 108.44(15), O4–Fe2–N4 99.64(17), O4–Fe2–O4^{ii} 77.36(14). Symmetry code: $^{i}1-x,+y,1-z$, $^{ii}1-x,+y,-z$.

Table 2.5: Hydrogen bonds in crystals of **3a** · 2 H_2O. Coordinates of hydrogen atoms bonded to oxygen atoms were refined freely with a SADI constraint for equivalent H–O and H–H distances (standard deviation: H–O 0.01, H–H 0.02). All other hydrogen atoms were calculated in idealized positions, riding on their parent atoms. U_{iso} was always coupled to the parent atom.

D–H· · ·A	d(D–H)/Å	d(H· · ·A)/Å	d(D–A)/Å	∠(D–H· · ·A)/°
O3–H831· · ·O2^{ii}	0.89(3)	1.99(3)	2.841(4)	159(5)
O3–H832· · ·O5^{iii}	0.89(3)	1.99(3)	2.870(4)	173(5)
O4–H841· · ·O5	0.89(3)	1.98(3)	2.865(4)	173(4)
O4–H842· · ·O2^{ii}	0.89(3)	1.92(3)	2.763(4)	158(5)

Symmetry code: $^{i}1-x,1-y,-z$, $^{ii}-1+x,+y,+z$, $^{iii}+x,1+y,+z$, $^{iv}1+x,+y,+z$, $^{v}-x,1-y,-z$

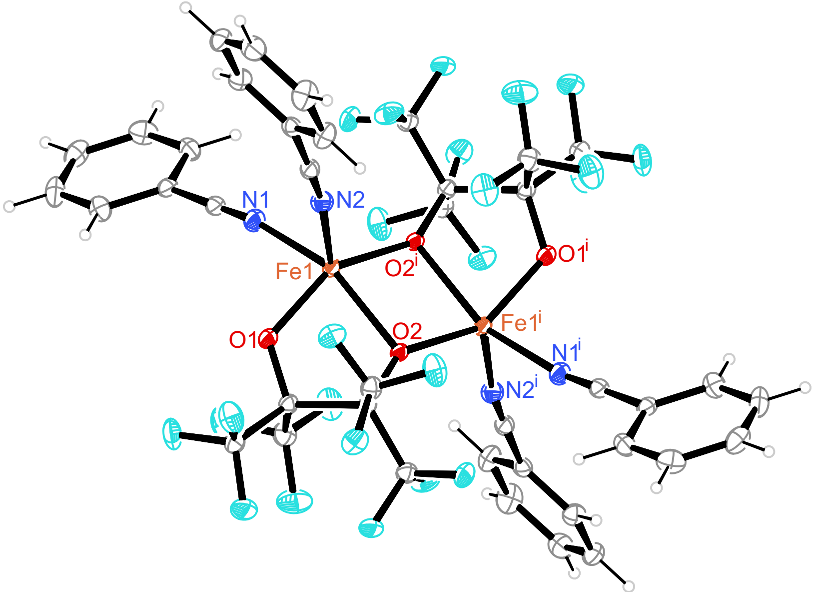

Figure 2.9: *Ortep* plot of $[\mathrm{Fe_2}(\mathrm{fpin}\text{-}1\kappa O{:}1,1'\kappa O')_2(\mathrm{PhCN})_4]$ in crystals of **3c**. Measurement temperature: 101(2) K. Space group: $P\bar{1}$. CShM$_{SPY\text{-}5}$(Fe1) = 1.222. The thermal ellipsoids are drawn at 50% probability level. Atoms: carbon (gray), hydrogen (light gray), fluorine (green), iron (orange), nitrogen (blue), oxygen (red). Interatomic distances (Å) and angles (°) with the standard deviation in parentheses: Fe1–Fe1$^{\mathrm{i}}$ 3.2351(5), Fe1–O1 1.9416(13), Fe1–O2 1.9888(12), Fe1–O2$^{\mathrm{i}}$ 2.1938(12), Fe1–N1 2.1336(17), Fe1–N2 2.0985(17); O1–Fe1–O2 77.61(5), O1–Fe1–O2$^{\mathrm{i}}$ 148.21(5), O1–Fe1–N1 90.28(6), O1–Fe1–N2 100.03(6), O2–Fe1–O2$^{\mathrm{i}}$ 78.78(5), O2$^{\mathrm{i}}$–Fe1–N1 101.35(6), O2$^{\mathrm{i}}$–Fe1–N2 107.93(6), O2–Fe1–N1 152.70(6), O2–Fe1–N2 110.13(6), N1–Fe1–N2 95.93(7). Symmetry code: $^{\mathrm{i}}1-x, 1-y, 1-z$.

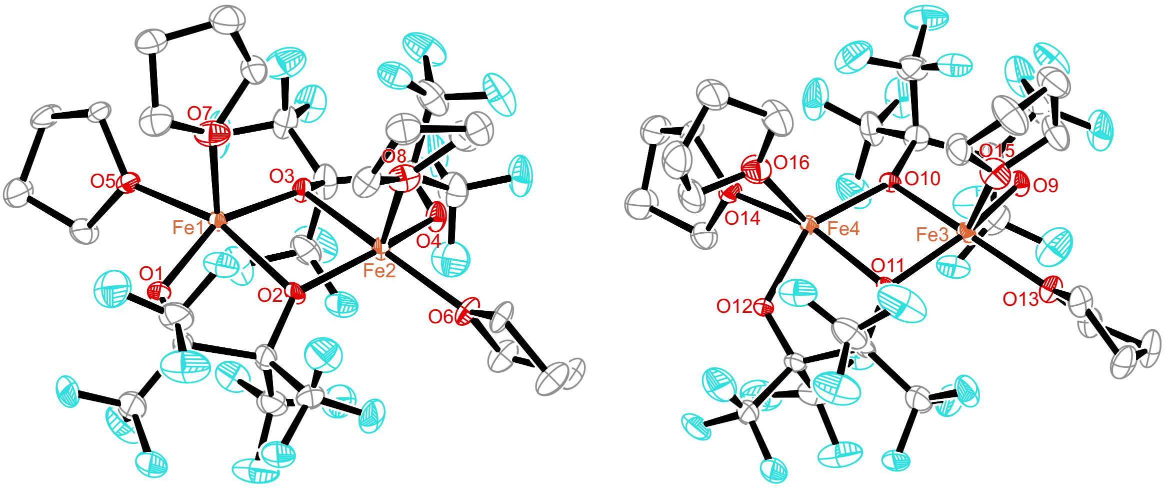

Figure 2.10: *Ortep* plot of the two entities of $[\mathrm{Fe}_2(\text{fpin-1}\kappa O\text{:1,1}'\kappa O')_2(\mathrm{thf})_4]$ in crystals of **3d** (Hydrogen atoms are omitted for better clarity). Note that the relative arrangement does not resemble the actual arrangement in the crystal structure. Measurement temperature: 100(2) K. Space group: $P\bar{1}$. CShM$_{SPY\text{-}5}$(Fe1) = 2.016, CShM$_{SPY\text{-}5}$(Fe2) = 1.988, CShM$_{SPY\text{-}5}$(Fe3) = 2.706, CShM$_{SPY\text{-}5}$(Fe4) = 2.743; CShM$_{vOC\text{-}5}$(Fe1) = 2.546, CShM$_{vOC\text{-}5}$(Fe2) = 2.605, CShM$_{vOC\text{-}5}$(Fe3) = 3.593, CShM$_{vOC\text{-}5}$(Fe4) = 3.760. The thermal ellipsoids are drawn at 50% probability level. Atoms: carbon (gray), fluorine (green), iron (orange), oxygen (red). Interatomic distances (Å) and angles (°) with the standard deviation in parentheses: Fe1–Fe2 3.1546(7), Fe3–Fe4 3.2357(7), Fe1–O1 1.923(5), Fe1–O2 2.238(5), Fe1–O3 1.981(5), Fe1–O5 2.120(5), Fe1–O7 2.130(5), Fe2–O2 1.986(5), Fe2–O3 2.240(4), Fe2–O4 1.929(5), Fe2–O6 2.122(5), Fe2–O8 2.129(5), Fe3–O9 1.950(3), Fe3–O11 1.972(3), Fe3–O15 2.136(3), Fe3–O13 2.140(3), Fe3–O10 2.217(3), Fe4–O12 1.937(3), Fe4–O10 1.984(3), Fe4–O14 2.130(3), Fe4–O16 2.144(3), Fe4–O11 2.218(3); O1–Fe1–O2 76.75(19), O1–Fe1–O3 152.3(2), O1–Fe1–O5 88.3(2), O1–Fe1–O7 105.3(2), O2–Fe1–O3 82.23(18), O2–Fe1–O5 161.92(18), O2–Fe1–O7 103.8(2), O2–Fe2–O3 82.06(18), O2–Fe2–O4 150.5(2), O2–Fe2–O6 107.2(2), O2–Fe2–O8 99.1(2), O3–Fe1–O5 108.2(2), O3–Fe1–O7 97.0(2), O3–Fe2–O4 77.27(19), O3–Fe2–O6 163.13(19), O3–Fe2–O8 103.9(2), O4–Fe2–O6 88.7(2), O4–Fe2–O8 106.1(2), O5–Fe1–O7 89.8(2), O6–Fe2–O8 88.9(2), O9–Fe3–O11 147.82(13), O9–Fe3–O15 94.83(12), O11–Fe3–O15 113.42(13), O9–Fe3–O13 89.94(12), O11–Fe3–O13 107.66(12), O15–Fe3–O13 83.40(11), O9–Fe3–O10 77.00(11), O11–Fe3–O10 78.22(10), O15–Fe3–O10 112.03(12), O13–Fe3–O10 160.29(12), O12–Fe4–O10 145.87(13), O12–Fe4–O14 91.14(12), O10–Fe4–O14 106.37(12), O12–Fe4–O16 94.45(13), O10–Fe4–O16 116.29(13), O14–Fe4–O16 82.74(12), O12–Fe4–O11 77.06(11), O10–Fe4–O11 77.95(10), O14–Fe4–O11 161.81(12), O16–Fe4–O11 111.62(12).

2.4 Synthesis of aquanitrosyliron compounds

2.4.1 [Fe(H_2O)$_5$(NO)][M^{III}(fpin)$_2$(H_2O)]$_2$ · *x* H_2O (M=Ga, Fe; $x = 8.34, 8.31$; 4a, 4b)

4a · 8.34 H_2O was prepared in a yield of 47% by the reaction of 1 equiv iron(II) triflate with 2 equiv gallium(III) triflate with 4 equiv perfluoropinacol and 4 equiv sodium hydroxide in a highly concentrated aqueous solution of approximately 3.4 mol L^{-1} with pH = 1.2. After introducing gaseous nitric oxide, a sudden change in color from colorless to greenish brown occurred. Dark brown platelets of **4a** · 8.34 H_2O formed under nitric-oxide atmosphere within approximately 12 h. A similar reaction with iron(III) triflate instead of gallium(III) triflate did not produce the ferrate salt. Instead, **4b** · 8.31 H_2O was synthesized in a yield of 38% by preparing a suspension of **3a** in water by the reaction of 1 equiv iron(II) triflate with 1 equiv perfluoropinacol and 1 equiv sodium hydroxide and subsequent introduction of gaseous nitric oxide. The first contact of the reaction mixture with nitric oxide led to an immediate color change from colorless to red. After approximately 1 min, a second color change occurred from red to dark brown. At 7 °C brown platelets of **4b** · 8.31 H_2O crystallized in the course of 12 h under nitric-oxide atmosphere. During the reaction with nitric oxide the formation of nitrous oxide was observed. Figure 2.11 shows the time-dependent increase of nitrous oxide in the head space as determined by IR after the introduction of nitric oxide into a suspension of **3a**.

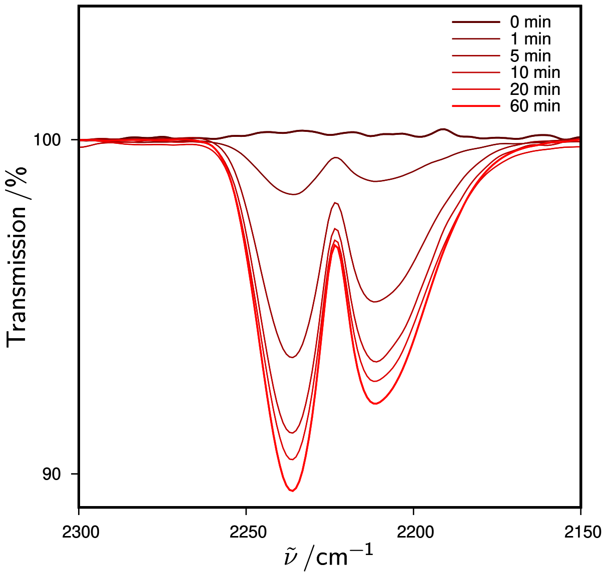

Figure 2.11: Formation of nitrous oxide during nitric-oxide introduction in the synthesis of **4b** as monitored by IR spectroscopy. Nitric oxide was introduced into a suspension of 0.54 mmol **3a** in 0.2 mL water at room temperature. Samples were taken off the head space of the reaction mixture right before introduction of NO (0 min) and after 1, 5, 10, 20 and 60 min.

In both cases, the formation of crystals highly depended on the exact dosage of base, as even slight underdosage completely prevented the formation of crystals or led to very poor yields and small crystal size. In these cases, the addition of 0.1 to 0.2 equiv of base and repeated treatment with nitric oxide promoted crystal growth.

Solutions containing $[Fe(H_2O)_5(NO)]^{2+}$ are known to be prone to releasing nitric oxide when not kept in a nitric-oxide atmosphere[35], as was the case with **4a** and **4b**. A constant flow of argon over the reaction solutions led to discoloration within minutes. In contrast the solids, when completely free from surface moisture, only showed visible signs of decomposition after 1 to 2 h of exposure to ambient air. When cooled to −20 °C the compounds were even stored for months without significant signs of deterioration. However, remaining moisture on the surface of the crystals significantly increased the rate of decay which was complete within minutes. The dry products were obtained from the reaction mixtures by quickly removing the supernatant solution after opening the vessel and removing the nitric-oxide atmosphere. The remaining solid and adherent reaction solution were then frozen in liquid nitrogen and left to thaw on water-absorbent material such as tissue or a clay plate. The nitrosylation process was reversible so that various cycles of NO fixation and release were realized. However, after the first cycle the reaction solution of **4b** was no longer colorless but bright orange. **4a** showed oxidation, indicated by the bright orange coloration, only after exposure to ambient oxygen.

Both compounds were characterized by single-crystal X-ray diffraction, elemental analysis, IR, UV/Vis and Mößbauer spectroscopy. Furthermore, the formation reactions were monitored via *in situ* IR spectroscopy. Due to omitted purification, the elemental analyses showed a significant deviance from the theoretical mass ratios. The presence of sulfur in samples of **4a** suggested contamination by sodium triflate. The nitrosyl stretching frequencies of solid samples were observed at 1843 cm^{-1} for **4a** and at 1841 cm^{-1} for **4b**. The solid-state UV/Vis spectra of mixtures of $[Fe(H_2O)_5(NO)]^{2+}$ salts with $BaSO_4$ featured absorption bands at <300, 336, 452, 589 and 759 nm for **4a** · 8.34 H_2O (see also Section 2.7.4) and at 253, 322, 459, 581 and 758 and 886 nm for **4b** · 8.31 H_2O.

In situ IR measurements of the formation reaction of **4a** showed the generation of a single nitrosyl stretching band at 1816 cm^{-1}, corresponding to the formation of $[Fe(H_2O)_5(NO)]^{2+}$ cations (Figure 2.12). Directly after the introduction of nitric oxide, the band showed a steep rise and then slowly flattened in the course of 20 min. Afterwards, the slow increase suggested incipient saturation of the reaction mixture. In the formation reaction of **4b**, at first, a single nitrosyl stretching band at 1774 cm^{-1} was observed within 10 min after introduction of nitric oxide. Subsequently, the band vanished within 2 min and was then replaced by an intense band at 1808 cm^{-1} corresponding to the nitrosyl stretching vibration of a $[Fe(H_2O)_5(NO)]^{2+}$ cation (Figure 2.13).

Zero-Field ^{57}Fe Mößbauer spectroscopy was conducted by Prof. Friedrich Wagner (TU München). The spectrum of **4a** showed a quadrupole with an isomer shift of $\delta = 0.81(3)\ mm\,s^{-1}$

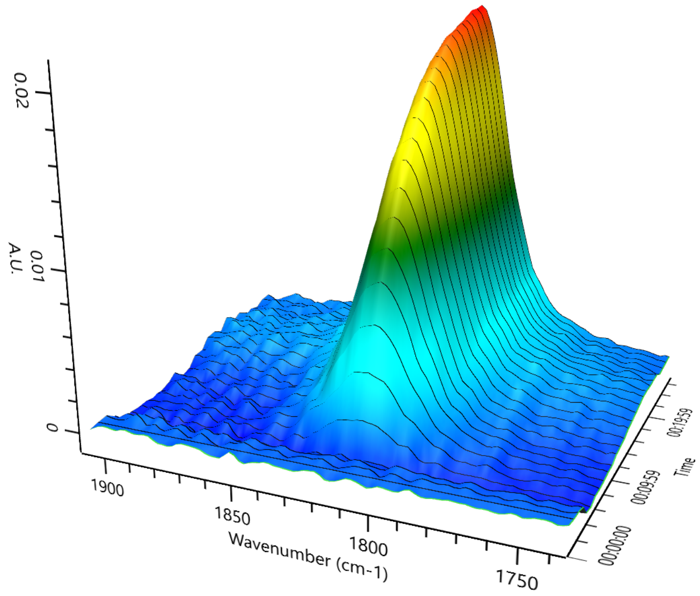

Figure 2.12: Three-dimensional plot of the time-dependent IR spectrum of the formation reaction yielding **4a**. All measurements are relative to a background spectrum taken of the reaction mixture prior to introduction of nitric oxide taken at 1:54 min.

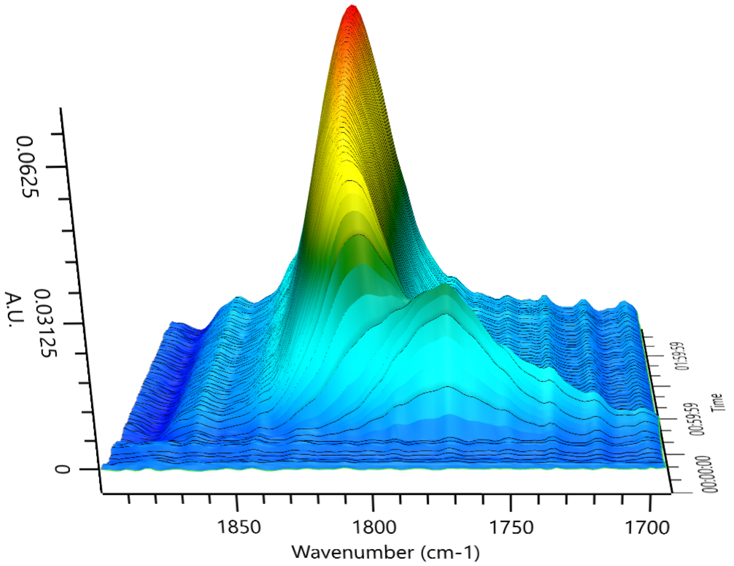

Figure 2.13: Three-dimensional plot of the time-dependent IR spectrum of the formation reaction yielding **4b**. All measurements are relative to a background spectrum taken of the reaction mixture prior to introduction of nitric oxide taken at 2:54 min.

and a quadrupole splitting of $|\Delta E_\mathrm{Q}| = 2.23(4)\,\mathrm{mm\,s^{-1}}$ for the $[\mathrm{Fe(H_2O)_5(NO)}]^{2+}$ ion at 4.2 K. Probably due to residual mother liquor on the surface of the measured crystals, a quadruplet of $[\mathrm{Fe(H_2O)_6}]^{2+}$ was present at $\delta = 1.39(4)\,\mathrm{mm\,s^{-1}}$, $|\Delta E_\mathrm{Q}| = 3.12(9)\,\mathrm{mm\,s^{-1}}$. Also, a broad doublet at $\delta = 0.16(9)\,\mathrm{mm\,s^{-1}}$, $|\Delta E_\mathrm{Q}| = 0\,\mathrm{mm\,s^{-1}}$ hinted at a further unidentified species. In the spectrum of **4b** at 133 K a quadrupole with an isomer shift of $\delta = 0.655(3)\,\mathrm{mm\,s^{-1}}$ and a quadrupole splitting of $|\Delta E_\mathrm{Q}| = 2.031(8)\,\mathrm{mm\,s^{-1}}$ was assigned to the $[\mathrm{Fe(H_2O)_5(NO)}]^{2+}$ ion. As a result of the 1:2 molar ratio of iron in the cation and the anion, a quadruplet with approximately twice the intensity was found for the ferrate(III) anion at $\delta = 0.187(7)\,\mathrm{mm\,s^{-1}}$ $[|\Delta E_\mathrm{Q}| = 1.70(2)\,\mathrm{mm\,s^{-1}}]$. The quadruplet at $\delta = 1.076(5)\,\mathrm{mm\,s^{-1}}$ $[|\Delta E_\mathrm{Q}| = 3.464(10)\,\mathrm{mm\,s^{-1}}]$ indicated the presence of $[\mathrm{Fe(H_2O)_6}]^{2+}$, most likely stemming from residual mother liquor on the surface of the solid material. A quadruplet at $\delta = 0.274(2)\,\mathrm{mm\,s^{-1}}$ $[|\Delta E_\mathrm{Q}| = 0.727(6)\,\mathrm{mm\,s^{-1}}]$ could not be assigned and indicated the presence of a yet unidentified component.

4a and **4b** showed thermochromic properties. At room temperature, both the solutions and the solid were dark brown. Upon cooling, a green tint intensified until at around 120 K a bright green color appeared, as can be seen in Figure 2.14 for **4a**.

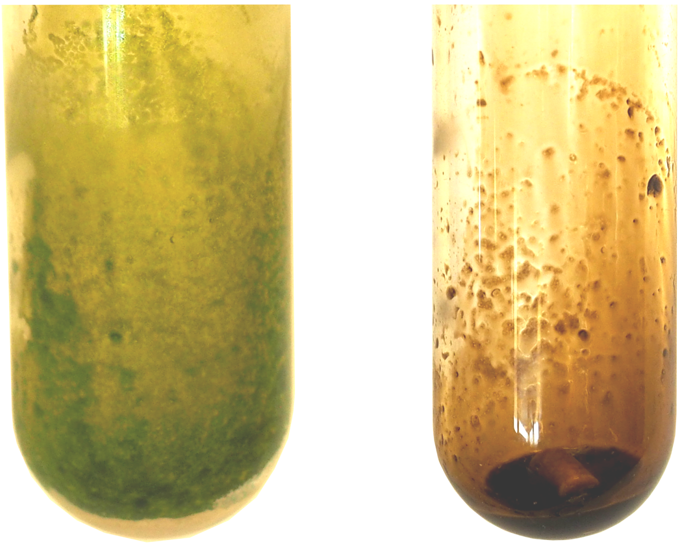

Figure 2.14: Thermochromic effect of a suspension of **4a** in water at −196 °C (left) and room temperature (right).

4a and **4b** are isotypic and crystallized in the monoclinic space group $P2_1/n$. The structures are displayed in Figure 2.15 (**4a**) and Figure 2.16 (**4b**) with relevant distances, angles and CShM values listed in the respective caption. The primitive cells contained four formula units with one formula unit per asymmetric unit. The asymmetric units consist of one $[\mathrm{Fe(H_2O)_5(NO)}]^{2+}$ complex cation, two $[\mathrm{M^{III}(fpin)_2(H_2O)}]^-$ complex anions and 8.34 (**4a**) or 8.31 (**4b**) partially disordered molecules of water of crystallization. In each $[\mathrm{Fe(H_2O)_5(NO)}]^{2+}$ cation, an iron center was octahedrally coordinated by five aqua ligands and one nitrosyl ligand. The nitrosyl ligand, that defines the axial position, coordinated the iron center to produce a slightly bent FeNO unit. The Fe–O distances ranged from 2.031(3) Å to 2.121(3) Å in **4a** and from 2.037(2) Å to 2.118(2) Å in **4b** with each the longest Fe–O bond to the aqua ligand in *trans*-nitrosyl position. The mean Fe–O distance was 2.077 Å in **4a** and 2.079 Å in **4b**. In the equatorial positions, the aqua ligands with the smallest dihedral angle O91–Fe1–N1–O1 of 37.8° in**4a** and 42.28° in **4b** showed the longest Fe–O bond. The Fe–O bond lengths decreased from Fe1–O91 to Fe1–O94. The aqua ligands H911–O91–H912 showed a twist towards the equatorial plane, while the other equatorial aqua ligands were almost perpendicular.

In the complex anions, the metal(III) centers were each coordinated fivefold by an aqua ligand and two bidentate perfluoropinacolato ligands via five-membered chelate rings The coordination spheres of the complex anions differed as each one was in between a square pyramidal and trigonal bipyramidal coordination and the other was coordinated, almost ideally, in a trigonal bipyramid. The mean M^{III}–O distances were 1.905 Å in **4a** (M=Ga) and 1.945 Å in **4b** (M=Fe). Both crystal structures showed disorder in respect to the position and occupation of molecules of water of crystallization represented by O13 – O19 in **4a** (M=Ga) and O14 to O19 in **4b**. In consequence, the assignment of corresponding hydrogen positions was obsolete and was therefore omitted. In the further course, this led to the non-integer number of molecules of water of crystallization per formula unit.

The high number of water molecules and perfluoropinacolato hydrogen-bond-acceptor functions led to the formation of a complex two-dimensional networks of hydrogen bonds. The layers consisted of three sub-layers with a hydrophilic inner layer, featuring the hydrogen-bond network, and two hydrophobic outer layers containing mainly CF_3 groups from the backbones of the perfluoropinacolato ligands. An overview of the hydrogen bonds in the $[Fe(H_2O)_5(NO)]^{2+}$ salts is given in Table 2.6 (**4a** · 8.34 H_2O) and Table 2.7 (**4b** · 8.31 H_2O). However, due to the mentioned disorders, these lists are not complete.

2.4.2 $[\{Fe(H_2O)(NO)(\mu\text{-}ox)\}_{n/n}] \cdot H_2O$ (5 · H_2O)

5 · H_2O was prepared by the reaction of 1 equiv iron(II) triflate with 1 equiv oxalic acid in water yielding a yellow precipitate of iron(II) oxalate with a colorless supernatant solution. Subsequently, upon the introduction of nitric oxide, the solution turned brownish green accompanied by the slow dissolution of the precipitate. After two weeks of storage under nitric-oxide atmosphere at room temperature, the formation of scattered brown platelet-shaped crystals was observed within the remaining precipitate. Crystals fit for single-crystal X-ray diffraction were obtained after three months.

Both the solution and the solid readily discharged nitric oxide after the nitric-oxide atmosphere had been removed. **5** · H_2O was characterized by single-crystal X-ray diffraction and IR spectroscopy. The formation reaction was monitored using *in situ* IR spectroscopy. The

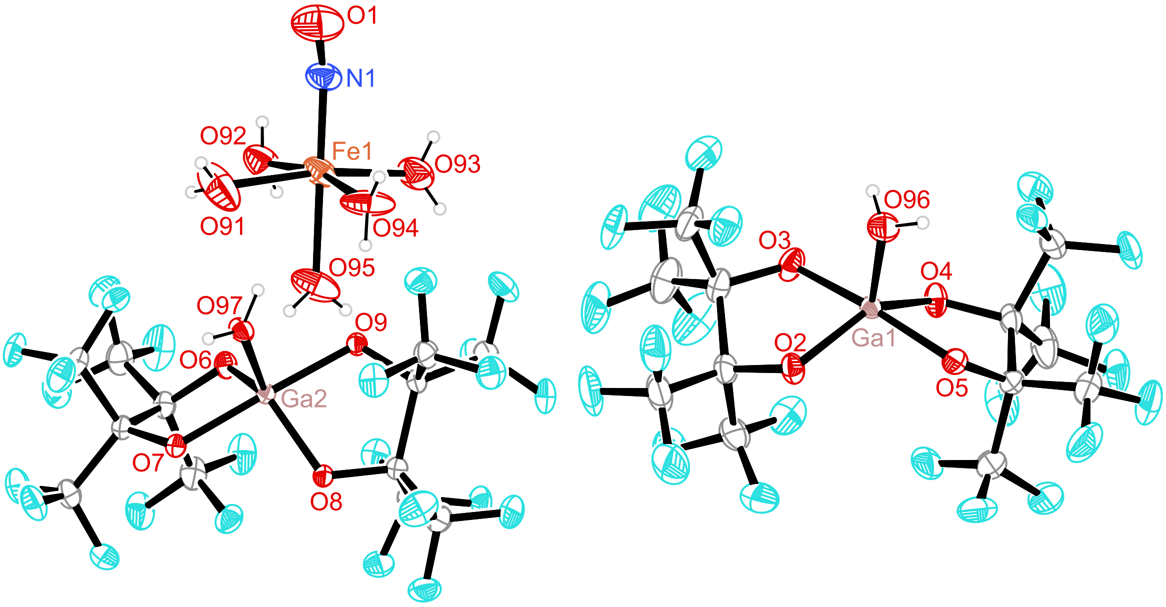

Figure 2.15: *Ortep* plot of $[Fe(H_2O)_5(NO)][Ga(fpin)_2(H_2O)]_2$ in crystals of **4a** $\cdot$ 8.34 H_2O (water of crystallization not depicted). Note that the relative arrangement does not resemble the actual arrangement in the crystal structure. Measurement temperature: 100(2) K. Space group: $P2_1/n$. $\mathrm{CShM}_{OC\text{-}6}(\mathrm{Fe1}) = 0.271$; $\mathrm{CShM}_{SPY\text{-}5}(\mathrm{Ga1}) = 1.709$, $\mathrm{CShM}_{TBPY\text{-}5}(\mathrm{Ga1}) = 2.022$; $\mathrm{CShM}_{TBPY\text{-}5}(\mathrm{Ga2}) = 0.342$. The thermal ellipsoids are drawn at 50% probability level. Atoms: carbon (gray), hydrogen (light gray), fluorine (green), iron (orange), nitrogen (blue), oxygen (red). Interatomic distances (Å) and angles (°) with the standard deviation in parentheses: Fe1–N1 1.786(4), Fe1–O91 2.102(4), Fe1–O92 2.067(3), Fe1–O93 2.064(3), Fe1–O94 2.031(3), Fe1–O95 2.121(3), Ga1–O2 1.898(3), Ga1–O3 1.898(3), Ga1–O4 1.886(2), Ga1–O5 1.919(3), Ga1–O96 1.919(3), Ga2–O6 1.895(2), Ga2–O7 1.913(2), Ga2–O8 1.877(2), Ga2–O9 1.914(2), Ga2–O97 1.927(2), N1–O1 1.143(5); Fe1–N1–O1 160.6(4), N1–Fe1–O91 92.95(19), N1–Fe1–O92 97.62(16), N1–Fe1–O93 96.04(16), N1–Fe1–O94 93.40(15), N1–Fe1–O95 178.87(16), O2–Ga1–O3 85.01(11), O4–Ga1–O5 84.42(11), O6–Ga2–O7 84.92(10), O8–Ga2–O9 85.74(10).

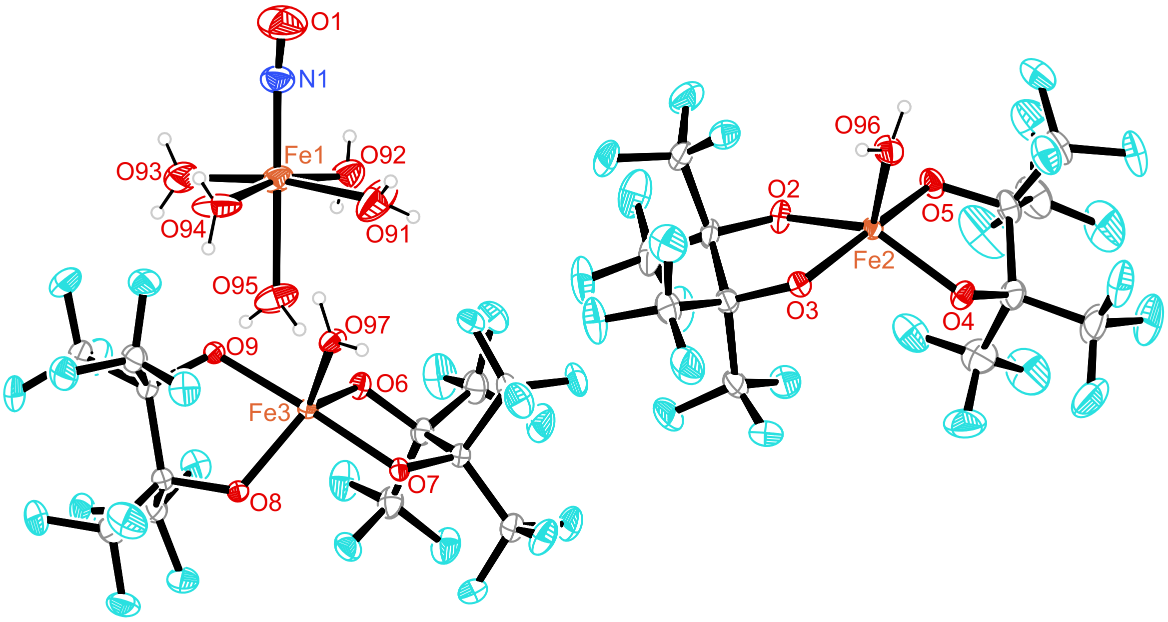

Figure 2.16: *Ortep* plot of $[Fe(H_2O)_5(NO)][Fe(fpin)_2(H_2O)]_2$ in crystals of **4b** $\cdot$ 8.31 H_2O (water of crystallization not depicted). Note that the relative arrangement does not resemble the actual arrangement in the crystal structure. Measurement temperature: 100(2) K. Space group: $P2_1/n$. $\mathrm{CShM}_{OC\text{-}6}(\mathrm{Fe1}) = 0.276$; $\mathrm{CShM}_{SPY\text{-}5}(\mathrm{Fe2}) = 2.096$, $\mathrm{CShM}_{TBPY\text{-}5}(\mathrm{Fe2}) = 2.198$; $\mathrm{CShM}_{TBPY\text{-}5}(\mathrm{Fe3}) = 0.462$. The thermal ellipsoids are drawn at 50% probability level. Atoms: carbon (gray), hydrogen (light gray), fluorine (green), iron (orange), nitrogen (blue), oxygen (red). Interatomic distances (Å) and angles (°) with the standard deviation in parentheses: N1–O1 1.134(4), Fe1–N1 1.780(3), Fe1–O91 2.101(3), Fe1–O92 2.070(2), Fe1–O93 2.070(2), Fe1–O94 2.036(2), Fe1–O95 2.118(2), Fe2–O2 1.9251(19), Fe2–O3 1.9488(19), Fe2–O4 1.9369(19), Fe2–O5 1.943(2), Fe2–O96 1.972(2), Fe3–O6 1.9345(19), Fe3–O7 1.9469(18), Fe3–O8 1.9145(18), Fe3–O9 1.9487(18), Fe3–O97 1.9841(19); Fe1–N1–O1 162.2(3), N1–Fe1–O91 93.20(13), N1–Fe1–O92 98.00(11), N1–Fe1–O93 96.28(12), N1–Fe1–O94 93.13(11), N1–Fe1–O95 179.02(12), O2–Fe2–O3 81.68(8), O4–Fe2–O5 81.94(8), O6–Fe3–O7 82.16(8), O8–Fe3–O9 82.95(8), O8–Fe3–O97 117.64(9).

Table 2.6: Hydrogen bonds in crystals of **4a** · 8.34 H_2O. Coordinates of hydrogen atoms bonded to oxygen atoms were refined freely with a SADI constraint for equivalent H–O and H–H distances (standard deviation: H–O 0.01, H–H 0.02).

D–H···A	d(D–H)/Å	d(H···A)/Å	d(D–A)/Å	∠(D–H···A)/°
O91–H912···O911	0.798(13)	1.96(2)	2.730(6)	161(6)
O92–H921···O5$^{\text{i}}$	0.802(13)	1.92(3)	2.677(4)	157(5)
O92–H922···O912	0.802(13)	2.15(3)	2.865(6)	148(5)
O93–H931···O2$^{\text{i}}$	0.800(13)	2.04(2)	2.787(4)	155(5)
O93–H932···O913	0.801(13)	2.01(3)	2.764(15)	156(6)
O93–H932···O914	0.801(13)	2.05(3)	2.763(9)	148(6)
O94–H941···O910$^{\text{ii}}$	0.799(13)	1.967(16)	2.762(4)	172(7)
O94–H942···O9	0.800(13)	1.909(14)	2.708(4)	177(6)
O95–H951···O6	0.802(13)	1.926(14)	2.725(4)	175(6)
O95–H952···O914	0.801(13)	2.16(3)	2.877(12)	149(5)
O95–H952···O919	0.801(13)	1.74(4)	2.461(17)	149(7)
O96–H961···O916$^{\text{iii}}$	0.800(13)	1.95(3)	2.663(5)	147(5)
O96–H962···O912$^{\text{iii}}$	0.798(13)	2.00(2)	2.729(5)	152(4)
O97–H971···O99$^{\text{ii}}$	0.799(13)	1.99(2)	2.730(4)	153(4)
O97–H972···O98$^{\text{ii}}$	0.800(13)	1.826(17)	2.608(4)	165(4)
O98–H981···O7$^{\text{iv}}$	0.800(13)	1.922(16)	2.713(4)	170(5)
O98–H982···O910	0.800(13)	2.05(2)	2.807(4)	158(5)
O99–H991···O911$^{\text{v}}$	0.801(13)	2.41(3)	3.016(5)	133(4)
O99–H992···O8$^{\text{v}}$	0.801(13)	2.172(14)	2.972(4)	178(4)
O910–H901···O99	0.800(13)	2.18(2)	2.914(4)	152(5)
O911–H913···O98$^{\text{ii}}$	0.804(13)	2.07(3)	2.811(4)	152(5)
O912–H923···O917	0.806(13)	2.14(3)	2.893(10)	156(6)

Symmetry code: $^{\text{i}}+x, -1+y, +z$, $^{\text{ii}}-1/2+x, 1/2-y, 1/2+z$, $^{\text{iii}}+x, 1+y, +z$, $^{\text{iv}}1-x, 1-y, 1-z$, $^{\text{v}}1-x, -y, 1-z$

Table 2.7: Hydrogen bonds in crystals of **4b** · 8.31 H_2O. Coordinates of hydrogen atoms bonded to oxygen atoms were refined freely with a SADI constraint for equivalent H–O and H–H distances (standard deviation: H–O 0.01, H–H 0.02).

D–H···A	d(D–H)/Å	d(H···A)/Å	d(D–A)/Å	∠(D–H···A)/°
O91–H912···O910^{i}	0.795(11)	1.950(15)	2.730(4)	167(5)
O92–H921···O912	0.796(11)	2.13(2)	2.856(4)	152(4)
O92–H922···O3^{ii}	0.798(11)	1.909(17)	2.683(3)	163(4)
O93–H931···O4^{ii}	0.793(11)	2.023(18)	2.759(3)	154(4)
O93–H932···O913	0.795(11)	2.04(2)	2.769(5)	153(4)
O94–H941···O911^{iii}	0.795(11)	2.001(19)	2.765(3)	161(5)
O94–H942···O9	0.795(11)	1.935(17)	2.707(3)	164(5)
O95–H951···O913	0.795(11)	2.17(2)	2.889(6)	151(4)
O95–H951···O914	0.795(11)	1.84(4)	2.54(2)	146(5)
O95–H952···O6	0.798(11)	1.935(13)	2.719(3)	167(4)
O96–H961···O917^{iv}	0.797(11)	1.89(5)	2.560(5)	141(8)
O96–H961···O918^{iv}	0.797(11)	1.94(3)	2.721(4)	165(9)
O96–H962···O912^{v}	0.793(11)	1.979(16)	2.741(4)	161(4)
O97–H971···O98^{vi}	0.796(11)	1.977(15)	2.746(3)	162(3)
O97–H972···O99^{iii}	0.794(11)	1.838(13)	2.622(3)	169(3)
O98–H981···O8	0.796(11)	2.152(11)	2.947(3)	176(3)
O98–H982···O910^{vii}	0.797(11)	2.45(2)	3.038(4)	132(3)
O99–H991···O7^{i}	0.796(11)	1.917(12)	2.707(3)	171(4)
O99–H992···O911	0.793(11)	2.030(14)	2.809(3)	167(4)
O910–H901···O99^{viii}	0.800(11)	2.07(2)	2.813(3)	154(4)
O911–H914···O98^{ix}	0.793(11)	2.167(18)	2.900(3)	154(4)
O912–H923···O915	0.800(11)	2.088(14)	2.886(8)	176(5)
O912–H923···O916	0.800(11)	1.88(2)	2.548(16)	140(3)
O912–H923···O919	0.800(11)	2.39(2)	3.158(16)	163(4)
O913–H933···O915	0.808(11)	2.05(5)	2.747(9)	145(9)
O913–H933···O916	0.808(11)	2.35(6)	3.022(17)	141(8)

Symmetry code: $^{i}1-x, 1-y, 1-z$, $^{ii}+x, 1+y, +z$, $^{iii}-1/2+x, 3/2-y, 1/2+z$, $^{iv}1/2-x, -1/2+y, 1/2-z$, $^{v}+x, -1+y, +z$, $^{vi}1/2-x, 1/2+y, 3/2-z$, $^{vii}1-x, -y, 1-z$, $^{viii}3/2-x, -1/2+y, 1/2-z$, $^{ix}1/2+x, 1/2-y, -1/2+z$

nitrosyl stretching frequency was observed at 1823 $\mathrm{cm^{-1}}$ for the solid and at 1806 $\mathrm{cm^{-1}}$ in solution. *In situ* IR measurements showed the formation of a single nitrosyl stretching band at 1809 $\mathrm{cm^{-1}}$, corresponding to the formation of FeNO species directly after the introduction of nitric oxide (Figure 2.17). Also, bands at 1318, 1361, 1619 and 1648 $\mathrm{cm^{-1}}$, representing the oxalato ligand, showed a steep rise due to initiated solubilization. After approximately 1 h, bands no longer showed growth.

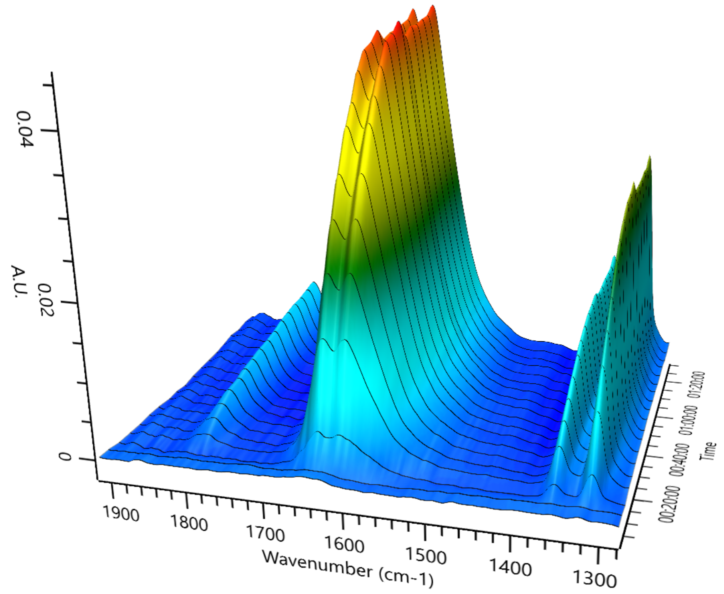

Figure 2.17: Three-dimensional plot of the time-dependent IR spectrum of the formation reaction yielding **5**. All measurements are relative to a background spectrum taken of the reaction mixture prior to introduction of nitric oxide taken at 7:40 min.

5 crystallized as **5** $\cdot$ H_2O in the triclinic space group $P\bar{1}$, with the measured crystal having been treated as a two-component entity [Transformation matrix of the minor component as analyzed by *CELL_NOW* = −1 0 0 −0.557 1 −0.08 0 0 −1. BASF: 0.379.]. The structure is shown in Figure 2.18. Relevant distances, angles and CShM values are listed in the caption. The primitive cell contained two formula units with one formula unit per asymmetric unit. The iron center was coordinated octahedrally by one aqua ligand, one nitrosyl ligand and two bidentate oxalato ligands via two five-membered chelate rings. Each oxalato ligand was bridging between two iron centers, consequently forming chains of a coordination polymer. The nitrosyl ligand, defining the axial position, exhibited a slightly bent coordination of the iron center. The aqua ligand was in *cis*-position to the nitrosyl ligand. The Fe1–O91 bond of the aqua ligand was the shortest Fe–O bond with a length of 2.035(5) Å. The remaining Fe–O bonds of the oxalato ligands ranged from 2.083(5) to Fe1–O3 2.166(4) Å with the longest bond to the oxygen atom O3 in *trans*-position to the nitrosyl ligand. Overall the Fe–O distances averaged at 2.095 Å.

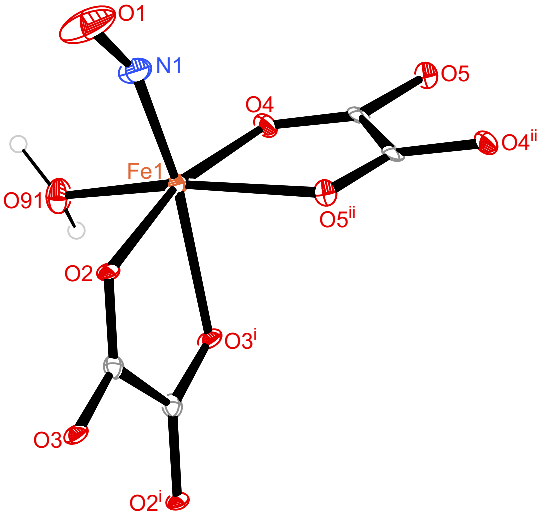

Figure 2.18: *Ortep* plot of $[\{\mathrm{Fe(H_2O)(NO)(\mu\text{-}ox)}\}_{n/n}] \cdot \mathrm{H_2O}$ in crystals of **5** $\cdot$ $\mathrm{H_2O}$ (water of crystallization not depicted). Measurement temperature: 100(2) K. Space group: $P\bar{1}$. CShM$_{OC\text{-}6}$(Fe1) = 1.087. The thermal ellipsoids are drawn at 50% probability level. Atoms: carbon (gray), hydrogen (light gray), iron (orange), nitrogen (blue), oxygen (red). Interatomic distances (Å) and angles (°) with the standard deviation in parentheses: N1–O1 1.135(8), Fe1–N1 1.784(6), Fe1–O2 2.083(5), Fe1–O3 2.166(4), Fe1–O4 2.084(5), Fe1–O5 2.108(4), Fe1–O91 2.035(5); Fe1–N1–O1 155.6(6), N1–Fe1–O2 89.7(2), N1–Fe1–O3 166.9(2), N1–Fe1–O4 102.2(2), N1–Fe1–O5 98.7(2), N1–Fe1–O91 97.1(2), O2–Fe1–O3 77.23(17), O2–Fe1–O4 167.24(18), O2–Fe1–O5 95.21(17), O2–Fe1–O91 94.82(18), O3–Fe1–O4 90.88(17), O3–Fe1–O5 83.32(17), O3–Fe1–O91 83.63(19), O4–Fe1–O5 78.60(17), O4–Fe1–O91 88.36(18), O5–Fe1–O91 161.36(19). Symmetry code: $^{\mathrm{i}}-x, 2-y, 1-z$, $^{\mathrm{ii}}1-x, 2-y, -z$.

The polymer chains ran along [$\bar{1}$01] in zig-zag lines. Between the chains, intermolecular linkage was realized by hydrogen bonds via ring motifs with the descriptors $R_5^5(14)$ (e.g. quaternary graph-set –Fe1–O91–H912···O92–O922···O3$^{\text{v}}$–Fe1$^{\text{vi}}$–O5$^{\text{vii}}$···H921$^{\text{viii}}$–O92$^{\text{viii}}$···H921$^{\text{viii}}$–O91$^{\text{viii}}$–H911$^{\text{viii}}$···O2–) and $R_4^4(16)$ (e.g. binary graph-set –Fe1–O91–H912···O92–H922···O3$^{\text{v}}$–C1$^{\text{v}}$–O2$^{\text{v}}$–Fe1$^{\text{v}}$–O91$^{\text{v}}$–H912$^{\text{v}}$···O92$^{\text{v}}$–H922$^{\text{v}}$···O3–C1–O2–) according to graph-set analysis. Table 2.8 lists symmetry codes and all hydrogen bonds in **5** · H_2O.

Table 2.8: Hydrogen bonds in crystals of **5** · H_2O. Coordinates of hydrogen atoms bonded to oxygen atoms were refined freely with a SADI constraint for equivalent H–O and H–H distances (standard deviation: H–O 0.01, H–H 0.02).

D–H···A	d(D–H)/Å	d(H···A)/Å	d(D–A)/Å	∠(D–H···A)/°
O91–H911···O2$^{\text{iii}}$	0.90(5)	1.94(5)	2.829(6)	171(8)
O91–H912···O92	0.90(5)	1.82(6)	2.654(7)	154(7)
O92–H921···O5$^{\text{iv}}$	0.90(5)	1.94(6)	2.811(7)	162(11)
O92–H922···O3$^{\text{v}}$	0.90(5)	1.93(5)	2.822(7)	173(10)

Symmetry code: $^{\text{iii}}1+x,+y,+z$, $^{\text{iv}}2-x,1-y,-z$, $^{\text{v}}-x,1-y,1-z$, $^{\text{vi}}+x,-1+y,+z$, $^{\text{vii}}1-x,1-y,-z$, $^{\text{viii}}-1+x,+y,+z$

2.5 Synthesis of $(NHEt_3)_2[Fe(fpin)_2(NO)]$ (6)

6 was synthesized in a yield of 70% by the reaction of 1 equiv iron(II) triflate with 2 equiv perfluoropinacol and 4 equiv of triethylamine in methanol to give a lavender precipitate of precursor **1**. Subsequently, nitric oxide was introduced to the reaction mixture, changing the color of the solution to burgundy while dissolving the precipitate. The product was precipitated by the addition of water. Products obtained by this procedure exhibited disorder with nitrito-κ^2*O,O* ligands on the point positions of the nitrosyl ligands in approximately 27% of all instances. This issue was resolved by an alternative procedure, where the introduction of gaseous nitric oxide was substituted by decreasing triethylamine dosage to 3 equiv and adding 1.5 equiv sodium nitrite. This method gave products that exhibited no disorder at higher yields of up to 78%.

The solid product, when devoid of a nitric-oxide atmosphere and in vacuum, showed no release of nitric oxide. It could be stored permanently in an inert gas atmosphere. Solutions showed discoloration after long exposure to nitric oxide, leading to the formation of iron(III) compounds. Also, iron(III) compounds like $(NHEt_3)_2[Fe(fpin)_2(OH)]$ were isolated from the filtrate after the precipitation of the product with water.

6 was characterized by single-crystal X-ray diffraction, elemental analysis, IR and UV/Vis spectroscopy. The nitrosyl stretching frequency of the solid product was observed at 1739 cm^{-1}. The UV/Vis spectrum of a mixture of **6** and $BaSO_4$ featured absorption bands at 251, 300, 352 and 575 nm.

Burgundy rod-shaped crystals suitable for diffraction analysis were obtained after recrystallization in methanol. **6** crystallized in the monoclinic space group $P2_1/c$. The structure is shown in Figure 2.19 with relevant distances, angles and CShM values listed in the caption. The primitive cell contained four formula units with one formula unit per asymmetric unit. In the complex anion, the iron center Fe1 was coordinated fivefold by a nitrosyl ligand and two bidentate perfluoropinacolato ligands via five-membered chelate rings. The coordination sphere was in between a square pyramid and a trigonal bipyramid. The nitrosyl ligand coordinated the iron center in axial position slightly bent. The Fe–O distances range from 1.9426(12) to 2.0576(12) Å with an average of 1.999 Å. The triethylammonium cations were connected to the complex anion via the hydrogen bonds N2–H72···O5 and N3–H73···O3$^{\mathrm{i}}$. Table 2.9 shows a list of the hydrogen bonds in **6**.

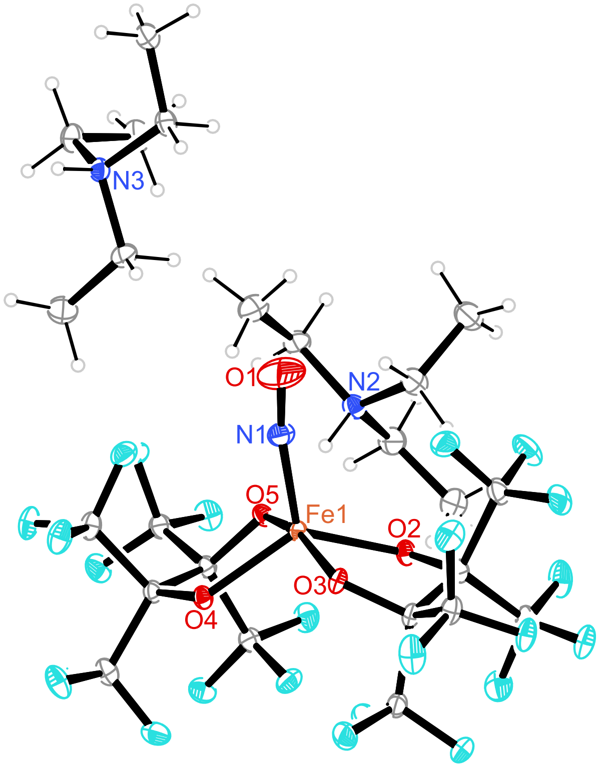

Figure 2.19: *Ortep* plot of the $(\mathrm{NHEt_3})_2[\mathrm{Fe(fpin)_2(NO)}]$ in crystals of **6**. Measurement temperature: 100(2) K. Space group: $P2_1/c$. $\mathrm{CShM}_{SPY\text{-}5}(\mathrm{Fe1}) = 1.930$, $\mathrm{CShM}_{TBPY\text{-}5}(\mathrm{Fe1}) = 1.692$. The thermal ellipsoids are drawn at 50% probability level. Atoms: carbon (gray), hydrogen (light gray), fluorine (green), iron (orange), nitrogen (blue), oxygen (red). Interatomic distances (Å) and angles (°) with the standard deviation in parentheses: N1–O1 1.149(2), Fe1–N1 1.7572(17), Fe1–O2 1.9426(12), Fe1–O3 2.0423(13), Fe1–O4 1.9532(12), Fe1–O5 2.0576(12); Fe1–N1–O1 168.52(17), N1–Fe1–O2 114.73(7), N1–Fe1–O3 98.80(6), N1–Fe1–O4 114.19(7), N1–Fe1–O5 98.96(6), O2–Fe1–O3 80.80(5), O2–Fe1–O4 131.07(5), O2–Fe1–O5 91.65(5), O3–Fe1–O4 92.60(5), O3–Fe1–O5 162.24(5), O4–Fe1–O5 80.21(5).

Table 2.9: Hydrogen bonds in crystals of **6**. Coordinates of hydrogen atoms were calculated in idealized positions, riding on their parent atoms.

D–H···A	d(D–H)/Å	d(H···A)/Å	d(D–A)/Å	∠(D–H···A)/°
N2–H72···O5	0.90(2)	1.84(2)	2.737(2)	171(2)
N3–H73···O3^{i}	0.89(2)	1.97(2)	2.825(2)	162(2)

Symmetry code: $^{i}1-x, 1-y, 1-z$

2.6 Synthesis of neutral nitrosylperfluoropinacolatoiron compounds

The nature of the products obtained from nitrosylated reaction mixtures with an equimolar ratio of iron(II) triflate to perfluoropinacolate depended highly on the base dosage and the solvent used. In methanol and ethanol, more acidic conditions, as were induced by substoichiometrical base dosage, in general, led to the crystallization of mononuclear products of the general formula $[\mathrm{Fe(fpin)(NO)(solv)_2}]$ (solv=MeOH, EtOH; **7a**, **7b**). Alkaline conditions, caused by stochiometric or even excessive base dosage, led mostly to the formation of tetranuclear species of the general formula $[\{\mathrm{Fe_2(fpin\text{-}1}\kappa O,O')(\mathrm{ROH\text{-}2}\kappa O)(\mathrm{NO\text{-}2}\kappa N)(\mathrm{OR\text{-}1{:}2}\kappa O,\mathrm{1{:}2'}\kappa O,\text{-}\mathrm{1{:}2{:}2'}\kappa O)_3\}_2]$ (R=Me, H/Et; **8a**, **7b**). In benzonitrile, $[\{\mathrm{Fe(fpin\text{-}1}\kappa O{:}1,1'\kappa O')(\mathrm{NO})(\mathrm{PhCN})\}_2]$ (**9**) was obtained after nitrosylation at a stochiometric addition of base.

2.6.1 [Fe(fpin)(NO)(solv)$_2$] (solv=MeOH, EtOH; 7a, 7b)

7a was prepared by the reaction of a methanolic solution of 1 equiv iron(II) triflate, 1 equiv perfluoropinacol and 1 equiv potassium methoxide with gaseous nitric oxide. Red crystals of **7a** · MeOH containing one molecule of methanol of crystallization were obtained from the reaction mixture after approximately 20 min. **7b** was obtained as red rod-shaped crystals by the introduction of gaseous nitric oxide into an ethanolic suspension of 1 equiv iron(II) triflate with 1 equiv perfluoropinacol and 2 equiv *n*-butyllithium or by nitrosylation of **2b**.

7a and **7b** were characterized by single-crystal X-ray diffraction and IR spectroscopy. Furthermore, the formation reaction of **7a** was monitored via *in situ* IR spectroscopy. The nitrosyl stretching frequencies of the solid products were observed at $1801\,\mathrm{cm^{-1}}$ for **7a** and at $1808\,\mathrm{cm^{-1}}$ for **7b**. *In situ* IR measurements of the formation reaction of **7a** showed the generation of a single nitrosyl stretching band at $1765\,\mathrm{cm^{-1}}$ directly after the introduction of nitric oxide, corresponding to the formation of the red nitrosyl species (Figure 2.20). In the further course of the measurement, the band at $1765\,\mathrm{cm^{-1}}$ disappeared and was then replaced by a nitrosyl stretching band at $1785\,\mathrm{cm^{-1}}$ with high intensity within approximately 2 min. In addition, a further band appeared at $1722\,\mathrm{cm^{-1}}$.

Both compounds crystallized in the triclinic space group $P\overline{1}$. The molecular structures are depicted in Figure 2.21 (**7a** · MeOH) and Figure 2.22 (**7b**) with relevant distances, angles and CShM values in the respective caption. The primitive cells contained two formula units with one formula unit per asymmetric unit in **7a** · MeOH and four formula units with two formula units per asymmetric units in **7b**. The iron centers were coordinated fivefold by each a nitrosyl ligand, two solvent ligands and one bidentate perfluoropinacolato ligand via a five-membered chelate ring. The coordination spheres were best described as a square pyramids. The nitrosyl ligands exhibited a slightly bent coordination of the iron centers. The mean Fe–O distances were 2.002 Å in **7a** · MeOH and 2.0240 Å in **7b**.

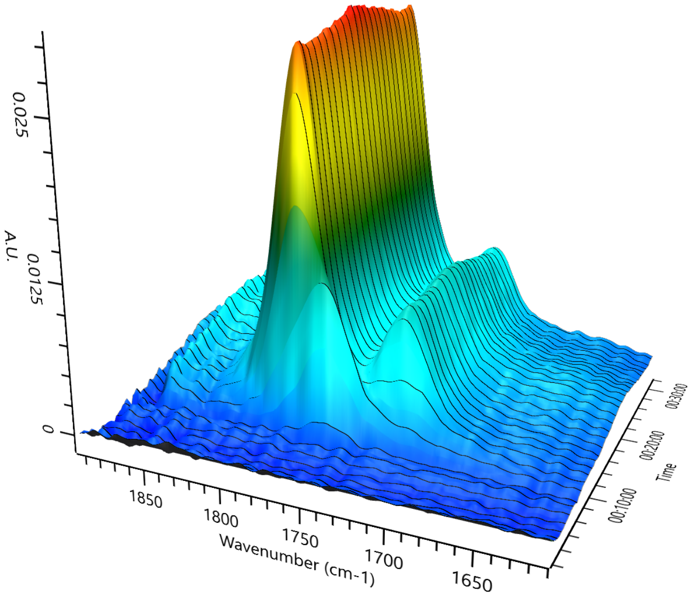

Figure 2.20: Three-dimensional plot of the time-dependent IR spectrum of the formation reaction yielding **7a**. All measurements are relative to a background spectrum taken of the reaction mixture prior to introduction of nitric oxide taken at 0:55 min.

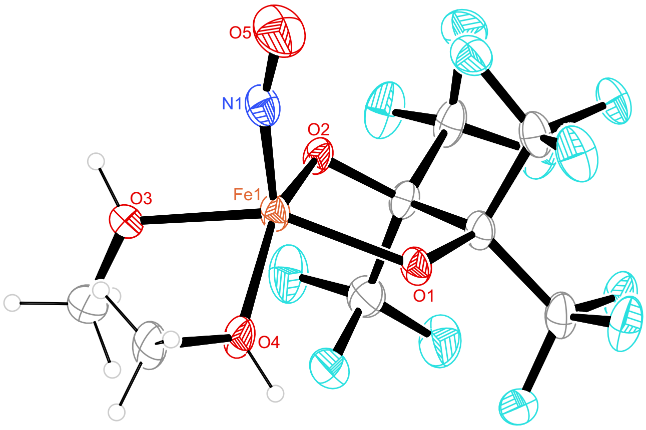

Figure 2.21: *Ortep* plot of [Fe(fpin)(MeOH)$_2$(NO)] in crystals of **7a** (methanol of crystallization not depicted). Measurement temperature: 100(2) K. Space group: $P\overline{1}$. CShM$_{SPY\text{-}5}$(Fe1) = 0.394. The thermal ellipsoids are drawn at 50% probability level. Atoms: carbon (gray), hydrogen (light gray), fluorine (green), iron (orange), nitrogen (blue), oxygen (red). Interatomic distances (Å) and angles (°) with the standard deviation in parentheses: N1–O5 1.152(4), Fe1–N1 1.745(4), Fe1–O1 1.958(2), Fe1–O2 1.991(2), Fe1–O3 2.045(3), Fe1–O4 2.015(3); Fe1–N1–O5 162.8(3), N1–Fe1–O1 112.76(13), N1–Fe1–O2 105.43(13), N1–Fe1–O3 98.98(13), N1–Fe1–O4 106.49(14), O1–Fe1–O2 80.88(10), O1–Fe1–O3 148.23(11), O1–Fe1–O4 86.89(11), O2–Fe1–O3 89.74(10), O2–Fe1–O4 148.09(12), O3–Fe1–O4 85.33(11).

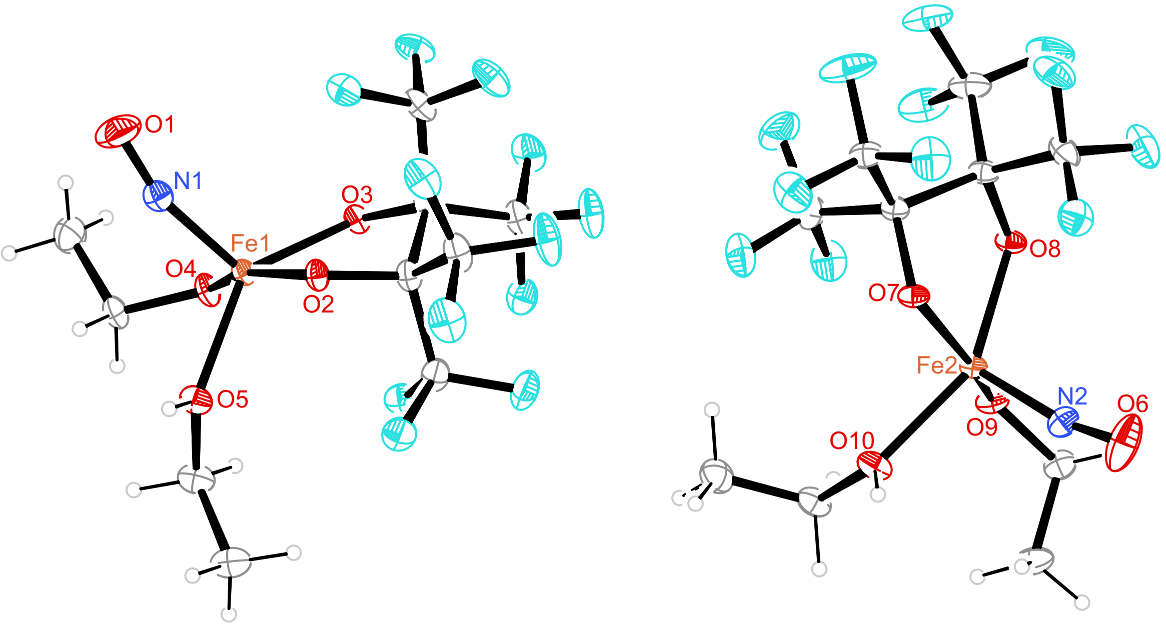

Figure 2.22: *Ortep* plot of both entities of [Fe(fpin)(EtOH)$_2$(NO)] in the asymmetric unit in crystals of **7b**. Measurement temperature: 103(2) K. Space group: $P\bar{1}$. The thermal ellipsoids are drawn at 50% probability level. Atoms: carbon (gray), hydrogen (light gray), fluorine (green), iron (orange), nitrogen (blue), oxygen (red). Interatomic distances (Å) and angles (°) with the standard deviation in parentheses: N1–O1 1.151(2), Fe1–N1 1.7515(19), Fe1–O2 1.9992(14), Fe1–O3 1.9681(14), Fe1–O4 2.0656(15), Fe1–O5 2.0436(15), Fe2–N2 1.7508(19), Fe2–O10 2.0642(15), Fe2–O7 1.9937(14), Fe2–O8 1.9992(14), Fe2–O9 2.0584(15); Fe1–N1–O1 163.86(18), N1–Fe1–O2 100.28(7), N1–Fe1–O3 116.60(7), N1–Fe1–O4 98.67(7), N1–Fe1–O5 107.11(7), O2–Fe1–O3 81.18(6), O2–Fe1–O4 160.41(6), O2–Fe1–O5 90.78(6), O3–Fe1–O4 85.94(6), O3–Fe1–O5 136.28(6), O4–Fe1–O5 88.37(6), N2–Fe2–O10 99.55(8), N2–Fe2–O7 103.65(7), N2–Fe2–O8 110.17(7), N2–Fe2–O9 103.22(7), O7–Fe2–O10 89.91(6), O7–Fe2–O8 80.71(6), O7–Fe2–O9 152.73(6), O8–Fe2–O10 150.16(6), O8–Fe2–O9 85.78(6), O9–Fe2–O10 90.18(6).

The crystal structure of **7a** · MeOH showed chains along [001] in which methanol and complex molecules were connected via hydrogen bonds (Figure 2.23). Hydrogen bonds in crystals of **7a** are listed in Table 2.10. The connections alternated between a $R_2^2(8)$ ring motif (unary graph-set –Fe1–O3–H83$\cdots$O2$^{\mathrm{ii}}$–Fe1$^{\mathrm{ii}}$–O3$^{\mathrm{ii}}$–H83$^{\mathrm{ii}}\cdots$O2–) and a $R_4^4(12)$ ring motif (binary graph-set –Fe1–O4–H84$\cdots$O6–H86$\cdots$O1$^{\mathrm{i}}$–Fe1$^{\mathrm{i}}$–O4$^{\mathrm{i}}$–H84$^{\mathrm{i}}$ O6$^{\mathrm{i}}$–H86$^{\mathrm{i}}\cdots$O1–). A section of the chain is shown in Figure 2.23. In **7b** chains of complex molecules along [1$\bar{1}$1] were present and connected via hydrogen bonds (Figure 2.23). Hydrogen bonds in crystals of **7b** are listed in Table 2.11. All complex molecules were connected via $R_2^2(8)$ ring motifs (e.g. unary graph-set –Fe2–O10–H810$\cdots$O7$^{\mathrm{i}}$–Fe2$^{\mathrm{i}}$–O10$^{\mathrm{i}}$–H810$^{\mathrm{i}}\cdots$O7–) to their adjacent molecules according to graph-set analysis.

Table 2.10: Hydrogen bonds in crystals of **7a** · MeOH. Coordinates of hydrogen atoms bonded to oxygen atoms were refined freely with a SADI constraint for equivalent H–O bonds (standard deviation: H–O 0.01). All other hydrogen atoms were calculated in idealized positions, riding on their parent atoms.

D–H$\cdots$A	d(D–H)/Å	d(H$\cdots$A)/Å	d(D–A)/Å	∠(D–H$\cdots$A)/°
O3–H83$\cdots$O2$^{\mathrm{ii}}$	0.88(3)	1.70(3)	2.571(4)	172(4)
O4–H84$\cdots$O6	0.88(3)	1.68(3)	2.550(4)	172(5)
O6–H86$\cdots$O1$^{\mathrm{i}}$	0.88(3)	1.90(3)	2.777(4)	177(4)

Symmetry code: $^{\mathrm{i}}1-x, 1-y, 1-z$, $^{\mathrm{ii}}1-x, 1-y, -z$

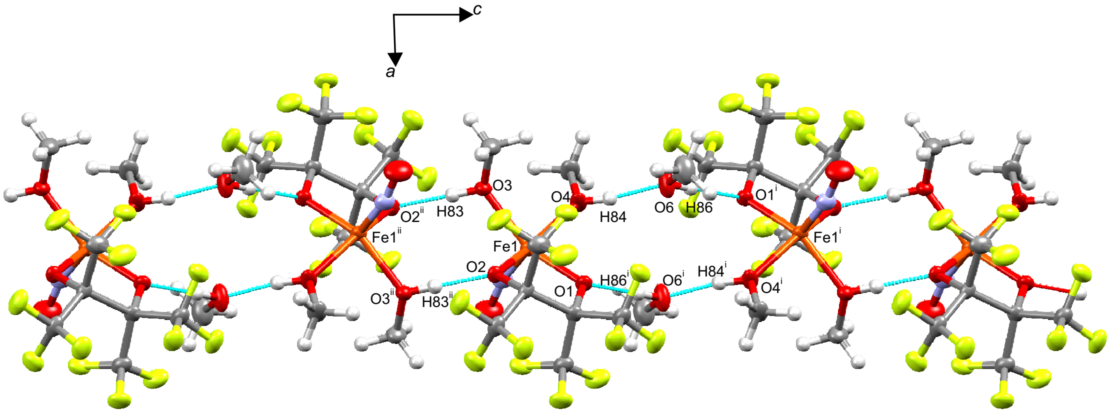

Figure 2.23: *POV-Ray* plot of the hydrogen-bond network (cyan dashed lines) in crystals of **7a** with view along [010].

Table 2.11: Hydrogen bonds in crystals of **7b**. Coordinates of hydrogen atoms bonded to oxygen atoms were refined freely with a SADI constraint for equivalent H–O bonds (standard deviation: H–O 0.01). All other hydrogen atoms were calculated in idealized positions, riding on their parent atoms.

D–H···A	d(D–H)/Å	d(H···A)/Å	d(D–A)/Å	∠(D–H···A)/°
O10–H810···O7$^{\mathrm{i}}$	0.758(16)	1.907(17)	2.660(2)	172(3)
O9–H89···O3$^{\mathrm{ii}}$	0.757(16)	1.939(16)	2.690(2)	172(3)
O5–H85···O2$^{\mathrm{iii}}$	0.759(16)	1.880(16)	2.637(2)	175(3)
O4–H84···O8$^{\mathrm{ii}}$	0.762(16)	1.916(16)	2.676(2)	175(3)

Symmetry code: $^{\mathrm{i}}-x, 1-y, 1-z$, $^{\mathrm{ii}}1-x, 1-y, 1-z$, $^{\mathrm{iii}}1-x, 2-y, -z$, $^{\mathrm{iv}}+x, -1+y, 1+z$, $^{\mathrm{v}}-1+x, +y, +z$

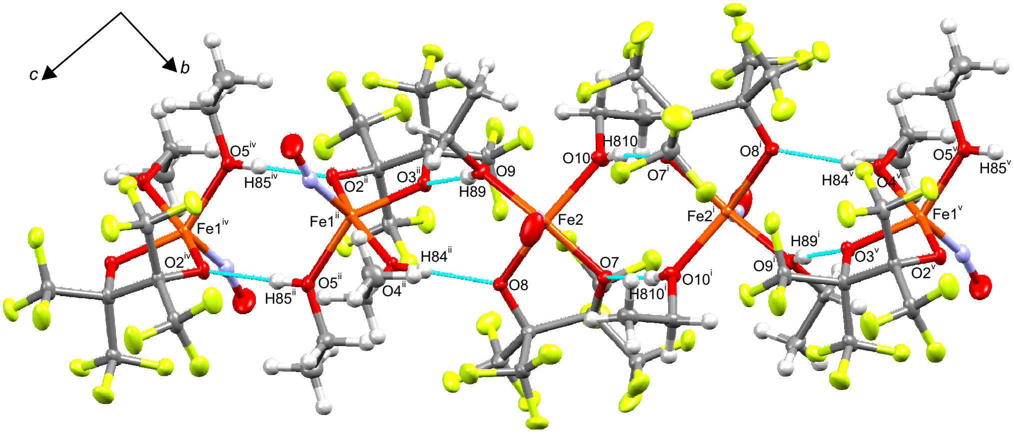

Figure 2.24: *POV-Ray* plot of the hydrogen-bond network (cyan dashed lines) in crystals of **7b** with view along [100].

2.6.2 $[\{\mathrm{Fe_2(fpin\text{-}1\kappa}O,O')(\mathrm{ROH\text{-}2\kappa}O)(\mathrm{NO\text{-}2\kappa}N)(\mathrm{OR\text{-}1{:}2\kappa}O,\mathrm{1{:}2'\kappa}O,\mathrm{1{:}2{:}2'\kappa}O)_3\}_2]$ (R=Me, H/Et; 8a, 8b)

8a · 2 MeOH was prepared in methanol as brown rod-shaped crystals either by the reaction of **2a** with nitric oxide or by the introduction of nitric oxide into a mixture of 1 equiv iron(II) triflate with 1 equiv perfluoropinacol and 2 equiv potassium methoxide. **8b** · 2 EtOH was synthesized by the reaction of 1 equiv iron(II) triflate with 1 equiv perfluoropinacol, 2 equiv *n*-butyllithium with gaseous nitric oxide in ethanol yielding brown block-shaped crystals.

8a · 2 MeOH and **8b** · 2 EtOH were characterized by single-crystal X-ray diffraction and IR spectroscopy. Furthermore the formation reaction of **8a** · 2 MeOH was monitored by *in situ* IR spectroscopy. The nitrosyl stretching frequencies of the solid products were observed at 1765 $\mathrm{cm^{-1}}$ in **8a** · 2 MeOH and at 1762 $\mathrm{cm^{-1}}$ in **8b** · 2 EtOH.

In situ IR measurements of the formation reaction of **8a** · 2 MeOH showed the generation of a single nitrosyl stretching band at 1766 $\mathrm{cm^{-1}}$ directly after introduction of nitric oxide (Figure 2.25). In the further course of the measurement, this band decreased and a nitrosyl stretching band at 1786 $\mathrm{cm^{-1}}$ was formed within 2 min. After approximately 50 min, a high-intensity band at 1768 appeared and rose further in the following 30 min. Thereafter, its intensity decreased, as the beginning crystallization of **8a** · 2 MeOH lowered the concentration of the observed nitrosyl species.

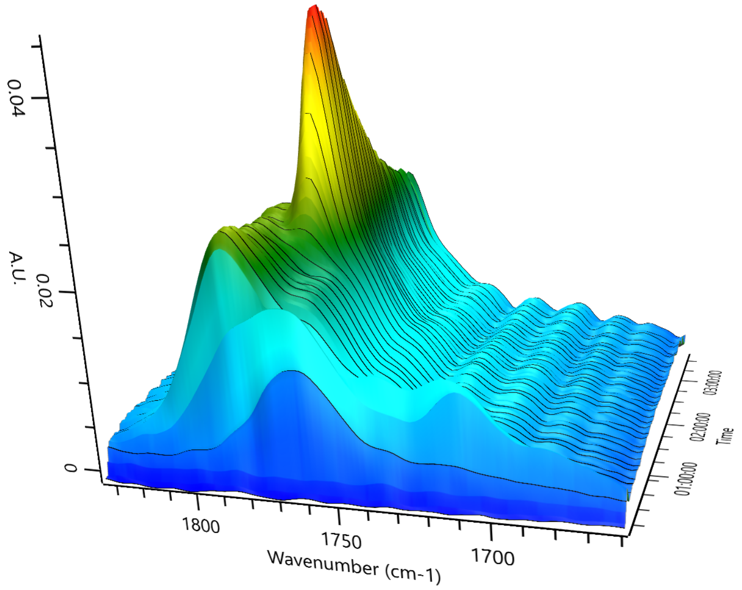

Figure 2.25: Three-dimensional plot of the time-dependent IR spectrum of the formation reaction yielding **8a**. All measurements are relative to a background spectrum taken of the reaction mixture prior to introduction of nitric oxide taken at 3:25 min.

As in the preparation of **4b** (Section 2.4.1), the formation of nitrous oxide was also observed in the headspace of the formation reactions of **8a** and **8b** upon nitrosylation. The time-dependent increase of nitrous oxide in the head space as determined by IR spectroscopy is shown in Figure 2.26 for **8a** and in Figure 2.27 for **8b**.

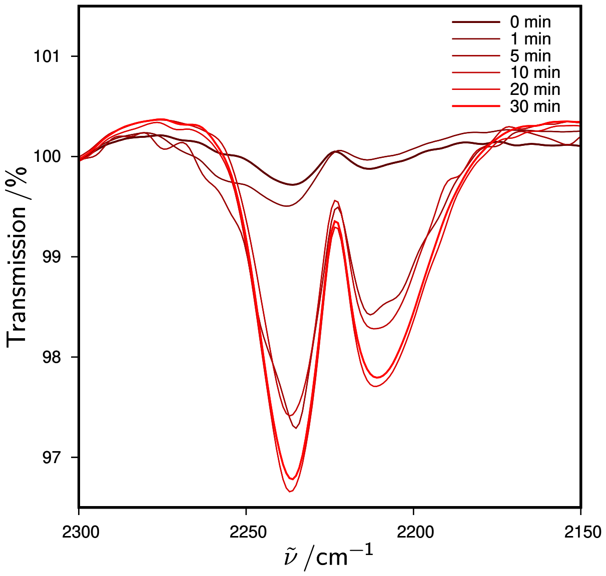

Figure 2.26: Formation of nitrous oxide during nitric-oxide introduction in the synthesis of **8a** as monitored by IR spectroscopy. Nitric oxide was introduced into a suspension of 1.35 mmol **2a** in 25 mL methanol at room temperature. Samples were taken off the head space of the reaction mixture directly after introduction of NO (0 min) and after 1, 5, 10, 20 and 30 min.

Crystallization of the compounds occurred in the monoclinic space groups $P2_1/n$ for **8a** · 2 MeOH and $P2_1/c$ for **8b** · 2 EtOH. The molecular structures are shown in Figure 2.28 (**8a** · 2 MeOH) and Figure 2.29 (**8b** · 2 MeOH) with the relevant distances, angles and CShM values in the respective caption. The primitive cells of **8a** · 2 MeOH and **8b** · 2 EtOH each contained two formula units with half a formula unit per asymmetric unit. Both compounds crystallized with each two solvent molecules of crystallization. The complex molecules were tetranuclear with two different types of iron centers due to inversion symmetry. The outer iron(III) centers were coordinated fivefold by each two, doubly bridging alkoxido ligands, one triply bridging methoxido (**8a** · 2 MeOH) or hydroxido ligand (**8b** · 2 EtOH) and one bidentate perfluoropinacolato ligand via a five-membered chelate ring. The coordination spheres were best described as trigonal bipyramidal. The mean Fe^{III}–O distances were 1.9454 Å in **8a** · 2 MeOH and 1.9516 Å in **8b** · 2 EtOH. The inner iron centers of the FeNO moieties exhibited octahedral coordination, by one slightly bent nitrosyl ligand, one alcohol ligand, two doubly bridging alkoxido ligands and two triply bridging methoxido (**8a** · 2 MeOH) or hydroxido ligands (**8b** · 2 EtOH) ligands. The nitrosyl ligands in **8a** · 2 MeOH were disordered with both partitions showing different Fe–N–O angles and rotation around the Fe–N axis ($\angle_{dih.}$(O4–Fe2–N1–O7) = −125(5)°, $\angle_{dih.}$(O4–Fe2–N1–O7) = 170(3)°). The mean Fe–O distances of the inner $\{FeNO\}^7$ species were 2.0925 Å in **8a** · 2 MeOH and 2.0876 Å in

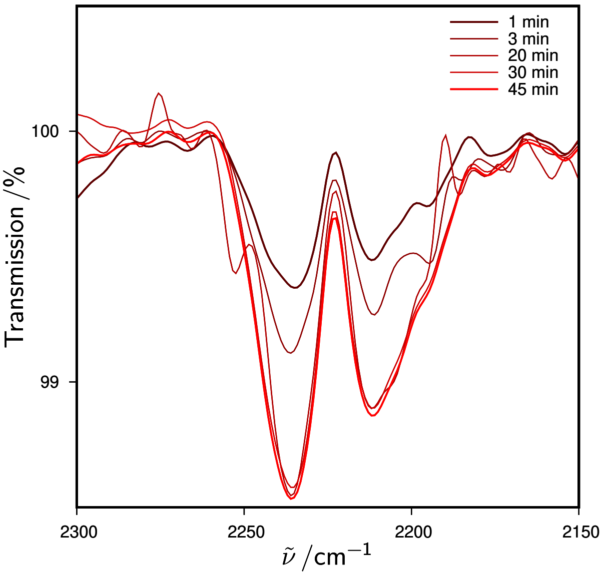

Figure 2.27: Formation of nitrous oxide during nitric-oxide introduction in the synthesis of **8b** as monitored by IR spectroscopy. Nitric oxide was introduced into a suspension of 648 µmol **2b** in 5 mL ethanol at room temperature. Samples were taken off the head space of the reaction mixture after 1, 3, 20, 30 and 45 min.

8b · 2 EtOH. The molecule of ethanol of crystallization in **8b** · 2 EtOH showed disorder at the backbone in respect to its relative arrangement to the hydroxy group, while the hydroxy moiety showed no disorder.

In crystals of **8a** · 2 MeOH and **8b** · 2 EtOH, intermolecular hydrogen-bond linkage was present exclusively between the complex molecules and their two adjacent solvent molecules of crystallization. According to graph-set analysis discrete ring motifs with the descriptor $R_2^2(8)$ (binary graph-set –Fe1–O4–Fe2–O6–H86· · ·O8–H88· · ·O2–) in **8a** · 2 MeOH and $R_2^1(6)$ (binary graph-set –Fe1–O2–H82· · ·O8· · ·H84–O4–), $R_2^2(6)$ (binary graph-set –Fe2–O4–H84· · ·O8· · ·H84–O4–) and $R_2^2(8)$ (binary graph-set –Fe2–O3–Fe1–O2–H82· · ·O8–H88· · ·O5–) in **8a** · 2 MeOH were formed. Hydrogen bonds are listed in Table 2.12 (**8a** · 2 MeOH) and Table 2.13 (**8b** · 2 EtOH).

Table 2.12: Hydrogen bonds in crystals of **8a** · 2 MeOH. H86 was refined freely with a SADI constraint for equivalent H–O bonds (standard deviation: H–O 0.01). All other hydrogen atoms were calculated in idealized positions, riding on their parent atoms.

D–H· · ·A	d(D–H)/Å	d(H· · ·A)/Å	d(D–A)/Å	∠(D–H· · ·A)/°
O8–H88· · ·O2	0.81	1.94	2.744(2)	169.7
O6–H86· · ·O8	0.80(3)	1.79(3)	2.576(3)	167(2)

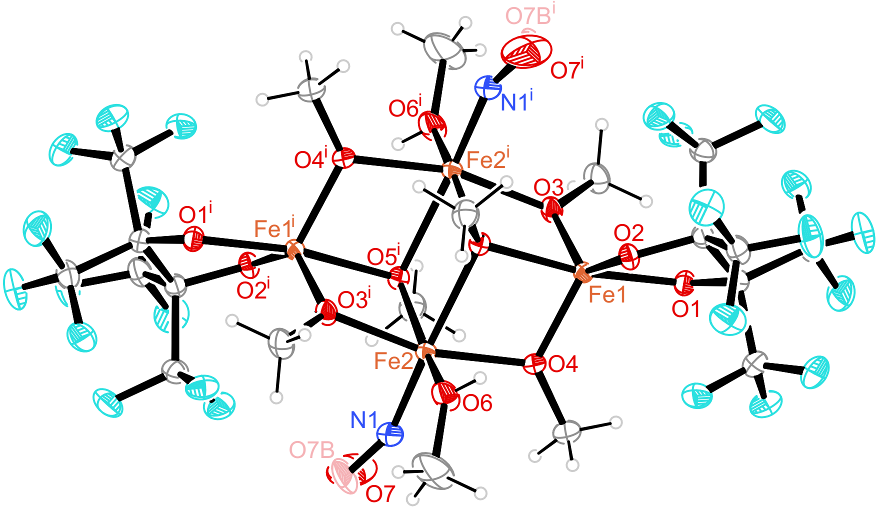

Figure 2.28: *Ortep* plot of [{Fe$_2$(fpin-1κO,O')(MeOH-2κO)(NO-2κN)(OMe-1:2κO,1:2$'$κO,1:2:2$'$κO)$_3$}$_2$] in crystals of **8a** · 2 MeOH (methanol of crystallization not depicted, O17B of the minor disorder form in light red). Measurement temperature: 153(2) K. Space group: $P2_1/n$. CShM$_{TBPY\text{-}5}$(Fe1) = 1.866; CShM$_{OC\text{-}6}$(Fe2) = 1.098. The thermal ellipsoids are drawn at 50% probability level. Atoms: carbon (gray), hydrogen (light gray), fluorine (green), iron (orange), nitrogen (blue), oxygen (red). Interatomic distances (Å) and angles (°) with the standard deviation in parentheses: N1–O7 1.163(15), N1–O7B 1.125(14), Fe1–O1 1.9117(15), Fe1–O2 1.9506(15), Fe1–O3 1.8954(15), Fe1–O4 1.8955(16), Fe1–O5 2.0736(15), Fe2–N1 1.770(2), Fe2–O3$^{\mathrm{i}}$ 2.0183(16), Fe2–O4 2.0211(16), Fe2–O5 2.2419(15), Fe2–O5$^{\mathrm{i}}$ 2.1113(15), Fe2–O6 2.0700(18), Fe1–Fe2 3.1760(4), Fe1–Fe2$^{\mathrm{i}}$ 3.1006(4), Fe2–Fe2$^{\mathrm{i}}$ 3.4495(6); O1–Fe1–O2 82.10(6), O1–Fe1–O3 97.93(7), O1–Fe1–O4 107.94(7), O1–Fe1–O5 170.05(6), O2–Fe1–O3 135.24(7), O2–Fe1–O4 117.75(7), O2–Fe1–O5 91.24(6), O3–Fe1–O4 104.88(7), O3–Fe1–O5 81.58(6), O4–Fe1–O5 81.69(6), Fe2–N1–O7 156.8(9), Fe2–N1–O7B 153.0(9), N1–Fe2–O3$^{\mathrm{i}}$ 95.14(9), N1–Fe2–O4 99.52(8), N1–Fe2–O5 170.50(9), N1–Fe2–O5$^{\mathrm{i}}$ 98.09(9), N1–Fe2–O6 96.34(10), O3$^{\mathrm{i}}$–Fe2–O4 164.96(6), O3$^{\mathrm{i}}$–Fe2–O5 77.87(6), O3$^{\mathrm{i}}$–Fe2–O5 90.08(6), O3$^{\mathrm{i}}$–Fe2–O6 90.98(7), O4–Fe2–O5 74.94(6), O4–Fe2–O5$^{\mathrm{i}}$ 96.63(6), O4–Fe2–O6 90.73(7), O5–Fe2–O5$^{\mathrm{i}}$ 75.22(6), O5–Fe2–O6 91.49(7), O5$^{\mathrm{i}}$–Fe2–O6 162.46(7).

Table 2.13: Hydrogen bonds in crystals of **8b** · 2 EtOH. Coordinates of hydrogen atoms bonded to oxygen atoms were refined freely. All other hydrogen atoms were calculated in idealized positions, riding on their parent atoms.

D–H···A	d(D–H)/Å	d(H···A)/Å	d(D–A)/Å	∠(D–H···A)/°
O2–H82···O8	0.75(2)	1.95(2)	2.691(3)	170(4)
O4–H84···O8	0.76(3)	2.33(3)	2.917(3)	136(3)
O8–H88···O5	0.75(2)	1.97(3)	2.694(3)	163(3)

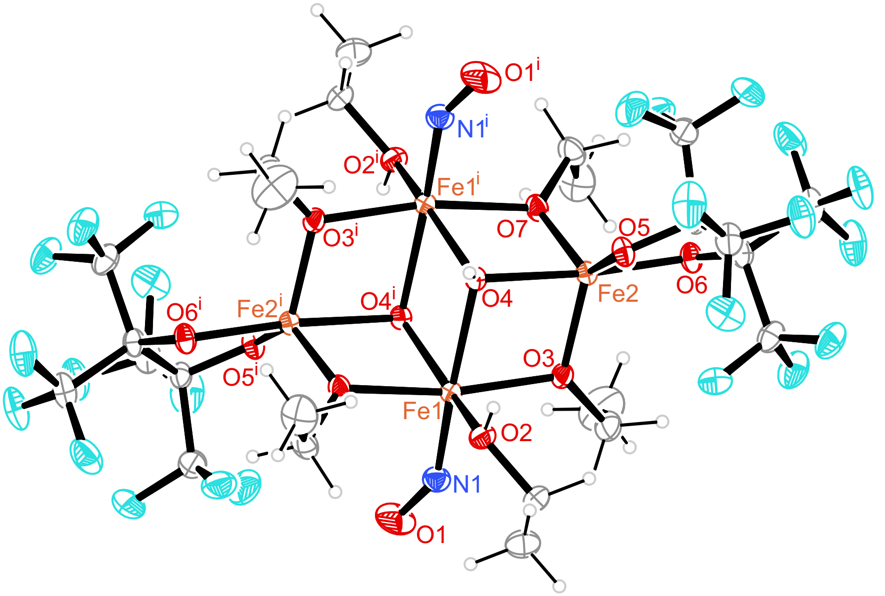

Figure 2.29: *Ortep* plot of $[\{\mathrm{Fe_2(EtOH\text{-}2\kappa}O)(\mathrm{fpin\text{-}1\kappa}O,O')(\mathrm{NO\text{-}2\kappa}N)(\mathrm{OEt\text{-}1{:}2\kappa}O,1{:}2'\kappa O)_2(\mathrm{OH\text{-}1{:}2{:}2'\kappa}O)\}_2]$ in crystals of **8b** $\cdot$ 2 EtOH (ethanol of crystallization not depicted for better clarity). Measurement temperature: 103(2) K. Space group: $P2_1/c$. CShM$_{OC\text{-}6}$(Fe1) = 1.268; CShM$_{TBPY\text{-}5}$(Fe2) = 1.450. The thermal ellipsoids are drawn at 50% probability level. Atoms: carbon (gray), hydrogen (light gray), fluorine (green), iron (orange), nitrogen (blue), oxygen (red). Interatomic distances (Å) and angles (°) with the standard deviation in parentheses: N1–O1 1.151(3), Fe1–N1 1.774(2), Fe1–O2 2.0836(17), Fe1–O3 2.0305(16), Fe1–O4 2.0943(17), Fe1–O4$^\mathrm{i}$ 2.1755(17), Fe1–O7$^\mathrm{i}$ 2.0542(16), Fe2–O3 1.9112(16), Fe2–O4 2.0892(16), Fe2–O5 1.9539(17), Fe2–O6 1.9041(16), Fe2–O7 1.8997(16), Fe1–Fe1$^\mathrm{i}$ 3.3851(7), Fe1–Fe2 3.1598(5), Fe1–Fe2$^\mathrm{i}$ 3.1314(5); Fe1–N1–O1 148.6(2), N1–Fe1–O2 99.04(8), N1–Fe1–O3 98.02(8), N1–Fe1–O4 170.69(8), N1–Fe1–O4$^\mathrm{i}$ 98.70(8), N1–Fe1–O7$^\mathrm{i}$ 92.53(8), O2–Fe1–O3 91.02(7), O2–Fe1–O4 88.60(7), O2–Fe1–O4$^\mathrm{i}$ 158.27(7), O2–Fe1–O7$^\mathrm{i}$ 89.37(7), O3–Fe1–O4 76.40(6), O3–Fe1–O4$^\mathrm{i}$ 98.83(7), O3–Fe1–O7$^\mathrm{i}$ 169.25(7), O4–Fe1–O4$^\mathrm{i}$ 75.12(7), O4–Fe1–O7$^\mathrm{i}$ 92.87(6), O4$^\mathrm{i}$–Fe1–O7$^\mathrm{i}$ 77.40(6), O3–Fe2–O4 81.07(7), O3–Fe2–O5 119.48(7), O3–Fe2–O6 106.77(7), O3–Fe2–O7 107.16(7), O4–Fe2–O5 88.53(7), O4–Fe2–O6 170.21(7), O4–Fe2–O7 80.98(7), O5–Fe2–O6 82.51(7), O5–Fe2–O7 129.81(7), O6–Fe2–O7 101.76(7).

2.6.3 [{Fe(fpin-1κ*O*:1,1′κ*O*′)(NO)(PhCN)}$_2$] (9)

9 was synthesized by the reaction of 1 equiv iron(II) triflate, 1 equiv perfluoropinacol and 2 equiv triethylamine with gaseous nitric oxide in benzonitrile, giving a dark green crystalline solid in 35% yield. **9** was characterized by single-crystal X-ray diffraction, elemental analysis, IR and UV/Vis spectroscopy.

The nitrosyl stretching frequency was observed at 1808 cm^{-1}. The solid-state UV/Vis spectrum featured absorption bands at <400, 425, and 614 nm. Crystals fit for single-crystal X-ray diffraction were obtained directly from the reaction mixture. **9** was poorly soluble in benzonitrile and toluene. The addition of protic solvents like methanol led to discoloration and decomposition. Removal of the nitric-oxide atmosphere and evacuation did not lead to the release of nitric oxide from the product. Contact with oxygen led to oxidation within 1 h, which was accompanied by a change of color to dark brown.

9 crystallized in the monoclinic space group $C2/c$. The molecular structure of **9** is shown in Figure 2.30 with the relevant distances, angles and CShM values in the caption. The primitive cell contained four formula units with half a complex molecule per asymmetric unit. The complex molecule was dinuclear with two symmetrically equivalent Fe1 centers at a Fe1–Fe1$^{\mathrm{i}}$ distance of 3.2302(7) Å. The coordination sphere of the iron centers was best described as square pyramids with both tips of the pyramids facing in the same direction. In consequence, Fe1 was coordinated fivefold by one benzonitrile ligand in apical position, one nitrosyl ligand in terminal equatorial position, a bidentate perfluoropinacolato ligand via a five-membered chelate ring and a bridging oxygen atom from the adjacent perfluoropinacolato ligand. The Fe1–N1–O1 moiety was bent with an angle of 150.34(19)°. The Fe1–O bond lengths averaged at 2.0123 Å. The phenyl rings of the benzonitrile ligands faced eachother, suggesting π–π interaction. The distance between both planes was 3.74 Å approximately.

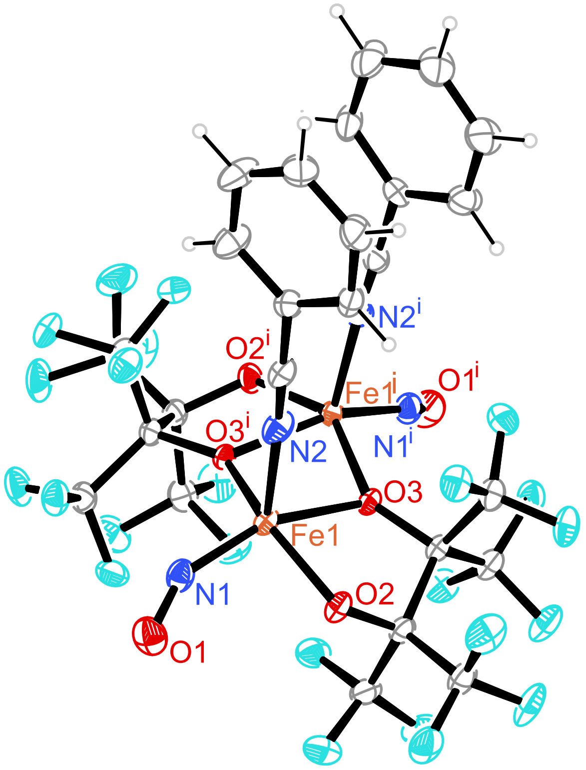

Figure 2.30: *Ortep* plot of [{Fe(fpin-1κ*O*:1,1′κ*O*′)(NO)(PhCN)}$_2$] in crystals of **9**. Measurement temperature: 100(2) K. Space group: $C2/c$. The thermal ellipsoids are drawn at 50% probability level. Atoms: carbon (gray), hydrogen (light gray), fluorine (green), iron (orange), nitrogen (blue), oxygen (red). Interatomic distances (Å) and angles (°) with the standard deviation in parentheses: N1–O1 1.149(3), Fe1–N1 1.769(2), Fe1–N2 2.062(2), Fe1–O2 1.9217(16), Fe1–O3 2.1116(16), Fe1–O3$^{\mathrm{i}}$ 2.0037(16), Fe1–Fe1$^{\mathrm{i}}$ 3.2302(7) Å; Fe1–N1–O1 150.34(19), N1–Fe1–N2 102.30(10), N1–Fe1–O2 90.73(8), N1–Fe1–O3 105.39(8), N1–Fe1–O3 156.12(9), N2–Fe1–O2 106.03(8), N2–Fe1–O3 101.22(8), N2–Fe1–O3$^{\mathrm{i}}$ 98.73(7), O2–Fe1–O3 78.82(6), O2–Fe1–O3$^{\mathrm{i}}$ 146.81(7), O3–Fe1–O3$^{\mathrm{i}}$ 74.91(7). Symmetry code: $^{\mathrm{i}}1-x, +y, 1/2-z$.

2.7 DFT calculations

DFT calculations were performed on mononuclear nitrosyliron compounds to achieve a better understanding of their electronic properties. Thus, bond distances and the Fe–N–O angle of the FeNO fragment as well as the corresponding nitrosyl stretching frequencies were of special interest.

2.7.1 Structural optimization

Initial geometries for structural optimizations were taken from the respective crystal structure. All calculations were performed using the def2-TZVP[71] basis set with D3 dispersion correction,[72] RI-J[73,74] approximation for non-hybrid functionals or RIJCOSX[75,76] approximation for hybrid functionals using a def2/J[77] auxiliary basis set. The results of optimization calculations were expected to reproduce the experimentally determined Fe–N and N–O distances as well as the Fe–N–O angle and the nitrosyl stretching vibration frequencies. Especially in the case of pentacoordinated compounds, the shape of the coordination sphere was of interest. Therefore CShM values of experimental and calculated structures will also be compared. Structural optimizations were performed with BP86[78,79] and B97-D[80] pure density functionals and TPSSh[81–83] (10% HF exchange) and B3LYP[84–87] (20% HF exchange) hybrid functionals.

Solvation models

As calculated Fe–O bond lengths in $\{FeNO\}^7(S = 3/2)$ compounds are known to show poor accuracy[39], several solvation models were tested on the $[Fe(H_2O)_5(NO)]^{2+}$ cation. Table 2.14 shows a comparison between experimental data and calculations on the BP86/def2-TZVP level of theory using no solvation model, CPCM with a dieletricity constant of $\epsilon = 80.4$ to simulate a hydrate shell ($CPCM_{H_2O}$), CPCM with an infinite dieletricity constant to simulate a crystal lattice ($CPCM_\infty$),[88] CPCM with a COSMO[89] epsilon function (CPCMC) and a RISM.[90,91] Calculations using the RISM solvation model were conducted by Marc Reimann (AK Kaupp, TU Berlin).

Using no solvation model led to Fe–O bond lengths that were 0.083 Å longer in the average than in the experimental data. Also, the Fe–N–O angle showed a significant deviation rendering an almost linear FeNO moiety. The Fe–N bond was predicted too short, whereas the N–O bond length showed almost no deviation. The nitrosyl stretching vibration was calculated 96 cm^{-1} too high.

Using a solvation model in all cases yielded more realistic Fe–O bond lengths, with $CPCM_{H_2O}$, $CPCM_\infty$ and CPCMC giving comparable results that were approximately 0.055 Å longer than in the experimental data. RISM showed the best compliance, with an overestimation by 0.032 Å.

Table 2.14: Results of DFT calculations on the $[Fe(H_2O)_5(NO)]^{2+}$ cation with various solvation models. BP86/def2-TZVP, D3, RI-J: def2/J. Distances in Å, angles in ° and $\tilde{\nu}$(NO) in cm^{-1}.

	exp.	Gas phase	$CPCM_{H_2O}$	$CPCM_{\infty}$	CPCMC	RISM
$Fe–O_{eq}$	2.031(3)	2.117	2.097	2.096	2.087	2.074
$Fe–O_{eq}$	2.065(3)	2.121	2.111	2.111	2.096	2.083
$Fe–O_{eq}$	2.067(3)	2.186	2.118	2.121	2.143	2.091
$Fe–O_{eq}$	2.104(4)	2.189	2.156	2.159	2.163	2.133
$Fe–O_{ax}$	2.121(4)	2.194	2.177	2.179	2.175	2.170
mean Fe–O	2.078	2.161	2.132	2.133	2.133	2.110
Fe–N	1.786(4)	1.759	1.742	1.741	1.742	1.737
N–O	1.143(5)	1.142	1.150	1.150	1.150	1.155
Fe–N–O	160.6(4)	179.2	163.0	164.3	164.1	159.2
$\tilde{\nu}$(NO)	1845	1941	1873	1875	1877	1853
$CShM_{OC\text{-}6}$	0.271	0.554	0.509	0.520	0.601	0.503

When using solvation models, the Fe–N bond length exhibited further shortening with the highest deviance for RISM. At the same time, the N–O bond was elongated again with the greatest effect generated by RISM. Without exception, solvation models rendered a slightly bent FeNO moiety with RISM slightly underestimating the Fe–N–O angle by 1.4° and $CPCM_{H_2O}$, $CPCM_{\infty}$ and CPCMC overestimating the Fe–N–O angle by 2.4, 3.7, and 3.5° respectively. Accordingly, the nitrosyl stretching vibration showed the smallest deviation for RISM by $8\,cm^{-1}$ and 28, 30 and $32\,cm^{-1}$ each for $CPCM_{H_2O}$, $CPCM_{\infty}$ and CPCMC. All calculations overestimated the distortion of the coordination octahedron with $CShM_{OC\text{-}6}$ values between 0.503 and 0.601 in comparison to the experimental data with a $CShM_{OC\text{-}6}$ value of 0.271.

In the following, only calculations using $CPCM_{H_2O}$ will be regarded as this model appeared as an adequate compromise between accuracy and computing time. RISM, which in some aspects showed closest agreement with experimental data, leads to very expensive calculations. This rendered it unsuitable for extensive studies, especially on more extensive systems.

The $[Fe(H_2O)_5(NO)]^{2+}$ cation

A precise description of the $[Fe(H_2O)_5(NO)]^{2+}$ cation was not achieved with any of the above mentioned functionals. However, every aspect of the $[Fe(H_2O)_5(NO)]^{2+}$ cation was reproduced best by different functionals.

BP86 showed a rather great discrepancy between both the Fe–O bond lengths and the bond lengths within the FeNO moiety. At the same time, the Fe–N–O angle and the nitrosyl stretching vibration were best reproduced by BP86. All other functionals led to a rather linear FeNO moiety which in every case was accompanied by a considerable overestimation of the nitrosyl stretching vibration. The bond lengths were best reproduced by the hybrid functionals, at which TPSSh led to a better description of the Fe–O bond lengths and B3LYP gave a better description of the Fe–N–O bond lengths. The computational results are listed in Table 2.15.

Table 2.15: Results of DFT calculations on the $[Fe(H_2O)_5(NO)]^{2+}$ cation with various hybrid and non-hybrid density functionals. def2-TZVP, D3, RI-J: def2/J. Distances in Å, angles in ° and $\tilde{\nu}(NO)$ in cm^{-1}.

	exp.	BP86	B97-D	TPSSh	B3LYP
$Fe–O_{eq}$	2.031(3)	2.097	2.109	2.083	2.095
$Fe–O_{eq}$	2.065(3)	2.111	2.115	2.089	2.097
$Fe–O_{eq}$	2.067(3)	2.118	2.167	2.135	2.144
$Fe–O_{eq}$	2.104(4)	2.156	2.170	2.136	2.149
$Fe–O_{ax}$	2.121(4)	2.177	2.199	2.146	2.160
mean Fe–O	2.078	2.132	2.152	2.118	2.129
Fe–N	1.786(4)	1.742	1.773	1.766	1.785
N–O	1.143(5)	1.150	1.144	1.142	1.140
Fe–N–O	160.6(4)	163.0	176.6	177.7	175.5
$\tilde{\nu}(NO)$	1845	1873	1905	1935	1935
$CShM_{OC\text{-}6}$	0.271	0.509	0.473	0.561	0.452

The $[Fe(fpin)_2(NO)]^{2-}$ anion

The $[Fe(fpin)_2(NO)]^{2-}$ anion was best described by the TPSSh functional leading to good agreement concerning Fe–O bond lengths and the nitrosyl stretching vibration frequency. However, the bond lengths and angle of the FeNO moiety showed a considerable deviation in respect to experimental data. In fact, a suitable description of the FeNO moiety was achieved with any of the tested functionals. The Fe–N distance was either too short (BP86) or too long (B97-D, TPSSh). In every case, the N–O distance was overestimated while, at the same time, the Fe–N–O angle was estimated too small at consistently around 150°. Also, in all cases the distortion of the square pyramid was underestimated. No data is available for the B3LYP functional, as its use caused the calculations to not converge.

Notably, when the $NHEt_3^+$ cations were taken into account, the accuracy of BP86 regarding the Fe–N–O angle, the N–O distance, the nitrosyl stretching frequency and the shape of the coordination sphere was greatly improved, allowing a satisfactory description of the $[Fe(fpin)_2(NO)]^{2-}$ anion. Results of the calculations are summarized in Table 2.16.

Table 2.16: Results of DFT calculations on the $[Fe(fpin)_2(NO)]^{2-}$ anion with various hybrid and non-hybrid density functionals. def2-TZVP, D3, RI-J: def2/J. Distances in Å, angles in ° and $\tilde{\nu}$(NO) in cm^{-1}.

	exp.	BP86	BP86*	B97-D	TPSSh
$Fe–O1_{fpin1}$	1.942(1)	1.976	1.960	1.988	1.961
$Fe–O2_{fpin1}$	2.042(1)	2.020	2.091	2.033	2.023
$Fe–O3_{fpin2}$	1.953(1)	1.977	1.969	1.992	1.958
$Fe–O4_{fpin2}$	2.058(1)	2.053	2.089	2.050	2.014
mean Fe–O	1.999	2.007	2.027	2.016	1.989
Fe–N	1.757(2)	1.728	1.720	1.782	1.786
N–O	1.149(2)	1.189	1.179	1.184	1.182
Fe–N–O	168.5(2)	147.6	158.4	146.9	152.0
$\tilde{\nu}$(NO)	1739	1665	1733	1689	1731
$CShM_{SPY\text{-}5}$	1.930	4.096	1.707	3.550	4.323
$CShM_{TBPY\text{-}5}$	1.692	0.870	2.472	0.968	0.631

*: The structural optimization was performed under addition of two $NHEt_3^+$ cations.

$[Fe(fpin)(MeOH)_2(NO)]$

Bond lengths and distances in $[Fe(fpin)(MeOH)_2(NO)]$ were best reproduced by B97-D. For this functional, the mean Fe–O distance shows little deviation in respect to experimental data. Notably, for all functionals, the individual Fe–O distances exhibited significant differences which, ultimately, more or less canceled eachother out. Using B97-D the Fe–N–O moiety was well predicted as far as distances and angle, consequently leading to the agreement of the nitrosyl stretching frequency. In the experimental data, the coordination sphere of the iron center was almost perfectly square pyramidal. Computational data, on the other hand, overestimated the distortion of the square pyramid for all functionals. The results are listed in Table 2.17.

$[Fe(EtOH)_2(fpin)(NO)]$

In the asymmetric unit of **7b** two crystallographically independent complex molecules were found differing mostly in the shape of the coordination sphere with one showing an almost perfect square pyramid and the other more distorted. The best description of **7b** was achieved using the TPSSh functional. In the calculations, individual Fe–O bond lengths showed a significant deviation in respect to the experimental data. However, these errors ultimately seemed to cancel each other out as the calculated mean Fe–O bond lengths, especially from BP86 and TPSSh, were in good agreement with the data from crystal-structure measurements. Also, both Fe–N and N–O distances, as well as the Fe–N–O angle, were adequately predicted

Table 2.17: Results of DFT calculations on [Fe(fpin)(MeOH)$_2$(NO)] with various hybrid and non-hybrid density functionals. def2-TZVP, D3, RI-J: def2/J. Distances in Å, angles in ° and $\tilde{\nu}$(NO) in cm^{-1}.

	exp.	BP86	B97-D	TPSSh	B3LYP
Fe–O1$_{\text{fpin}}$	1.958(2)	1.944	1.950	1.939	1.957
Fe–O2$_{\text{fpin}}$	1.991(2)	1.948	1.958	1.954	1.959
Fe–O3$_{\text{MeOH}}$	2.014(3)	2.143	2.156	2.078	2.113
Fe–O4$_{\text{MeOH}}$	2.045(3)	2.145	2.165	2.186	2.122
mean Fe–O	2.002	1.995	2.007	2.014	1.988
Fe–N	1.745(4)	1.719	1.758	1.760	1.786
N–O	1.153(4)	1.169	1.165	1.161	1.160
Fe–N–O	162.8(3)	159.0	158.2	158.2	158.6
$\tilde{\nu}$(NO)	1801	1776	1795	1830	1835
CShM$_{SPY\text{-}5}$	0.394	1.003	0.798	2.007	1.458

by TPSSh. A distorted square pyramid was reliably obtained by all functionals except B97-D, which favored a trigonal bipyramid. Results of the calculations can be seen in Table 2.18.

Table 2.18: Results of DFT calculations on [Fe(EtOH)$_2$(fpin)(NO)] with various hybrid and non-hybrid density functionals. def2-TZVP, D3, RI-J: def2/J. Distances in Å, angles in ° and $\tilde{\nu}$(NO) in cm^{-1}.

	exp.		BP86	B97-D	TPSSh	B3LYP
Fe–O1$_{\text{fpin}}$	1.994(1)	1.968(1)	1.912	1.951	1.944	1.961
Fe–O2$_{\text{fpin}}$	1.999(1)	1.999(1)	1.972	1.964	1.953	1.961
Fe–O3$_{\text{EtOH}}$	2.058(2)	2.044(2)	2.071	2.103	2.090	2.107
Fe–O4$_{\text{EtOH}}$	2.064(2)	2.066(2)	2.126	2.200	2.123	2.120
mean Fe–O	2.029	2.019	2.020	2.055	2.028	2.037
Fe–N	1.751(2)	1.751(2)	1.722	1.758	1.759	1.786
N–O	1.144(2)	1.151(2)	1.175	1.166	1.162	1.161
Fe–N–O	167.2(2)	163.9(2)	147.8	154.4	160.5	160.8
$\tilde{\nu}$(NO)	1808		1729	1782	1830	1834
CShM$_{SPY\text{-}5}$	1.401	0.571	0.706	4.193	1.061	0.856

2.7.2 Electronic properties of the FeNO unit

To gain a better understanding of the bonding situation in the FeNO moiety, the electronic structure of the [Fe(H$_2$O)$_5$(NO)]$^{2+}$ cation was analyzed representatively with respect to the nature of its canonical molecular orbitals. They were obtained by calculations with spin-unrestricted open-shell systems and, in consequence, separated the orbitals for the α (spin-up) and the β (spin-down) channel. The molecular orbitals of the HUMO-LUMO border region of the [Fe(H$_2$O)$_5$(NO)]$^{2+}$ cation are displayed in Figure 2.31. The z-axis is defined as parallel to the Fe–N bond for the following.

The five energetically highest occupied molecular orbitals (MOs) of the α channel α-MOs 42 to 46 exhibited mainly an Fe-d character with antibonding contributions from O-p orbitals of the aqua co-ligands. The contribution of the nitrosyl ligand can be seen in α-MOs 42, 43, 44 and 46. α-MOs 42 to 44 exhibited mostly non-bonding and slight π-bonding interaction between the Fe-d and the NO-π^* orbitals. The α-HOMO, α-MO 46, represented the anti-bonding interaction of the Fe-d_{z^2} and the NO-σ orbitals. To alleviate this antibonding interaction, the FeNO deviated from a linear to a slightly bent formation with a bonding angle of around 163°, as is also pointed out in Reference [92]. The α-LUMO and α-LUMO+1, α-MOs 47 and 48, showed the NO-centered π-antibonding interactions between the Fe-d_{xz} and Fe-d_{xy} orbitals and the NO-π^*_x and NO-π^*_y orbitals. The HOMO and the HOMO−1 of the β-channel, β-MOs 42 and 43, featured a considerable NO-contribution to both π-backbonds between the Fe-d_{xz} and Fe-d_{yz} orbitals and both NO-π^* orbitals. The LUMOs in the β-channel, β-MOs 44 to 48, were all either iron-centered or at least showed significant contribution by the Fe-d orbitals. Of the latter cases, β-MOs 45 and 46 corresponded to the α-LUMO and α-LUMO+1, α-MOs 47 and 48, but were decidedly more iron-centered. Notably, β-MO 45, which represents an unoccupied π-antibonding between the Fe-d_{yz} and the NO-π^*_y orbitals, developed a bonding interaction in consequence of the angled FeNO moiety.

2.7.3 Charge and population analysis

Charge and population analysis was performed to gain a better understanding of the FeNO moieties in $[Fe(H_2O)_5(NO)]^{2+}$, $[Fe(fpin)_2(NO)]^{2-}$, **7a** and **7b**. Results using Mulliken population analysis (MPA),[93] natural population analysis (NPA)[94] and quantum theory of atoms in molecules (QTAIM)[95] are shown in Table 2.19 for optimized geometries, obtained from calculations using the functionals BP86 (B) and TPSSh (T). In all cases, the iron center was allocated a positive charge with MPA generally leading to considerably lower values in the range of 0.48 to 0.69 than both NPA (1.21 to 1.48) and QTAIM (1.47 –1.62). The nitrogen atom was assigned a positive charge with the exception of two cases with a slightly negative charge. Remarkably, the charges were always close to zero within a range of −0.04 to 0.13, except for $[Fe(H_2O)_5(NO)]^{2+}$ with more positive values in the range of 0.13 to 0.27. The oxygen atom always showed a negative charge. While MPA and NPA gave comparable results for NO, values obtained by QTAIM, in general, were more negative. In sum, the nitrosyl ligand was predominantly negatively charged except for $[Fe(H_2O)_5(NO)]^{2+}$, where, according to MPA and NPA, a slightly positive charge was assigned. In general, MPA assigned the most positive charge (−0.22 to 0.22), NPA a more negative charge (−0.31 to 0.09) and QTAIM the most negative charge (−0.43 to −0.10).

Population analyses by MPA and NPA clearly showed spin polarization with the accumulation of α-spin density at the iron center and β-spin density at the nitrosyl ligand. Notably, while the BP86 and TPSSh gave comparable results concerning charges, the spin population results showed considerable deviation. With TPSSh (Fe: 3.43 to 3.82; NO: −1.22 to −0.69) spin polarization was more prominent than with BP86 (Fe: 2.84 to 3.43; NO: −0.79 to −0.40).

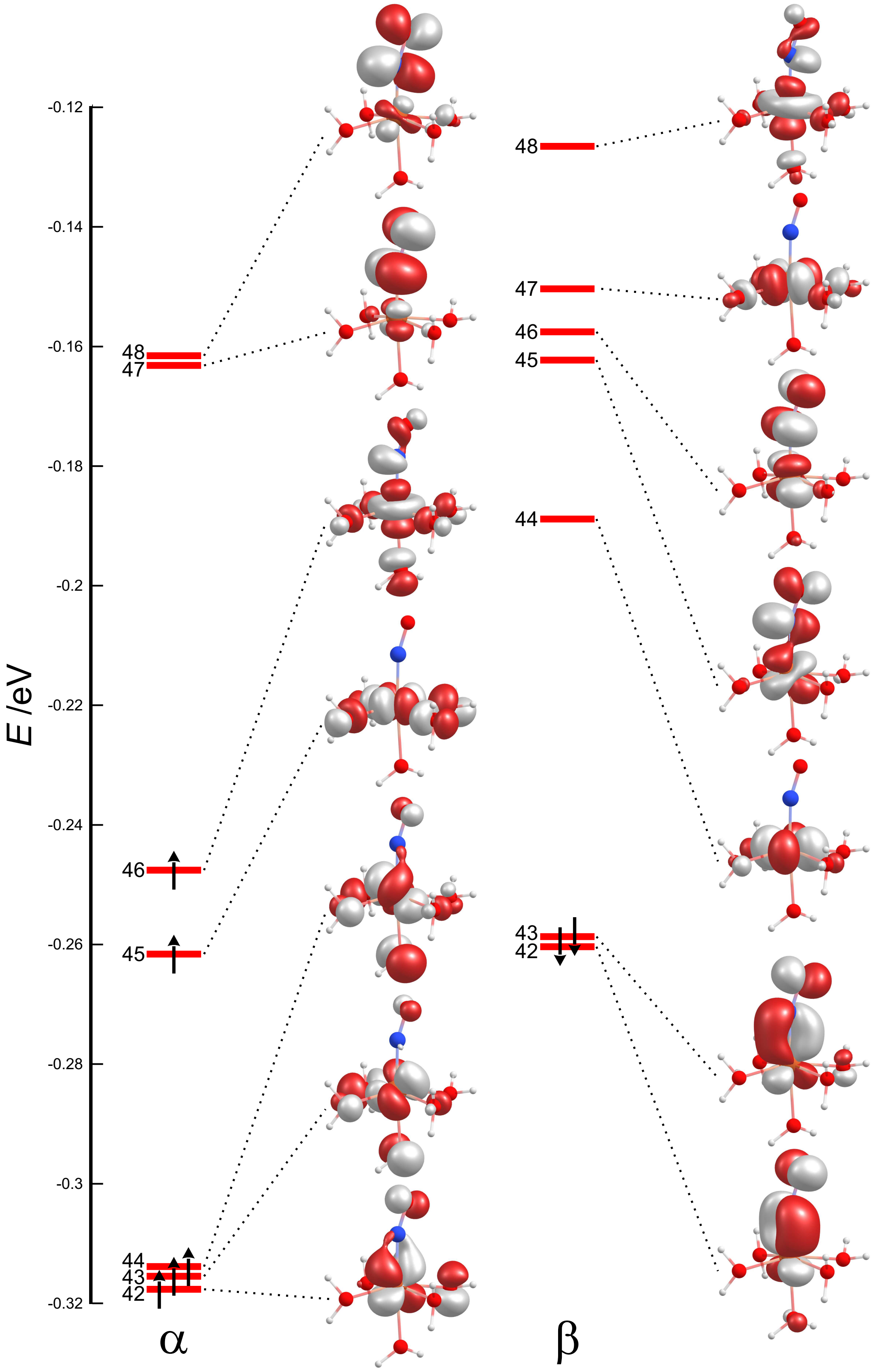

Figure 2.31: Energy diagram of the HOMO-LUMO border region in the $[Fe(H_2O)_5(NO)]^{2+}$ cation. Molecular orbital energies and contours are calculated using a spin-unrestricted system with BP86/def2-TZVP and dispersion correction (D3). Isovalue: 0.05.

Table 2.19: Population and charge analysis of $[Fe(H_2O)_5(NO)]^{2+}$, $[Fe(fpin)_2(NO)]^{2-}$, **7a** and **7b** according to Mulliken, NPA and QTAIM. All values are given in elementary charges. The calculations were performed with BP86 (B) or TPSSh (T) functionals, the def2-TZVP basis set, dispersion correction D3, CPCM solvent model with $\epsilon(H_2O)$.

			Charges				Spin			
			Fe	N	O	NO	Fe	N	O	NO
$[Fe(H_2O)_5(NO)]^{2+}$	MPA	B	0.64	0.22	−0.03	0.19	3.43	−0.35	−0.33	−0.68
		T	0.69	0.27	−0.05	0.22	3.74	−0.50	−0.46	−0.96
	NPA	B	1.27	0.15	−0.06	0.09	3.18	−0.25	−0.33	−0.58
		T	1.40	0.13	−0.07	0.06	3.50	−0.39	−0.45	−0.84
	QTAIM	B	1.52	0.19	−0.29	−0.10				
		T	1.62	0.21	−0.32	−0.11				
$[Fe(fpin)_2(NO)]^{2-}$	MPA	B	0.48	−0.01	−0.21	−0.22	3.27	−0.45	−0.34	−0.79
		T	0.55	0.02	−0.23	−0.21	3.82	−0.73	−0.52	−1.22
	NPA	B	1.29	0.02	−0.26	−0.24	3.02	−0.35	−0.34	−0.69
		T	1.48	−0.04	−0.27	−0.31	3.51	−0.62	−0.52	−1.14
	QTAIM	B	1.51	0.02	−0.43	−0.41				
		T	1.65	0.02	−0.45	−0.43				
7a	MPA	B	0.58	0.04	−0.12	−0.08	3.32	−0.39	−0.34	−0.69
		T	0.64	0.13	−0.14	−0.01	3.69	−0.58	−0.48	−1.06
	NPA	B	1.26	0.06	−0.16	−0.10	3.04	−0.29	−0.34	−0.59
		T	1.41	0.03	−0.17	−0.14	3.43	−0.48	−0.48	−0.96
	QTAIM	B	1.47	0.08	−0.36	−0.28				
		T	1.58	0.10	−0.38	−0.28				
7b	MPA	B	0.51	0.12	−0.15	−0.03	3.10	−0.25	−0.23	−0.48
		T	0.63	0.08	−0.13	−0.05	3.72	−0.59	−0.50	−1.09
	NPA	B	1.21	0.07	−0.18	−0.11	2.84	−0.17	−0.23	−0.40
		T	1.43	0.02	−0.17	−0.15	3.44	−0.49	−0.49	−0.98
	QTAIM	B	1.45	0.08	−0.37	−0.29				
		T	1.60	0.09	−0.39	−0.30				

2.7.4 TD-DFT

To obtain an understanding beyond the ground states of the nitrosyliron compounds, time-dependent DFT calculations (TD-DFT) were performed which allow to take excited states into account. The electronic transitions derived from said calculations were then compared with the respective experimental UV/Vis spectra of both solid and solution. For better comparison, the experimental data was deconvolved into a number of Pseudo-Voigt functions representing absorption bands. The sum of these functions was fitted as closely as possible to the experimental data (Figure 2.32 and Figure 2.34, grey and black lines). The best agreement with experimental data was obtained by the use of BP86/def2-TZVP (D3, CPCM). Experimental absorption bands and excitation energies, as well as transition pathways obtained from TD-DFT calculations, are summarized in Table 2.20.

Table 2.20: Experimental absorption bands after deconvolution and results of TD-DFT calculations for $[Fe(H_2O)_5(NO)]^{2+}$, **1a** and **6**. Solid samples were mixed with $BaSO_4$. The $[Fe(H_2O)_5(NO)]_2^+$ solution was obtained after saturation of an aqueous iron(II) triflate solution (c = 0.36 mmol L^{-1} with gaseous nitric oxide. **1a** was analyzed as solution in acetone (3.39 mmol L^{-1}), **6** as methanolic solution (0.147 mmol L^{-1}).

	λ /nm			Transition
	solid	solv.	TD-DFT	
$[Fe(H_2O)_5(NO)]^{2+}$	743	773	772, 753	β: Fe-$d_{xz,yz}$ + NO-π^* $\longrightarrow$ Fe-d_{xy}
	592	593	613, 607	α: Fe-d_{z^2} − NO-σ $\longrightarrow$ Fe-$d_{xz,yz}$ − NO-π^*
	465	455, 396	482, 409	α: Fe-d_{xy,x^2-y^2} $\longrightarrow$ Fe-$d_{xz,yz}$ − NO-π^*
				β: Fe-$d_{xz,yz}$ + NO-π^* $\longrightarrow$ Fe-d_{xy,x^2-y^2}
	322	336	322	β: O-p $\longrightarrow$ Fe-d_{xy}
1a	576	582	552	β: Fe-d_{z^2} $\longrightarrow$ Fe-$d_{x^2-y^2}$ − O-p
	321	375	423, 327	β: O-p $\longrightarrow$ Fe-d_{xy}
6		949	882	β: Fe-d_{xz} + NO-π^* $\longrightarrow$ Fe-d_{xy}
	745	739	747	α: Fe-$d_{x^2-y^2}$ $\longrightarrow$ Fe-d_{xz+yz} − NO-π^*
		616	608	α: Fe-$d_{x^2-y^2}$ $\longrightarrow$ Fe-d_{xz}− NO-π^*
				β: Fe-d_{xz} + NO-π^* $\longrightarrow$ Fe-d_{z^2} − NO-π^*
	523	518	551, 502	β: O-p, O-p + Fe-d_{xz} + NO-π^* $\longrightarrow$ Fe-d_{xy}
	454	443	457	β: O-p $\longrightarrow$ Fe-d_{xy}

In the range of 250 to 1000 nm five absorption bands at 336, 396, 455, 593 and 764 nm of dissolved and four bands at 322, 465, 594 and 752 nm of solid $[Fe(H_2O)_5(NO)]^{2+}$ salts were observed (Figure 2.32). TD-DFT calculations reproduced these excitations well and, thus, aided in their assignment. As can be seen in Table 2.20, excitations in the visible range between 400 and 800 nm all showed involvement of NO-centered orbitals, explaining the color change in consequence of NO introduction (compare to colorless $[Fe(H_2O)_6]^{2+}$ solutions). Ligand-to-metal charge transfer (LMCT) from the aqua ligand O-p orbitals into the Fe-d_{xy} orbital occurred below 400 nm without any involvement of the nitrosyl ligand.

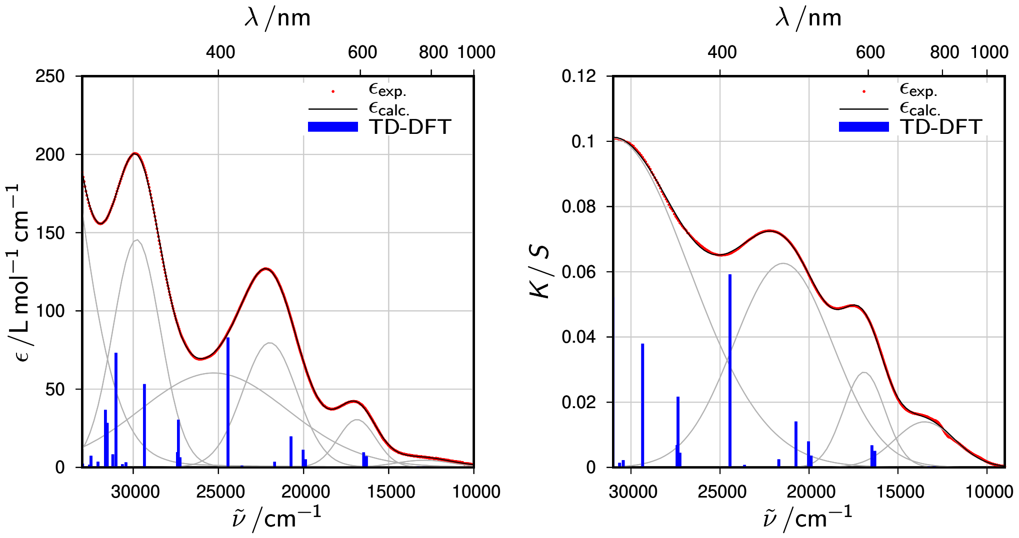

Figure 2.32: Left: UV/Vis spectrum of a solution of iron(II) triflate ($c = 3.60\,\mathrm{mmol\,L^{-1}}$) after saturation with gaseous nitric oxide (red). The experimental data was fitted (black) with six Pseudo-Voigt functions (grey, $\eta = 0.06$) using the wavenumber as the normally distributed variable. Positions of the maxima: $\nu\,/\mathrm{cm}^{-1} = 36904, 29802, 25276, 21983, 16866, 12927$; $\lambda\,/\mathrm{nm} = 271, 336, 396, 455, 593, 774$. Transition energies from a BP86/def2-TZVP (D3, CPCM) TD-DFT calculation are shown as blue columns. **Right**: UV/Vis spectrum of solid **4a** $\cdot$ $8.34\,\mathrm{H_2O}$ in $\mathrm{BaSO_4}$ by diffuse reflexion (red). The experimental data was fitted (black) with four Gauss functions (grey) using the wavenumber as the normally distributed variable. Positions of the maxima: $\nu\,/\mathrm{cm}^{-1} = 31034, 21499, 16902, 13505$; $\lambda\,/\mathrm{nm} = 322, 466, 592, 740$. Transition energies from a BP86/def2-TZVP (D3, CPCM) TD-DFT calculation are shown as blue columns.

In the case of **6**, a comparison with the nitrosyl-free compound **1a** was appropriate as both showed comparable color depth and shared features of their UV/Vis spectra. **1a** showed a broad band at approximately 580 nm (Figure 2.33) due to an excitation from the non-bonding Fe-d_{z^2} orbital into an antibonding Fe-$d_{x^2-y^2}$ −O-p orbital. Below 400 nm strong absorption induced by LMCT was observed.

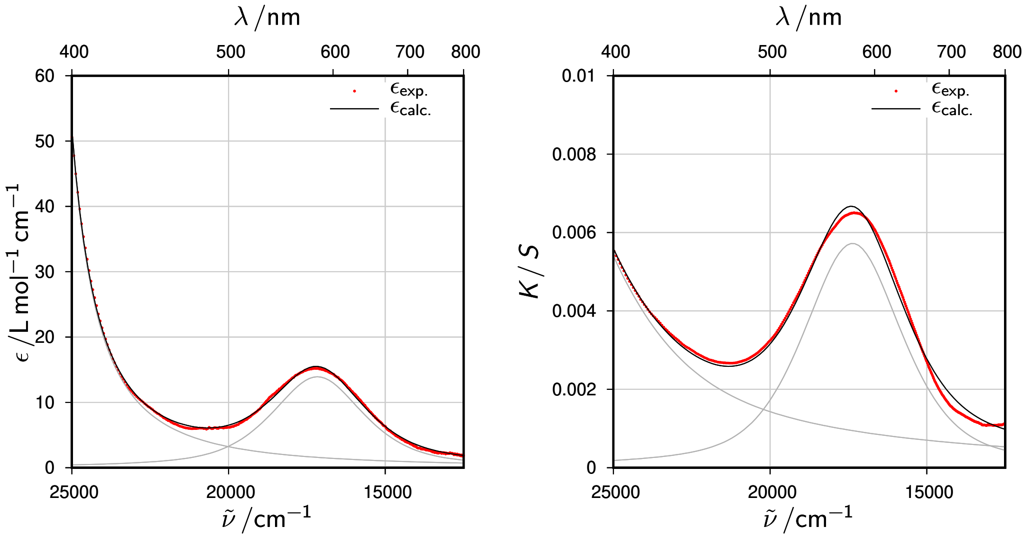

Figure 2.33: Left: UV/Vis spectrum of a solution of **1a** (c = 3.39 mmol L^{-1}) in acetone (red). The experimental data was fitted (black) with two Pseudo-Voigt functions (grey, η = 0.74) using the wavenumber as the normally distributed variable. Positions of the maxima: ν /cm^{-1} = 26668, 17163; λ /nm = 375, 582. **Right**: UV/Vis spectrum of solid **1a** in $BaSO_4$ by diffuse reflexion (red). The experimental data was fitted (black) with two Pseudo-Voigt functions (grey, η = 0.66) using the wavenumber as the normally distributed variable. Positions of the maxima: ν /cm^{-1} = 31142, 17366; λ /nm = 321, 575.

6, too, showed an excitation at approximately 520 nm which, in part, resulted from a nitrosyl-independent LMCT (Figure 2.34). At the same time, this can also be attributed to an LMCT-type excitation of a bonding MO with contributions from the perfluoropinacolato O-p orbitals and the FeNO moiety into the Fe-d_{xy} orbital. The absorption bands at around 450 nm were also assigned to a LMCT from perfluoropinacolato O-p orbitals into the Fe-d_{xy} orbital. The other absorption bands at 745 nm of the solid and 616, 739 and 949 nm of the solution all showed contribution from the nitrosyl ligand explaining the change of color from lavender to burgundy upon nitrosylation.

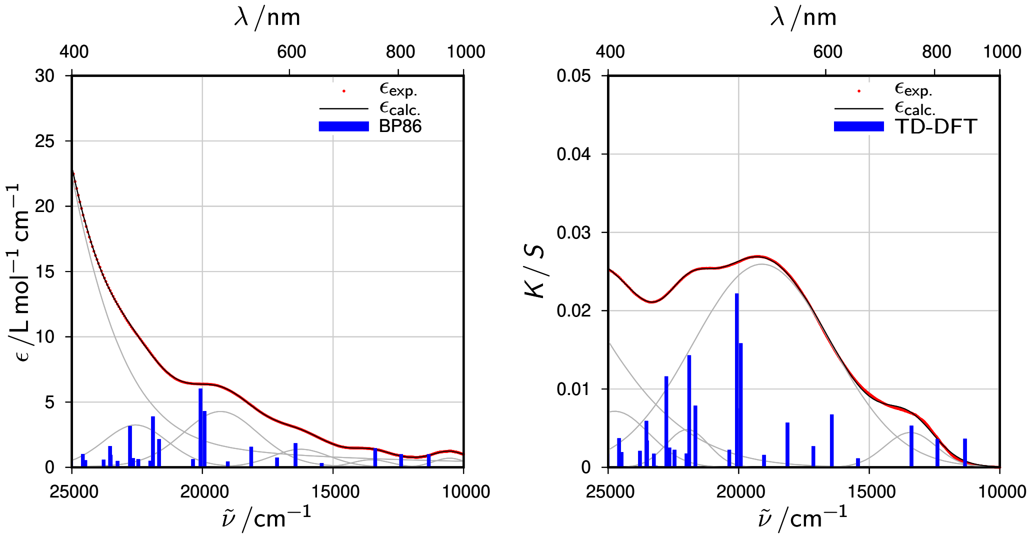

Figure 2.34: Left: UV/Vis spectrum of a solution of **6** (c = 14.7 mmol L^{-1}) in acetone (red). The experimental data was fitted (black) with two Pseudo-Voigt functions (grey, η = 0.21) using the wavenumber as the normally distributed variable. Positions of the maxima: ν /cm^{-1} = 30661, 22562, 19304, 16235, 13528, 10539; λ /nm = 326, 443, 518, 616, 739, 949. Transition energies from a BP86/def2-TZVP (D3, CPCM) TD-DFT calculation are shown as blue columns. **Right**: UV/Vis spectrum of solid **6** in BaSO$_4$ by diffuse reflexion (red). The experimental data was fitted (black) with five Gauss functions (grey) using the wavenumber as the normally distributed variable. Positions of the maxima: ν /cm^{-1} = 31094, 24749, 21969, 19108, 13421; λ /nm = 322, 404, 455, 523, 745. Transition energies from a BP86/def2-TZVP (D3, CPCM) TD-DFT calculation are shown as blue columns.

2.7.5 Calculation of oxidation states

Oxidation states were calculated by Daniel Schröder with Salvador's EOS[96] method after geometry optimization with BP86 and TPSSh using the def2-TZVP basis set, D3 dispersion correction and a CPCM solvation model. Corresponding reliability indices R are given for the α and the β channel as a measure for the difference in the occupation number between the last occupied and the first unoccupied effective atomic orbitals. The lowest possible value of $R = 50$ signals equal occupation, while $R = 100$ indicates a difference of at least 0.5.

The results for $[Fe(H_2O)_5(NO)]^{2+}$, $[Fe(fpin)_2(NO)]^{2-}$, **7a** and **7b** are shown in Table 2.21. With BP86, the Fe centers in $[Fe(H_2O)_5(NO)]^{2+}$ and **7b** were assigned the oxidation state +I with NO^+ ligands while in $[Fe(fpin)_2(NO)]^{2-}$ and **7a** the Fe centers were attributed an oxidation state of +III with NO^- ligands. Using TPSSh, in all cases a formulation as $Fe^{III}NO^-$ was obtained. Reliability indices of the α channel, in all cases but one, showed a value of 100 except for **7b** using BP86. An opposite situation was found in the β channel, as in almost all cases values close to the lowest possible value were found with the only exception being $[Fe(fpin)_2(NO)]^{2-}$ using TPSSh. Oxidation states calculated using Head-Gordon's LOBA method[97] can be found in Table 6.1 in the appendix.

Table 2.21: Assignment of oxidation states of Fe and charge of the NO ligands in $[Fe(H_2O)_5(NO)]^{2+}$, $[Fe(fpin)_2(NO)]^{2-}$, **7a** and **7b** according to Salvador's EOS approach.[96] Results were obtained by Daniel Schröder.

	BP86		R(%)	TPSSh		R(%)
	Fe	NO	α/β	Fe	NO	α/β
$[Fe(H_2O)_5(NO)]^{2+}$	+I	1	100/55	+III	−1	100/54
$[Fe(fpin)_2(NO)]^{2-}$	+III	−1	100/56	+III	−1	100/81
7a	+III	−1	100/54	+III	−1	100/54
7b	+I	1	83/52	+III	−1	100/71

2.7.6 Calculation of parameters in Mößbauer spectroscopy

Isomer shifts (δ) and quadrupol shifts ($|\Delta E_Q|$) in Mößbauer spectroscopy were calculated and adjusted with calibration parameters from Reference [98] for several iron complex entities to aid in the assignment of experimental data.[99] Computations were performed on the TPSSh level of theory with a CP(PPP) basis set for Fe and def2-TZVP for all other atoms. Experimental values were adequately reproduced with considerable deviation only for the isomer shifts of the gallate $[Fe(H_2O)_5(NO)]^{2+}$ cation and the $[Fe(fpin)_2(H_2O)]^-$ anion. Table 2.22 shows an overview of experimental and calculated results.

Table 2.22: Experimental and computational results of parameters in Mößbauer spectroscopy. Values in mm s^{-1}.

	Gallate		Ferrate		DFT	
	δ	$\lvert\Delta E_\mathrm{Q}\rvert$	δ	$\lvert\Delta E_\mathrm{Q}\rvert$	δ	$\lvert\Delta E_\mathrm{Q}\rvert$
$[Fe(H_2O)_5(NO)]^{2+}$	0.81(3)	2.23(4)	0.655(3)	2.031(8)	0.652	2.188
$[Fe(H_2O)_6]^{2+}$	1.39(4)	3.12(9)	1.076(5)	3.464(10)	1.026	3.547
$[Fe(fpin)_2(H_2O)]^{-}$	-		0.187(7)	1.70(2)	0.409	1.854

2.8 Photoirradiation experiments

Photoirradiation experiments were conducted on compounds **6** and **9**. In order to monitor photoinduced effects on these specimen, samples were irradiated with light of a well-defined light source and IR spectra were recorded in direct succession. Typically, these experiments were performed at low temperatures of approximately 10 K.

2.8.1 Photoirradiation of 6

Upon cooling, the nitrosyl stretching band of **6** showed blueshift from 1748 cm^{-1} at 298 K to 1771 cm^{-1} at 10 K. Also, the appearance of a shoulder suggested splitting into two bands. After 5 min of irradiation with light of a wavelength of 590 nm, the intensity of the nitrosyl stretching band at 1771 cm^{-1} decreased by 4%. In the meantime a new band at 1875 cm^{-1} appeared. At 15 K the newly formed band rapidly decayed while the band at 1771 cm^{-1} gained intensity indicating reversibility. This behavior was also shown by $(PPN)[FeCl_3(NO)]$[100] and was possibly caused by the photoinduced oxidation of the quartet $\{FeNO\}^7$ moiety. Thereby, the N–O bond was strengthened, resulting in a blueshift of the nitrosyl stretching frequency, as was supported by DFT calculations. In DFT calculations on the TPSSh level of theory (basis set: def2-TZVP, D3, CPCM) the one-electron oxidation was simulated by the removal of one spin-down electron from the wave-function ensuing in a quintet state. The result was a decrease of the calculated N–O bond length to 1.134 Å and bending of the Fe–N–O moiety to 123°. The nitrosyl stretching frequency was shifted towards 1921 cm^{-1}, adequately agreeing with the observed vibration at 1875 cm^{-1} in the photoirradiation experiments. Table 2.23 shows a comparison of experimental data and results from DFT calculations for the $\{FeNO\}^7$ entity and its oxidized form.

Further irradiation with light of a wavelength of 470 nm led to a decrease of the newly formed band at 1875 cm^{-1} while the original nitrosyl stretching band at 1771 cm^{-1} showed increased intensity. Also, the formation of nitrous oxide was suggested by the appearance of its charateristic bands at 2228 and 2236 cm^{-1}.[101] A differential plot of the IR spectra after irradiation with light of the wavelengths 590 and 470 nm at 10 K is displayed in Figure 2.35.

Table 2.23: Results of DFT calculations on the photo-oxidation of the $[Fe(fpin)_2(NO)]^{2-}$ anion on the TPSSh level of theory (def2-TZVP, D3, CPCM). Distances in Å, angles in ° and $\tilde{\nu}$(NO) in cm^{-1}.

	exp.	$\{FeNO\}^7$	Ox
Fe–O1_{fpin1}	1.942(1)	1.961	1.901
Fe–O2_{fpin1}	2.042(1)	2.023	1.927
Fe–O3_{fpin2}	1.953(1)	1.958	1.901
Fe–O4_{fpin2}	2.058(1)	2.014	1.931
mean Fe–O	1.999	1.989	1.915
Fe–N	1.757(2)	1.786	2.209
N–O	1.149(2)	1.182	1.134
Fe–N–O	168.5(2)	152.0	123.1
$\tilde{\nu}$(NO)	1739	1731	1921
CShM$_{SPY\text{-}5}$	1.930	4.323	4.797
CShM$_{TBPY\text{-}5}$	1.692	0.631	4.681

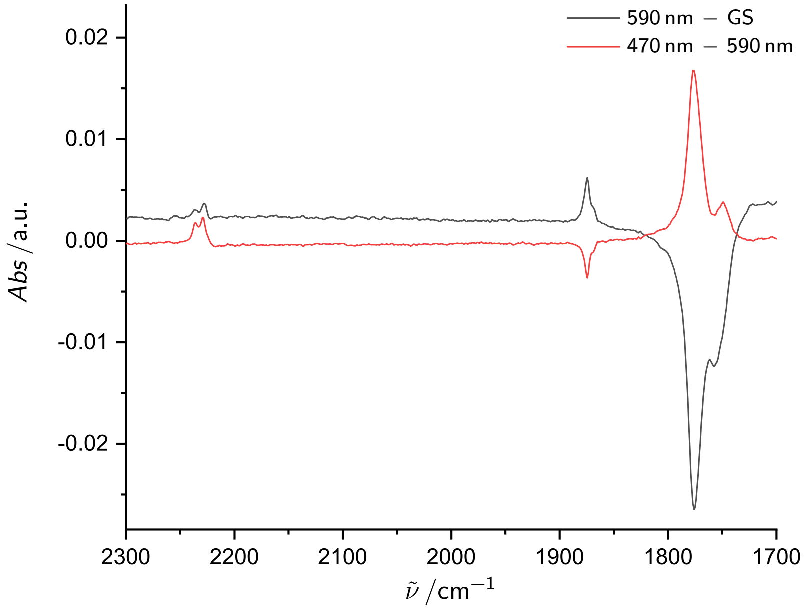

Figure 2.35: Plot of the IR spectra of irradiation experiments on **6** with light of the wavelengths of 590 and 470 nm at 10 K. The spectra are referenced to the respective spectra before irradiation with light of the specified wavelength showing only the change of intensity induced by irradiation.

2.8.2 Photoirradiation of 9

Upon the irradiation of **9** with light of a wavelength of 590 nm at 10 K, a decrease in intensity of the nitrosyl stretching bands at 1815 and 1826 cm^{-1} was observed, while, at the same time, a new band was formed at 1685 cm^{-1} (Figure 2.36). The observed redshift of the nitrosyl stretching band is typical for linkage isomerization from a nitrosyl-κ*N* species to an nitrosyl-κ*O* species (also isonitrosyl). The depopulation of the newly formed isonitrosyl species was, even at 10 K, so fast that in the time-frame of a measurement, a significant decay was observed. Thus, while a first measurement 1 min after irradiation exhibited the aforementioned effect, the next measurement 1 min later showed significant decrease of the band at 1685 cm^{-1} and an increase of the bands at 1815 and 1826 cm^{-1}. After 5 min, the IR spectrum was almost identical to the spectrum before irradiation.

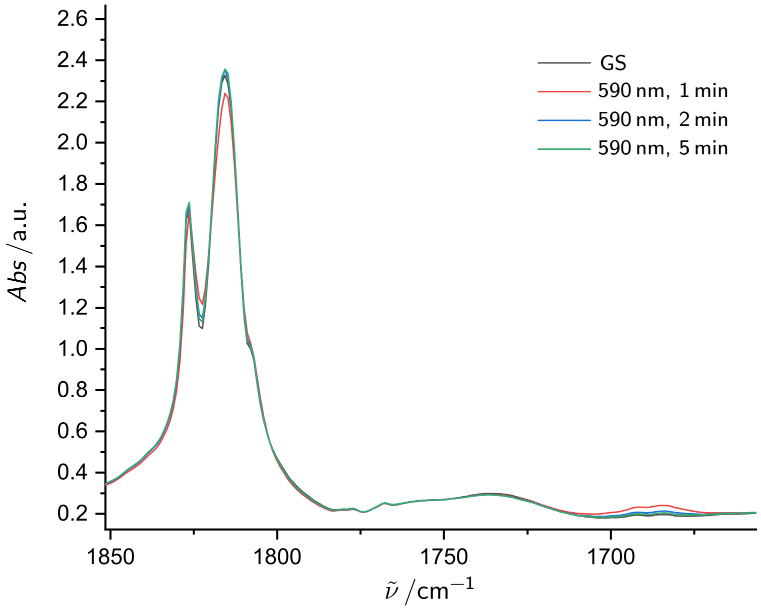

Figure 2.36: Plot of the IR spectrum of **9** at 10 K and after irradiation with light of the wavelength of 590 nm at 10 K after periods of 1, 2 and 5 min.

3 Discussion

3.1 Perfluoropinacolatoiron(II) compounds

As a means for the synthesis and crystallization of $\{FeNO\}^7$ compounds, establishing reliable routes to the precursor compounds is of great interest. During this work eight different nitrosyl-free perfluoropinacolatoiron(II) compounds were obtained in crystalline form. They can be classified in three groups: anionic bis(perfluoropinacolato)ferrates(II), neutral mono(perfluoropinacolato)iron(II) and dinuclear perfluoropinacolatoiron(II) compounds with an Fe:fpin ratio of 2:2. The nature of the synthesized product highly depended on the iron(II) source, the kind of base, the solvent and the ratio of perfluoropinacol to iron(II) source to base.

Bis(perfluoropinacolato)ferrates(II) were obtained mainly when 1 equiv of an iron(II) salt was reacted with 2 equiv perfluoropinacol and 4 equiv of a base. The syntheses using this 1:2:4 ratio were very robust concerning the reaction medium, as deep-blue solutions, indicating bis(perfluoropinacolato)ferrates(II), were observed in a variety of solvents like water, methanol, ethanol, acetonitrile and THF.[70] Also, the kind of base used for the reaction only mattered little. Synthesis was possible with hydroxides and alkoxides just as well as with amine and Schiff bases like triethylamine or 1,8-Diazabicyclo(5.4.0)undec-7-ene (DBU).[102] In fact, the presence of ammonium cations like $NHEt_3^+$ and $NBnMe_3^+$ led to the formation of blue solutions even at substoichiometric amounts of the respective base, most likely due to beneficial hydrogen bonding.

Syntheses of compounds of the latter two groups involving a 1:1 ratio of iron(II) source to perfluoropinacol were more sensitive to the variation of reaction parameters. In this respect, mono(perfluoropinacolato)iron(II) compounds were obtained only as a solid from methanol or ethanol using alkoxides like potassium methoxide or potassium *tert*-butoxide and alkoxide-generating bases like *n*-butyllithium. At the same ratio of iron(II) source to perfluoropinacol, the reaction in aprotic solvents like acetonitrile, benzonitrile and THF but, notably, also water gave dinuclear species. Suitable bases were hydroxides like NaOH in water and triethylamine in acetonitrile and benzonitrile. In THF, the formation of crystalline products was observed only after reaction with elemental lithium.

While the synthesis reactions of bis(perfluoropinacolato)ferrates(II) tolerated the presence of halogenides introduced by iron(II) halogenides, reactions with Fe:fpin ratios of 1:1 yielded halogenidoiron(II) complexes that were not suitable for further nitrosylation reactions leading to nitrosyliron complexes with oxygen-donor ligands. Instead nitrosylation of said species led to trihalogenidonitrosyl- and dihalogenidodinitrosylferrates.[39] Consequentially, iron(II) sources with weakly coordinating anions like iron(II) triflate were used in all syntheses to avoid such side reactions.

All perfluoropinacolatoiron(II) complexes quickly showed oxidation, indicated by discoloration upon contact with oxygen, especially in solution. In this matter, solutions, at first, turned opaque grey and then a yellow-to-orange color was attained under further influence of oxygen, evidencing the presence of iron(III) compounds. Thus, diligently removing traces from solvents and reactants and consequently avoiding contact with ambient oxygen was therefore essential.

In compliance with published bis(perfluoropinacolato)ferrates(II), **1a** and **1b** showed perfectly planar coordination of the iron(II) centers that can be described as square planar with a rhomboid distortion.[70] Due to tension induced by the perfluoropinacolato backbones, O_{fpin}–Fe–O_{fpin} angles are reduced from 90° to around 82°. In **1b**, the independent Fe–O bond lengths are very similiar with a deviance of only 0.012 Å. In **1a**, however, the difference is much bigger at 0.150 Å with the Fe1–O1 bond being considerably elongated. As that bond originates from the accepting oxygen atom of the H-bond donated by the $NHEt_3^+$ cation, the elongation is likely caused by this additional interaction. In **1b** similar interactions can be observed, namely non-classical hydrogen bonds of the C–H$\cdots$O type donated by the cation's methylene moiety of the benzyl group and a methyl group. In that case, however, the interaction is equally distributed across both acceptor oxygen atoms O1 and O2', as is indicated by the mostly equal distances between all acceptors and donors. Apart from that, non-classical hydrogen bonds of the C–H$\cdots$O type typically are relatively weak, so that considerable bond elongation was not to be expected here.[103]

All perfluoropinacolatoiron(II) compounds with an equimolar ratio of Fe and fpin showed fivefold coordination of the iron(II) centers that can best be described as square pyramids (*SPY*-5) or vacant octahedra (*vOC*-5) according to CShM analysis. Depending on the solvent, either a mono- or a dinuclear structure was formed. All tested aprotic solvents gave dinuclear species, while protic solvents, except water, gave mononuclear species. The mono-centered products with alcohol co-ligands are able to build energetically favorable extensive networks of hydrogen bonds. For aprotic co-ligands this ability is very limited. These systems compensate the issue by dimerization, enabling further energetically favorable Fe–O interactions. For the aqua complex, which exhibited the same structural motif, this, obviously, is no issue. Here, a network of hydrogen bonds was also formed, facilitating very efficient packing of the complex molecules with the lowest intermolecular distances. Mean Fe–Fe distances of adjacent complex molecules are comparably short at 4.7 Å. In the mono-centered compound with methanol ligands **2a** these distances, on average, measure 4.8 Å and, in the analogous dinuclear compound with acetonitrile ligands, intermolecular Fe–Fe distances are almost double at 8.3 Å. As a result, **3a** has the highest calculated density of all perfluoropinacolatoiron(II) compounds.

3.2 $[Fe(H_2O)_5(NO)]^{2+}$ salts and polymeric aquanitrosyloxalatoiron

In the course of this work three nitrosylaquairon compounds were crystallized and analyzed by X-ray diffraction, including the two first isolated examples of $[Fe(H_2O)_5(NO)]^{2+}$ salts, famously known as the "brown-ring" chromophore in the analytical nitrate test. In literature, only eleven other instances of structurally analyzed aquanitrosyliron compounds were mentioned as of September 2019. Of those, two can be assigned to the group of heme $\{FeNO\}^6$ compounds.[104,105] The other examples are members of the $\{FeNO\}^7(S = 3/2)$ family with co-ligands being several different aminocarboxylates[38,39] or a tris(imidazolyl)phosphine.[51] The $[Fe(H_2O)_5(NO)]^{2+}$ salts were obtained as compounds of the general formula $[Fe(H_2O)_5(NO)]$-$[M^{III}(fpin)_2(H_2O)]_2 \cdot x\,H_2O$ (M=Fe, $x = 8.31$; M=Ga, $x = 8.34$). Moreover, a coordination polymer of the formula $[\{Fe(H_2O)(NO)(\mu\text{-ox})\}_{n/n}] \cdot H_2O$ was isolated.

The $[Fe(H_2O)_5(NO)]^{2+}$ salts were synthesized using different pathways. While the gallate **4a** was obtained directly from aqueous reaction mixtures with a 1:2:4:4 ratio of iron(II) triflate, gallium(III) triflate, perfluoropinacol and sodium hydroxide after nitrosylation with gaseous nitric oxide, the respective reaction with iron(III) triflate did not produce the ferrate(III) salt **4b** in crystalline form. Instead, a modified synthetic procedure of compound **3a** with a ratio of 1:1:1 of iron(II) triflate, perfluoropinacol and sodium hydroxide was applied. In doing so, a colorless reaction mixture with a precipitate of **3a** was obtained. The introduction of gaseous nitric oxide then immediately induced a change of color to red generating a reactive intermediate nitrosyl species as indicated by the formation of a nitrosyl stretching band that was observed by means of *in situ* IR spectroscopy. The similarity regarding the color of the intermediate nitrosyl species and compounds **7a** and **7b** with the general formula [Fe(fpin)(NO)(ROH)] (R=Me, Et) suggests kinship. Possibly, the nitrosylation of **3a** led to the cleavage of the dinuclear complex, succeeded by the formation of a tentative $[Fe(fpin)(H_2O)_2(NO)]$ species. The intermediate quickly decomposed to an iron(III) species, in the further course releasing nitrous oxide, which was then detected in the gas phase by means of its IR signature. This was accompanied by another change of color to greenish brown indicating the formation of $[Fe(H_2O)_5(NO)]^{2+}$. The ferrate salt **4b** was then obtained from the reaction mixture after several hours as brown crystals. In both cases, the fpin ligand clearly showed a higher affinity for M^{III} centers, as suggested by the formation of aquabis(perfluoropinacolato)metallate(III) anions.

The polymeric aquanitrosyloxalatoiron species **5** was synthesized by the reaction of iron(II) triflate and oxalic acid in a ratio of 1:1 in aqueous solution, first giving off a yellow precipitate of poorly soluble iron(II) oxalate with a colorless supernatant. The introduction of gaseous nitric oxide enabled slight solubilization of the precipitate, accompanied by a color change of the supernatant solution to dark green. The formation of brown crystals amidst remaining the precipitate was observed over the course of weeks.

For the syntheses of all aquanitrosyliron compounds substoichiometrical amounts of base were used. In the case of **5**, the addition of base was not necessary. Crystallization of the products took place only at a pH between 1 and 2. At higher pH values, the formation of amorphous brownish orange precipitates of hydroxido- and alkoxidoiron species was observed instead.

All aquanitrosyliron compounds were sensitive towards purging with inert gas and evacuation of the reaction vessels. In this manner, nitric oxide was liberated and the products showed decoloration, giving off the corresponding iron(II) compounds: $[Fe(H_2O)_6]^{2+}$ salts from **4a** and **4b** and iron(II) oxalate from **5**. Nevertheless, this behavior was reversible and could be undone by simply restoring an atmosphere of nitric oxide. However, the stability of the solid material of **4a** and **4b** was greatly increased when the adhering solvent was quickly and completely removed, as the equilibrium according to Equation 3.1 is shifted towards the $[Fe(H_2O)_5(NO)]^{2+}$ cation, when the supply of aqua ligands is limited. This way, at temperatures below −20°C, storage in air was possible for months without visible signs of deterioration.

$$[Fe(H_2O)_5(NO)]^{2+} + H_2O \rightleftharpoons [Fe(H_2O)_6]^{2+} + NO \tag{3.1}$$

The stability of the solid material was somewhat astonishing considering the long history of failed efforts to crystallize unambiguous $[Fe(H_2O)_5(NO)]^{2+}$ salts. Consistently, in a survey of more than 100 $\{FeNO\}^7$ compounds performed by the *van Eldik* group the highest tendency in respect to liberation of NO was shown by the $[Fe(H_2O)_5(NO)]^{2+}$ species.[35] With that in mind, the closest results to stable $[Fe(H_2O)_5(NO)]^{2+}$ salts were evidently obtained with sulfate anions, as questionably successful synthesis of a compound of the formula $2\,FeSO_4 \cdot NO \cdot 13\,H_2O$ was claimed by *Manchot.*[106] Attempts to reproduce this result, however, yielded only $[Fe(H_2O)_6]SO_4 \cdot H_2O$ with approximately 7% of the $[Fe(H_2O)_6]^{2+}$ cations having one aqua ligand replaced by a nitrosyl ligand.[92] Compounds, **4a** and **4b**, on the other hand, exhibited no disorder on the point positions of the nitrosyl ligands.

The gallate(III) and the ferrate(III) salts were isotypic, as both Ga^{3+} and Fe^{3+} exhibited similar ionic radii in hexa-coordination of 0.620 and 0.645 Å respectively.[107] The water content of **4a** and **4b** was almost identical with approximately 8.3 molecules of water of crystallization. The slight discrepancy stemmed from the disorder of the solvent molecules.

In contrast to previous computational studies that suggested linearity of the FeNO moiety in $[Fe(H_2O)_5(NO)]^{2+}$, the nitrosyl ligands coordinated to the Fe centers with a slight bend in the $[Fe(H_2O)_5(NO)]^{2+}$ salts **4a** and **4b** but also in the oxalato complex **5**.[33,34] The bonding situation of the respective FeNO units will be discussed in more detail in section 3.6.

Upon crystallization, the nitrosyl stretching frequencies of **4a**, **4b** **5** showed a significant blueshift in respect to the solutions, with **4a** and **4b** surpassing even the highest-recorded nitrosyl stretching frequency of hexa-coordinated $\{FeNO\}^7(S = 3/2)$ compounds at $1831\,cm^{-1}$.[57]

UV/Vis data of solid samples of **4a** and aqueous solutions of $Fe(OTf)_2$ at $pH = 1$ are in good agreement. This indicates that the $[Fe(H_2O)_5(NO)]^{2+}$ chromophore, which is present in crystalline material, is also the prevalent chromophore in solutions.

Zero-field ^{57}Fe Mößbauer data of **4b** agreed well with published data on frozen aqueous solutions.[32,108] However, in contrast to the solutions where the $[Fe(H_2O)_5(NO)]^{2+}$ cation occured only as a minor species in an equilibrium with hexaaquairon(II) according to Equation 3.1, the solid material clearly contained $[Fe(H_2O)_5(NO)][Fe(fpin)_2(H_2O)]_2$ as the major component. The $[Fe(fpin)_2(H_2O)]^-$ anion exhibited a quadruplet with approximately twice the area of the $[Fe(H_2O)_5(NO)]^{2+}$ signal. A minor quadruplet of $[Fe(H_2O)_6]^{2+}$ stemmed likely from the adhering mother liquor or, possibly, decayed surface material. Data from the gallate showed the corresponding signals for $[Fe(H_2O)_5(NO)]^{2+}$ as well as $[Fe(H_2O)_6]^{2+}$ with the gallate anion invisible in Mößbauer spectroscopy. Noteworthy is that, here, the ratio of the areas of both signals was shifted dramatically in favor of the hexaaquairon(II) species. As the samples showed no obvious signs of degradation, the missing intensity of the $[Fe(H_2O)_5(NO)]^{2+}$ species has to be suspected elsewhere. In fact, in these samples, as opposed to the ferrate samples, a broad doublet with a large area occurred, that likely originated from a $[Fe(H_2O)_5(NO)]^{2+}$ species, possibly after spin-crossover to a $S = 1/2$ state at low temperatures. Experimental values were reasonably well reproduced by means of DFT calculations using TPSSh with a combination of a CP(PPP) basis set for Fe and def2-TZVP for all other atoms.

3.3 The nitrosylbis(perfluoropinacolato)ferrate anion

Although nitrosylbis(perfluoropinacolato)ferrates could be obtained with various cations including benzyltrimethylammonium or protonated 1,8-Diazabicyclo(5.4.0)undec-7-ene (DBU) only the triethylammonium salt will be discussed in this work due to the quality of available analytical data.[102,109]

6 was synthesized in high yields by the reaction of **1a** with either gaseous nitric oxide or nitrite salts like $NaNO_2$. As prolonged contact to excess nitric oxide induced oxidation of the product to ferrates(III), quick precipitation by the addition of water and purging with inert gas ensured high yields. Nitrosylation by gaseous nitric oxide yielded products that showed disorder with nitrite on the point positions of the nitrosyl ligands. No disorder, however, was observed in products obtained via nitrosylation with nitrite salts. The nitrite route will be discussed in more detail in Section 3.5.

3.4 Neutral nitrosylperfluoropinacolatoiron compounds

Five different neutral $\{FeNO\}^7$ compounds have been synthesized and characterized by single-crystal X-ray diffraction in this work and can be assigned to three groups. The first can be described as mononuclear nitrosylperfluoropinacolatoiron compounds of the type $[Fe(fpin)(NO)(ROH)_2]$ (R=Me, Et) including **7a** and **7b**. The second group consisted of the side products **8a** and **8b** in the respective formation reactions of the first group compounds. They were both tetranuclear with each two outer pentacoordinated perfluoropinacolatoiron(III) centers connected to two inner hexacoordinated $\{FeNO\}^7$ centers via bridging alkoxido or hydroxido ligands. The only example of the third group, **9** is a dinuclear compound with two $\{FeNO\}^7$ centers. It derived from **3c** by substitution of each one benzonitrile ligand per iron center by a nitrosyl ligand.

3.4.1 [Fe(fpin)(NO)(ROH)$_2$] (R=Me, Et; 7a, 7b)

7a was obtained from reaction mixtures with a ratio of iron(II) triflate and perfluoropinacol of 1:1 in methanolic solution with substoichiometrical amounts of base. **7b**, as opposed to **7a**, was synthesized either by direct nitrosylation of its percursor compound **2b** in ethanolic suspension or by the nitrosylation of a reaction mixture with iron(II) triflate and perfluoropinacol at a 1:1 ratio and stochiometrical base dosage. The preparation procedures were, however, quite unreliable and produced only compounds heavily contaminated by byproducts such as the respective tetranuclear compounds **8a** and **8b**. In addition, as **7a** and **7b** were very prone to decay on contact with other coordinating solvents, no method of purification has yet been applicable. In consequence, pure samples of **7a** and **7b** are, to date, not available, prohibiting reliable characterization by UV/Vis spectroscopy and elemental analysis.

Crystals of both compounds exhibited a bright-red color which is uncommon for $\{FeNO\}^7(S = 3/2)$ compounds. A similar red color was observed upon formation of an unknown nitrosyl species in the synthesis of **4b** (Section 3.2). Also, upon close inspection, in the analytical nitrate test, a red nitrosylsulfatoiron species is present in the border region between the "brown-ring", containing mainly $[Fe(H_2O)_5(NO)]^{2+}$ chromophores, and the colorless phase of concentrated sulphuric acid.[110]

3.4.2 $[\{Fe_2(fpin\text{-}1\kappa O,O')(ROH\text{-}2\kappa O)(NO\text{-}2\kappa N)(OR\text{-}1{:}2\kappa O,1{:}2'\kappa O,1{:}2{:}2'\kappa O)_3\}_2]$ (R=Me, H/Et; 8a, 7b)

After the nitrosylation of a reaction mixture of equimolar amounts of iron(II) triflate and perfluoropinacol with stoichiometric amounts (or a slight excess) of a base, the formation of mainly brown crystals of **8a** and **8b** were observed, instead of the red crystals of the respective mononuclear species **7a** and **7b**. As the tetranuclear compounds consisted of each two iron(III) and two $\{FeNO\}^7(S = 3/2)$ centers, nitrosylation obviously induced the oxidation of a portion of the iron(II) precursor compounds. Considering the accumulation of nitrous oxide in the headroom during the reaction, this process seemed very similar to what was observed in the formation of **4b** and, indeed, the resulting tetranuclear products were very reminiscent of the pentaaquanitrosyliron ferrate(III) salt (the oxidation process will be discussed in more detail in Section 3.7). Thus, the hexacoordinate $\{FeNO\}^7$ moieties corresponded to the $[Fe(H_2O)_5(NO)]^{2+}$ portion of the ferrate salt and can be regarded as the deprotonated alcoholic analoga. Naturally, in consequence of deprotonation, the alkoxido- and hydroxido ligands fulfilled a bridging function. At the same time, the perfluoropinacolatoiron(III) moieties correspond to the aquabis(perfluoropinacolato)ferrate(III) anions. Here, the coordination spheres of the iron(III) centers were saturated by the bridging alkoxido and hydroxido ligands instead of a second perfluoropinacolato ligand. The similarity among these compounds is also represented by the apparent brown color, shared by all three mentioned compounds. A considerable difference was, nevertheless, exhibited by the nitrosyl stretching frequency, which was significantly lower for **8a** and **8b**. In this matter, the redshift originated from the highly charged environment of the FeNO unit, as tentative solutions of $[Fe(MeOH)_5(NO)]^{2+}$ obtained by nitrosylation of iron(II) salts in methanol showed a higher nitrosyl stretching frequency at around $1805\,cm^{-1}$.[109]

3.4.3 $[\{Fe(fpin\text{-}1\kappa O{:}1,1'\kappa O')(NO)(PhCN)\}_2]$

9 was obtained by the substitution of each one benzonitrile ligand per iron center in **3c** with a nitrosyl ligand after the introduction of gaseous nitric oxide. A similar reaction can be expected, and supposedly was observed, in the acetonitrile analogue originating from **3b**, as nitrosylation induced a change of color. However, due likely to the limited ability of the terminal acetonitrile methyl groups to form intermolecular interaction, crystallization has not yet been observed. In contrast, the forest-green nitrosylation product of the benzonitrile product has a low solubility in toluene and benzonitrile and crystallized well as a result of intra- and intermolecular π–π interactions. Uncommon for square-pyramidal $\{FeNO\}^7$ compounds, the nitrosyl ligand was not located in the apical but rather in an equatorial position.

3.5 Nitrosylation by the nitrite route

The standard procedure for the nitrosylation of high-spin iron(II) is the introduction of gaseous nitric oxide into the headroom of a reaction mixture. However, in some cases this led to a poor quality of the nitrosyl product. For example, nitrosylation of $(NHEt_3)_2[Fe(fpin)_2]$ by gaseous nitric oxide tended to give products that showed disorder with the nitrosyl ligands partially replaced by nitrito ligands. In such cases, an alternative route of nitrosylation by using nitrite salts as a source of NO was of merit.

The reactivity of iron(II) compounds with nitrite is well known in literature, which leads to the fact that, to date, no binary nitrite of the form $Fe(NO_2)_2$ is known.

Typically, a reaction scheme is formulated according to Equation 3.2 with oxidation of iron(II) to iron(III) and reduction of nitrite to nitric oxide under consumption of protons.[111,112]

$$\mathrm{Fe^{2+} + NO_2^- + 2\,H^+ \longrightarrow Fe^{3+} + NO + H_2O} \tag{3.2}$$

In literature, nitrites were rarely utilized for the nitrosylation of iron(II) compounds but, rather, with other transition metals, partly due to the spontaneous liberation of nitric oxide under acidic conditions according to Equation 3.3.[113–118]In this matter, a maximum yield of only 50% was possible in nitrosylation reactions, as half of the applied quantity of iron(II) was used simply to generate nitric oxide. However, under consideration of the disproportionation reaction that is common for nitrite (Equation 3.3), the efficiency of the nitric oxide generation was increased.[1]

$$\mathrm{3\,NO_2^- + 2\,H^+ \longrightarrow 2\,NO + NO_3^- + H_2O} \tag{3.3}$$

At a 1:1 ratio of the iron(II) centers to the nitrite salt, the reaction produced the desired $\{FeNO\}^7$ compounds in a theoretical yield of 75%, with iron(III) species and nitrate as side products according to Equation 3.4. Thus, when a solution of the precursor complex was treated with a nitrite salt like $NaNO_2$, instant nitrosylation indicated by the change of color was observed.

$$\mathrm{4\,Fe^{2+} + 4\,NO_2^- + 4\,H^+ \longrightarrow 3\,[Fe(NO)]^{2+} + Fe^{3+} + NO_3^- + 2\,H_2O} \tag{3.4}$$

In this course, proton equivalents are consumed increasing the overall pH. In pH-sensitive systems this can then lead to the generation of bright-brown precipitates of amorphous hydroxido and/or oxido iron species. At the same time, this way a proportion of the added base used to deprotonate ligands can be substituted to attenuate this effect. In theory, this should also avoid the oxidation of the iron(II) precursors allowing a yield of 100% according to Equation 3.5 in the example of the synthesis of **6**.

$$\begin{aligned} &2\,\mathrm{Fe}^{2+} + 3\,\mathrm{NO_2^-} + 4\,\mathrm{H_2fpin} + 6\,\mathrm{NEt_3} \longrightarrow \\ &\qquad 2\,(\mathrm{NHEt_3})_2[\mathrm{Fe(fpin)_2(NO)}] + 2\,\mathrm{NHEt_3^+} + \mathrm{NO_3^-} + \mathrm{H_2O} \end{aligned} \tag{3.5}$$

The respective reaction can also be formulated in the synthesis of nitrosylmono(perfluropinacolato)iron compounds (Equation 3.6). These systems, however, tended to yield alkoxidoiron species, so that it may be sensible to omit the dosage of additional base altogether.

$$\begin{aligned} &2\,\mathrm{Fe}^{2+} + 3\,\mathrm{NO_2^-} + 2\,\mathrm{H_2fpin} + 2\,\mathrm{RO^-} + 2\,\mathrm{ROH} \longrightarrow \\ &\qquad 2\,[\mathrm{Fe(fpin)(NO)(ROH)_2}] + \mathrm{NO_3^-} + \mathrm{H_2O} \end{aligned} \tag{3.6}$$

In both examples 1.5 equiv of nitrite replaced 1 equiv of base in order to fully deprotonate the ligands. Although the theoretical yield of 100% was not closely approached in any case, yields like 78% in the case of **6**, that exceed the border at 75% predicted by Equation 3.4, were achieved when a 2:3 ratio of iron(II) source and nitrite salt was dosed.

3.6 Structural varieties of $\{\mathrm{FeNO}\}^7$ compounds

In this work, nine separate compounds featuring $\{\mathrm{FeNO}\}^7(S = 3/2)$ units were obtained and structurally characterized. Of those compounds, five showed hexacoordination and the remaining four pentacoordination of the nitrosylated iron centers. With the exception of **9**, all nitrosyliron compounds featured purely O-bound co-ligands. **6**, **7a**, **7b** and **9** are the first pentacoordinated examples. Regarding the hexacoordinated case, four other instances have been published to date.[39,47,55,56] A $(\mathrm{NO_3})$ co-ligation as apparent in **9** has not been reported yet. The Fe–N distances range from 1.745(4) Å (**7a**) to 1.786(4) Å (**4a**), while the N–O distances span from 1.134(4) Å (**4b**) to 1.152(4) Å (**7a**). All compounds exhibited a bent FeNO moiety with angles between 148.6(2)° and 168.52(17)°. The values of the different nitrosyl stretching frequencies ranged from 1739 to 1843 cm^{-1}. Regarding these findings, the synthesized compounds fit well with other penta- and hexacoordinated quartet $\{\mathrm{FeNO}\}^7$ compounds already known to literature.[38–40,47,100,119,120] Table 3.1 gives an overview of the relevant bonding parameters in all $\{\mathrm{FeNO}\}^7(S = 3/2)$ compounds presented in this work. Regarding the structural influence of the fpin ligand, a striking quality was its high steric demand. All perfluoropinacolato compounds presented showed pentacoordination of the ligated iron center at the highest, while a lack thereof in all cases led to hexacoordinated iron centers. In fact, coordination numbers of perfluoropinacolato complexes of six and higher are only known for the late transition metals Tungsten and Cerium.[121–123] However, an

Table 3.1: Relevant bonding parameters in the FeNO moieties of **4a**, **4b**, **6**, **7a**, **7b**, **8a**, **8b** and **9**.

	4a	**4b**	**5**	**6**	**7a**
Fe–N	1.786(4)	1.780(3)	1.784(6)	1.7572(17)	1.745(4)
N–O	1.143(5)	1.134(4)	1.135(8)	1.149(2)	1.152(4)
Fe–N–O	160.6(4)	162.2(3)	155.6(6)	168.52(17)	162.8(3)
$\tilde{\nu}$(NO)	1843	1841	1823	1739	1801
	7b*	**8a****	**8b**	**9**	
Fe–N	1.7515(19)/1.7508(19)	1.770(2)	1.774(2)	1.769(2)	
N–O	1.151(2)/1.144(2)	1.163(15)/1.125(14)	1.151(3)	1.149(3)	
Fe–N–O	163.86(18)/167.24(19)	156.8(9)/153.0(9)	148.6(2)	150.34(19)	
$\tilde{\nu}$(NO)	1808	1765	1762	1807	

*: Values are given for both symmetrically independent entities.
**: Values are given for both partitions due to apparent disorder of the NO moiety.

exception is found in [{Fe(en)(fpin)(μ-OMe)}$_2$].[109] Despite perfluorinated alkoxido ligands being known to avoid bridging in consequence of their decreased basicity,[70] the fpin ligand constituted bridging under formation of coordination dimers in aprotic solvents as well as in water.

3.7 Reactivity and stability of {FeNO}^{7} compounds with oxygen-donor co-ligands

The quartet {FeNO}^{7} compounds presented in this work showed quite different properties concerning their reactivities and stabilities. The aquanitrosyliron compounds **4a**, **4b** and **5** reversibly liberated nitric oxide under formation of their original iron(II) species when they were removed from a nitric-oxide atmosphere. This was especially true and immediate for solutions, but also solid material underwent rapid decay at ambient conditions. On the other hand, the remaining quartet {FeNO}^{7} compounds showed no such behavior and, in all cases, even sustained in vacuum without liberating NO. A higher stability of the Fe–NO linkage is generally attributed to an irreversible electron transfer from the iron center to NO along the higher trivalent character of the central atom.[124–126] The central iron atoms in [Fe(H$_2$O)$_5$(NO)]$^{2+}$ salts consistently show monovalent character according to the formulation as Fe^{I}(NO$^+$).[92]

Another aspect to consider regarding the stability upon nitrosylation was the consecutive oxidation of the metal center along with a simultaneous reduction of nitrosyl groups to form nitrous oxide according to Equation 3.7.

$$2\,[\mathrm{Fe(L)(NO)}]^{2+} + 2\,\mathrm{ROH} \longrightarrow 2\,[\mathrm{Fe^{III}(L)(OR)}]^{2+} + \mathrm{N_2O} + \mathrm{H_2O} \tag{3.7}$$

This process took place upon nitrosylation of **2a**, **2b** and **3a** and led to the formation of red reactive nitrosyl species that were monitored visually and by *in situ* IR. For **2a** and **2b** these intermediates were isolated as **7a** and **7b**, whereas in water the intermediate was too short-lived. Furthermore, **6** and **9** also showed the same behavior, albeit significantly slower, upon extended contact to an excess of nitric oxide. Due to their poor solubilities in their respective reaction media, they removed themselves from the critical reactions by precipitation, rendering this effect less obvious. Notably, as in **4b** the final product featured an FeNO unit, that reversibly released NO, besides $[\mathrm{Fe^{III}(fpin)_2(H_2O)}]^-$ anions, the mentioned redox process relied on the occurence of perfluoropinacolatoiron(II) species. Once all fpin ligands were consumed by $\mathrm{Fe^{III}}$, to which they showed a higher affinity, the redox process suddenly stopped. This behavior is well documented for quartet $\{\mathrm{FeNO}\}^7$ compounds with mainly O-bound ligand functions and has been a main research focus due to its relevance in nitric oxide reduction by flavodiiron-nitric-oxide reductases.[45,47,124,127–132] The similarity in reactivity between some of the presented compounds such as **3a** and FNORs was hardly surprising on direct comparison. **3a** as well as the active center in the FNOR of *Desulfovibrio gigas* feature diiron(II) units at comparable Fe–Fe distances [FNOR: 3.4 Å; **3a**: 3.1854(11) Å] with each iron center in a weak field ligand pentacoordination.[66] This resemblance, on the other hand, rendered the perfluoropinacolatoiron(II) compounds ideal models for further research on FNOR chemistry.

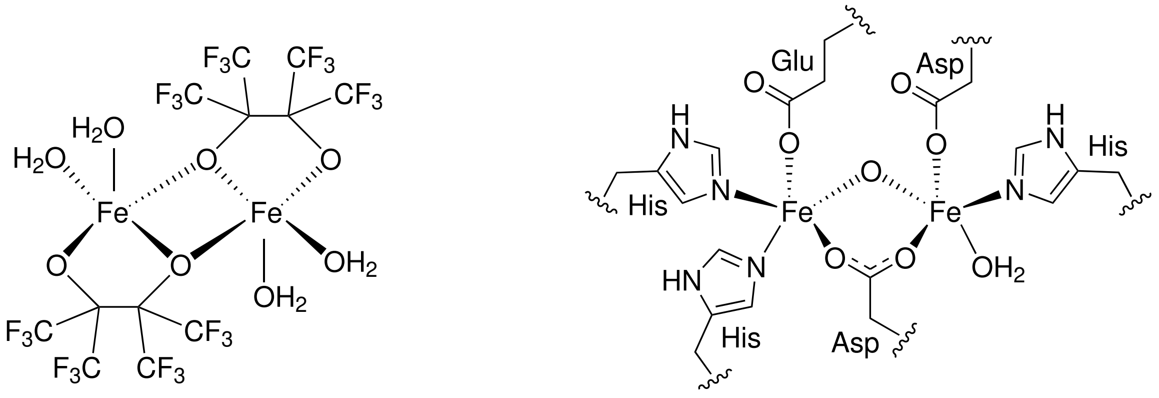

Figure 3.1: Comparison of **3a** (left) and a FNOR active site from *Desulfovibrio gigas*[66] (right).

3.8 The oxidation states in $\{FeNO\}^7$ compounds

The determination of oxidation states in quartet $\{FeNO\}^7$ compounds has been, due to the non-innocent quality of the nitrosyl ligand, a complex and, therefore, highly contested issue in literature. In this matter, the opposing sides promoted contradicting formulations as either $Fe^{I}(NO^{+})$,[31,133,134] $Fe^{II}(NO^{0})$[33,135–139], $Fe^{III}(NO^{-})$[32,54,55,140–151] or a state in between $Fe^{II}(NO^{0})$ and $Fe^{III}(NO^{-})$[152–154]. Due to the fact, that in some cases the assigned oxidation number was to simply mirror "real" charges,[153] the IUPAC corroborated the original definition of determining oxidation states per ionic approximation.[155] For assessment in the cases on hand, evidence gained by structure analysis, spectroscopy and quantum-chemical calculations will be reviewed in the following.

3.8.1 Structural and spectroscopic evidence

For the assignment of oxidation states, a first look should be focused on Fe–ligand bond-lengths. A comparison with the respective Fe^{II} or Fe^{III} compounds, where possible, should present a first estimation. Table 3.2 shows a decrease of the mean Fe–O bond lengths for all iron(II) compounds upon nitrosylation, as also supported by DFT calculations. In two cases, data of the respective iron(III) compound is available, showing that, while in $[Fe(fpin)_2(NO)]^{2-}$ the mean Fe–O bond length lies exactly in between Fe^{II} and Fe^{III}, $[Fe(H_2O)_5(NO)]^{2+}$ has more Fe^{II} character.

Table 3.2: Average Fe–O distances in various Fe^{II}, $\{FeNO\}^7(S = 3/2)$ and Fe^{III} compounds. Distances in Å.

Fe^{II}	⌀ Fe–O	$\{FeNO\}^7$	⌀ Fe–O	Fe^{III}	⌀ Fe–O
$[Fe(H_2O)_6]^{2+}$	2.104[156]	$[Fe(H_2O)_5(NO)]^{2+}$	2.078	$[Fe(H_2O)_6]^{3+}$	1.985
$[Fe(fpin)(MeOH)_3]$	2.050	$[Fe(fpin)(MeOH)_2(NO)]$	2.002	n.a	
$[Fe(EtOH)_3(fpin)]$	2.061	$[Fe(EtOH)_2(fpin)(NO)]$	2.029	n.a	
$[Fe(fpin)_2]^{2-}$	2.041	$[Fe(fpin)_2(NO)]^{2-}$	1.999	$[Fe(fpin)_2(H_2O)]^{-}$	1.946

The same assessment is applied on the nitrosyl ligand by comparing the respective N–O bond lengths and the nitrosyl stretching frequencies. However, a direct comparison with the border cases of NO^{+} and NO^{-} has only limited applicability, due to the inherent quality of NO being a π-acceptor ligand. As it forms π-backbonds to metal centers, this results in a stretch of the N–O bond, expressed as a redshift of the stretching frequency. At the same time, nitrosyl coordination of a metal center, in general, results in a blueshift of the stretching frequency, due to the increased total interaction of the binding N atom as a result of additional metal bonding.

While for NO^{+} several salts have been isolated with N–O distances between 1.020 and 1.061 Å and nitrosyl stretching frequencies between 2225 and 2328 cm^{-1},[157–161] the situation is quite different for NO^{-}. Only one stable salt has been successfully synthesized as LiNO to date.[162]

However, it lacks structure information due to the impure nature of the product. Available electron scattering data, however, arrived at a bond length of 1.267 Å and from neon-matrix experiments a tentative nitrosyl stretching frequency is obtained at 1370 cm^{-1}.[163,164] The neutral $NO^{\bullet}$ molecule lies in between with a N–O distance of 1.151 Å[165] and a nitrosyl stretching frequency at 1876 cm^{-1} with pronounced broadening of the band in the gas phase.[166]

In the presented compounds N–O bond lengths ranged from 1.134(4) Å to 1.152(4) Å (only considering the mean N–O distance in the disordered nitrosyl ligand of **8a**), placing them altogether in the vicinity of neutral $NO^{\bullet}$ with a tendency towards NO^{+}. A similar situation wass present regarding the nitrosyl stretching frequencies that ranged from 1739 to 1843 cm^{-1}, again, showing close proximity to $NO^{\bullet}$. Notably, the aquanitrosyliron compounds stood out with their significantly shorter N–O bonds and higher nitrosyl stretching frequencies compared to the rest, thus, showing the most $Fe^{I}(NO^{+})$ character among the presented compounds. The alkoxido ligated iron complexes, on the other hand, exhibited comparably more $Fe^{III}(NO^{-})$ character. This was also expressed by their apparent reactivity towards N_2O generation, which is shared with actual NO^{-} salts like LiNO.[162]

3.8.2 Quantum-chemical evidence

As the issue of oxidation states in high-spin $\{FeNO\}^7$ centers cannot be tackled alone by the analysis of experimental data due to its unique complexity, quantum-chemical data was essential for further evaluation. In general, nitrosyl-metal moieties show a high degree of nondynamical correlation, as is evidenced by weakened M–NO bonds in consequence of depopulation of π-M–NO and population of the respective π*-M–NO antibond.[92,167] In fact, in the case of iron, the antibonding orbitals can reach significant occupation numbers of up to 0.3.[153] Supposedly, the non-dynamic correlation originated from multiple instances of Pauli repulsion due to overlap density of occupied 3*s* and 3*p* orbitals with 3*d* orbitals,[168] overlap of the antibonding N–O-π* portion in the M–NO bond and the bonding N–O-π and, lastly, occupation of the repulsive Fe-d_{z^2}–NO σ-contact special to the quartet $\{FeNO\}^7$ species.[92a] The latter seems responsible for the Fe–N–O bending in order to attenuate this unfavorable interaction (see Orbitals α-46 and β-48 in Figure 2.31).

Another important aspect in quartet $\{FeNO\}^7$ species was the prevalent spin polarization. Namely, α-spin was concentrated on the Fe atom while the NO ligand always showed higher β-spin density, equally by MPA and NPA, as can be seen in Table 2.19. This is consistent with other published studies on quartet $\{FeNO\}^7$ species showing the same effect.[39,100,119,120,153]

In this matter, the discrepancy in the results obtained by the pure density functional BP86 and the hybrid functional TPSSh was striking. In all instances, TPSSh allocated significantly higher β density on the NO ligand than BP86. The apparent overestimation of spin polarization is typical for hybrid functionals and is regarded in literature as unphysical behavior.[153,169]

The evaluation of charges calculated by MPA, NPA and QTAIM yielded a more-or-less neutral charge of the nitrosyl ligand in all cases (Table 2.19) with the most positive charge in $[Fe(H_2O)_5(NO)]^{2+}$ and increasingly negative charge from **7b** to **7a** and $[Fe(fpin)_2NO]^{2-}$. The apparent NO^0 character agreed mostly with spectroscopic data, as mentioned above, and, putatively, with published studies suggesting a formulation as $Fe^{II}NO^0$.[33] However, in unison with the ionic approximation, the $Fe^{II}NO^0$ formulation is a highly unlikely one, when taking into account only the share of an atom's atomic orbital in the respective molecular orbital.[155] In the example of $[Fe(H_2O)_5(NO)]^{2+}$, the prevalent metal character of the relevant Fe–NO-π bonds, thus, led to a formulation as $Fe^{I}NO^+$.[92] When considering spin-polarization, the assignment of oxidation states becomes highly method-dependent, as full polarization coincides with the allocation of both β-spin electrons in the Fe–NO-π bonds towards the nitrosyl ligand – thus, resulting in the $Fe^{III}NO^-$ formulation. In this matter, oxidation states were calculated using LOBA and EOS, with, especially, the latter being able to treat spin-polarized species appropriately.[96,97] As mentioned above, overpolarization was prevalent mostly in hybrid functionals and, indeed, TPSSh, without fail, assigned oxidation states according to $Fe^{III}NO^-$ both using EOS (Table 2.21) and LOBA (Table 6.1). Using BP86, with more realistic spin-polarization,[153,169] EOS assigned oxidation states according to $Fe^{I}NO^+$ in $[Fe(H_2O)_5(NO)]^{2+}$ and **7b**, while **7a** and $[Fe(fpin)_2(NO)]^{2-}$ remained with the $Fe^{III}NO^-$ formulation. The BP86 results from LOBA calculations seem unreliable, as they assigned the oxidation state +III to the Fe center in all cases but **7b**, where a $Fe^{II}NO^-$ unit was formulated.

3.9 Photo-irradiation experiments

Upon irradiation of **6** with light of 590 nm at 10 K, a shift of the nitrosyl stretching frequency towards higher energy was observed. As a possible linkage isomerization in $\{FeNO\}^7(S = 3/2)$ from a NO-κN to a NO-κO mode would typically result in a shift of the nitrosyl stretching frequency to lower energy. The apparent blueshift, hence, was likely the result of another process.[100,120] A possible explanation is a photoinduced oxidation by one electron of the $\{FeNO\}^7(S = 3/2)$ species as was suggested by Wolf.[100] Consistently, DFT calculations suggested a shift of the stretching frequency upon oxidation to $\{FeNO\}^6(S = 1)$ towards the region in question at higher energy. In the example of $(PPN)[FeCl_3(NO)]$, the PPN^+ cation was assumed to be the recipient in the electron transaction. In the case in hand, an analog reduction of the $NHEt_3^+$ cations could be possible as well but lacks unambiguous spectroscopic evidence.

In **9**, irradiation with light of 590 nm at 10 K led to the formation of a new band at 1685 cm^{-1}, indicating linkage isomerism from NO-κN to a NO-κO MS1 state. However, as the newly formed band was very weak, presumably only a small portion populated an MS1 state. In addition, the depopulation was very fast, so that even at 10 K a significant fraction of the excited molecules returned to the ground state in the time frame of a measurement.

3.10 UV/Vis spectra and TD-DFT

Both solutions and solid material of $[Fe(H_2O)_5(NO)]^{2+}$ salts exhibited a brown color, characteristic of the "brown-ring" in the nitrate analytical test. The comparison of the solution and the, now available, solid-state UV/Vis spectra indicated the presence of the same chromophore. The brown color is the consequence of a broadband absorption in the visible region with relatively high absorption in the blue and the green region at 400 – 550 nm and higher transmission in the red region. In the case of the gallate **4a**, as the original $[Fe^{II}(H_2O)_6]^{2+}$ salt was colorless, the brown color is directly attributed to the nitrosyl ligand. This was also reproduced by TD-DFT calculations, showing the involvement of the nitrosyl ligand for all visible excitations. Only in the UV region was intense nitrosyl-independent LMCT from water to Fe observed. **6**, on the other hand, exhibited a burgundy color both in solution and in solid-state due to a relatively higher absorption in the green region than in $[Fe(H_2O)_5(NO)]^{2+}$, while at the same time, the overall extinction was lower by a factor of 10. Here, the color could not automatically be attributed to the presence of the nitrosyl ligand as the precursor compound **1a** exhibited a lavender color at comparable extinction. Thus, in **6** nitrosyl-independent visible excitations were present as well, according to TD-DFT.

4 Summary

This thesis covers the synthesis, characterization and computational analysis via DFT methods of high-spin $\{FeNO\}^7$ compounds with mainly O-bound co-ligands. The main focus lies on the preparation and analysis of stable $[Fe(H_2O)_5(NO)]^{2+}$ salts, that have been attempted for well over a century.

Originating from the work of Tahsini[70] and Wurzenberger[68,69] on square-planar high-spin complex anions with the bidentate perfluoropinacolato-κ^2O:O' chelator of the type $[Fe(fpin\text{-}\kappa^2O{:}O')_2]^{2-}$, among others, these and derivative mono(perfluoropinacolato)iron(II) compounds were synthesized and used as starting materials in further nitrosylation experiments. The perfluoropinacolato ligand recommended itself in particular in this context, as it enabled facile deprotonation even in acidic conditions, avoiding formation of unreactive hydroxido- and oxidoiron precipitates. In the course of this work, eight different iron(II) complex compounds with perfluoropinacolato ligands were synthesized and structurally characterized. For the preparation, iron(II) triflate was reacted in various coordinating solvents with either 1 or 2 equiv H_2fpin and stoichiometric amounts of a base. The resulting products can be divided into three groups: square-planar bis(perfluoropinacolato)ferrates(II) of the general formula $A_2[Fe(fpin)_2]$ [A = $NHEt_3^+$ (**1a**), $NBnMe_3^+$(**1b**)], neutral trialcoholmono(perfluoropinacolato)iron(II) of the type $[Fe(fpin)(ROH)_3]$ [R = Me (**2a**), Et (**2b**)] and dinuclear bis(perfluoropinacolato)diiron(II) compounds of the general formula $[Fe_2(fpin\text{-}1\kappa O{:}1{,}1'\kappa O')_2(L)_4]$ [L = H_2O (**3a**), MeCN (**3b**), PhCN (**3c**), thf (**3d**)]. Apart from the tetracoordinated first group, all compounds exhibited pentacoordination of the iron(II) centers. All compounds showed immediate reaction with nitric oxide and were easily oxidized by even small amounts of oxygen.

The unambiguous isolation of the $[Fe(H_2O)_5(NO)]^{2+}$ cation, the renowned chromophore in the "brown-ring" of the analytical nitrate test, which had been a target of Kohlschütter and Manchot in the early 20th century[29,30,36,106] and later of Wilkinson[31] and van Eldik[170], was accomplished as salts of the general formula $[Fe(H_2O)_5(NO)][M^{III}(fpin)_2(H_2O)]_2 \cdot x\,H_2O$ ($M = Fe, Ga$; $x \approx 8.3$).[92] Along with supplying the first reliable crystal structures of the $[Fe(H_2O)_5(NO)]^{2+}$ cation, this enabled solid phase analysis via IR, UV/Vis and Mößbauer-spectroscopy. The syntheses were carried out either by nitrosylation of **3a** in acidic conditions to obtain **4b** after a nitrous oxide liberating redox process or by the introduction of nitric oxide into an aqueous suspension of iron(II) triflate, gallium(III) triflate, H_2fpin and NaOH in a 1:2:4:4 ratio to obtain **4a**. As opposed to solutions, the dry crystalline material could be stored for months at $-20\,°C$. The FeNO moiety exhibited a slightly bent geometry contrasting with prior rebutting predictions stating, instead, linearity.[33,34]

A polymeric aquanitrosyloxalatoiron species of the type $[\{Fe(H_2O)(NO)(\mu\text{-ox})\}_{n/n}] \cdot H_2O$ (**5** $\cdot$ H_2O) was crystallized after the introduction of nitric oxide into an aqueous suspension of iron(II) triflate and oxalic acid. The highly decomposable product was characterized by IR and single-crystal X-ray diffraction.

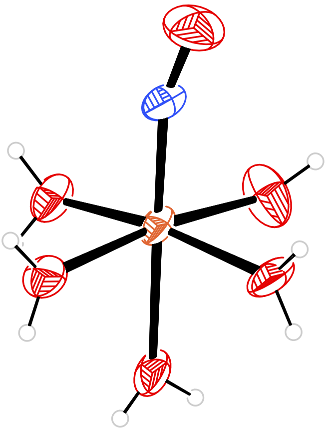

Figure 4.1: ORTEP plot of the $[Fe(H_2O)_5(NO)]^{2+}$ cation in crystals of **4b** at 50% probability level.

Six different nitrosyliron compounds with perfluoropinacolato co-ligands were isolated with different Fe:fpin ratios of 1:2 (**6**), 1:1 (**7a**, **7b**, **9**) and 2:1 (**8a**, **8b**). $(NHEt_3)_2[Fe(fpin)_2(NO)]$ was prepared by nitrosylation of **1a** with nitric oxide or nitrite salts. **7a**, **7b**, **8a** and **8b** were obtained from the same reaction mixtures in their respective solvents at different base dosages. The substoichiometric addition of a base favorably yielded the red mononuclear products **7a** and **7b** of the general formula $[Fe(fpin)(NO)(ROH)_2]$ [R = Me (**7a**), Et (**7b**)]. At stochiometric base dosage, crystallization of the brown tetranuclear compounds **8a** and **8b** of the general formula $[\{Fe_2(\text{fpin-}1\kappa O,O')(\text{ROH-}2\kappa O)(\text{NO-}2\kappa N)(\text{OR-}1{:}2\kappa O,1{:}2'\kappa O,1{:}2{:}2'\kappa O)_3\}_2] \cdot 2\,ROH$ [R = Me (**8a**), Et/H (**8b**)] took places instead. As iron was partly oxidized to Fe^{III}, these were the products of a consecutive redox process, releasing nitrous oxide. The reaction of **3c** with nitric oxide in toluene gave green crystals of $[\{Fe(\text{fpin-}1\kappa O{:}1,1'\kappa O')(NO)(PhCN)\}_2]$ (**9**). For further insight into the FeNO moiety quantum-chemical calculations using DFT methods were performed of $[Fe(H_2O)_5(NO)]^{2+}$, **7a**, **7b** and $[Fe(fpin)_2(NO)]^{2-}$. All calculations were executed with the def2-TZVP basis set and D3 dispersion correction. Several solvation models were compared for further use, with CPCM_{H_2O} the best compromise between accuracy and processing speed. Structures were optimized using the BP86, B97-D, TPSSh and B3LYP functionals. A bent FeNO unit in $[Fe(H_2O)_5(NO)]^{2+}$ was only rightly predicted using BP86. A satisfactory replication of $[Fe(fpin)_2(NO)]^{2-}$ using BP86 was achieved only after taking the $NHEt_3^+$ cations into account. **7a** can be reasonably well described by BP86 and B97-D, while **7b** is better reproduced using the hybrid functionals TPSSh and B3LYP. According to population and charge analysis by Mulliken, NPA, and QTAIM, $[Fe(H_2O)_5(NO)]^{2+}$ showed a tendency towards a description as $Fe^{I}(NO^{+})$ with successively increasing character of $Fe^{III}(NO^{-})$ in **7b**, **7a** and $[Fe(fpin)_2(NO)]^{2-}$. These findings were supported by EOS analyses on the BP86 level of theory, assigning oxidation states according to $Fe^{I}(NO^{+})$ in $[Fe(H_2O)_5(NO)]^{2+}$ and **7b**, and according to $Fe^{III}(NO^{-})$ in **7a** and $[Fe(fpin)_2(NO)]^{2-}$. The overestimation of spin polarization in TPSSh calculations, however, led to the assignment of oxidation states according to $Fe^{III}(NO^{-})$ in all cases. TD-DFT analysis of $[Fe(H_2O)_5(NO)]^{2+}$ and $[Fe(fpin)_2(NO)]^{2-}$ reasonably well reproduced experimental absorption bands and assigned them to excitations between molecular orbitals, mainly involving the Fe-d, NO-σ and NO-π^* orbitals.

Photo-irradiation experiments were conducted on **6** and **9** in order to investigate possible photoactivation of these compounds. Irradiation of **6** with light of a wavelength of 590 nm at 10 K led to a blueshift of the nitrosyl stretching frequency to 1875 cm^{-1} by approximately 100 cm^{-1}. DFT studies suggested photo-oxidation with formation of a $[Fe(fpin)_2(NO)]^{-}$ anion, possibly along reduction of the $NHEt_3^{+}$ cation. Further irradiation with light of 470 nm repopulated the ground state, while at the same time the formation of nitrous oxide was observed. **9**, however, showed typical short-lived photoinduced linkage isomerism (PLI) at 10 K with a redshift of the nitrosyl-stretching frequency by approximately 130 cm^{-1} to 1685 cm^{-1} after irradiation with light of 590 nm.

5 Experimental Section

5.1 Common working techniques

All reactions involving iron compounds were carried out via standard Schlenk techniques in an inert argon atmosphere. Prior to use, reaction vessels and laboratory commodities like syringes, canulae and pipettes were purged with argon at least three times successively.

Solvents used in the reactions were degassed by either flushing with argon gas over a period of at least 15 minutes in the case of water, methanol, ethanol, acetonitrile and benzonitrile or by using *freeze, pump, thaw* techniques in the case of tetrahydrofurane, diethyl ether, pentane and hexane. Air sensitive and hygroscopic compounds were stored in Schlenk tubes in an argon atmosphere. Weighing of air-sensitive and hygroscopic solids was performed by quickly charging an empty Schlenk vessel, whose empty tax weight (including the inert gas atmosphere) was known, in inert gas counterflow and, afterwards, weighing again to determine the gain in weight.

The introduction of gaseous nitric oxide was conducted at a specialized installation, which combined a Schlenk line with an additional inlet for nitric oxide (Figure 5.1). This apparatus made it, therefore, possible to treat reaction mixtures with nitric oxide under strict exclusion of air and ambient moisture. The installation was made up of, each, an argon, a vacuum and a nitric oxide inlet, which were all separably joined in a central chamber connected to the reaction vessel. Nitric oxide was retrieved directly from a compressed gas cylinder, depressurized to approximately ambient pressure and led over Ascarite II® (silica coated with sodium hydroxide for quantitative adsorption of acid gases).[171] Prior to the introduction of nitric oxide, reaction vessels were slightly evacuated to accelerate the diffusion of nitric oxide into the reaction mixture.

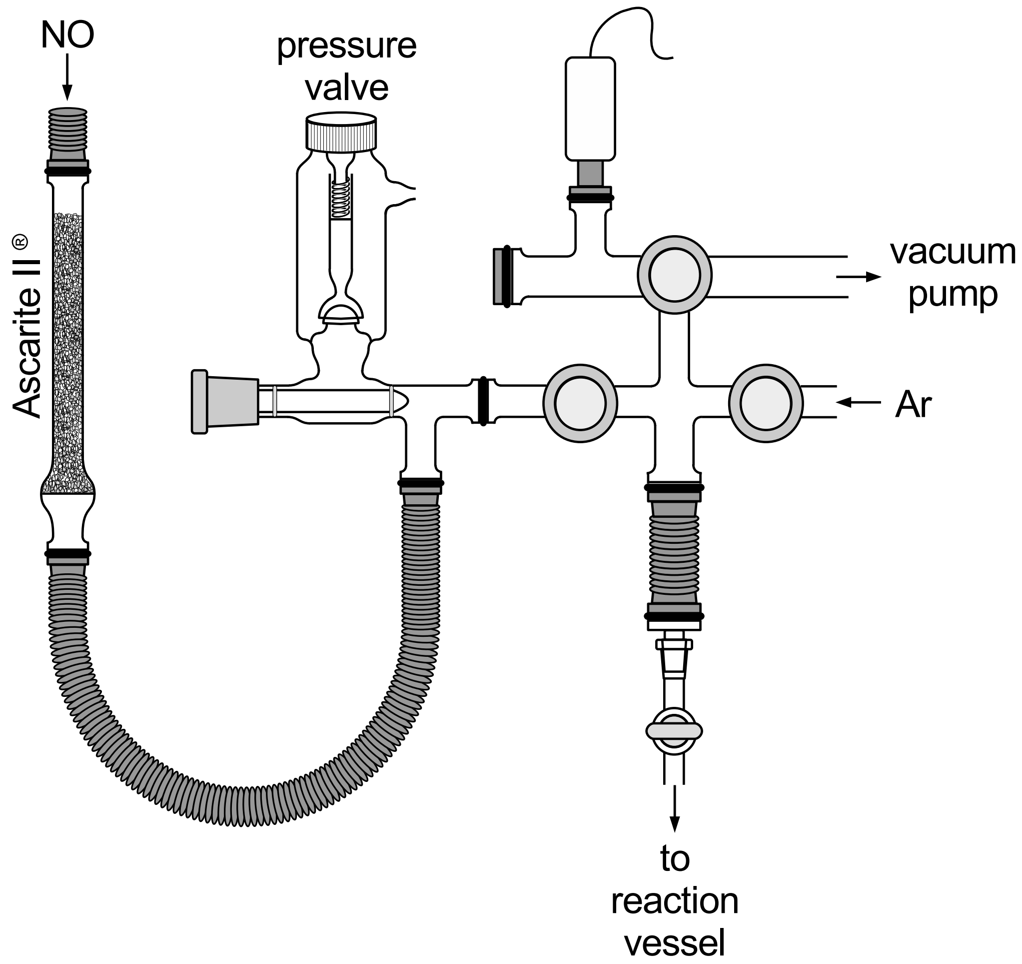

Figure 5.1: Schematic depiction of the apparatus for the introduction of gaseous nitric oxide.

5.2 Analytical methods

5.2.1 IR spectroscopy

IR spectra were recorded on a *Jasco FT/IR-4600 spectrometer*. For solid samples an *PIKE MIRacle™ Single Reflection* ATR unit was used with a diamond crystal plate. Gaseous samples were measured in a *Specac Storm™10 Pyrex™ Glass Gas Cell* in transmission mode. *In situ* IR spectra were recorded on a *Mettler Toledo ReactIR 15* using an ATR probe with diamond crystal plate. Three-dimensional plot of the time-dependent IR spectra were generated using the program *iC IR 7.1* by Mettler Toledo.

5.2.2 UV/Vis spectroscopy

UV/Vis spectra of solutions were recorded on a *Cary 50 Bio UV-Visible-Spectrophotometer* using sealable quartz glass cuvettes with a thickness of 10 mm. All spectra were corrected against a background spectrum of the utilized solvent and cuvette.

The preparation of air-sensitive samples was performed by applying an inert gas atmosphere to an empty cuvette inside a Schlenk tube. The cuvette was filled under inert gas counterflow with the desired background solvent or sample solution and sealed with a silicone septum. To minimize the diffusion of air through the silicone septum, the sample cuvette remained in the Schlenk tube right until the measurement.

Solid samples were measured on a *Cary 500 Scan UV-Vis-NIR-Spectrophotometer* with a *Labsphere DRA-CA-5500* photometer sphere. The *Kubelka-Munk* function (Equation 5.1) was used to translate the measured diffuse reflection into data, which can be compared to absorption experiments. Highly colored samples were diluted with $BaSO_4$ in order to keep the diffuse reflectance above at least 60% at all times.

$$\frac{K}{S} = \frac{(1-R)^2}{2R} \tag{5.1}$$

(R = remission; K = absorption coefficient; S = scattering coefficient)

For comparison with quantum chemical TD-DFT calculations the deconvolution of the spectra into elemental absorption bands was performed. This was accomplished, first, by manually approximating the experimental spectra in the desired range with several Pseudo-Voigt functions $V_{pseudo}(\tilde{\nu})$ (Equation 5.2), that mix Gaussians $G(\tilde{\nu})$ (Equation 5.3) and Lorentzians $L(\tilde{\nu})$ (Equation 5.4), until the sum of all functions showed satisfactory agreement with the experimental data. Secondly, the sum of all functions was then fitted to the experimental data using *Gnuplot 5.0* by variation of the wavelengths of the maxima x_0, the signal intensities I, the full widths at half maximum γ of the functions, and the mixing parameter η in the linear combination of Gaussian of Lorentzian.

$$V_{pseudo}(\tilde{\nu}) = I\{(1-\eta)\, G(\tilde{\nu}) + \eta\, L(\tilde{\nu})\} \tag{5.2}$$

$$G(\tilde{\nu}) = \frac{2\sqrt{\ln 2}}{\gamma\sqrt{\pi}} e^{-4\ln 2 (\frac{\tilde{\nu}-\tilde{\nu}_0}{\gamma})^2} \tag{5.3}$$

$$L(\tilde{\nu}) = \frac{1}{2\pi} \frac{\gamma}{(\tilde{\nu}-\tilde{\nu}_0)^2 + (\frac{\gamma}{2})^2} \tag{5.4}$$

($\tilde{\nu}_0$ = wavenumber at maximum, I = signal intensity; γ = full width at half maximum; η = portion of Lorentzian)

5.2.3 Single-crystal X-ray diffraction

Crystals suitable for X-ray diffraction were selected using a *Leica MZ6* microscope with polarization filters. Measurements were performed on diffractometers of the types *Bruker D8Venture* with a rotating anode or *Oxford XCalibur* with a fine-focus sealed tube using MoK_α radiation. Raw data was processed with *Bruker APEX* and the structure solutions were performed using direct methods with *SHELXT-2014*.[172] Structures were refined by full-matrix least-squares calculations on F^2 with *SHELXL-2014*[173] and *ShelXle*.[174] *Platon* was used for the determination of space groups and to test for twinning.[175] Unit cell parameters of twin domains and the associated twin laws and transformation matrices were identified by *CELL_NOW*.[176] Molecule structures were visualized with *Ortep*.[177] Package diagrams and plots of graph-set analyses were created using *Mercury*[178,179] and visualized by *POV-Ray*.[180] Detailed informations on crystal measurements of each individual compound are attached under Section 6.3.

5.2.4 Mass spectroscopy

FAB mass spectra were measured on a *Jeol MStation 700* after the ionization of the sample in a nitrobenzylalcohol or glycerine matrix with an argon atom beam of 8 kV.

5.2.5 Elemental analysis

CHNS analysis was performed on devices of the type *Elementar vario EL* and *Elementar vario micro tube*. Residual contents of solvents were calculated using *JASPER v2.0*.[181]

5.2.6 Mößbauer spectroscopy

Mößbauer spectra were recorded by Prof. Dr. Friedrich Wagner at TU Munich. ^{57}Co in a rhodium matrix served as the γ-ray source and was always kept at the same temperature as the sample. For reference against α-Fe 0.11 mm s^{-1} have to be added to the measured values.

5.3 Computational methods

Quantum-chemical calculations using density functional theory (DFT) were performed with *Orca* in its versions 4.1.1 and 4.1.2.[182] Initial geometries were taken from crystal structure analyses when available. When no experimental data was accessible, such as in the case of presumed excited states in PLI experiments, molecule structures of closely related compounds were altered to obtain initial geometries. Wave functions were calculated with def2-TZVP[71] and auxiliary def2/J[77] basis sets using the multipole-accelerated *resolution of identity approximation* (RI-DFT)[73,74] for the functionals BP86[78,79] and B97-D[80] and the *resolution of identity approximation* with *chain-of-spheres exchange* (RIJCOSX)[75,76] for the hybrid functionals TPSSh[81–83] and B3LYP.[84–87] In all calculations D3 dispersion correction[72] with BJ-damping[183] was applied. Solvation was modeled using a *conductor-like polarizable continuum model* (CPCM)[88], a *conductor-like polarizable continuum model* with an COSMO[89] epsilon function (CPCMC) and a *reference interaction site model* (RISM).[90,91] Calculations using the RISM solvation model were conducted by Marc Reimann (AK Kaupp, TU Berlin). Frequency analyses were carried out numerically. Excited states were calculated with *time-dependent density functional theory* (TD-DFT).[184,185] Mößbauer parameters were calculated using a CP(PPP) basis set for Fe and adjusted with calibration parameters from [98].[99] *Mulliken population analysis* (MPA)[93] was performed by the *Orca* program system. *Natural population analysis* (NPA)[94] was conducted using the *NBO6* program.[186] *Quantum theory of atoms in molecules* analyses (QTAIM)[187] were carried out with the program *MultiWFN*.[95] Oxidation states were calculated by Head-Gordon's *localized orbital bonding analysis* (LOBA)[97] and Salvador's *effective oxidation state analysis* (EOS).[96] EOS analyses were conducted by Daniel Schröder (AK Klüfers, LMU München). *Continuous shape measures* (CShM) were calculated using *SHAPE*.[188,189] *Chemcraft* Version 1.8 (build 536b) was used in the evaluation of computational results as well as for rendering molecular orbitals plots.[190] Isovalues are given in atomic units.

5.4 Reagents and solvents

Table 5.1: Overview over chemicals used in experiments and their respective purities and distributors.

Reagent	Purity	Distributor
acetonitrile	99.9%	Acros Organics
benzonitrile	≥98%	Fluka Analytical
benzyltrimethylammonium methoxide	40% in methanol	ChemCruz
ethanol	abs.	VWR
gallium(III) triflate	99%	Acros Organics
iron(II) triflate	90 – 96%*	[156]
iron(III) triflate	90%	Aldrich Chemistry
lithium	for synthesis	Merck
methanol	99.8%	Acros Organics
n-butyllithium	1.6 M in hexanes	Aldrich Chemistry
nitric oxide	99.5%	Air Liquide
oxalic acid	≥99.0%	Sigma Aldrich
perfluoropinacol	97%	Fluorochem
potassium methoxide	25% in methanol	Sigma
potassium *tert*-butanolate	≥98.0%	Aldrich Chemistry
sodium hydroxide	≥98.0%	Honeywell
sodium nitrite	98%	VWR
tetrahydrofurane	99.5%	Acros Organics
triethylamine	purum	Riedel-de Haën
water	deionized	house installation

*: In the following, the specified quantities used in the syntheses are given in respect to a theoretical purity of 100%.

5.5 Synthesis of bis(perfluoropinacolato)ferrates(II)

5.5.1 $(NHEt_3)_2[Fe(fpin)_2]$ (1a)

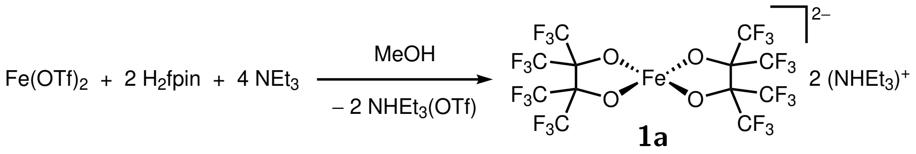

Starting materials: Iron(II) triflate, perfluoropinacol, triethylamine, methanol.
Procedure: To a solution of iron(II) triflate (161 mg, 0.454 mmol) in methanol (5 mL) perfluoropinacol (312 mg, 0.167 mL, 0.907 mmol) was added. Triethylamine (185 mg, 1.81 mmol) was slowly added, yielding a light blue solution with a lavender precipitate. For full precipitation water (5 mL) was added. The precipitate was filtered off, washed with water (3 × 3 mL) and dried *in vacuo*. Lavender crystals were obtained by slowly cooling a saturated methanolic solution to 4 °C.

Empirical Formula:	$C_{24}H_{32}F_{24}FeN_2O_4$ (924.34 $g\,mol^{-1}$, **1a**).
Yield:	383 mg (0.415 mmol), 91.3% of th., lavender crystals.
Elemental analysis:	found (calcd.): C 31.08% (31.19%), H 3.36% (3.49%), N 3.29% (3.03%).
IR: (solid, ATR)	$\tilde{\nu}$ = 3011 (br, w), 2729 (w), 2699 (w), 1478 (w), 1443 (w), 1395 (w), 1257 (m), 1225 (s), 1202 (s), 1172 (vs), 1138 (vs), 1107 (s), 1050 (s), 1017 (m), 985 (m), 961 (w), 931 (vs), 865 (vs), 840 (m), 814 (w), 785 (w), 756 (m), 739 (s), 729 (m), 712 (s), 675 (w) cm^{-1}.
UV/Vis: (solution, acetone)	λ = 375, 582 nm.
UV/Vis: (solid, $BaSO_4$)	λ = 321, 575 nm.

5.5.2 $(NBnMe_3)_2[Fe(fpin)_2]$ (1b)

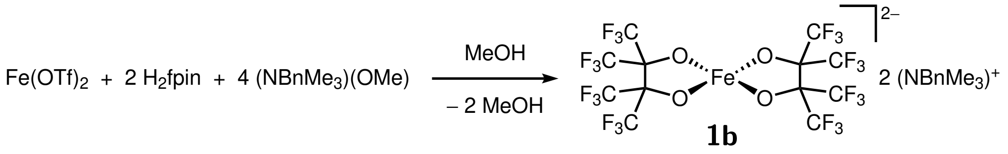

Starting materials: Iron(II) triflate, perfluoropinacol, benzyltrimethylammonium methoxide, methanol.

Procedure: To a solution of iron(II) triflate (913 g, 2.58 mmol) in methanol (20 mL) perfluoropinacol (1.78 g, 0.952 mL, 5.19 mmol) was added. Benzyltrimethylammonium methoxide (40% in methanol, 5.11 mL, 10.4 mmol) was slowly added yielding a blue solution. The mixture was stirred for 30 min until the solvent was evaporated under reduced pressure forming a lavender precipitate. The precipitate was washed with cold methanol (3 × 1.5 mL) and dried *in vacuo*. Lavender crystals were obtained by slowly cooling a saturated methanolic solution to 4 °C.

Empirical Formula:	$C_{32}H_{32}F_{24}FeN_2O_4$ (1020.42 g mol^{-1}, **1b**).
Yield:	849 mg (1.90 mmol), 74% of th., lavender crystals.
Elemental analysis:	found (calcd.): C 36.70% (37.67%), H 3.33% (3.16%), N 2.79% (2.75%), S 0.77% (0%).
IR: (solid, ATR)	$\tilde{\nu}$ = 1490 (m), 1474 (m), 1456 (m), 1404 (w), 1256 (s), 1227 (vs), 1204 (vs), 1151 (vs), 1118 (s), 1102 (s), 1083 (m), 1033 (m), 984 (m), 973 (m), 930 (vs), 886 (m), 861 (vs), 782 (m), 755 (m), 738 (s), 728 (vs), 711 (vs), 670 (m) cm^{-1}.
UV/Vis: (solution, MeOH)	λ = 647 nm.
MS: (FAB$^+$)	m/z = 1020.1 [M]$^+$, 150.2 [NBnMe$_3$]$^+$, 91.1 [Bn]$^+$, 58.1 [NMe$_3$]$^+$.
MS: (FAB$^-$)	m/z = 1021.9 [M + H]$^-$, 870.1 [M − NBnMe$_3$]$^-$, 720.0 [M − 2 NBnMe$_3$]$^-$.

5.6 Synthesis of mono(perfluoropinacolato)iron(II) compounds

5.6.1 [Fe(fpin)(MeOH)$_3$] (2a)

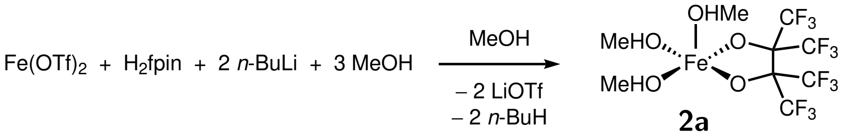

Starting materials: *n*-Butyllithium in hexanes, iron(II) triflate, methanol, *n*-pentane, perfluoropinacol.

Procedure: Perfluoropinacol (706 mg, 1.32 mL, 7.14 mmol) was added to a solution of iron(II) triflate (2.53 g, 7.14 mmol) in methanol (25 mL). *n*-Butyllithium (1.6 M in hexanes, 8.93 mL, 14.3 mmol) was added dropwise, while the solution was cooled to 0 °C. Upon addition of the base, the raw product forms as a colorless precipitate. The solution was concentrated *in vacuo* to a volume of approximately 20 mL and decanted off the precipitate. The solid was recrystallized by dissolving in methanol (95 mL) at 60 °C and slowly being cooled to 7 °C. The solid was separated from the solution by decantation, washed with cold methanol (3 mL) and *n*-pentane (2 mL) and dried *in vacuo*.

Empirical Formula:	$C_9H_{12}F_{12}FeO_5$ (484.02 g mol^{-1}, **2a**).
Yield:	712 mg (1.47 mmol), 21% of th., colorless crystals.
Elemental analysis:	found (calcd.): C 22.13% (22.33%), H 2.35% (2.50%), N 0% (0%).
IR: (solid, ATR)	$\tilde{\nu}$ = 2965 (w), 2192 (w), 1366 (w), 1223 (vs), 1182 (vs), 1144 (vs), 1110 (m), 1012 (s), 977 (m), 937 (s), 870 (s), 760 (w), 740 (m), 714 (s) cm^{-1}.
UV/Vis: (solution, MeOH)	λ = 244 nm.

5.6.2 [Fe(fpin)(EtOH)$_3$] · EtOH (2b · EtOH)

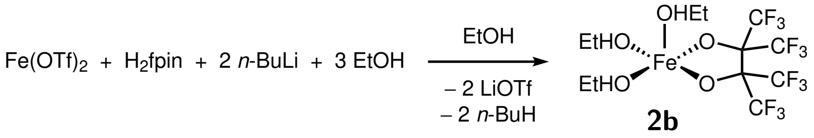

Starting materials: *n*-Butyllithium in hexanes, ethanol, iron(II) triflate, *n*-pentane, perfluoropinacol.

Procedure: Perfluoropinacol (127 mg, 0.237 mL, 1.29 mmol) was added to a solution of iron(II) triflate (457 mg, 1.29 mmol) in ethanol (2.5 mL). *n*-Butyllithium (1.6 M in hexanes, 1.61 mL, 2.58 mmol) was added dropwise while the solution was cooled to 0 °C. The solution was concentrated *in vacuo* to a volume of approximately 1 mL and decanted off the precipitate. The solid was recrystallized in ethanol. The solid was separated from the solution by decantation, washed with cold ethanol (3 × 1 mL) and *n*-pentane (1 mL) and dried *in vacuo*. The product was obtained as **2b** · EtOH.

Empirical Formula:	$C_{14}H_{21}F_{12}FeO_6$ (569.14 g mol^{-1}, **2b** · EtOH)
Yield:	389 mg (684 µmol), 53% of th., colorless crystals.
Elemental analysis:	found (calcd.): C 27.74% (27.98%), H 3.73% (3.97%), N 0% (0%).
IR: (solid, ATR)	$\tilde{\nu}$ = 2990 (w), 1454 (w), 1383 (w),1227 (vs), 1197 (vs), 1179 (vs), 1142 (s), 1107 (s), 1086 (m), 1038 (s) 982 (w), 937 (s), 868 (s), 810 (w), 760 (m), 740 (s), 714 (s), 686 (w) cm^{-1}.
UV/Vis: (solution, EtOH)	λ = <350, 652, 867 nm.

5.7 Synthesis of dinuclear perfluoropinacolatoiron(II) compounds

5.7.1 $[Fe_2(fpin\text{-}1\kappa O{:}1,1'\kappa O')_2(H_2O)_4] \cdot 2\,H_2O$ (3a · $2\,H_2O$)

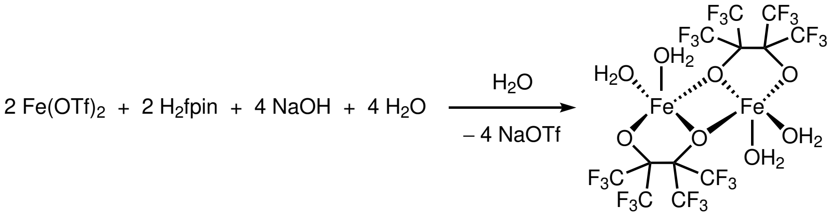

3a

Starting materials: Iron(II) triflate, *n*-pentane, perfluoropinacol, sodium hydroxide, water.
Procedure: Perfluoropinacol (99.8 mg, 53.4 µL, 290 µmol) was added to a solution of iron(II) triflate (103 mg, 290 µmol) in water (1 mL). Sodium hydroxide (23.2 mg, 580 µmol) was then added, leading to the formation of a colorless crystalline precipitate. The solution was decanted off and the solid was washed with *n*-pentane (3 × 1 mL). The product was obtained as **3a** · $2\,H_2O$.

Empirical Formula:	$C_{12}H_8F_{24}Fe_2O_{10}$ (883.92 $g\,mol^{-1}$, **3a** · $2\,H_2O$).
Yield:	82.4 mg (93.2 µmol), 64% of th., colorless crystals.
Elemental analysis:	found (calcd.): C 13.38% (17.00%), H 1.13% (0.95%), N 0% (0%), S 9.64% (0%).
IR: (solid, ATR)	$\tilde{\nu}$ = 3674 (w), 1841 (w), 1625 (w), 1225 (s), 1200 (s), 1153 (s), 1096 (s), 1037 (m), 984 (m), 939 (s), 875 (s), 843 (m), 761 (m), 742 (s), 733 (s), 714 (s), 677 (s), 667 (s) cm^{-1}.
UV/Vis: (solution, H_2O)	λ = 208, 291, 970 nm.

5.7.2 [Fe$_2$(fpin-1κ*O*:1,1′κ*O*′)$_2$(MeCN)$_4$] (3b)

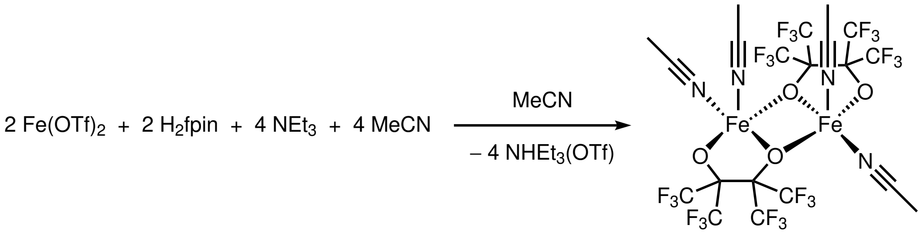

3b

Starting materials: Acetonitrile, iron(II) triflate, perfluoropinacol, triethylamine.
Procedure: Iron(II) triflate (2.24 g, 6.34 mmol) was dissolved in acetonitrile (10 mL). To this solution perfluoropinacol (1.17 mL, 2.19 g, 6.34 mmol) and triethylamine (1.77 mL, 12.7 mmol) were successively added. The reaction mixture was concentrated *in vacuo* to a volume of approximately 10 mL, leading to the formation of a pale violet precipitate. The solution was heated to 70 °C and slowly cooled to 7 °C, accompanied by the formation of pale violet crystals. The solution was decanted off and the remaining solid was washed with acetonitrile (2 mL) and *n*-pentane (2 mL).

Empirical Formula:	$C_{22}H_{18}F_{24}Fe_2N_4O_4$ (970.04 g mol^{-1}, **3b**).
Yield:	2.16 g (2.23 mmol), 70% of th., pale violet crystals.
Elemental analysis:	found (calcd.): C 25.72% (25.56%), H 1.42% (1.29%), N 5.88% (5.96%).
IR: (solid, ATR)	$\tilde{\nu}$ = 2320 (w), 2290 (w), 1379 (w), 1225 (vs), 1188 (vs), 1146 (vs), 1132 (s), 1115 (s), 1034 (m), 975 (w), 935 (s), 866 (s), 758 (m), 739 (s), 718 (s), 684 (m) cm^{-1}.
UV/Vis: (solution, MeCN)	λ = 250, 832 nm.

5.7.3 [Fe_2(fpin-1κ*O*:1,1′κ*O*′)$_2$(PhCN)$_4$] (3c)

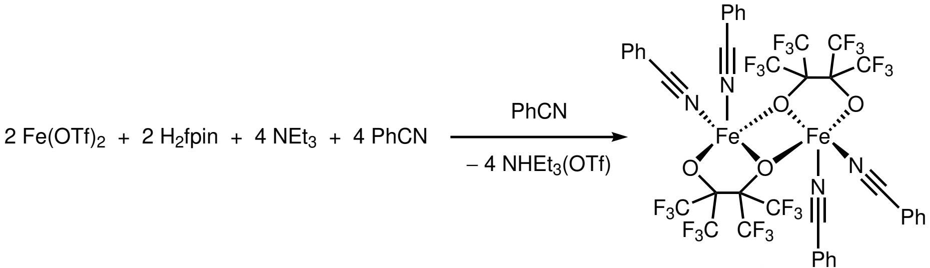

3c

Starting materials: Benzonitrile, iron(II) triflate, *n*-pentane perfluoropinacol, triethylamine, toluene.

Procedure: Iron(II) triflate (327 mg, 924 µmol) was dissolved in benzonitrile (10 mL). Perfluoropinacol (382 mg, 924 µmol) and triethylamine (187 mg, 1.85 mmol) were consecutively added to the solution, giving a violet suspension with a colorless precipitate. After the solution was warmed to 60 °C for 2 h, the suspension turned orange with a bright green crystalline solid. The liquid phase was decanted off and the product was recrystallized in toluene (10 mL) by cooling very slowly from 60 °C to 7 °C. After removal of the supernatant solution, the remaining solid was washed with *n*-pentane (3 × 5 mL) and dried *in vacuo*.

Empirical Formula: $C_{40}H_{20}F_{24}Fe_2N_4O_4$ (1188.28 g mol^{-1}, **3c**).

Yield: 371 mg (312 µmol), 68% of th., light green crystals.

Elemental analysis: found (calcd.): C 40.15% (40.43%), H 1.78% (1.70%), N 4.71% (4.72%).

IR: (solid, ATR) $\tilde{\nu}$ = 2262 (w), 1597 (w), 1490 (w), 1450 (w), 1256 (m), 1230 (s), 1211 (vs), 1177 (vs), 1140 (vs), 1112 (s), 1070 (m), 1028 (m), 989 (m), 966 (m), 937 (s), 864 (s), 756 (s), 739 (s), 730 (m), 717 (s), 682 (s), 655 (m) cm^{-1}.

UV/Vis: (solid, $BaSO_4$) λ = <400, 835 nm.

5.7.4 [Fe_2(fpin-1κ*O*:1,1′κ*O*′)$_2$(thf)$_4$] (3d)

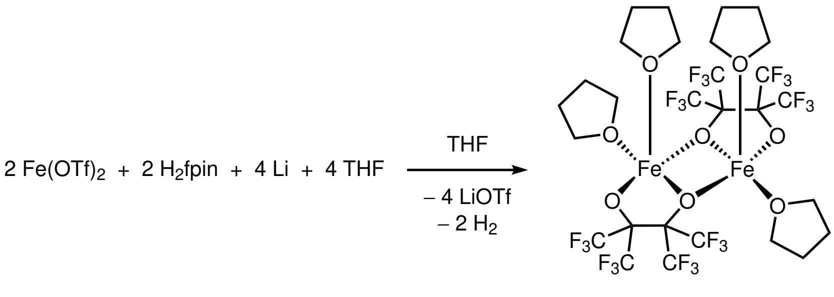

3d

Starting materials: Iron(II) triflate, lithium, perfluoropinacol, tetrahydrofurane.

Procedure: Perfluoropinacol (333 µL, 623 mg, 1.81 mmol) was added to a suspension of iron(II) triflate (640 mg, 1.81 mmol) in tetrahydrofurane (5 mL). While cooling to 0 °C lithium granules (25.1 mg, 3.62 mmol) were added, leading to the formation of hydrogen beside precipitation of a black solid. The reaction mixture was heated to 65 °C for 1 h, filtrated and concentrated to a volume of approximately 0.5 mL. After 14 d of storage at 7 °C, the formation of few colorless crystals could be observed. The supernatant solution was decanted off and the remaining solid was dried *in vacuo*.

Empirical Formula:	$C_{28}H_{32}F_{24}Fe_2O_8$ (1064.04 g mol^{-1}, **3d**).
Yield:	37 mg (34.8 µmol), 3.8% of th., colorless crystals.
Elemental analysis:	found (calcd.): C 28.44% (31.60%), H 3.18% (3.03%), N 0% (0%), S 7.57% (0%).
IR: (solid, ATR)	$\tilde{\nu}$ = 2986 (w), 2891 (w), 1463 (w), 1272 (s), 1277 (vs), 1173 (vs), 1115 (m), 1038 (s), 987 (w), 934 (m), 869 (s), 760 (w), 740 (m), 717 (m), 687 (w) cm^{-1}.

5.8 Synthesis of aquanitrosyliron compounds

5.8.1 $[Fe(H_2O)_5(NO)][Ga(fpin)_2(H_2O)]_2 \cdot 8.34\,H_2O$ (4a · $8.34\,H_2O$)

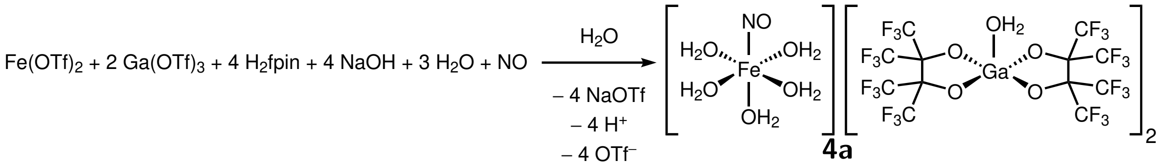

4a

Starting materials: Gallium(III) triflate, iron(II) triflate, nitric oxide, perfluoropinacol, sodium hydroxide.

Procedure: To a solution of gallium(III) triflate (888 mg, 1.70 mmol) in water (0.5 mL) an aqueous solution of iron(II) triflate (38.5%, 590 µL, 850 µmol) was added. After addition of perfluoropinacol (626 µL, 1.17 g, 3.40 mmol) the solution was treated with sodium hydroxide (136 mg, 3.4 mmol). While stirring vigorously, the argon atmosphere was replaced with nitric oxide. Within 48 h at 7 °C brown crystals of $[Fe(H_2O)_5(NO)][Ga(fpin)_2(H_2O)]_2 \cdot 8.34\,H_2O$ could be observed and filtered off the solution. The product is only stable under nitric-oxide atmosphere and was therefore stored in such. Prolonged exposure to atmospheres devoid of nitric oxide lead to the decomposition of the product. The product was obtained as **4a** · $8.34\,H_2O$.

Empirical Formula:	$C_{24}H_{30.67}F_{48}FeGa_2NO_{24.34}$ ($1829.83\,g\,mol^{-1}$, **4a** · $8.34\,H_2O$)
Yield:	730 mg (399 µmol), 47% of th., brown crystals.
Elemental analysis:	found (calcd.): C 14.81% (15.75%), H 1.63% (1.69%), N 0.45% (0.77%), S 10.52% (0%).
IR: (solid, ATR)	$\tilde{\nu}$ = 3667 (w), 3359 (m, br), 1843 (w, NO), 1623 (m), 1227 (vs), 1195 (vs), 1143 (vs), 1109 (s), 1032 (m), 987 (m), 948 (vs), 875 (vs), 763 (s), 743 (vs), 716 (vs), 687 (s), 661 (s) cm^{-1}.
UV/Vis: (solid, $BaSO_4$)	λ = <300, 336, 452, 589, 759 nm.
Mößbauer: (solid, 4.2 K, α-Fe)	$\delta\,/\,mm\,s^{-1}$ [$|\Delta E_Q|\,/\,mm\,s^{-1}$] = 1.39(4) [3.12(9)], 0.81(3) [2.23(4)], 0.16(9) [0].

5.8.2 $[Fe(H_2O)_5(NO)][Fe(fpin)_2(H_2O)]_2 \cdot 8.31\,H_2O$ (4b · $8.31\,H_2O$)

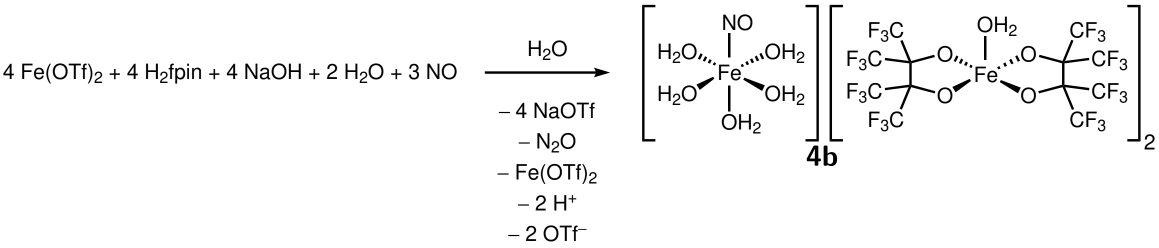

Starting materials: Iron(II) triflate, nitric oxide, perfluoropinacol sodium hydroxide, water
Procedure: Iron(II) triflate (344 mg, 971 µmol) was dissolved in water (1 mL). After addition of perfluoropinacol (179 µL, 334 mg, 971 µmol) the solution was treated with sodium hydroxide (38.8 mg, 971 µmol). While stirring vigorously the argon atmosphere was replaced with nitric oxide. Nitric oxide was introduced and immediately led to a red color, which was then quickly replaced by a greenish brown color. Within 48 h at 7 °C brown crystals of $[Fe(H_2O)_5(NO)][Fe(fpin)_2(H_2O)]_2 \cdot 8.31\,H_2O$ could be observed and filtered off the solution. The product is only stable under nitric-oxide atmosphere and was therefore stored in such. Prolonged exposure to atmospheres devoid of nitric oxide lead to the decomposition of the product. The product was obtained as **4b** · $8.31\,H_2O$.

Empirical Formula:	$C_{24}H_{30.62}F_{48}Fe_3NO_{24.31}$ ($1801.58\,g\,mol^{-1}$, **4b** · $8.31\,H_2O$).
Yield:	223 mg (124 µmol), 38% of th., brown crystals.
Elemental analysis:	found (calcd.): C 15.61% (16.07%), H 2.10% (1.57%), N 0.49% (0.78%).
IR: (solid, ATR)	$\tilde{\nu}$ = 3674 (w), 3294 (w, br), 1841 (w, NO), 1650 (m), 1625 (m), 1225 (vs), 1200 (vs), 1153 (s), 1096 (vs), 1037 (m), 984 (m), 939 (s), 875 (s), 843 (m), 761 (s), 742 (s), 733 (s), 714 (s), 677 (s), 667 (s) cm^{-1}.
UV/Vis: (solid, $BaSO_4$)	λ = 253, 322, 459, 581, 758, 886 nm.
Mößbauer: (solid, 4.2 K, α-Fe)	$\delta\,/\,mm\,s^{-1}$ [$\lvert\Delta E_Q\rvert\,/\,mm\,s^{-1}$] = 0.187(7) [1.70(2)], 0.655(3) [2.031(8)], 1.076(5) [3.464(10)], 0.274(2) [0.727(6)].

5.8.3 $[\{Fe(H_2O)(NO)(\mu\text{-}ox)\}_{n/n}] \cdot H_2O$ (5 · H_2O)

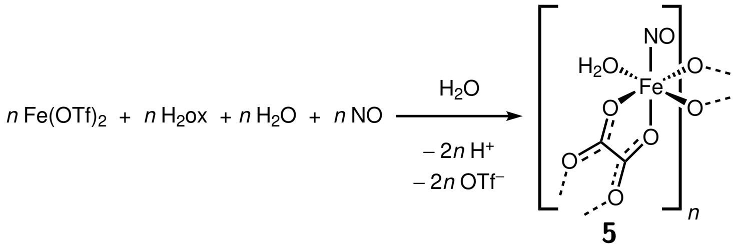

5

Starting materials: Iron(II) triflate, nitric oxide, oxalic acid, water.
Procedure: Oxalic acid (18.7 mg, 208 µmol) and iron(II) triflate (73.6 mg, 208 µmol) were dissolved in water (8 mL), yielding a yellow precipitate of iron(II) oxalate. The suspension was thoroughly stirred and put under an atmosphere of nitric oxide. In the course of the fumigation with nitric oxide the solution turned olive green, while the precipitate slowly dissolved in the course of 24 h. After two weeks the formation of small brown needles was observed. Crystals fit for single-crystal X-ray diffraction were obtained after three months. The product was obtained as $[\{Fe(H_2O)(NO)(\mu\text{-}ox)\}_{n/n}] \cdot H_2O$ and showed to be only stable under nitric-oxide atmosphere. Prolonged exposure to atmospheres devoid of nitric oxide lead to decomposition of the product.

Empirical Formula:	$(C_2H_4FeNO_7)_n$ (209.90 g mol^{-1} n^{-1}, **5**).
Yield:	n.a, brown crystals.
IR: (solid, ATR)	$\tilde{\nu}$ = 3331 (s), 2109 (w), 1823 (w, NO), 1632 (s), 1348 (w), 1308 (w), 1183 (w), 1032 (w) cm^{-1}.

5.9 Synthesis of triethylammonium nitrosylbis(perfluoropinacolato)ferrate

5.9.1 $(NHEt_3)_2[Fe(fpin)_2(NO)]$ (6)

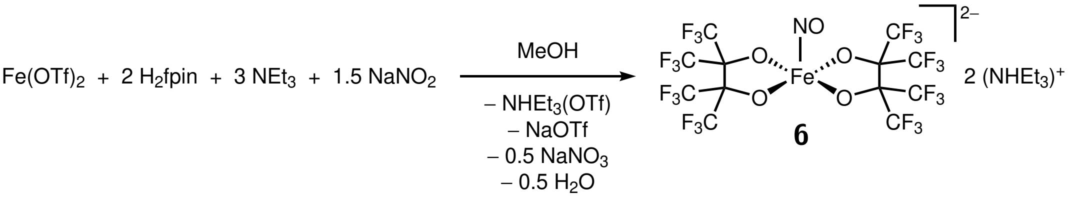

Starting materials: Iron(II) triflate, methanol, perfluoropinacol, sodium nitrite, triethylamine, water.

Procedure: To a solution of iron(II) triflate (435 mg, 1.23 mmol) in methanol (5 mL) perfluoropinacol (848 mg, 453 µL, 2.46 mmol) was added. The solution was treated with triethylamine (515 µL, 3.69 mmol), inducing the formation of a lavender precipitate. Addition of sodium nitrite (127 mg, 1.85 mmol) led to a color change of the reaction mixture to burgundy. Water (24 mL) was then immediately added, fully precipitating the product. After filtration the burgundy solid was washed with water (3 × 5 mL) and dried *in vacuo*. Yield: 915 mg (959 µmol, 78% of th.).

Alternative:

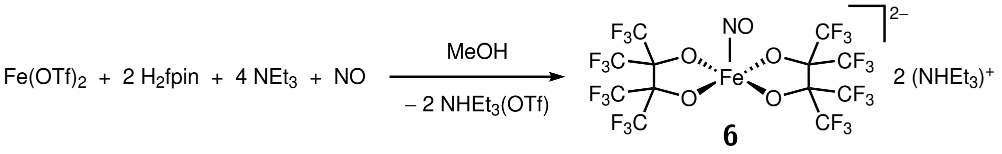

Starting materials: Iron(II) triflate, methanol, nitric oxide, perfluoropinacol, triethylamine, water.

Alternative procedure: Perfluoropinacol (333 mg, 178 µL, 968 µmol) was added to a solution of iron(II) triflate (171 mg, 484 µmol) in methanol (24 mL). After treatment with triethylamine (270 µL, 1.93 mmol) the solution turned blue, which was accompanied by the formation of a lavender precipitate. The suspension was vigorously stirred in an atmosphere of nitric oxide, leading to a color change of both solution and precipitate to burgundy. The nitric-oxide atmosphere was removed and water (24 mL) was added to the reaction mixture. After filtration the burgundy product was washed with water (3 × 5 mL) and dried *in vacuo*. Crystals fit for single-crystal X-ray diffraction were obtained after recrystallization of the product in methanol. Yield: 324 mg (340 µmol, 70% of th.).

Empirical Formula: $C_{24}H_{32}F_{24}FeN_3O_5$ (954.34 g mol^{-1}, **6**).

Yield: 915 mg (959 µmol), 78% of th., burgundy crystals.

Elemental analysis: found (calcd.): C 29.69% (30.21%), H 3.32% (3.38%), N 4.04% (4.40%).

IR: (solid, ATR) $\tilde{\nu}$ = 3356 (w, br), 2996 (w), 2952 (w), 2833 (w), 2659 (w), 2498 (w), 1739 (m, NO), 1481 (m), 1467 (m), 1449 (w), 1392 (m), 1370 (w), 1254 (m), 1225 (s), 1198 (s), 1169 (s), 1156 (s), 1145 (s), 1125 (s), 1104 (s), 1078 (m), 1061 (m), 1016 (m), 985 (m), 962 (w), 930 (s), 863 (s), 843 (m), 814 (w), 782 (w), 757 (m), 740 (s), 730 (m), 712 (s), 670 (m) cm^{-1}.

UV/Vis: (solid, $BaSO_4$) λ = 251, 300, 352, 575 nm.

5.10 Synthesis of neutral nitrosylperfluoropinacolatoiron compounds

5.10.1 [Fe(fpin)(MeOH)$_2$(NO)] (7a)

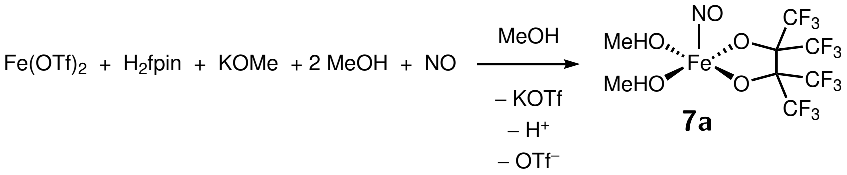

Starting materials: Iron(II) triflate, methanol, nitric oxide, perfluoropinacol, potassium methoxide.

Procedure: Iron(II) triflate (581 mg, 1.64 mmol) was dissolved in methanol (10 mL) and treated with perfluoropinacol (303 µL, 566 mg, 1.64 mmol). After addition of potassium methoxide (25% in methanol, 485 µL, 1.64 mmol) a white crystalline solid slowly precipitated. Introduction of nitric oxide led to a change of the reaction mixture's color to red accompanied by crystallization of red rods of **7a** · MeOH.

Empirical Formula: $C_9H_{12}F_{12}FeNO_6$ (514.05 g mol^{-1}, **7a** · MeOH).

Yield: n.a., red crystals.

IR: (solid, ATR) $\tilde{\nu}$ = 3533 (m), 2962 (s), 2849 (s), 1801 (m, NO), 1477 (s), 1385 (m), 1247 (vs), 1228 (vs), 1190 (s), 1169 (vs), 1114 (m), 1027 (s), 1008 (s), 942 (m), 871 (m), 768 (m), 759 (m), 740 (m), 714 (m) cm^{-1}.

5.10.2 [Fe(fpin)(EtOH)$_2$(NO)] (7b)

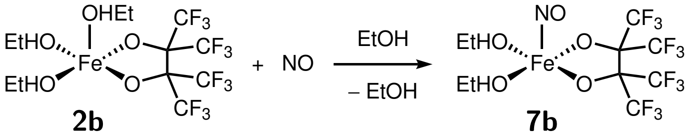

Starting materials: Ethanol, **2b**, nitric oxide.

Procedure: 2b (1.29 g, 2.26 mmol) was suspended in ethanol (1 mL) and treated with nitric oxide to yield a dark reddish brown reaction mixture. After 15 h at 7 °C red rods could be observed.

Alternative:

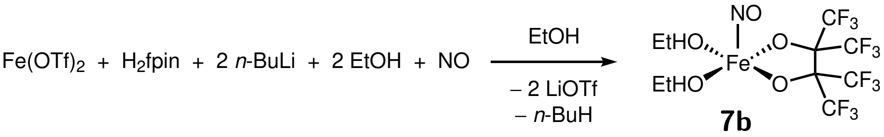

Starting materials: *n*-Butyllithium, ethanol, iron(II) triflate, nitric oxide, perfluoropinacol.

Alternative procedure: Iron(II) triflate (800 mg, 2.26 mmol) was dissolved in ethanol (15 mL) and treated with perfluoropinacol (417 mg, 779 µL, 2.26 mmol) and *n*-butyllithium (2.83 mL, 4.52 mmol). The solution was concentrated under reduced pressure until formation of a white precipitate was observed. Introduction of nitric oxide induced a change of color to red and formation of red rod-shaped crystals.

Empirical Formula:	$C_{10}H_{12}F_{12}FeNO_5$ (510.06 g mol^{-1}, **7b**).
Yield:	n.a., red crystals.
IR: (solid, ATR)	$\tilde{\nu}$ = 2988 (w), 1808 (m, NO), 1765 (w), 1641 (w), 1455 (w), 1389 (w), 1258 (m), 1225 (s), 1185 (s), 1141 (s), 1108 (s), 1091 (s), 1032 (s), 984 (m), 940 (s), 872 (s), 810 (m), 761 (m), 741 (s), 714 (s), 685 (m) cm^{-1}.

5.10.3 [{Fe$_2$(fpin-1κO, O')(MeOH-2κO)(NO-2κN)(OMe-1:2κO,1:2′κO,-1:2:2′κO)$_3$}$_2$] · 2 MeOH (8a · 2 MeOH)

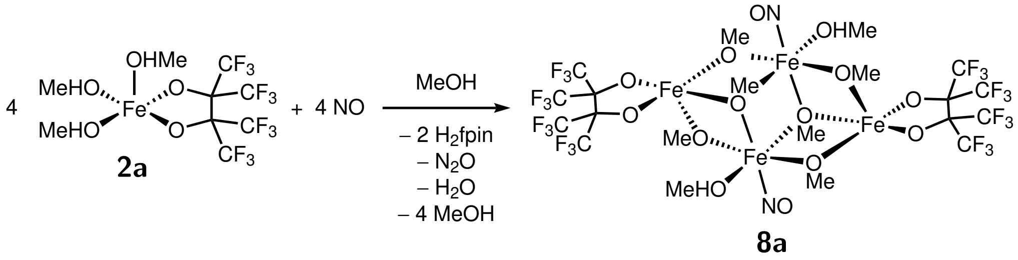

Starting materials: **2a**, methanol, nitric oxide

Procedure: **2a** (17 mg, 35.1 µmol) was dissolved in methanol (0.5 mL) and treated with gaseous nitric oxide, yielding a reddish brown solution. After cooling to 7 °C brown rod shaped crystals of **8a** form within 20 min. The product was obtained as **8a** · 2 MeOH.

Alternative:

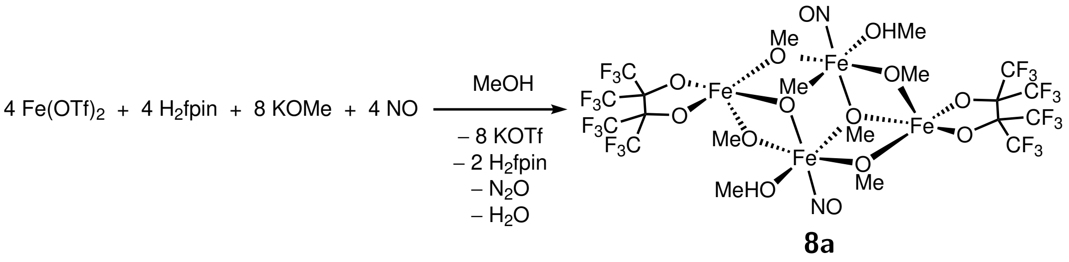

Starting materials: Iron(II) triflate, methanol, nitric oxide, perfluoropinacol, potassium methoxide.

Alternative procedure: To a methanolic solution of iron(II) triflate (20%, 106 µL, 56.9 µmol) perfluoropinacol (10.5 µL, 56.9 µmol) and potassium methoxide (31.9 mg, 114 µmol) were added, yielding a white precipitate. After introduction of gaseous nitric oxide the precipitate dissolved and the color of the solution changed to brown. After 20 min the formation of brown block shaped crystals could be observed. The product was obtained as **8a** · 2 MeOH.

Empirical Formula: $C_{22}H_{34}F_{24}Fe_4N_2O_{16}$ (1261.91 g mol^{-1}, **8a** · 2 MeOH.).

Yield: n.a., brown crystals.

IR: (solid, ATR) $\tilde{\nu}$ = 3350 (m, br), 3064 (w), 2947 (m), 2834 (m), 1765 (m, NO), 1585 (m), 1484 (m), 1436 (s), 1340 (w), 1315 (w), 1262 (vs), 1227 (s), 1188 (m), 1166 (m), 1142 (vs), 1107 (vs), 1072 (m), 1029 (vs), 996 (m), 937 (m), 871 (m), 855 (m), 810 (m), 752 (s), 721 (vs), 687 (vs) cm^{-1}.

5.10.4 [{$\mathrm{Fe_2}$(EtOH-2κ*O*)(fpin-1κ*O*, *O*′)(NO-2κ*N*)(OEt-1:2κ*O*,1:2′κ*O*)$_2$(OH-1:2:2′κ*O*)}$_2$] · 2 EtOH

(8b · 2 EtOH)

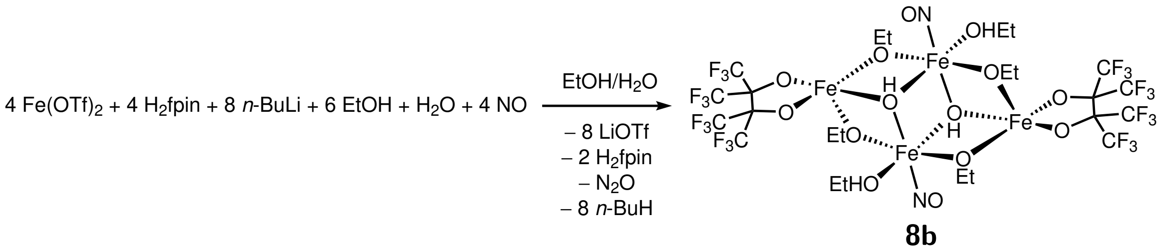

8b

Starting materials: *n*-Butyllithium, ethanol, iron(II) triflate, nitric oxide, perfluoropinacol.
Procedure: Iron(II) triflate (321 mg, 908 µmol) was added to a solution of perfluoropinacol in ethanol (5%, 6.81 mL, 908 µmol) and then treated with *n*-butyllithium (1.6 M in hexanes, 1.13 mL, 1.82 mmol) yielding a white precipitate. After introduction of gaseous nitric oxide the precipitate dissolved and the color of the solution changed to brown. After 20 min the formation of brown block shaped crystals could be observed. The product was obtained as **8b** · 2 EtOH.

Empirical Formula: $C_{28.2}H_{46.4}F_{24}Fe_4N_2O_{15.8}$ (1345.17 g mol^{-1}, **8b** · 2 EtOH).
Yield: n.a., brown crystals.
IR: (solid, ATR) $\tilde{\nu}$ = 3528 (w), 2985 (w), 1762 (w, NO), 1456 (w), 1425 (w), 1390 (w), 1363 (w), 1311 (m), 1286 (m), 1230 (vs), 1197 (vs), 1176 (vs), 1143 (s), 1105 (s), 1049 (s), 1024 (s), 991 (m), 938 (s), 873 (s), 808 (w), 763 (m), 742 (s), 733 (m), 717 (s), 684 (m) cm^{-1}.

5.10.5 $[\{\mathrm{Fe}(\mathrm{fpin}\text{-}1\kappa O{:}1,1'\kappa O')(\mathrm{NO})(\mathrm{PhCN})\}_2]$ (9)

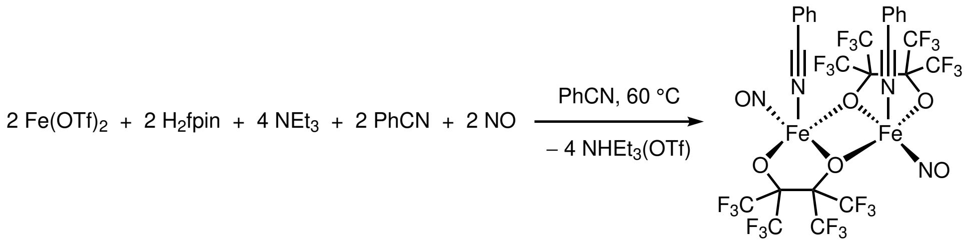

9

Starting materials: Benzonitrile, *n*-hexane, iron(II) triflate, nitric oxide, perfluoropinacol, toluene, triethylamine.

Procedure: Iron(II) triflate (665 mg, 1.88 mmol) was dissolved in benzonitrile (10 mL). To this solution perfluoropinacol (346 µL, 647 mg, 1.88 mmol) and triethylamine (380 mg, 3.76 mmol) were consecutively added, giving a violet suspension with a colorless precipitate. After the solution was warmed to 60 °C for 2 h the suspension turned orange with a bright green crystalline precipitate. While the reaction mixture still was heated, the atmosphere above the suspension was replaced by gaseous nitric oxide. This resulted in the solution changing color to deep brown after 1 min. A dark green crystalline precipitate formed shortly after. The suspension was filtrated and the solid was washed with toluene (3 × 3 mL) and *n*-hexane (3 × 3 mL) and was afterwards dried *in vacuo*. Dark green rod-shaped crystals suitable for single-crystal X-ray crystallography could directly be taken off the precipitate.

Empirical Formula: $C_{26}H_{10}F_{24}Fe_2N_4O_6$ ($1042.04\,\mathrm{g\,mol^{-1}}$, **9**).
Yield: 346 mg (332 µmol), 35.3% of th., dark green rod-shaped crystals.
Elemental analysis: found (calcd.): C 25.42% (29.97%), H 1.19% (0.97%), N 4.13% (5.38%).
IR: (solid, ATR) $\tilde{\nu}$ = 2278 (m), 1808 (s, NO), 1599 (w), 1492 (w), 1452 (w), 1257 (s), 1221 (s), 1190 (s), 1140 (s), 1104 (s), 1028 (m), 978 (m), 939 (s), 869 (s), 755 (s), 740 (s), 722 (s), 680 (s) $\mathrm{cm^{-1}}$.
UV/Vis: (solid, $BaSO_4$) λ = <400, 425, 614 nm.

6 Appendix

6.1 Packing diagrams of the crystal structures

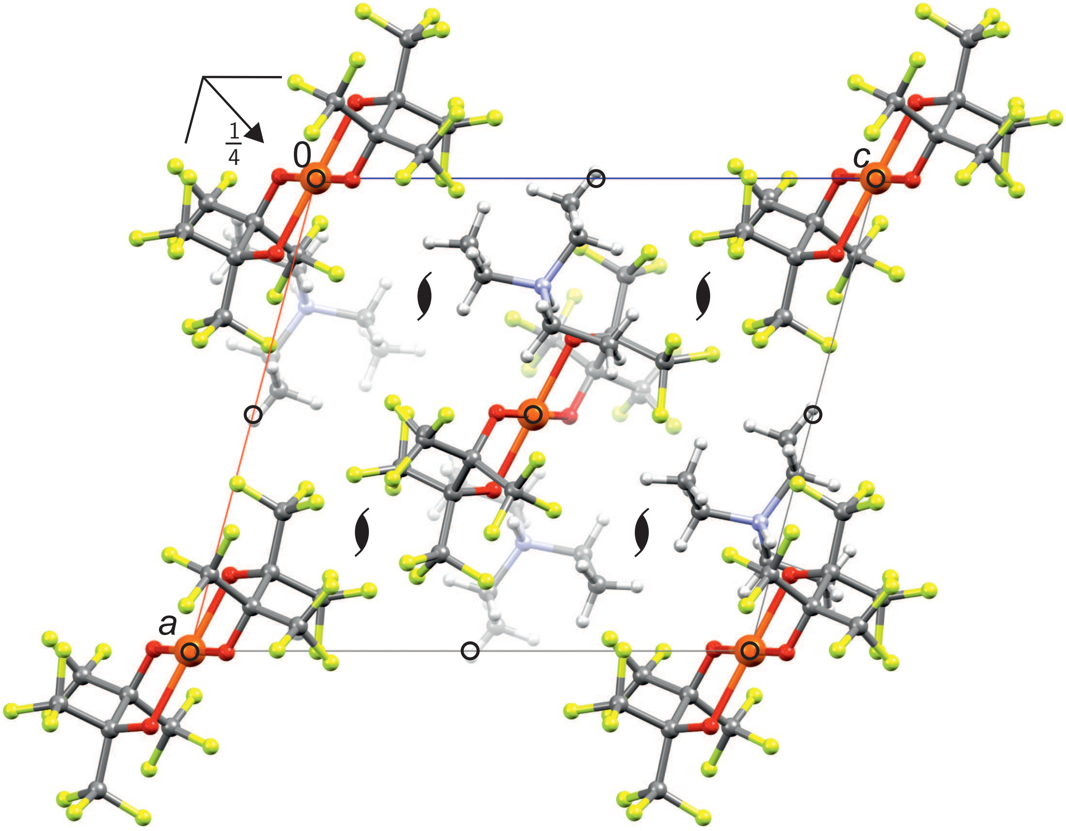

Figure 6.1: Packing diagram of **1a** in the monoclinic space group $P2_1/n$ with view along [010]. The symmetry elements of the space group $P2_1/n$ are overlaid. Atoms: carbon (gray), hydrogen (light gray), fluorine (green), iron (orange), nitrogen (blue), oxygen (red).

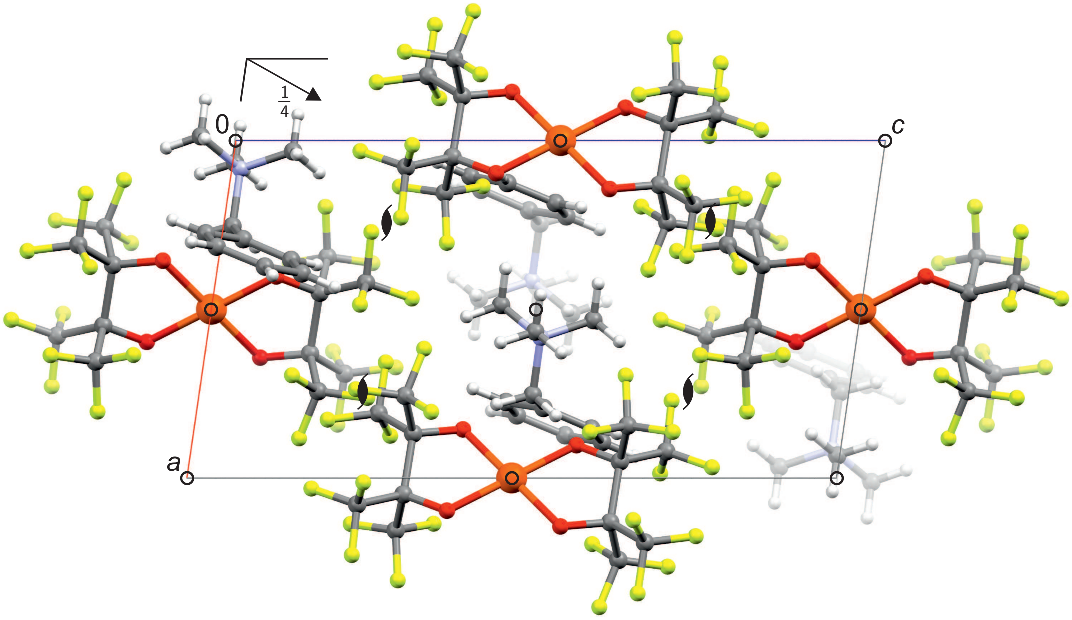

Figure 6.2: Packing diagram of **1b** in the monoclinic space group $P2_1/n$ with view along [010]. The symmetry elements of the space group $P2_1/n$ are overlaid. Atoms: carbon (gray), hydrogen (light gray), fluorine (green), iron (orange), nitrogen (blue), oxygen (red).

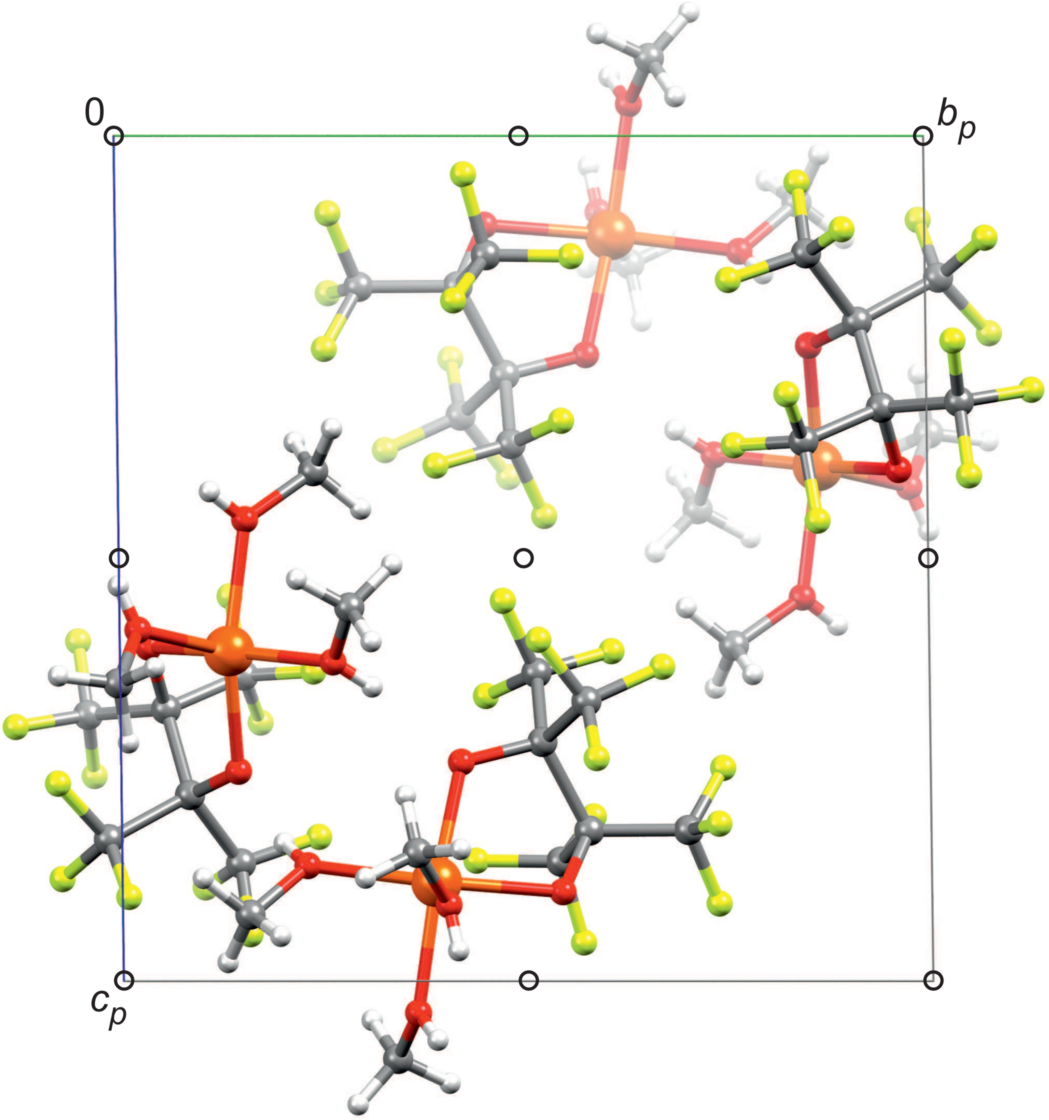

Figure 6.3: Packing diagram of **2a** in the triclinic space group $P\bar{1}$ with view along [100]. The symmetry elements of the space group $P\bar{1}$ are overlaid. Atoms: carbon (gray), hydrogen (light gray), fluorine (green), iron (orange), oxygen (red).

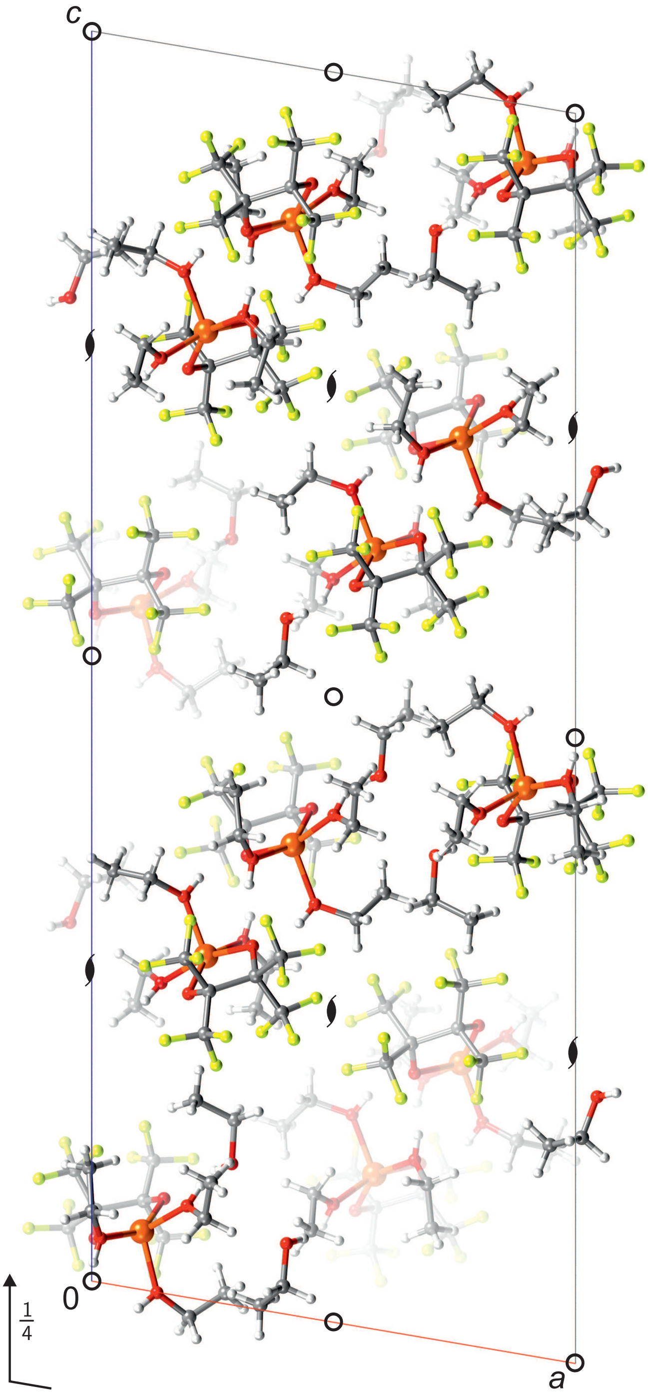

Figure 6.4: Packing diagram of **2b** · EtOH in the monoclinic space group $P2_1/c$ with view along [010]. The symmetry elements of the space group $P2_1/c$ are overlaid. Atoms: carbon (gray), hydrogen (light gray), fluorine (green), iron (orange), oxygen (red).

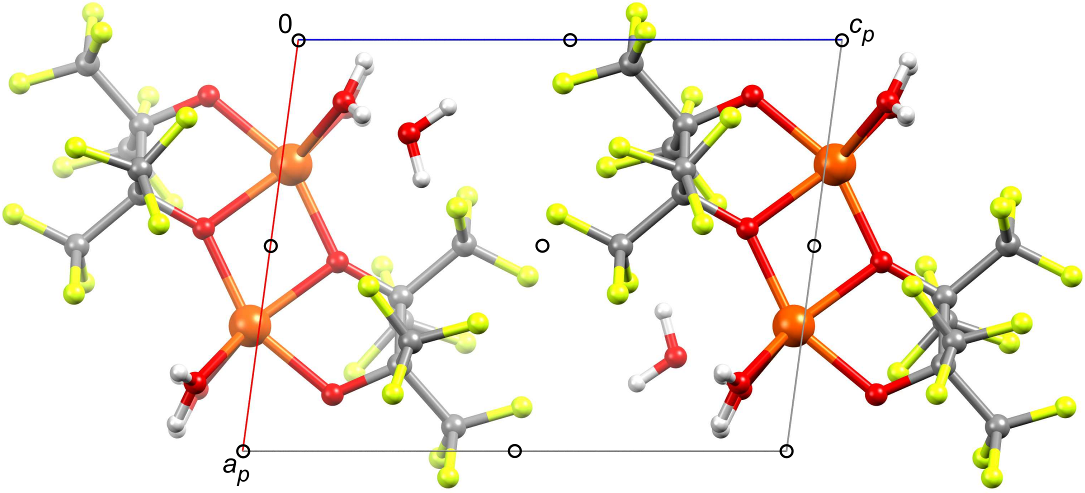

Figure 6.5: Packing diagram of **3a** $\cdot\ 2\,H_2O$ in the triclinic space group $P\bar{1}$ with view along [010]. The symmetry elements of the space group $P\bar{1}$ are overlaid. Atoms: carbon (gray), hydrogen (light gray), fluorine (green), iron (orange), oxygen (red).

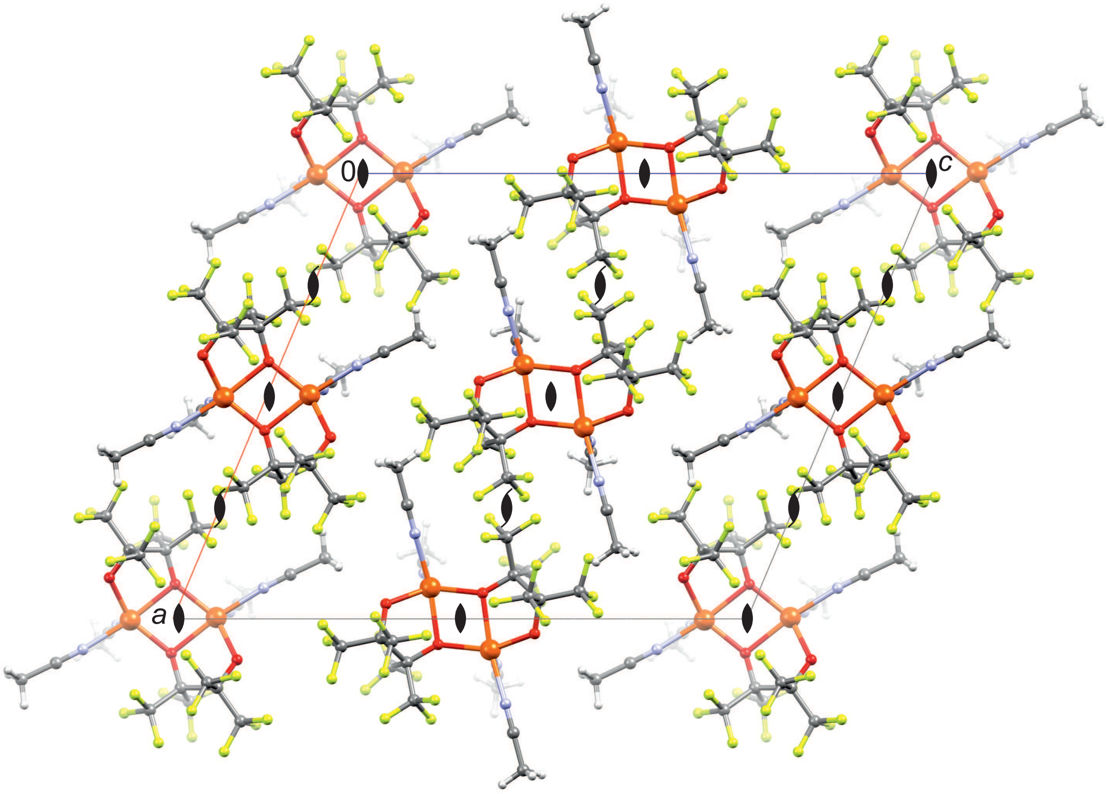

Figure 6.6: Packing diagram of **3b** in the monoclinic space group $C2$ with view along [010]. The symmetry elements of the space group $C2$ are overlaid. Atoms: carbon (gray), hydrogen (light gray), fluorine (green), iron (orange), nitrogen (blue), oxygen (red).

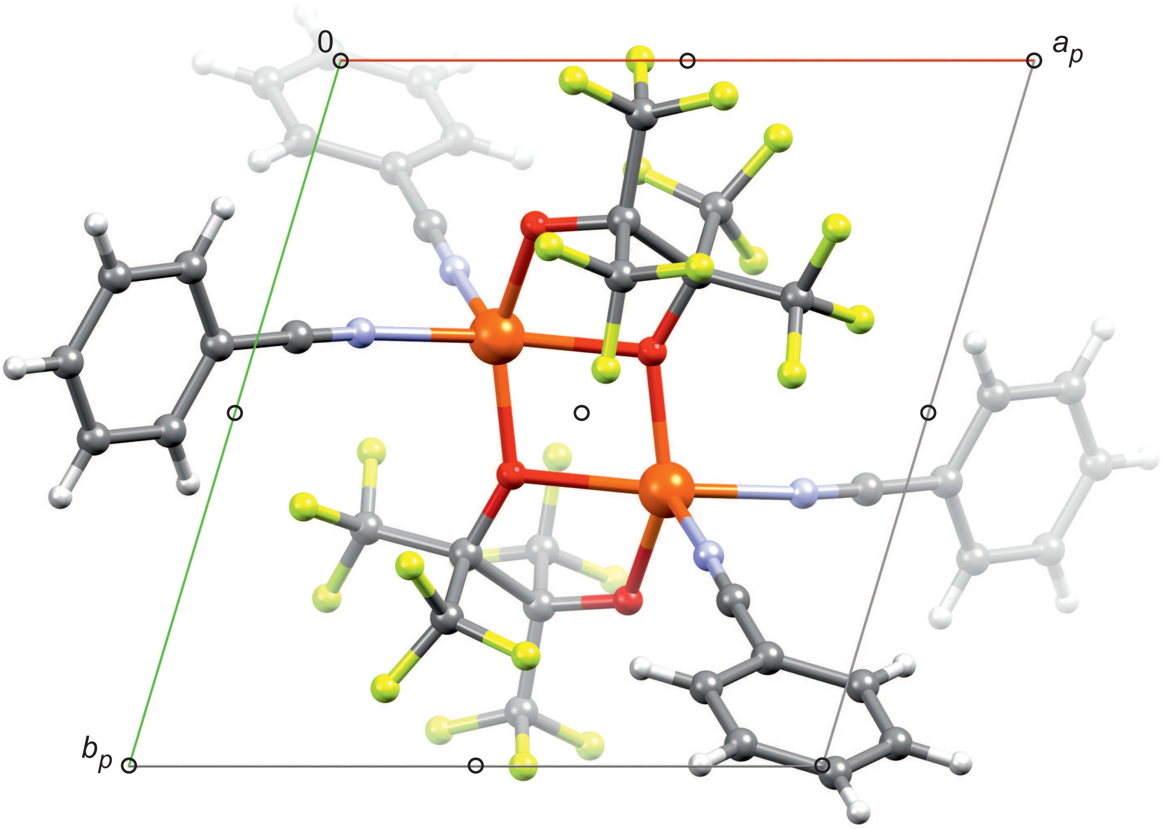

Figure 6.7: Packing diagram of **3c** in the triclinic space group $P\overline{1}$ with view along [001]. The symmetry elements of the space group $P\overline{1}$ are overlaid. Atoms: carbon (gray), hydrogen (light gray), fluorine (green), iron (orange), nitrogen (blue), oxygen (red).

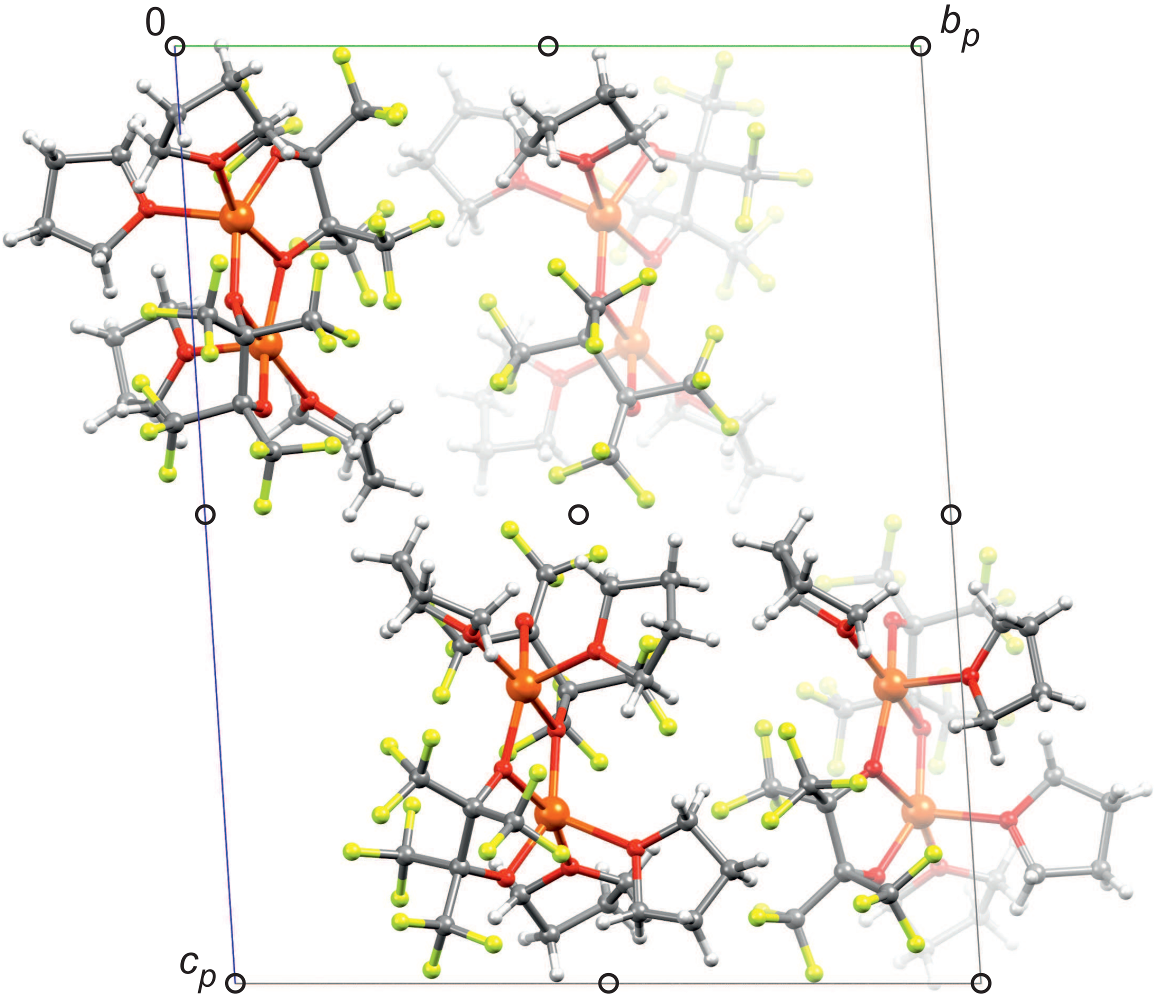

Figure 6.8: Packing diagram of **3d** in the triclinic space group $P\bar{1}$ with view along [100]. The symmetry elements of the space group $P\bar{1}$ are overlaid. Atoms: carbon (gray), hydrogen (light gray), fluorine (green), iron (orange), oxygen (red).

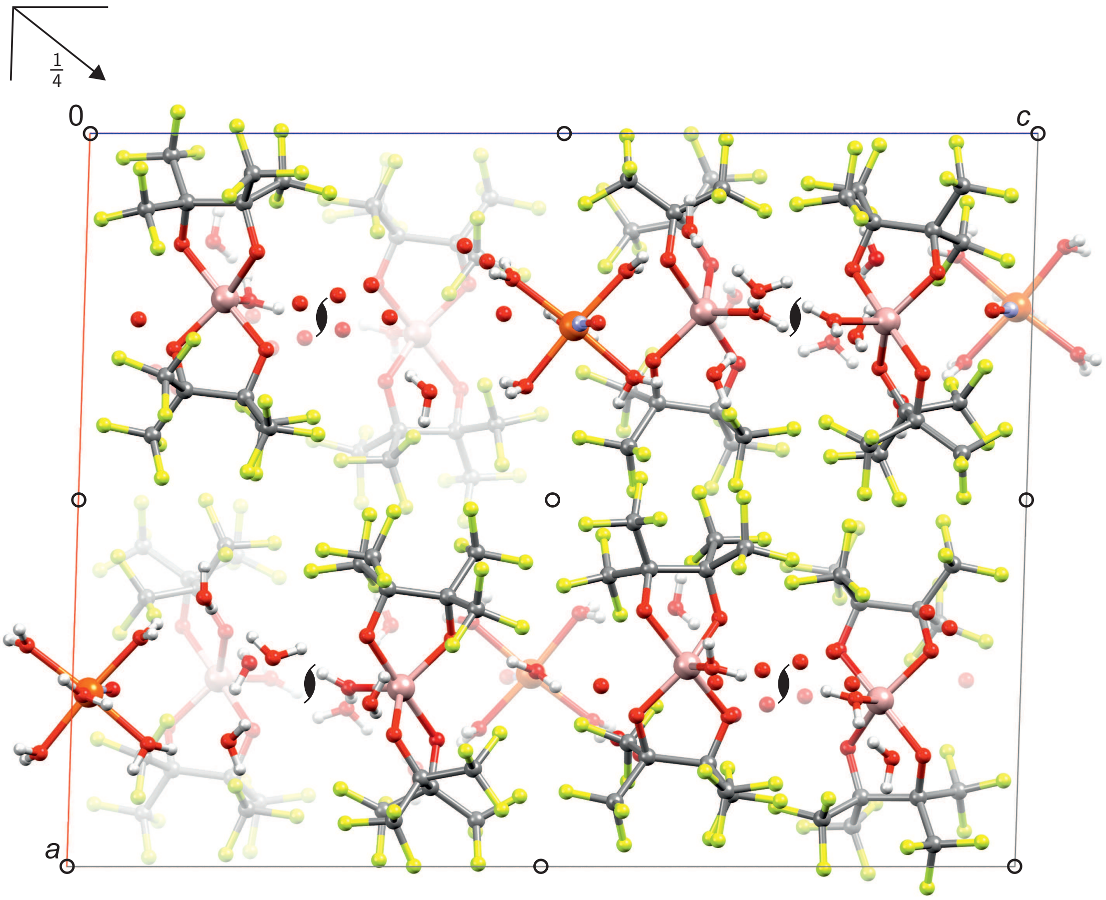

Figure 6.9: Packing diagram of **4a** $\cdot$ 8.34 H_2O in the monoclinic space group $P2_1/n$ with view along [010]. The symmetry elements of the space group $P2_1/n$ are overlaid. Atoms: carbon (gray), hydrogen (light gray), fluorine (green), gallium (rose), iron (orange), nitrogen (blue), oxygen (red).

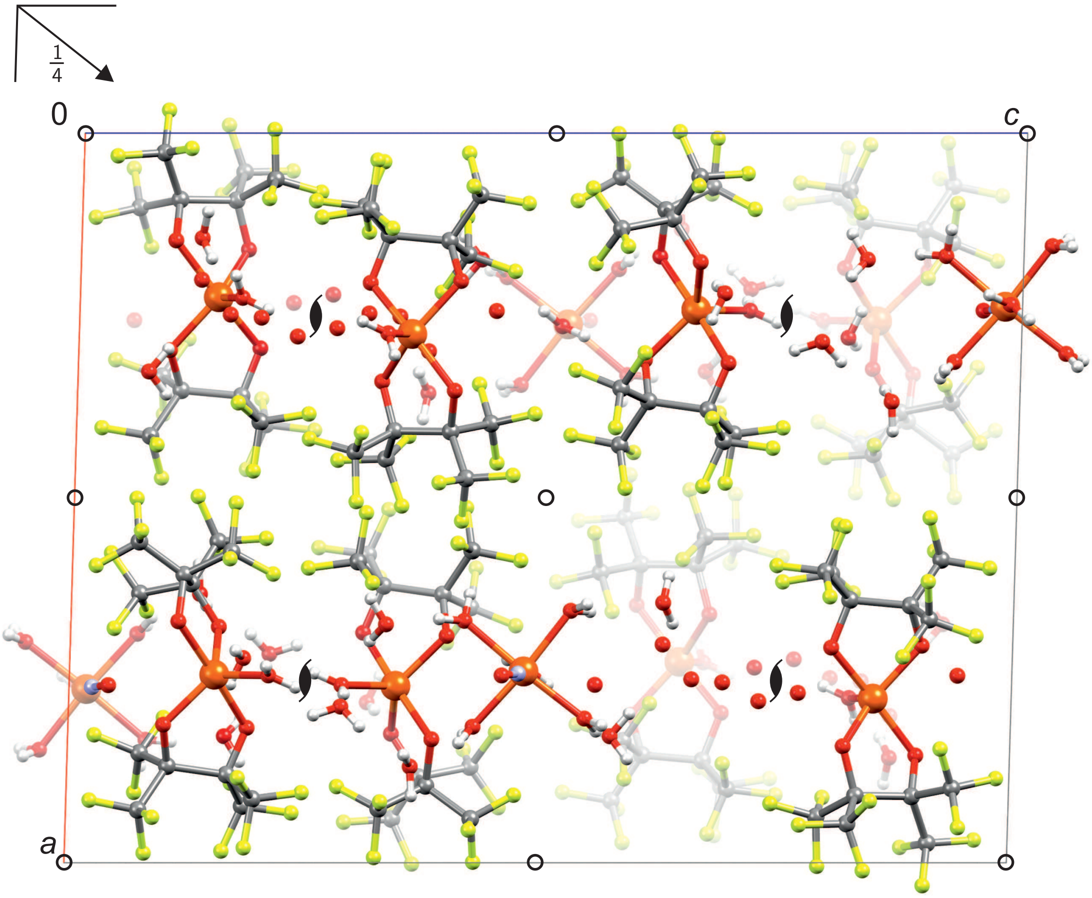

Figure 6.10: Packing diagram of **4b** · 8.31 H_2O in the monoclinic space group $P2_1/n$ with view along [010]. The symmetry elements of the space group $P2_1/n$ are overlaid. Atoms: carbon (gray), hydrogen (light gray), fluorine (green), iron (orange), nitrogen (blue), oxygen (red).

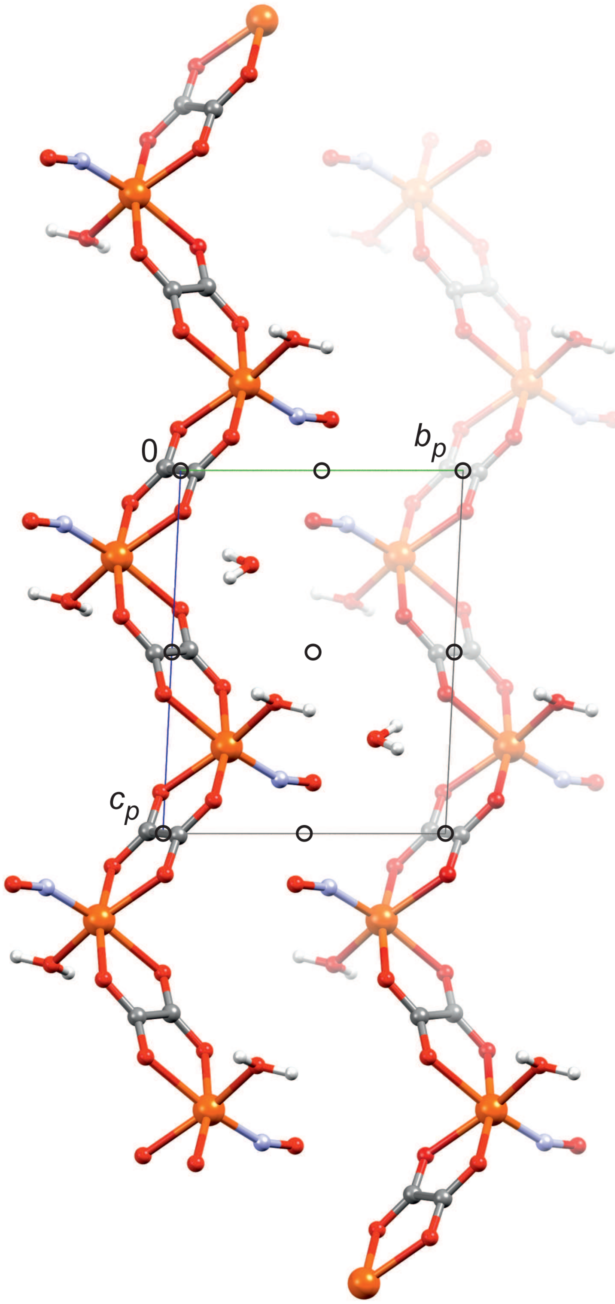

Figure 6.11: Packing diagram of **5** $\cdot$ H_2O in the triclinic space group $P\bar{1}$ with view along [100]. The symmetry elements of the space group $P\bar{1}$ are overlaid. Atoms: carbon (gray), hydrogen (light gray), iron (orange), nitrogen (blue), oxygen (red).

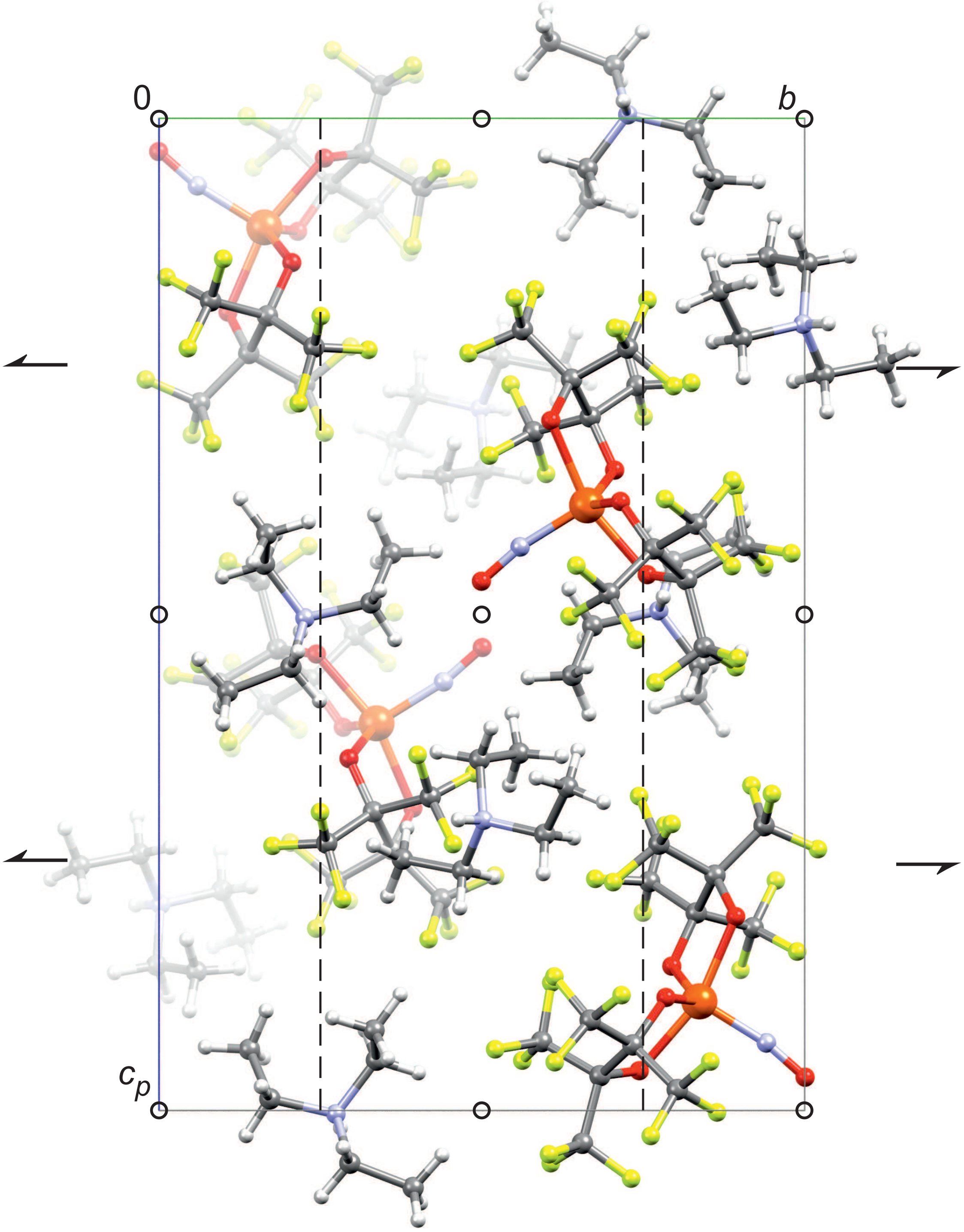

Figure 6.12: Packing diagram of **6** in the monoclinic space group $P2_1/c$ with view along [100]. The symmetry elements of the space group $P2_1/c$ are overlaid. Atoms: carbon (gray), hydrogen (light gray), fluorine (green), iron (orange), nitrogen (blue), oxygen (red).

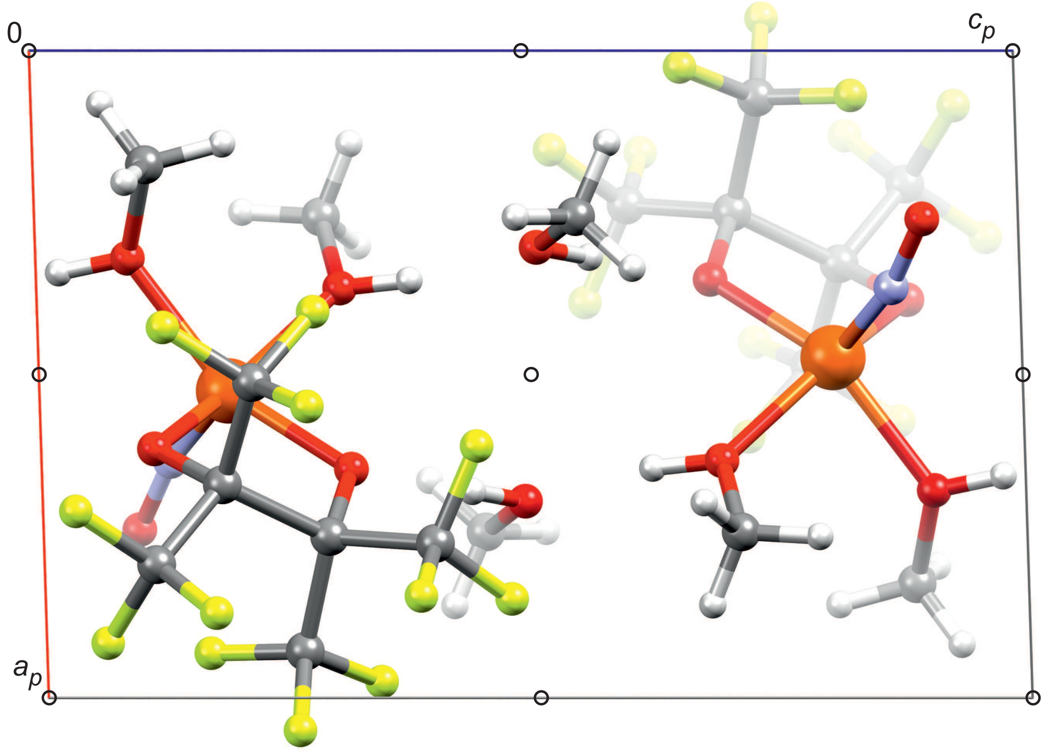

Figure 6.13: Packing diagram of **7a** · MeOH in the triclinic space group $P\bar{1}$ with view along [010]. The symmetry elements of the space group $P\bar{1}$ are overlaid. Atoms: carbon (gray), hydrogen (light gray), fluorine (green), iron (orange), nitrogen (blue), oxygen (red).

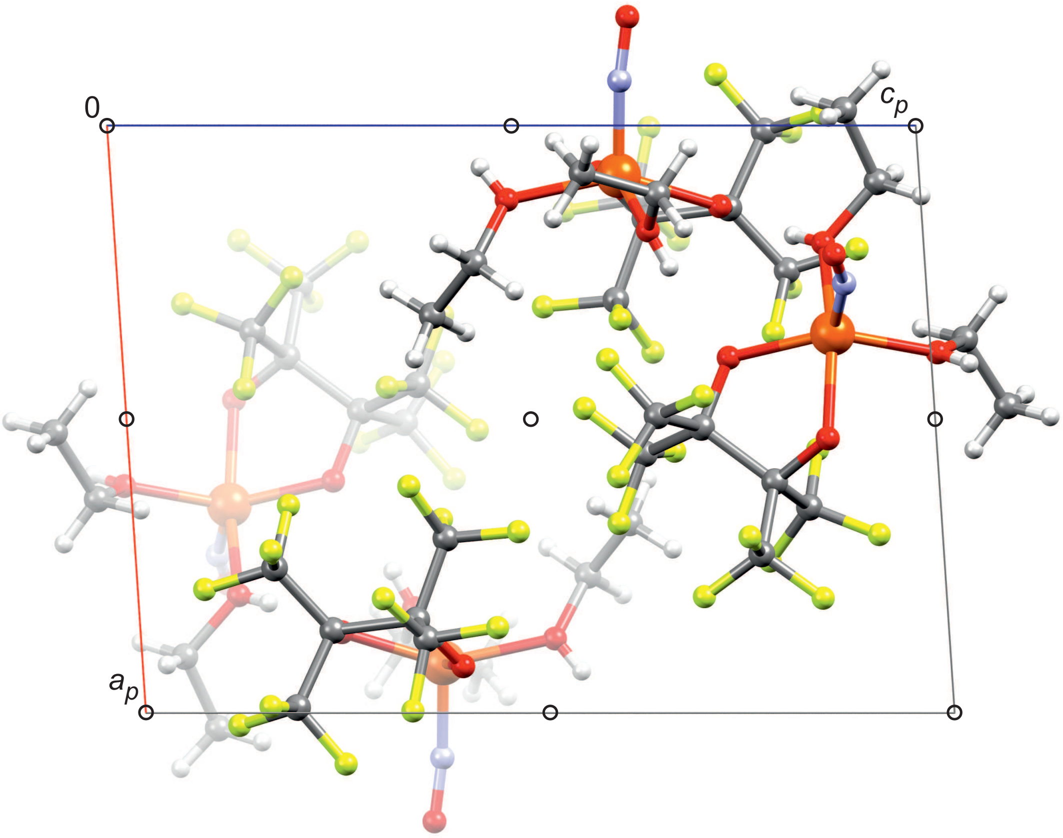

Figure 6.14: Packing diagram of **7b** in the triclinic space group $P\bar{1}$ with view along [010]. The symmetry elements of the space group $P\bar{1}$ are overlaid. Atoms: carbon (gray), hydrogen (light gray), fluorine (green), iron (orange), nitrogen (blue), oxygen (red).

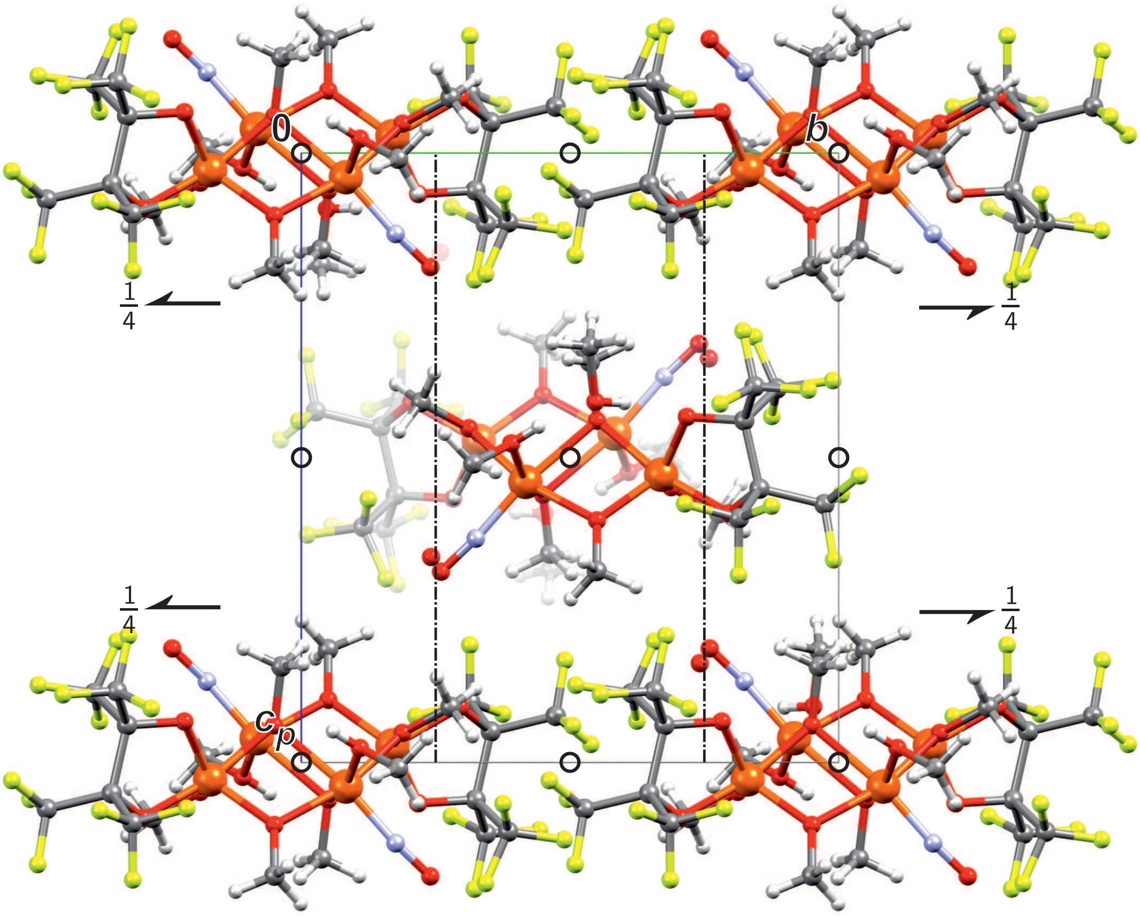

Figure 6.15: Packing diagram of **8a** · 2 MeOH in the monoclinic space group $P2_1/n$ with view along [100]. The symmetry elements of the space group $P2_1/n$ are overlaid. Atoms: carbon (gray), hydrogen (light gray), fluorine (green), iron (orange), nitrogen (blue), oxygen (red).

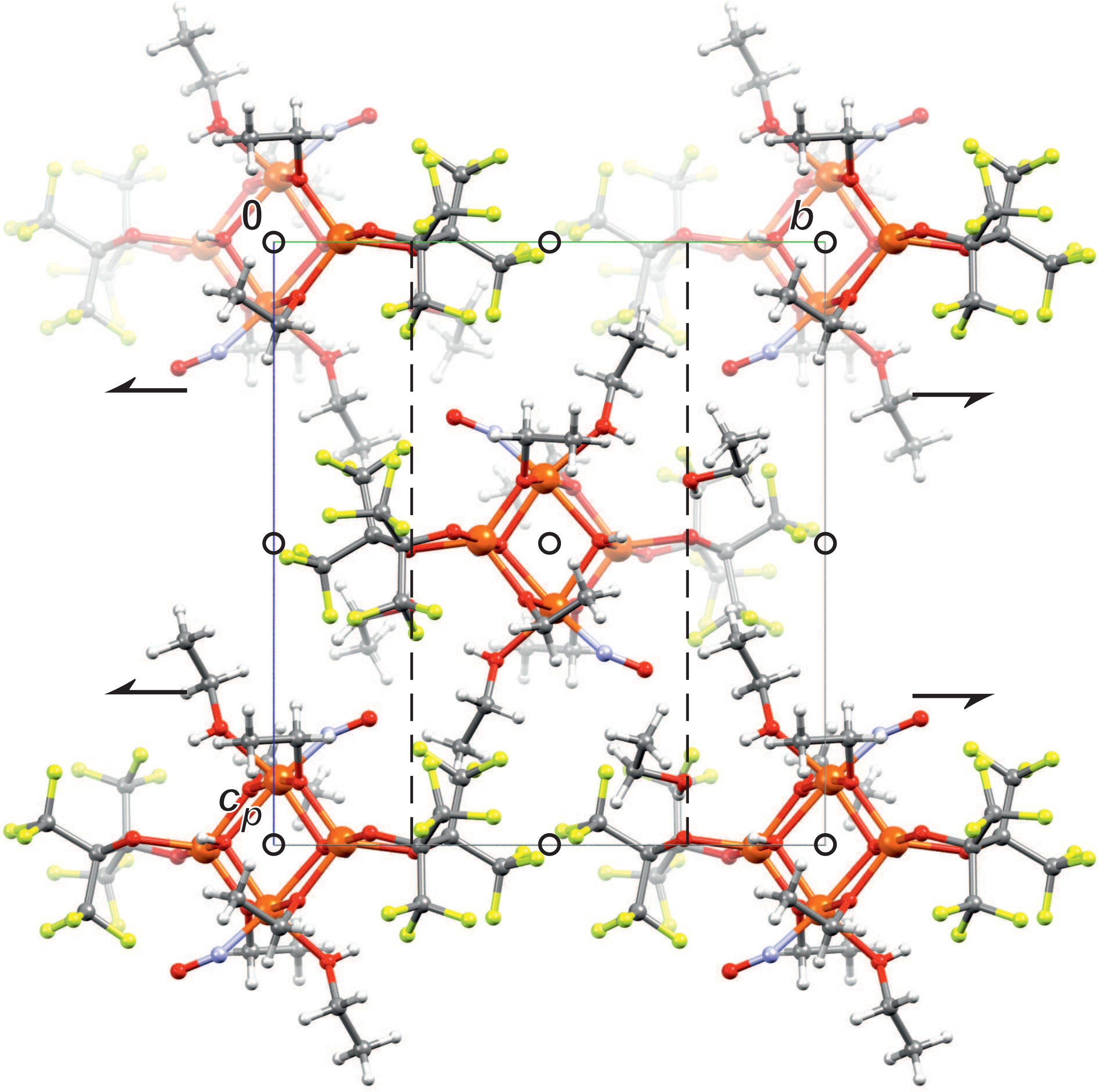

Figure 6.16: Packing diagram of **8b** · 2 EtOH in the monoclinic space group $P2_1/c$ with view along [100]. The symmetry elements of the space group $P2_1/c$ are overlaid. Atoms: carbon (gray), hydrogen (light gray), fluorine (green), iron (orange), nitrogen (blue), oxygen (red).

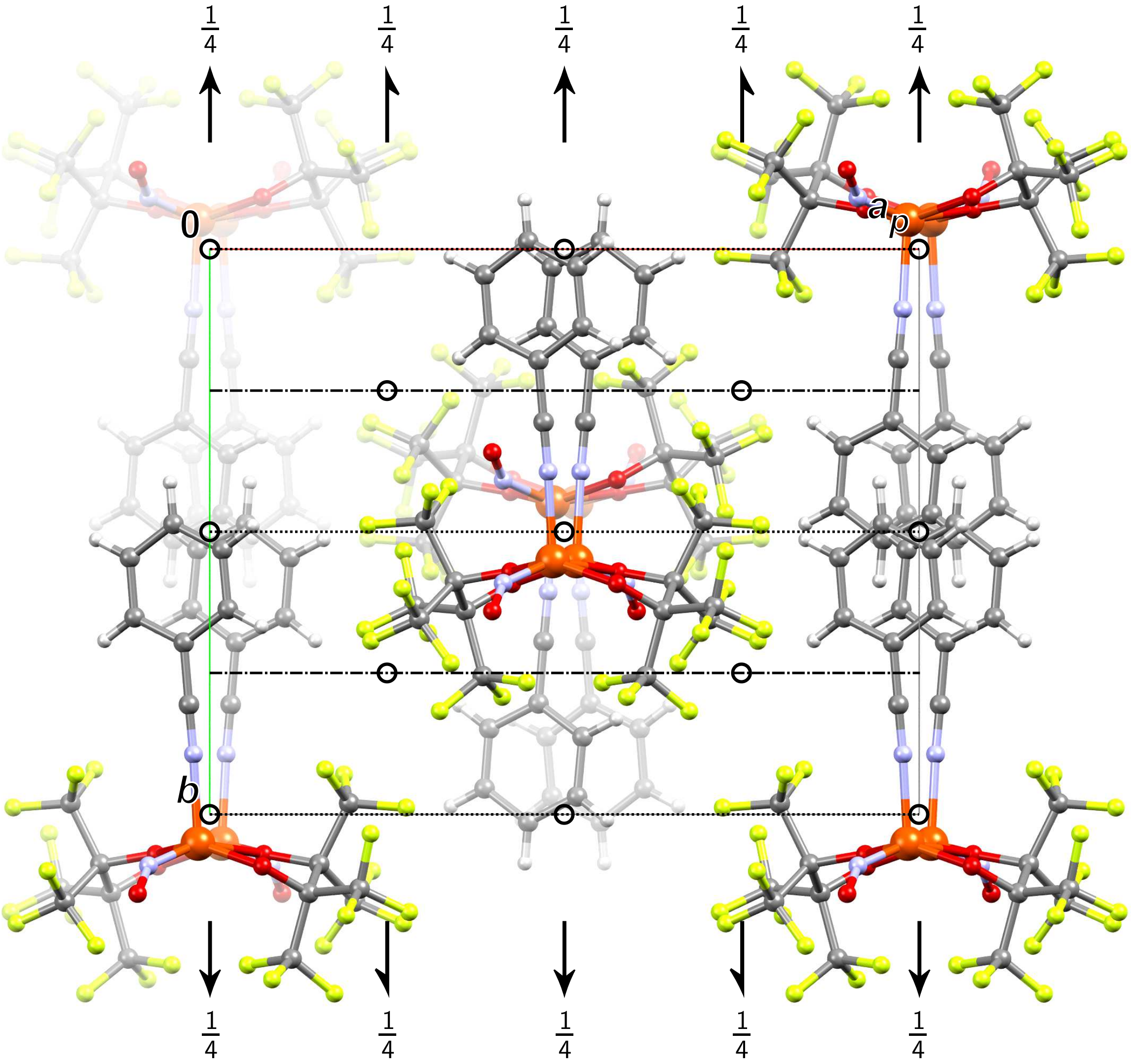

Figure 6.17: Packing diagram of **9** in the monoclinic space group $C2/c$ with view along [001]. The symmetry elements of the space group $C2/c$ are overlaid. Atoms: carbon (gray), hydrogen (light gray), fluorine (green), iron (orange), nitrogen (blue), oxygen (red).

6.2 Quantum-chemical calculations

Table 6.1: Analysis of Oxidation states of individual atoms in $[Fe(H_2O)_5(NO)]^{2+}$, $[Fe(fpin)_2(NO)]^{2-}$, **7a** and **7b** via Head-Gordon's LOBA method.[97] Values were obtained from *MultiWFN*[95] with optimized geometries from DFT calculations (def2/TZVP, D3, C-PCM$_{H_2O}$) after variation of an arbitrary parameter, until the sum of the atoms' oxidation states agreed with the entity's charge. Values of the lower and the upper border values are also given.

			BP86			TPSSh		
			< 43.6	43.7 – 53.9	> 54	< 39.1	39.2 – 56.2	> 56.3
$[Fe(H_2O)_5(NO)]^{2+}$	OS	Fe	2	3	3	3	3	3
		N	1	1	2	0	1	1
		O	−2	−2	−2	−2	−2	−1
		Σ	1	2	3	1	2	3
			< 44.2	44.3 – 44.5	> 44.6	< 44.3	44.4 – 45.3	> 45.5
$[Fe(fpin)_2(NO)]^{2-}$	OS	Fe	3	3	3	3	3	3
		N	1	1	1	1	1	1
		O	−2	−2	−2	−2	−2	−2
		Σ	−3	−2	−1	−3	−2	−1
			< 44.5	44.6 – 45.2	> 45.3			
7a	OS	Fe	3	3	3			
		N	1	1	1			
		O	−2	−2	−2			
		Σ	−1	0	1			
			< 45.2	45.3	> 45.3	< 45.37	45.38	> 45.39
7b	OS	Fe	2	2	2	3	3	3
		N	1	1	1	1	1	1
		O	−2	−2	−2	−2	−2	−2
		Σ	−1	0	1	−1	0	1

6.3 Crystallographic tables

Table 6.2: Crystallographic data of $(NHEt_3)_2[Fe(fpin)_2]$ (**1a**), $(NBnMe_3)_2[Fe(fpin)_2]$ (**1b**) and $[Fe(fpin)(MeOH)_3]$ (**2a**)

	1a	**1b**	**2a**
empirical formula	$C_{24}H_{32}F_{24}FeN_2O_4$	$C_{32}H_{32}F_{24}FeN_2O_4$	$C_9H_{12}F_{12}FeO_5$
$M_r/\mathrm{g\,mol^{-1}}$	924.36	1020.44	484.04
color	blue	colorless	colorless
habitus	block	needle	rod
crystal system	monoclinic	monoclinic	triclinic
space group	$P2_1/n$	$P2_1/n$	$P\overline{1}$
a/Å	12.0904(10)	8.8237(3)	9.8768(7)
b/Å	10.8096(7)	13.0099(4)	13.2748(9)
c/Å	13.8599(10)	16.8151(5)	13.3883(10)
$\alpha/°$	90	90	87.582(2)
$\beta/°$	104.910(8)	98.2750(10)	83.723(2)
$\gamma/°$	90	90	73.848(2)
$V/Å^3$	1750.4(2)	1910.20(10)	1675.8(2)
Z	2	2	4
$\rho_{\mathrm{calc}}/\mathrm{g\,cm^{-3}}$	1.754	1.774	1.918
$\mu/\mathrm{mm^{-1}}$	0.593	0.553	1.046
crystal size/mm	0.42 × 0.41 × 0.29	0.10 × 0.02 × 0.02	0.10 × 0.04 × 0.02
T/K	143(2)	100(2)	100(2)
diffractometer	Oxford XCalibur	Bruker D8Venture	Bruker D8Venture
radiation	Mo$K\alpha$	Mo$K\alpha$	Mo$K\alpha$
anode	fine-focus sealed tube	rotating anode (TXS)	rotating anode (TXS)
rated input/kW	2.0	2.5	2.5
θ-range/°	4.267–26.37	3.196–25.69	3.018–25.69
reflexes for metric	2630	9958	4687
absorption correction	multi-scan	multi-scan	multi-scan
transmission factors	0.7623–1.0000	0.7002–0.7453	0.6548–0.7453
reflexes measured	10541	45305	19835
independent reflexes	3543	3616	6302
R_{int}	0.0465	0.0440	0.0493
mean $\sigma(I)/I$	0.0494	0.0222	0.0520
reflexes with $I \geq 2\sigma(I)$	2609	3186	4702
x,y (weighting scheme)	0.0594, 0.2149	0.0414, 4.7474	0.0308, 4.4004
hydrogen refinement	[a]	[a]	[b]
Flack parameter	–	–	–
parameters	434	289	517
restraints	680	0	15
$R(F_{\mathrm{obs}})$	0.0454	0.0440	0.0422
$R_{\mathrm{w}}(F^2)$	0.1306	0.1115	0.0976
S	1.053	1.033	1.010
shift/error$_{\mathrm{max}}$	0.000	0.000	0.001
max. electron density/e Å^{-3}	0.420	1.428	0.687
min. electron density/e Å^{-3}	−0.357	−0.536	−0.400
measurement code	wo054	uv224	tv270

[a] Coordinates of hydrogen atoms were calculated in idealized positions, riding on their parent atoms. U_{iso} was coupled to the parent atom. [b] Coordinates of hydrogen atoms bonded to oxygen atoms were refined freely with a SADI constraint for equivalent H–O bonds (standard deviation: H–O 0.01). All other hydrogen atoms were calculated in idealized positions, riding on their parent atoms. U_{iso} was always coupled to the parent atom.

Table 6.3: Crystallographic data of $[\mathrm{Fe(fpin)(EtOH)_3}] \cdot \mathrm{EtOH}$ (**2b** · EtOH), $[\mathrm{Fe_2(fpin\text{-}1\kappa}O\mathrm{:1,1'\kappa}O')_2\mathrm{(H_2O)_4}] \cdot 2\,\mathrm{H_2O}$ (**3a** · $2\,\mathrm{H_2O}$) and $[\mathrm{Fe_2(fpin\text{-}1\kappa}O\mathrm{:1,1'\kappa}O')_2\mathrm{(MeCN)_4}]$ (**3b**).

	2b · EtOH	**3a** · $2\,\mathrm{H_2O}$	**3b**[a]
empirical formula	$C_{14}H_{24}F_{12}FeO_6$	$C_{12}H_{12}F_{24}Fe_2O_{10}$	$C_{20}H_{12}F_{24}Fe_2N_4O_4$
$M_\mathrm{r}/\mathrm{g\,mol^{-1}}$	572.18	883.92	940.04
color	colorless	colorless	colorless
habitus	block	rod	block
crystal system	monoclinic	triclinic	monoclinic
space group	$P2_1/c$	$P\bar{1}$	$C2$
a/Å	15.9226(5)	7.8360(4)	18.3126(6)
b/Å	10.5494(2)	7.9193(4)	8.2572(3)
c/Å	40.5494(11)	10.8806(5)	21.7680(7)
$\alpha/°$	90	110.217(2)	90
$\beta/°$	99.663(3)	94.971(2)	112.7725(8)
$\gamma/°$	90	96.372(2)	90
$V/\mathrm{Å^3}$	6714.6(3)	624.01(5)	3034.98(18)
Z	12	1	4
$\rho_\mathrm{calc}/\mathrm{g\,cm^{-3}}$	1.698	2.352	2.057
$\mu/\mathrm{mm^{-1}}$	0.800	1.392	1.142
crystal size/mm	0.418 × 0.360 × 0.231	0.060 × 0.010 × 0.010	0.100 × 0.050 × 0.050
T/K	123(2)	103(2)	100(2)
diffractometer	Oxford XCalibur	Bruker D8Venture	Bruker D8Venture
radiation	MoKα	MoKα	MoKα
anode	fine-focus sealed tube	rotating anode (TXS)	rotating anode (TXS)
rated input/kW	2.0	2.5	2.5
θ-range/°	4.143–26.37	3.098–26.39	3.045–26.38
reflexes for metric	11006	6311	9996
absorption correction	multi-scan	multi-scan	multi-scan
transmission factors	0.91356–1.00000	0.6681–0.7454	0.705–0.745
reflexes measured	39846	15722	25820
independent reflexes	13639	2521	3157
R_int	0.0332	0.0413	0.0457
mean $\sigma(I)/I$	0.0371	0.0375	0.0484
reflexes with $I \geq 2\sigma(I)$	10910	2154	2926
x,y (weighting scheme)	0.0411, 16.2900	0.0202, 2.6705	0.0228, 4.8029
hydrogen refinement	[b]	[c]	[b]
Flack parameter	–	–	0.068(17)
parameters	926	241	492
restraints	149	18	1
$R(F_\mathrm{obs})$	0.0537	0.0449	0.0331
$R_\mathrm{w}(F^2)$	0.1287	0.0980	0.0688
S	1.053	1.145	1.083
shift/error$_\mathrm{max}$	0.001	0.000	0.000
max. electron density/e Å^{-3}	0.960	1.217	0.346
min. electron density/e Å^{-3}	−0.451	−0.648	−0.399
measurement code	uo087	vv806	uv488

[a] Refinement of a two-component crystal. Transformation matrix of the minor component as analyzed by *CELL_NOW*: −1 0 0 0 −1 0 0.92 0 1. BASF = 0.09093. [b] Coordinates of hydrogen atoms were calculated in idealized positions, riding on their parent atoms. U_iso was coupled to the parent atom. [c] Coordinates of hydrogen atoms bonded to oxygen atoms were refined freely with a SADI constraint for equivalent H–O and H–H distances (standard deviation: H–O 0.01, H–H 0.02). All other hydrogen atoms were calculated in idealized positions, riding on their parent atoms. U_iso was always coupled to the parent atom.

Table 6.4: Crystallographic data of $[Fe_2(fpin\text{-}1\kappa O{:}1,1'\kappa O')_2(PhCN)_4]$ (**3c**), $[Fe_2(fpin\text{-}1\kappa O{:}1,1'\kappa O')_2(thf)_4]$ (**3d**) and $[Fe(H_2O)_5(NO)][Ga(fpin)_2(H_2O)]_2 \cdot 8.34\,H_2O$ (**4a** $\cdot$ $8.34\,H_2O$).

	3c	**3d**[a]	**4a** $\cdot$ $8.34\,H_2O$
empirical formula	$C_{40}H_{20}F_{24}Fe_2N_4O_4$	$C_{28}H_{32}F_{24}Fe_2O_8$	$C_{24}H_{30.67}F_{48}FeGa_2NO_{24.34}$
M_r/g mol^{-1}	1188.30	1064.23	1829.83
color	light green	colorless	brown
habitus	rod	rod	platelet
crystal system	triclinic	triclinic	monoclinic
space group	$P\bar{1}$	$P\bar{1}$	$P2_1/n$
a/Å	10.0147(3)	10.4673(9)	19.5162(6)
b/Å	10.7152(3)	16.9417(16)	11.4432(3)
c/Å	11.1881(3)	21.345(2)	25.1936(9)
α/°	104.5330(10)	85.535(3)	90
β/°	102.8220(10)	82.963(3)	91.8050(10)
γ/°	102.4650(10)	83.229(3)	90
V/Å^3	1085.29(5)	3722.8(6)	5623.6(3)
Z	1	4	4
ρ_{calc}/g cm^{-3}	1.818	1.899	2.161
μ/mm^{-1}	0.820	0.947	1.442
crystal size/mm	0.08 × 0.02 × 0.02	0.06 × 0.04 × 0.02	0.10 × 0.05 × 0.02
T/K	101(2)	100(2)	100(2)
diffractometer	Bruker D8Venture	Bruker D8Venture	Bruker D8Venture
radiation	Mo$K\alpha$	Mo$K\alpha$	Mo$K\alpha$
anode	rotating anode (TXS)	rotating anode (TXS)	rotating anode (TXS)
rated input/kW	2.5	2.5	2.5
θ-range/°	3.197–26.43	3.189–25.74	3.010–26.37
reflexes for metric	6603	9825	9955
absorption correction	multi-scan	multi-scan	multi-scan
transmission factors	0.6920–0.7454	0.6747–0.7453	0.6439–0.7455
reflexes measured	17086	95646	51878
independent reflexes	4418	14078	11504
R_{int}	0.0278	0.0551	0.0453
mean $\sigma(I)/I$	0.0348	0.0463	0.0390
reflexes with $I \geq 2\sigma(I)$	3795	10125	9157
x,y (weighting scheme)	0.0169, 0.7862	0.0257, 3.2346	0.0498, 16.8094
hydrogen refinement	[b]	[b]	[c]
Flack parameter	–	–	–
parameters	334	1118	989
restraints	0	5	343
$R(F_{obs})$	0.0311	0.0383	0.0451
$R_w(F^2)$	0.0625	0.0858	0.1190
S	1.045	1.019	1.015
shift/error$_{max}$	0.000	0.001	0.001
max. electron density/e Å^{-3}	0.364	0.501	2.258[d]
min. electron density/e Å^{-3}	−0.317	−0.453	−1.140
measurement code	vv564	uv659	wv108

[a] Refinement of a two-component crystal. Transformation matrix of the minor component as analyzed by *Platon* = −0.5 −0.5 0 −1.5 0.5 0 0 0 −1. BASF = 0.453. [b] Coordinates of hydrogen atoms were calculated in idealized positions, riding on their parent atoms. U_{iso} was coupled to the parent atom. [d] Maximum residual electron density in 0.843 Å distance from Fe1. [c] Coordinates of hydrogen atoms bonded to oxygen atoms were refined freely with a SADI constraint for equivalent H–O and H–H distances (standard deviation: H–O 0.01, H–H 0.02). U_{iso} was always coupled to the parent atom.

Table 6.5: Crystallographic data of $[Fe(H_2O)_5(NO)][Fe(fpin)_2(H_2O)]_2 \cdot 8.31\,H_2O$ (**4b** · $8.31\,H_2O$), $[\{Fe(H_2O)(NO)(\mu\text{-ox})\}_{n/n}] \cdot H_2O$ (**5** · H_2O) and $(NHEt_3)_2[Fe(fpin)_2(NO)]$ (**6**).

	4b · $8.31\,H_2O$	**5** · H_2O[a]	**6**
empirical formula	$C_{24}H_{30.62}F_{48}Fe_3NO_{24.31}$	$C_2H_4FeNO_7$	$C_{24}H_{32}F_{24}FeN_3O_5$
M_r/g mol^{-1}	1801.58	209.91	954.37
color	brown	brown	brown
habitus	platelet	platelet	Plate
crystal system	monoclinic	triclinic	monoclinic
space group	$P2_1/n$	$P\bar{1}$	$P2_1/c$
a/Å	19.6034(10)	5.2103(2)	10.9021(3)
b/Å	11.4386(5)	7.1449(3)	14.3474(5)
c/Å	25.3177(11)	9.3215(4))	22.0525(6)
α/°	90	89.2984(16)	90
β/°	91.682(2)	74.3480(16)	91.0400(10)
γ/°	90	77.5137(16)	90
V/Å^3	5674.7(5)	325.85(2)	3448.81(18)
Z	4	2	4
ρ_{calc}/g cm^{-3}	2.109	2.139	1.838
μ/mm^{-1}	0.990	2.309	0.608
crystal size/mm	0.10 × 0.06 × 0.02	0.06 × 0.03 × 0.01	0.05 × 0.03 × 0.01
T/K	103(2)	100(2)	100(2)
diffractometer	Bruker D8Venture	Bruker D8Venture	Bruker D8Venture
radiation	MoKα	MoKα	MoKα
anode	rotating anode (TXS)	rotating anode (TXS)	rotating anode (TXS)
rated input/kW	2.5	2.5	2.5
θ-range/°	2.737–26.371	3.614–26.44	3.008–26.38
reflexes for metric	9935	3354	9939
absorption correction	multi-scan	multi-scan	multi-scan
transmission factors	0.6902–0.7455	0.6397–0.7454	0.7099–0.7454
reflexes measured	52083	22718	55332
independent reflexes	11593	1325	7035
R_{int}	0.0417	0.0458	0.0519
mean $\sigma(I)/I$	0.0346	0.0286	0.0388
reflexes with $I \geq 2\sigma(I)$	9604	1214	5842
x,y (weighting scheme)	0.0352, 11.0352	0, 0.5798	0.0187, 2.6727
hydrogen refinement	[b]	[b]	[c]
Flack parameter	–	–	–
parameters	1000	113	528
restraints	406	10	0
$R(F_{obs})$	0.0405	0.0294	0.0301
$R_w(F^2)$	0.0982	0.0606	0.0708
S	1.033	1.163	1.035
shift/error$_{max}$	0.002	0.000	0.001
max. electron density/e Å^{-3}	1.385	0.486	0.406
min. electron density/e Å^{-3}	−0.723	−0.393	−0.359
measurement code	wv033	wv189	vv174

[a] Refinement of a two-component crystal. Transformation matrix of the minor component as analyzed by *CELL_NOW*: −1 0 0 −0.557 1 −0.08 0 0 −1. BASF: 0.379. [b] Coordinates of hydrogen atoms bonded to oxygen atoms were refined freely with a SADI constraint for equivalent H–O and H–H distances (standard deviation: H–O 0.01, H–H 0.02). U_{iso} was always coupled to the parent atom. [c] Coordinates of hydrogen atoms were calculated in idealized positions, riding on their parent atoms. U_{iso} was coupled to the parent atom except for N-bound hydrogen atoms, where U_{iso} was refined freely.

Table 6.6: Crystallographic data of $[\mathrm{Fe(fpin)(MeOH)_2(NO)}]\cdot\mathrm{MeOH}$ (**7a** · MeOH), $[\mathrm{Fe(EtOH)_2(fpin)(NO)}]$ (**7b**) and $[\{\mathrm{Fe_2}(\mathrm{fpin}\text{-}1\kappa O,O')(\mathrm{MeOH}\text{-}2\kappa O)(\mathrm{NO}\text{-}2\kappa N)(\mathrm{OMe}\text{-}1{:}2\kappa O,1{:}2'\kappa O,1{:}2{:}2'\kappa O)_3\}_2]\cdot 2\,\mathrm{MeOH}$ (**8a** · 2 MeOH).

	7a · MeOH	**7b**	**8a** · 2 MeOH
empirical formula	$C_9H_{12}F_{12}FeNO_6$	$C_{10}H_{12}F_{12}FeNO_5$	$C_{22}H_{34}F_{24}Fe_4N_2O_{16}$
$M_r/\mathrm{g\,mol^{-1}}$	514.05	510.06	1261.91
color	red	red	brown
habitus	platelet	rod	rod
crystal system	triclinic	triclinic	monoclinic
space group	$P\bar{1}$	$P\bar{1}$	$P2_1/n$
a/Å	8.3098(7)	10.6392(5)	12.0583(3)
b/Å	9.1372(7)	11.5378(5)	12.5212(4)
c/Å	12.2807(9)	14.4114(5)	14.7085(4)
$\alpha/°$	78.925(3)	86.2350(10)	90
$\beta/°$	85.042(3)	85.5950(10)	105.1710(10)
$\gamma/°$	72.601(3)	79.6260(10)	90
$V/\mathrm{Å}^3$	872.80(12)	1732.56(13)	2143.36(11)
Z	2	4	2
$\rho_{\mathrm{calc}}/\mathrm{g\,cm^{-3}}$	1.956	1.955	1.955
$\mu/\mathrm{mm^{-1}}$	1.016	1.019	1.496
crystal size/mm	0.05 × 0.03 × 0.01	0.10 × 0.03 × 0.02	0.10 × 0.05 × 0.02
T/K	100(2)	103(2)	153(2)
diffractometer	Bruker D8Venture	Bruker D8Venture	Bruker D8Venture
radiation	MoKα	MoKα	MoKα
anode	rotating anode (TXS)	rotating anode (TXS)	rotating anode (TXS)
rated input/kW	2.5	2.5	2.5
θ-range/°	2.372–26.45	3.192–27.11	3.014–26.44
reflexes for metric	3023	9458	9893
absorption correction	multi-scan	multi-scan	multi-scan
transmission factors	0.6440–0.7454	0.7033–0.7455	0.7041–0.7454
reflexes measured	14216	51506	55739
independent reflexes	3556	7592	4431
R_{int}	0.0603	0.0390	0.0324
mean $\sigma(I)/I$	0.1024	0.0299	0.0193
reflexes with $I \geq 2\sigma(I)$	2222	6283	4076
x,y (weighting scheme)	0.0275, 0.2286	0.0102, 2.1109	0.0355, 1.9132
hydrogen refinement	[a]	[a]	[b]
Flack parameter	–	–	–
parameters	277	543	329
restraints	3	6	3
$R(F_{\mathrm{obs}})$	0.0508	0.0306	0.0290
$R_{\mathrm{w}}(F^2)$	0.0928	0.0639	0.0823
S	1.032	1.086	1.234
shift/error$_{\mathrm{max}}$	0.000	0.001	0.001
max. electron density/e Å^{-3}	0.495	0.417	0.610
min. electron density/e Å^{-3}	−0.536	−0.335	−0.344
measurement code	uv703	vv667	uv309

[a] Coordinates of hydrogen atoms bonded to oxygen atoms were refined freely with a SADI constraint for equivalent H–O bonds (standard deviation: H–O 0.01). All other hydrogen atoms were calculated in idealized positions, riding on their parent atoms. U_{iso} was always coupled to the parent atom, except for O-bound hydrogen atoms where U_{iso} was refined freely. [b] H86 was refined freely with a SADI constraint for equivalent H–O bonds (standard deviation: H–O 0.01). All other hydrogen atoms were calculated in idealized positions, riding on their parent atoms. U_{iso} was always coupled to the parent atom.

Table 6.7: Crystallographic data of [{Fe_2(EtOH-2κ*O*)(fpin-1κ*O*,*O*′)(NO-2κ*N*)-(OEt-1:2κ*O*,1:2′κ*O*)$_2$(OH-1:2:2′κ*O*)}$_2$] · 2 EtOH (**8b** · 2 EtOH) and [{Fe(fpin-1κ*O*:1,1′κ*O*′)(NO)(PhCN)}$_2$] (**9**).

	8b · 2 EtOH	**9**
empirical formula	$C_{28.2}H_{46.4}F_{24}Fe_4N_2O_{15.8}$	$C_{26}H_{10}F_{24}Fe_2N_4O_6$
M_r/g mol^{-1}	1345.17	1042.08
color	brown	green-brown
habitus	block	rod
crystal system	monoclinic	monoclinic
space group	$P2_1/c$	$C2/c$
a/Å	10.9033(6)	18.6588(5)
b/Å	14.2516(8)	13.0112(4)
c/Å	16.1439(10)	15.8105(4)
α/°	90	90
β/°	105.114(2)	118.8210(10)
γ/°	90	90
V/Å^3	2421.8(2)	3362.91(16)
Z	2	4
ρ_{calc}/g cm^{-3}	1.845	2.058
μ/mm^{-1}	1.330	1.046
crystal size/mm	0.10 × 0.10 × 0.08	0.08 × 0.03 × 0.01
T/K	103(2)	100(2)
diffractometer	Bruker D8Venture	Bruker D8Venture
radiation	MoKα	MoKα
anode	rotating anode (TXS)	rotating anode (TXS)
rated input/kW	2.5	2.5
θ-range/°	3.143–27.53	3.460–26.39
reflexes for metric	9933	7297
absorption correction	multi-scan	multi-scan
transmission factors	0.6089–0.7456	0.6907–0.7454
reflexes measured	37385	26869
independent reflexes	5540	3435
R_{int}	0.0346	0.0442
mean $\sigma(I)/I$	0.0299	0.0349
reflexes with $I \geq 2\sigma(I)$	4564	2857
x,y (weighting scheme)	0.0171, 4.0711	0.0287, 7.2218
hydrogen refinement	[a]	[b]
Flack parameter	–	–
parameters	359	280
restraints	1	0
$R(F_{obs})$	0.0339	0.0343
$R_w(F^2)$	0.0798	0.0777
S	1.095	1.032
shift/error$_{max}$	0.001	0.001
max. electron density/e Å^{-3}	0.608	0.764
min. electron density/e Å^{-3}	−0.445	−0.330
measurement code	vv805	vv165

[a] Coordinates of hydrogen atoms bonded to oxygen atoms were refined freely. All other hydrogen atoms were calculated in idealized positions, riding on their parent atoms. U_{iso} was always coupled to the parent atom.
[b] All hydrogen atoms were calculated in idealized positions, riding on their parent atoms. U_{iso} was always coupled to the parent atom.

7 Bibliography

[1] A. F. Holleman, E. Wiberg, N. Wiberg in *Lehrbuch der Anorganischen Chemie*, Walter de Gruyter, Berlin, New York, **2007**, 707–724.

[2] C. P. Smyth, K. B. McAlpine, *J. Chem. Phys.* **1933**, *1*, 60–61, DOI `10.1063/1.1749220`.

[3] M. D. Lim, I. M. Lorković, P. C. Ford in *Methods in Enzymology*, Nitric Oxide, Part E, Academic Press, **2005**, 3–17, DOI `10.1016/S0076-6879(05)96001-1`.

[4] D. R. Lide, ed. in *CRC Handbook of Chemistry and Physics*, CRC Press/Taylor and Francis, BocaRaton, FL, **2010**, 9–51.

[5] J. H. Enemark, R. D. Feltham, *Coord. Chem. Rev.* **1974**, *13*, 339–406, DOI `10.1016/S0010-8545(00)80259-3`.

[6] J. A. McCleverty, *Chem. Rev.* **2004**, *104*, 403–418, DOI `10.1021/cr020623q`.

[7] F. Roncaroli, M. Videla, L. D. Slep, J. A. Olabe, *Coord. Chem. Rev.* **2007**, *251*, 1903–1930, DOI `10.1016/j.ccr.2007.04.012`.

[8] U. Hauser, V. Oestreich, H. D. Rohrweck, *Z. Phys. A At. Nucl.* **1977**, *280*, 17–25, DOI `10.1007/BF01438104`.

[9] M. Stallmann, *Wie sehr beeinträchtigt Stickstoffdioxid (NO_2) die Gesundheit der Bevölkerung in Deutschland?*, Umweltbundesamt, **2018**, `http://www.umweltbundesamt.de/publikationen/wie-sehr-beeintraechtigt-stickstoffdioxid-no2-die`.

[10] G. P. Chossière, R. Malina, A. Ashok, I. C. Dedoussi, S. D. Eastham, R. L. Speth, S. R. H. Barrett, *Environ. Res. Lett.* **2017**, *12*, 034014, DOI `10.1088/1748-9326/aa5987`.

[11] J. E. Jonson, J. Borken-Kleefeld, D. Simpson, A. Nyíri, M. Posch, C. Heyes, *Environ. Res. Lett.* **2017**, *12*, 094017, DOI `10.1088/1748-9326/aa8850`.

[12] M. B. Fromm, Thomas, K. Ott, Der Abgasskandal - ein Debakel für die gesamte Autoindustrie, **2016**, `https://www.sueddeutsche.de/wirtschaft/abgasaffaere-die-abgasaffaere-ein-debakel-fuer-die-gesamte-autoindustrie-1.2961703` (visited on 03/20/2019).

[13] P. Brimblecombe, D. H. Stedman, *Nature* **1982**, *298*, 460, DOI `10.1038/298460a0`.

[14] H. Ohshima, H. Bartsch, *Mutat. Res.* **1994**, *305*, 253–264, DOI `10.1016/0027-5107(94)90245-3`.

[15] D. A. Wink, Y. Vodovotz, J. Laval, F. Laval, M. W. Dewhirst, J. B. Mitchell, *Carcinogenesis* **1998**, *19*, 711–721, DOI `10.1093/carcin/19.5.711`.

[16] H. Johnston, *Science* **1971**, *173*, 517–522, DOI `10.1126/science.173.3996.517`.

[17] P. J. Crutzen, *Q. J. R. Meteorol. Soc.* **1970**, *96*, 320–325, DOI `10.1002/qj.49709640815`.

[18] A. R. Ravishankara, J. S. Daniel, R. W. Portmann, *Science* **2009**, *326*, 123–125, DOI `10.1126/science.1176985`.

[19] J. Loscalzo, G. Welch, *Prog. Cardiovasc. Dis.* **1995**, *38*, 87–104, DOI `10.1016/S0033-0620(05)80001-5`.

[20] C. J. Lowenstein, S. H. Snyder, *Cell* **1992**, *70*, 705–707, DOI `10.1016/0092-8674(92)90301-R`.

[21] C. Bogdan, *Nat. Immunol.* **2001**, *2*, 907–916, DOI `10.1038/ni1001-907`.

[22] M. A. Marletta, *J. Biol. Chem.* **1993**, *268*, 12231–12234.

[23] E. Culotta, D. E. Koshland, *Science* **1992**, *258*, 1862–1865, DOI `10.1126/science.1361684`.

[24] D. E. Koshland, *Science* **1992**, *258*, 1861–1861, DOI `10.1126/science.1470903`.

[25] (a) R. F. Furchgott, *Angew. Chem. Int. Ed.* **1999**, *38*, 1870–1880, DOI `10.1002/(SICI)1521-3773(19990712)38:13/14<1870::AID-ANIE1870>3.0.CO;2-8`; (b) R. F. Furchgott, *Angew. Chem.* **1999**, *111*, 1990–2000, DOI `10.1002/(SICI)1521-3757(19990712)111:13/14<1990::AID-ANGE1990>3.0.CO;2-5`.

[26] (a) F. Murad, *Angew. Chem. Int. Ed.* **1999**, *38*, 1856–1868, DOI `10.1002/(SICI)1521-3773(19990712)38:13/14<1856::AID-ANIE1856>3.0.CO;2-D`; (b) F. Murad, *Angew. Chem.* **1999**, *111*, 1976–1989, DOI `10.1002/(SICI)1521-3757(19990712)111:13/14<1976::AID-ANGE1976>3.0.CO;2-A`.

[27] (a) L. J. Ignarro, *Angew. Chem. Int. Ed.* **1999**, *38*, 1882–1892, DOI `10.1002/(SICI)1521-3773(19990712)38:13/14<1882::AID-ANIE1882>3.0.CO;2-V`; (b) L. J. Ignarro, *Angew. Chem.* **1999**, *111*, 2002–2013, DOI `10.1002/(SICI)1521-3757(19990712)111:13/14<2002::AID-ANGE2002>3.0.CO;2-Q`.

[28] Nobel Media AB 2019, The Nobel Prize in Physiology or Medicine 1998, **1998**, `https://www.nobelprize.org/prizes/medicine/1998/summary/` (visited on 12/04/2018).

[29] V. Kohlschütter, M. Kutscheroff, *Ber. Dtsch. Chem. Ges.* **1904**, *37*, 3044–3052, DOI `10.1002/cber.19040370389`.

[30] W. Manchot, K. Zechentmayer, *Justus Liebigs Ann. Chem.* **1906**, *350*, 368–389, DOI `10.1002/jlac.19063500307`.

[31] W. P. Griffith, J. Lewis, G. Wilkinson, *J. Chem. Soc.* **1958**, 3993–3998, DOI `10.1039/JR9580003993`.

[32] A. Wanat, T. Schneppensieper, G. Stochel, R. van Eldik, E. Bill, K. Wieghardt, *Inorg. Chem.* **2002**, *41*, 4–10, DOI `10.1021/ic010628q`.

[33] H.-Y. Cheng, S. Chang, P.-Y. Tsai, *J. Phys. Chem. A* **2004**, *108*, 358–361, DOI `10.1021/jp031136x`.

[34] J. Conradie, K. H. Hopmann, A. Ghosh, *J. Phys. Chem. B* **2010**, *114*, 8517–8524, DOI `10.1021/jp101847y`.

[35] T. Schneppensieper, S. Finkler, A. Czap, R. van Eldik, M. Heus, P. Nieuwenhuizen, C. Wreesmann, W. Abma, *Eur. J. Inorg. Chem.* **2001**, 491–501, DOI `10.1002/1099-0682(200102)2001:2<491::AID-EJIC491>3.0.CO;2-2`.

[36] V. Kohlschütter, M. Kutscheroff, *Ber. Dtsch. Chem. Ges.* **1907**, *40*, 873–878, DOI `10.1002/cber.190704001131`.

[37] M. Steimann, U. Nagel, R. Grenz, W. Beck, *J. Organomet. Chem.* **1983**, *247*, 171–174, DOI `10.1016/S0022-328X(00)98752-7`.

[38] B. M. Aas, P. Klüfers, *Eur. J. Inorg. Chem.* **2017**, 2313–2320, DOI `10.1002/ejic.201601330`.

[39] M. Wolf, P. Klüfers, *Eur. J. Inorg. Chem.* **2017**, 2303–2312, DOI `10.1002/ejic.201601329`.

[40] B. Weber, H. Görls, M. Rudolph, E.-G. Jäger, *Inorg. Chim. Acta* **2002**, *337*, 247–265, DOI `10.1016/S0020-1693(02)01114-3`.

[41] T. C. Berto, M. B. Hoffman, Y. Murata, K. B. Landenberger, E. E. Alp, J. Zhao, N. Lehnert, *J. Am. Chem. Soc.* **2011**, *133*, 16714–16717, DOI `10.1021/ja111693f`.

[42] K. J. Haller, P. L. Johnson, R. D. Feltham, J. H. Enemark, J. R. Ferraro, L. J. Basile, *Inorg. Chim. Acta* **1979**, *33*, 119–130, DOI `10.1016/S0020-1693(00)89464-5`.

[43] A. Majumdar, S. J. Lippard, *Inorg. Chem.* **2013**, *52*, 13292–13294, DOI `10.1021/ic4019508`.

[44] A. L. Feig, M. T. Bautista, S. J. Lippard, *Inorg. Chem.* **1996**, *35*, 6892–6898, DOI `10.1021/ic960552b`.

[45] M. Jana, N. Pal, C. J. White, C. Kupper, F. Meyer, N. Lehnert, A. Majumdar, *J. Am. Chem. Soc.* **2017**, *139*, 14380–14383, DOI `10.1021/jacs.7b08855`.

[46] S. Zheng, T. C. Berto, E. W. Dahl, M. B. Hoffman, A. L. Speelman, N. Lehnert, *J. Am. Chem. Soc.* **2013**, *135*, 4902–4905, DOI `10.1021/ja309782m`.

[47] D. P. Klein, V. G. Young, W. B. Tolman, L. Que, *Inorg. Chem.* **2006**, *45*, 8006–8008, DOI `10.1021/ic0610740`.

[48] E. Victor, M. A. Minier, S. J. Lippard, *Eur. J. Inorg. Chem.* **2014**, 5640–5645, DOI `10.1002/ejic.201402543`.

[49] N. Kindermann, A. Schober, S. Demeshko, N. Lehnert, F. Meyer, *Inorg. Chem.* **2016**, *55*, 11538–11550, DOI `10.1021/acs.inorgchem.6b02080`.

[50] Y.-M. Chiou, L. Que, *Inorg. Chem.* **1995**, *34*, 3270–3278, DOI `10.1021/ic00116a020`.

[51] A. Banerjee, J. Li, A. L. Speelman, C. J. White, P. L. Pawlak, W. W. Brennessel, N. Lehnert, F. A. Chavez, *Eur. J. Inorg. Chem.* **2018**, 4797–4804, DOI `10.1002/ejic.201800992`.

[52] A. L. Speelman, C. J. White, B. Zhang, E. E. Alp, J. Zhao, M. Hu, C. Krebs, J. Penner-Hahn, N. Lehnert, *J. Am. Chem. Soc.* **2018**, *140*, 11341–11359, DOI `10.1021/jacs.8b06095`.

[53] C.-C. Tsou, W.-L. Yang, W.-F. Liaw, *J. Am. Chem. Soc.* **2013**, *135*, 18758–18761, DOI `10.1021/ja4105864`.

[54] C. Hauser, T. Glaser, E. Bill, T. Weyhermüller, K. Wieghardt, *J. Am. Chem. Soc.* **2000**, *122*, 4352–4365, DOI `10.1021/ja994161i`.

[55] F.-T. Tsai, P.-L. Chen, W.-F. Liaw, *J. Am. Chem. Soc.* **2010**, *132*, 5290–5299, DOI `10.1021/ja100849r`.

[56] F.-T. Tsai, Y.-C. Lee, M.-H. Chiang, W.-F. Liaw, *Inorg. Chem.* **2013**, *52*, 464–473, DOI `10.1021/ic3023437`.

[57] J. Li, A. Banerjee, P. L. Pawlak, W. W. Brennessel, F. A. Chavez, *Inorg. Chem.* **2014**, *53*, 5414–5416, DOI `10.1021/ic500558j`.

[58] C. R. Randall, L. Shu, Y.-M. Chiou, K. S. Hagen, M. Ito, N. Kitajima, R. J. Lachicotte, Y. Zang, L. Que, *Inorg. Chem.* **1995**, *34*, 1036–1039, DOI `10.1021/ic00109a007`.

[59] G. de Ruiter, N. B. Thompson, D. Lionetti, T. Agapie, *J. Am. Chem. Soc.* **2015**, *137*, 14094–14106, DOI `10.1021/jacs.5b07397`.

[60] K. D. Hodges, R. G. Wollmann, S. L. Kessel, D. N. Hendrickson, D. G. Van Derveer, E. K. Barefield, *J. Am. Chem. Soc.* **1979**, *101*, 906–917, DOI `10.1021/ja00498a019`.

[61] S. Khatua, A. Majumdar, *J. Inorg. Biochem.* **2015**, *142*, 145–153, DOI `10.1016/j.jinorgbio.2014.09.018`.

[62] Y. Shiro, *Biochim. Biophys. Acta* **2012**, *1817*, 1907–1913, DOI `10.1016/j.bbabio.2012.03.001`.

[63] T. Hayashi, M. T. Lin, K. Ganesan, Y. Chen, J. A. Fee, R. B. Gennis, P. Moënne-Loccoz, *Biochemistry* **2009**, *48*, 883–890, DOI `10.1021/bi801915r`.

[64] P. Moënne-Loccoz, *Nat. Prod. Rep.* **2007**, *24*, 610–620, DOI `10.1039/B604194A`.

[65] D. M. Kurtz, Jr., *Dalton Trans.* **2007**, 4115–4121, DOI `10.1039/B710047G`.

[66] C. Frazão, G. Silva, C. M. Gomes, P. Matias, R. Coelho, L. Sieker, S. Macedo, M. Y. Liu, S. Oliveira, M. Teixeira, A. V. Xavier, C. Rodrigues-Pousada, M. A. Carrondo, J. Le Gall, *Nat. Struct. Mol. Biol.* **2000**, *7*, 1041–1045, DOI `10.1038/80961`.

[67] L. M. Blomberg, M. R. A. Blomberg, P. E. M. Siegbahn, *J. Biol. Inorg. Chem.* **2007**, *12*, 79–89, DOI `10.1007/s00775-006-0166-x`.

[68] (a) X. Wurzenberger, H. Piotrowski, P. Klüfers, *Angew. Chem. Int. Ed.* **2011**, *50*, 4974–4978, DOI `10.1002/anie.201006898`; (b) X. Wurzenberger, H. Piotrowski, P. Klüfers, *Angew. Chem.* **2011**, *123*, 5078–5082, DOI `10.1002/ange.201006898`.

[69] (a) X. Wurzenberger, C. Neumann, P. Klüfers, *Angew. Chem. Int. Ed.* **2013**, *52*, 5159–5161, DOI `10.1002/anie.201300787`; (b) X. Wurzenberger, C. Neumann, P. Klüfers, *Angew. Chem.* **2013**, *125*, 5264–5266, DOI `10.1002/ange.201300787`.

[70] L. Tahsini, S. E. Specht, J. S. Lum, J. J. M. Nelson, A. F. Long, J. A. Golen, A. L. Rheingold, L. H. Doerrer, *Inorg. Chem.* **2013**, *52*, 14050–14063, DOI `10.1021/ic401837y`.

[71] F. Weigend, R. Ahlrichs, *Phys. Chem. Chem. Phys.* **2005**, *7*, 3297–3305, DOI `10.1039/B508541A`.

[72] S. Grimme, J. Antony, S. Ehrlich, H. Krieg, *J. Chem. Phys.* **2010**, *132*, 154104, DOI `10.1063/1.3382344`.

[73] O. Treutler, R. Ahlrichs, *J. Chem. Phys.* **1995**, *102*, 346–354, DOI `10.1063/1.469408`.

[74] M. Sierka, A. Hogekamp, R. Ahlrichs, *J. Chem. Phys.* **2003**, *118*, 9136–9148, DOI `10.1063/1.1567253`.

[75] S. Kossmann, F. Neese, *Chem. Phys. Lett.* **2009**, *481*, 240–243, DOI `10.1016/j.cplett.2009.09.073`.

[76] F. Neese, F. Wennmohs, A. Hansen, U. Becker, *Chem. Phys.* **2009**, *356*, 98–109, DOI `10.1016/j.chemphys.2008.10.036`.

[77] F. Weigend, *Phys. Chem. Chem. Phys.* **2006**, *8*, 1057–1065, DOI `10.1039/B515623H`.

[78] A. D. Becke, *Phys. Rev. A* **1988**, *38*, 3098–3100, DOI `10.1103/PhysRevA.38.3098`.

[79] J. P. Perdew, *Phys. Rev. B* **1986**, *33*, 8822–8824, DOI `10.1103/PhysRevB.33.8822`.

[80] S. Grimme, *J. Comput. Chem.* **2006**, *27*, 1787–1799, DOI `10.1002/jcc.20495`.

[81] J. Tao, J. P. Perdew, V. N. Staroverov, G. E. Scuseria, *Phys. Rev. Lett.* **2003**, *91*, 146401, DOI `10.1103/PhysRevLett.91.146401`.

[82] J. P. Perdew, Y. Wang, *Phys. Rev. B* **1992**, *45*, 13244–13249, DOI `10.1103/PhysRevB.45.13244`.

[83] V. N. Staroverov, G. E. Scuseria, J. Tao, J. P. Perdew, *J. Chem. Phys.* **2003**, *119*, 12129–12137, DOI `10.1063/1.1626543`.

[84] A. D. Becke, *J. Chem. Phys.* **1993**, *98*, 1372–1377, DOI `10.1063/1.464304`.

[85] C. Lee, W. Yang, R. G. Parr, *Phys. Rev. B* **1988**, *37*, 785–789, DOI `10.1103/PhysRevB.37.785`.

[86] S. H. Vosko, L. Wilk, M. Nusair, *Can. J. Phys.* **1980**, *58*, 1200–1211, DOI `10.1139/p80-159`.

[87] P. J. Stephens, F. J. Devlin, C. F. Chabalowski, M. J. Frisch, *J. Phys. Chem.* **1994**, *98*, 11623–11627, DOI `10.1021/j100096a001`.

[88] V. Barone, M. Cossi, *J. Phys. Chem. A* **1998**, *102*, 1995–2001, DOI `10.1021/jp9716997`.

[89] A. Klamt, G. Schüürmann, *J. Chem. Soc. Perkin Trans. 2* **1993**, 799–805, DOI `10.1039/P29930000799`.

[90] A. Kovalenko, F. Hirata, *J. Chem. Phys.* **1999**, *110*, 10095–10112, DOI `10.1063/1.478883`.

[91] A. Kovalenko, F. Hirata, *J. Chem. Phys.* **2000**, *112*, 10391–10402, DOI `10.1063/1.481676`.

[92] (a) G. Monsch, P. Klüfers, *Angew. Chem. Int. Ed.* **2019**, *58*, 8566–8571, DOI `10.1002/anie.201902374`; (b) G. Monsch, P. Klüfers, *Angew. Chem.* **2019**, *131*, 8654–8659, DOI `10.1002/ange.201902374`.

[93] R. S. Mulliken, *J. Chem. Phys.* **1955**, *23*, 1833–1840, DOI `10.1063/1.1740588`.

[94] A. E. Reed, R. B. Weinstock, F. Weinhold, *J. Chem. Phys.* **1985**, *83*, 735–746, DOI `10.1063/1.449486`.

[95] T. Lu, F. Chen, *J. Comput. Chem.* **2012**, *33*, 580–592, DOI `10.1002/jcc.22885`.

[96] (a) V. Postils, C. Delgado-Alonso, J. M. Luis, P. Salvador, *Angew. Chem. Int. Ed.* **2018**, *57*, 10525–10529, DOI `10.1002/anie.201802745`; (b) V. Postils, C. Delgado-Alonso, J. M. Luis, P. Salvador, *Angew. Chem.* **2018**, *130*, 10685–10689, DOI `10.1002/ange.201802745`.

[97] A. J. W. Thom, E. J. Sundstrom, M. Head-Gordon, *Phys. Chem. Chem. Phys.* **2009**, *11*, 11297–11304, DOI `10.1039/B915364K`.

[98] M. Römelt, S. Ye, F. Neese, *Inorg. Chem.* **2009**, *48*, 784–785, DOI `10.1021/ic801535v`.

[99] F. Neese, *Inorg. Chim. Acta* **2002**, *337*, 181–192, DOI `10.1016/S0020-1693(02)01031-9`.

[100] M. Wolf, *Synthesis, characterization and quantum-chemical analysis of {FeNO}^{7} and {Fe(NO)$_2$}^{9} compounds*, Dissertation, Ludwig-Maximilians-Universität München, **2016**.

[101] E. K. Plyler, E. D. Tidwell, A. G. Maki, *J. RES. NATL. BUR. STAN. SECT. A.* **1964**, *68A*, 79, DOI `10.6028/jres.068A.006`.

[102] C. Neumann, *unpublished* **2019**.

[103] R. C. Johnston, P. H.-Y. Cheong, *Org. Biomol. Chem.* **2013**, *11*, 5057–5064, DOI `10.1039/C3OB40828K`.

[104] (a) N. Xu, D. R. Powell, G. B. Richter-Addo, *Angew. Chem. Int. Ed.* **2011**, *50*, 9694–9696, DOI `10.1002/anie.201103329`; (b) N. Xu, D. R. Powell, G. B. Richter-Addo, *Angew. Chem.* **2011**, *123*, 9868–9870, DOI `10.1002/ange.201103329`.

[105] W. R. Scheidt, Y. J. Lee, K. Hatano, *J. Am. Chem. Soc.* **1984**, *106*, 3191–3198, DOI `10.1021/ja00323a022`.

[106] W. Manchot, F. Huttner, *Justus Liebigs Ann. Chem.* **1910**, *372*, 153–178, DOI `10.1002/jlac.19103720202`.

[107] R. D. Shannon, *Acta Crystallogr. A* **1976**, *32*, 751–767, DOI `10.1107/S0567739476001551`.

[108] H. Mosbæk, K. G. Poulsen, T. Torgrimsen, G. Widmark, J. Koskikallio, S. Kachi, *Acta Chem. Scand.* **1971**, *25*, 2421–2427, DOI `10.3891/acta.chem.scand.25-2421`.

[109] G. Monsch, *unpublished* **2019**.

[110] G. Monsch, A. In-Iam, X. Kästele, P. Klüfers, *submitted.*

[111] L. Cambi, A. Ferrari, *Gazz. Chim. Ital.* **1951**, 1162–1180.

[112] L. Gmelin, *Gmelins Handbuch Der Anorganischen Chemie; Eisen, B*, Verlag Chemie, Berlin, **1932**, 157f.

[113] J. Woolins, *Inorganic Experiments*, 3rd ed., Wiley-VCH, Weinheim, **2003**, 456 pp.

[114] R. D. Feltham, *Inorg. Chem.* **1964**, *3*, 116–119, DOI `10.1021/ic50011a025`.

[115] J. B. Sheridan, J. R. Johnson, B. M. Handwerker, G. L. Geoffroy, A. L. Rheingold, *Organometallics* **1988**, *7*, 2404–2411, DOI `10.1021/om00101a022`.

[116] M. Göldner, B. Geniffke, A. Franken, K. S. Murray, H. Homborg, *Z. anorg. allg. Chem.* **2001**, *627*, 935–947, DOI `10.1002/1521-3749(200105)627:5<935::AID-ZAAC935>3.0.CO;2-J`.

[117] A. Gallien, *Synthesis, characterisation and DFT analysis of {Ru(NO)$_2$}^{8} compounds*, Dissertation, Ludwig-Maximilians-Universität München, **2014**.

[118] M. A. P. Yoosaf, S. Ghosh, Y. Narayan, M. Yadav, S. C. Sahoo, P. Kumar, *Dalton Trans.* **2019**, *48*, 13916–13920, DOI `10.1039/C9DT02834J`.

[119] B. M. Aas, *Synthesis, characterization and DFT analysis of stable {FeNO}^{7} compounds*, Dissertation, Ludwig-Maximilians-Universität München, **2018**.

[120] A. In-Iam, M. Wolf, C. Wilfer, D. Schaniel, T. Woike, P. Klüfers, *Chem. Eur. J.* **2019**, *25*, 1304–1325, DOI `10.1002/chem.201804565`.

[121] A. A. Danopoulos, C. Redshaw, A. Vaniche, G. Wilkinson, B. Hussain-Bates, M. B. Hursthouse, *Polyhedron* **1993**, *12*, 1061–1071, DOI `10.1016/S0277-5387(00)87185-5`.

[122] F. Edelmann, H. Plenio, K. Keller, H. W. Roesky, U. Behrens, *Z. anorg. allg. Chem.* **1988**, *565*, 111–117, DOI `10.1002/zaac.19885650112`.

[123] D. M. Kuzyaev, T. V. Balashova, M. E. Burin, G. K. Fukin, R. V. Rumyantcev, A. P. Pushkarev, V. A. Ilichev, I. D. Grishin, D. L. Vorozhtsov, M. N. Bochkarev, *Dalton Trans.* **2016**, *45*, 3464–3472, DOI `10.1039/C5DT04636J`.

[124] T. Schneppensieper, A. Zahl, R. van Eldik, *Angew. Chem. Int. Ed.* **2001**, *40*, 1678–1680, DOI `10.1002/1521-3773(20010504)40:9<1678::AID-ANIE16780>3.0.CO;2-A`.

[125] T. Schneppensieper, A. Wanat, G. Stochel, S. Goldstein, D. Meyerstein, R. van Eldik, *Eur. J. Inorg. Chem.* **2001**, 2317–2325, DOI `10.1002/1099-0682(200109)2001:9<2317::AID-EJIC2317>3.0.CO;2-F`.

[126] T. Schneppensieper, A. Wanat, G. Stochel, R. van Eldik, *Inorg. Chem.* **2002**, *41*, 2565–2573, DOI `10.1021/ic011220w`.

[127] S. Lu, E. Libby, L. Saleh, G. Xing, J. M. Bollinger, P. Moënne-Loccoz, *J. Biol. Inorg. Chem.* **2004**, *9*, 818–827, DOI `10.1007/s00775-004-0582-8`.

[128] D. E. Coufal, P. Tavares, A. S. Pereira, B. H. Hyunh, S. J. Lippard, *Biochemistry* **1999**, *38*, 4504–4513, DOI `10.1021/bi9823378`.

[129] C. J. Haskin, N. Ravi, J. B. Lynch, E. Munck, L. Que, *Biochemistry* **1995**, *34*, 11090–11098, DOI `10.1021/bi00035a014`.

[130] W.-Y. Wu, C.-N. Hsu, C.-H. Hsieh, T.-W. Chiou, M.-L. Tsai, M.-H. Chiang, W.-F. Liaw, *Inorg. Chem.* **2019**, *58*, 9586–9591, DOI `10.1021/acs.inorgchem.9b01635`.

[131] C. Van Stappen, N. Lehnert, *Inorg. Chem.* **2018**, *57*, 4252–4269, DOI `10.1021/acs.inorgchem.7b02333`.

[132] E. G. Abucayon, R. L. Khade, D. R. Powell, Y. Zhang, G. B. Richter-Addo, *J. Am. Chem. Soc.* **2018**, *140*, 4204–4207, DOI `10.1021/jacs.7b13681`.

[133] H. B. Gray, I. Bernal, E. Billig, *J. Am. Chem. Soc.* **1962**, *84*, 3404–3405, DOI `10.1021/ja00876a037`.

[134] J. Lewis, *Sci. Prog.* **1959**, *47*, 506–521.

[135] (a) S. Chakraborty, J. Reed, M. Ross, M. J. Nilges, I. D. Petrik, S. Ghosh, S. Hammes-Schiffer, J. T. Sage, Y. Zhang, C. E. Schulz, Y. Lu, *Angew. Chem. Int. Ed.* **2014**, *53*, 2417–2421, DOI `10.1002/anie.201308431`; (b) S. Chakraborty, J. Reed, M. Ross, M. J. Nilges, I. D. Petrik, S. Ghosh, S. Hammes-Schiffer, J. T. Sage, Y. Zhang, C. E. Schulz, Y. Lu, *Angew. Chem.* **2014**, *126*, 2449–2453, DOI `10.1002/ange.201308431`.

[136] J. Conradie, D. A. Quarless, H.-F. Hsu, T. C. Harrop, S. J. Lippard, S. A. Koch, A. Ghosh, *J. Am. Chem. Soc.* **2007**, *129*, 10446–10456, DOI `10.1021/ja0719982`.

[137] J. C. Salerno, J. N. Siedow, *Biochim. Biophys. Acta* **1979**, *579*, 246–251, DOI `10.1016/0005-2795(79)90104-1`.

[138] Y. Zhang, E. Oldfield, *J. Am. Chem. Soc.* **2004**, *126*, 9494–9495, DOI `10.1021/ja0401242`.

[139] H.-Y. Cheng, S. Chang, *Int. J. Quantum Chem.* **2005**, *105*, 511–517, DOI `10.1002/qua.20734`.

[140] C. A. Brown, M. A. Pavlosky, T. E. Westre, Y. Zhang, B. Hedman, K. O. Hodgson, E. I. Solomon, *J. Am. Chem. Soc.* **1995**, *117*, 715–732, DOI `10.1021/ja00107a015`.

[141] M. Li, D. Bonnet, E. Bill, F. Neese, T. Weyhermüller, N. Blum, D. Sellmann, K. Wieghardt, *Inorg. Chem.* **2002**, *41*, 3444–3456, DOI `10.1021/ic011243a`.

[142] G. Villar-Acevedo, E. Nam, S. Fitch, J. Benedict, J. Freudenthal, W. Kaminsky, J. A. Kovacs, *J. Am. Chem. Soc.* **2011**, *133*, 1419–1427, DOI `10.1021/ja107551u`.

[143] G. Schenk, M. Y. M. Pau, E. I. Solomon, *J. Am. Chem. Soc.* **2004**, *126*, 505–515, DOI `10.1021/ja036715u`.

[144] C. D. Brown, M. L. Neidig, M. B. Neibergall, J. D. Lipscomb, E. I. Solomon, *J. Am. Chem. Soc.* **2007**, *129*, 7427–7438, DOI `10.1021/ja071364v`.

[145] A. R. Diebold, C. D. Brown-Marshall, M. L. Neidig, J. M. Brownlee, G. R. Moran, E. I. Solomon, *J. Am. Chem. Soc.* **2011**, *133*, 18148–18160, DOI `10.1021/ja202549q`.

[146] N. Sun, L. V. Liu, A. Dey, G. Villar-Acevedo, J. A. Kovacs, M. Y. Darensbourg, K. O. Hodgson, B. Hedman, E. I. Solomon, *Inorg. Chem.* **2011**, *50*, 427–436, DOI `10.1021/ic1006378`.

[147] A. Earnshaw, E. A. King, L. F. Larkworthy, *J. Chem. Soc. A* **1969**, 2459–2463, DOI `10.1039/J19690002459`.

[148] H. Twilfer, F.-H. Bernhardt, K. Gersonde, *Eur. J. Biochem.* **1985**, *147*, 171–176, DOI `10.1111/j.1432-1033.1985.tb08733.x`.

[149] Y. Zhang, M. A. Pavlosky, C. A. Brown, T. E. Westre, B. Hedman, K. O. Hodgson, E. I. Solomon, *J. Am. Chem. Soc.* **1992**, *114*, 9189–9191, DOI `10.1021/ja00049a062`.

[150] T. A. Jackson, E. Yikilmaz, A.-F. Miller, T. C. Brunold, *J. Am. Chem. Soc.* **2003**, *125*, 8348–8363, DOI `10.1021/ja029523s`.

[151] S. Ye, J. C. Price, E. W. Barr, M. T. Green, J. M. Bollinger, C. Krebs, F. Neese, *J. Am. Chem. Soc.* **2010**, *132*, 4739–4751, DOI `10.1021/ja909715g`.

[152] J. H. Rodriguez, Y.-M. Xia, P. G. Debrunner, *J. Am. Chem. Soc.* **1999**, *121*, 7846–7863, DOI `10.1021/ja990129c`.

[153] M. Radoń, E. Broclawik, K. Pierloot, *J. Phys. Chem. B* **2010**, *114*, 1518–1528, DOI `10.1021/jp910220r`.

[154] E. Broclawik, A. Stępniewski, M. Radoń, *J. Inorg. Biochem.* **2014**, *136*, 147–153, DOI `10.1016/j.jinorgbio.2014.01.010`.

[155] P. Karen, P. McArdle, J. Takats, *Pure Appl. Chem.* **2016**, *88*, 831–839, DOI `10.1515/pac-2015-1204`.

[156] K. S. Hagen, *Inorg. Chem.* **2000**, *39*, 5867–5869, DOI `10.1021/ic000444w`.

[157] D. Beck, A. Belz, A. In-Iam, P. Mayer, P. Klüfers, *Z. anorg. allg. Chem.* **2017**, *643*, 1191–1194, DOI `10.1002/zaac.201700274`.

[158] B. Scheibe, S. Lippert, S. S. Rudel, M. R. Buchner, O. Burghaus, C. Pietzonka, M. Koch, A. J. Karttunen, F. Kraus, *Chem. Eur. J.* **2016**, *22*, 12145–12153, DOI `10.1002/chem.201602265`.

[159] S. Adam, A. Ellern, K. Seppelt, *Chem. Eur. J.* **1996**, *2*, 398–402, DOI `10.1002/chem.19960020408`.

[160] X. Zhang, K. Seppelt, *Z. anorg. allg. Chem.* **1998**, *624*, 667–670, DOI `10.1002/(SICI)1521-3749(199804)624:4<667::AID-ZAAC667>3.0.CO;2-D`.

[161] C. Bolli, T. Köchner, C. Knapp, *Z. anorg. allg. Chem.* **2012**, *638*, 559–564, DOI `10.1002/zaac.201100448`.

[162] C. H. Switzer, T. W. Miller, P. J. Farmer, J. M. Fukuto, *J. Inorg. Biochem.* **2013**, *118*, 128–133, DOI `10.1016/j.jinorgbio.2012.09.022`.

[163] D. Teillet-Billy, F. Fiquet-Fayard, *J. Phys. B: At. Mol. Phys.* **1977**, *10*, L111–L117, DOI `10.1088/0022-3700/10/4/006`.

[164] M. E. Jacox, W. E. Thompson, *J. Chem. Phys.* **1990**, *93*, 7609–7621, DOI `10.1063/1.459392`.

[165] F. J. Lovas, E. Tiemann, *J. Phys. Chem. Ref. Data* **1974**, *3*, 609–770, DOI `10.1063/1.3253146`.

[166] B. J. Bozlee, J. H. Luther, M. Buraczewski, *J. Chem. Educ.* **1992**, *69*, 370, DOI `10.1021/ed069p370`.

[167] L. Freitag, S. Knecht, S. F. Keller, M. G. Delcey, F. Aquilante, T. B. Pedersen, R. Lindh, M. Reiher, L. González, *Phys. Chem. Chem. Phys.* **2015**, *17*, 14383–14392, DOI `10.1039/C4CP05278A`.

[168] M. Kaupp, *J. Comput. Chem.* **2007**, *28*, 320–325, DOI `10.1002/jcc.20522`.

[169] K. Boguslawski, C. R. Jacob, M. Reiher, *J. Chem. Theory Comput.* **2011**, *7*, 2740–2752, DOI `10.1021/ct1006218`.

[170] S. Begel, F. W. Heinemann, G. Stopa, G. Stochel, R. van Eldik, *Inorg. Chem.* **2011**, *50*, 3946–3958, DOI `10.1021/ic1023357`.

[171] Sigma-Aldrich, Ascarite II Adsorbents, **2018**, `https://www.sigmaaldrich.com/chemistry/chemical-synthesis/learning-center/technical-bulletins/al-1430/ascarite-ii-adsorbents.html` (visited on 05/28/2018).

[172] G. M. Sheldrick, *Acta Crystallogr. A* **2015**, *71*, 3–8, DOI `10.1107/S2053273314026370`.

[173] G. M. Sheldrick, *Acta Crystallogr. C* **2015**, *71*, 3–8, DOI `10.1107/S2053229614024218`.

[174] C. B. Hübschle, G. M. Sheldrick, B. Dittrich, *J. Appl. Cryst.* **2011**, *44*, 1281–1284, DOI `10.1107/S0021889811043202`.

[175] A. L. Spek, *Acta Cryst D* **2009**, *65*, 148–155, DOI `10.1107/S090744490804362X`.

[176] G. M. Sheldrick, *CELL_NOW Version 2008/4*, Göttingen, Germany: Georg-August-Universität Göttingen, **2008**.

[177] L. J. Farrugia, *J. Appl. Cryst.* **2012**, *45*, 849–854, DOI `10.1107/S0021889812029111`.

[178] C. F. Macrae, P. R. Edgington, P. McCabe, E. Pidcock, G. P. Shields, R. Taylor, M. Towler, J. van de Streek, *J. Appl. Cryst.* **2006**, *39*, 453–457, DOI `10.1107/S002188980600731X`.

[179] C. F. Macrae, I. J. Bruno, J. A. Chisholm, P. R. Edgington, P. McCabe, E. Pidcock, L. Rodriguez-Monge, R. Taylor, J. van de Streek, P. A. Wood, *J. Appl. Cryst.* **2008**, *41*, 466–470, DOI `10.1107/S0021889807067908`.

[180] P. of Vision Pty. Ltd., *Persistence of Vision (TM) Raytracer.* Williamstown, Victoria, Australia.: Persistence of Vision Pty. Ltd., **2004**.

[181] P. G. Potvin, JASPER - JavaScript Percentage Elemental Calculator v2.0.PGP, `http://www.yorku.ca/pgpotvin/public/Jasper/jasper2.htm` (visited on 11/20/2019).

[182] F. Neese, *Wiley Interdiscip. Rev. Comput. Mol. Sci.* **2012**, *2*, 73–78, DOI `10.1002/wcms.81`.

[183] S. Grimme, S. Ehrlich, L. Goerigk, *J. Comput. Chem.* **2011**, *32*, 1456–1465, DOI `10.1002/jcc.21759`.

[184] R. Bauernschmitt, R. Ahlrichs, *Chem. Phys. Lett.* **1996**, *256*, 454–464, DOI `10.1016/0009-2614(96)00440-X`.

[185] F. Furche, R. Ahlrichs, *J. Chem. Phys.* **2002**, *117*, 7433–7447, DOI `10.1063/1.1508368`.

[186] E. D. Glendening, J. K. Badenhoop, A. E. Reed, J. E. Carpenter, J. A. Bohmann, C. M. Morales, C. R. Landis, F. Weinhold, *NBO 6.0.* Theoretical Chemistry Institute, University of Wisconsin, Madison, WI, **2013**.

[187] F. Cortés-Guzmán, R. F. W. Bader, *Coord. Chem. Rev.* **2005**, *249*, 633–662, DOI `10.1016/j.ccr.2004.08.022`.

[188] J. Cirera, E. Ruiz, S. Alvarez, *Chem. Eur. J.* **2006**, *12*, 3162–3167, DOI `10.1002/chem.200501516`.

[189] S. Alvarez, P. Alemany, D. Casanova, J. Cirera, M. Llunell, D. Avnir, *Coord. Chem. Rev.* **2005**, *249*, 1693–1708, DOI `10.1016/j.ccr.2005.03.031`.

[190] G. A. Andrienko, *Chemcraft - Graphical Program for Visualization of Quantum Chemistry Computations*, **2019**.

Danksagung

Mein größter Dank gebührt Prof. Dr. Peter Klüfers, der mich herzlich in seinen Arbeitskreis aufgenommen und mir das Vertrauen geschenkt hat, dieses interessante Thema mit großem wissenschaftlichen Freiraum zu bearbeiten. Er hatte dabei stets ein offenes Ohr und die Geduld sämtliche Fragen genauestens zu klären.

Prof. Dr. Hans-Christian Böttcher möchte ich für das Erstellen des Zweitgutachtens und die stete Hilfsbereitschaft in allen Belangen der Koordinationschemie danken.

Prof. Dr. Wolfgang Beck, Prof. Dr. Lena Daumann, Prof. Dr. Florian Kraus und Prof. Dr. Fritz Wagner danke ich für die Mitwirkung in der Promotionskommission.

Lida Holowatyj-den Toom danke ich für ihre unermüdliche Hilfe in allen organisatorischen Belangen, ihre immerwährende herzliche Art und die aufmerksame Korrektur der vorliegenden Arbeit.

Christine Neumann möchte ich dafür danken, dass sie mir und dem gesamten Arbeitskreis im Labor immer und aufopferungsvoll mit Rat und Tat zur Seite gestanden ist.

Dr. Peter Mayer danke ich für die stets kompetente Hilfe in allen Fragen der Einkristallstrukturanalyse und für die geduldige Einführung in die Praxis der Einkristalldiffraktometrie.

Sandra Albrecht, Dr. Anja Belz, Helen Funk, Areenan In-Iam und Dr. Peter Mayer danke ich für das anfängliche Messen meiner Einkristalle und die vielen hilfreichen Tipps für meine eigene Aufsetzertätigkeit.

Dem gesamten Analytik-Team danke ich für die gewissenhafte Bearbeitung meiner Proben.

Prof. Dr. Fritz Wagner an der TU München danke ich für die freundliche und geduldige Anfertigung von Mößbauerspektren.

Prof. Dr. Dominik Schaniel an der Université de Lorraine danke ich für die Betreuung während meines Aufenthalts in Nancy und für die geduldige Durchführung von zeitaufwändigen PLI-Experimenten an meinen Proben.

Jan Heinemann, Torsten Ampßler und Jens Popp danke ich vielmals für das aufmerksame Korrekturlesen dieser Arbeit.

Daniel Schröder danke ich für die Anfertigung von EOS-Rechnungen meiner Verbindungen, die ihm letztlich den Verstand raubten.

Oliver Richter danke ich für die sorgfältige Einarbeitung als Experimentator in der ACI-Vorlesung und die Einführung in die "Magic the Gathering"-Sucht.

Meinen Praktikanten Elen Baumann, Aylin Hirschvogel, Erol Ceylan, Henryk Laqua, Hyunzun Song und Sophie Gutenthaler danke ich für den vielen Fleiß und die Freude mit denen sie an meinen Themenstellungen gearbeitet haben.

Dem gesamten Arbeitskreis Klüfers und insbesondere meinen Laborkollegen Christine Neumann, Helen Funk, Bianca Aas und Jan Heinemann danke ich für die immer gute Atmosphäre, die interessanten Gespräche, die Hilfbereitschaft, die vielen $\mathrm{km\,h^{-1}}$ an Spaß und die insgesamt schöne Zeit im AK Klüfers. Es war mir ein Fest!

Steffi und meiner Familie danke ich dafür, dass sie immer und bedingungslos für mich da sind. Für euch habe ich das alles gemacht und ohne euch wäre es nicht möglich gewesen. Vielen Dank!